

**TEFLON AF COMPOSITE MATERIALS IN MEMBRANE SEPARATION AND
MOLECULAR RECOGNITION IN FLUOROUS MEDIA**

by

Hong Zhang

BS, Nanjing University, 2005

Submitted to the Graduate Faculty of the
Dietrich School of Arts and Science
in partial fulfillment
of the requirements for the degree of
Doctor of Philosophy

University of Pittsburgh

2013

UNIVERSITY OF PITTSBURGH

Dietrich School of Arts and Sciences

This dissertation was presented

by

Hong Zhang

It was defended on

November 26th, 2013

and approved by

Dennis P. Curran, Professor, Department of Chemistry

Robert M. Enick, Professor, Department of Chemical and Petroleum Engineering

David H. Waldeck, Professor, Department of Chemistry

Dissertation Advisor: Stephen G. Weber, Professor, Department of Chemistry

**TEFLON AF COMPOSITE MATERIALS IN MEMBRANE SEPARATION AND
MOLECULAR RECOGNITION IN FLUOROUS MEDIA**

Hong Zhang, PhD

University of Pittsburgh, 2013

The unique nature of fluoropolymers makes them potentially valuable in partitioning based separations and sensing. Molecular diffusion and partitioning determine the selectivity of a chemical separation or sensor based on a polymer film. Unlike in the liquid phase where diffusion and partitioning can be estimated by empirical methods, the physical properties including fractional free volume (FFV) as well as dynamics of polymer chains significantly impact diffusion and partitioning. Therefore, this work is focused on developing a fundamental understanding of solute transport behavior across Teflon AF 2400 composite films in liquid phase.

Three types of Teflon AF 2400 (AF) composite films including AF/FC-70, AF/fluorophilic silica nanoparticles (FNPs), and AF/FNP/FC-70 were investigated for the selective transport of fluorinated molecules against their hydrocarbon counterparts. AF films alone have a large FFV that, in the presence of liquids, absorbs them making the AF films less fluororous. AF/FC-70 films show lower FFV, less sorption of CHCl_3 , and restore the fluorophilicity of the film with an increase in transport selectivity. AF/FNP composites containing ≥ 50 wt% FNP show a significant increase of FFV, sorption of CHCl_3 , increased solute permeability, and decreased transport selectivity. AF/FNP/FC-70 composites represent a novel type of composite film: the soft AF/FC-70 phase which is not dimensionally stable by

itself is well supported by the FNPs. The AF/FC-70 phase in the three-component film shows low CHCl_3 sorption, and high solute permeability as well as transport selectivity.

Molecular recognition-based extractions based on fluorocarbon matrices should be highly selective. To gain a quantitative understanding of noncovalent interactions in fluorocarbons, the association of perfluorodecanoic acid with pyridine and quinazoline (separately) was investigated via isothermal titration calorimetry (ITC). Thermodynamic data show the formation of complexes with acid:base (HA:B) stoichiometry greater than 1:1. Proton transfer occurs as follows: $\text{HA}_2\text{B} + \text{HA} \rightarrow \text{HA}_2\text{A}^- \cdot \text{HB}^+$. The high, favorable free energy of complex formation between organic compounds and perfluorinated molecular receptors can serve as the driving force to improve molecular receptor-based extraction and sensing in fluororous media.

TABLE OF CONTENTS

PREFACE	XX
1.0 INTRODUCTION	1
1.1 FLUOROUS MEDIA	1
1.2 TEFLON AF FAMILY	3
1.2.1 Free Volume of Teflon AFs	5
1.2.2 Gas Transport and Pervaporation	8
1.2.3 Liquid Phase Transport	15
1.3 MOLECULAR RECOGNITION	18
1.4 OBJECTIVE AND MOTIVATION	21
2.0 PROPERTIES AND TRANSPORT BEHAVIOR OF PERFLUOROTRIPENTYLAMINE (FC-70)-DOPED AMORPHOUS TEFLON AF 2400 FILMS	25
2.1 INTRODUCTION	25
2.2 EXPERIMENTAL	28
2.2.1 Materials	28
2.2.2 Film Preparation and Morphological Characterization	29
2.2.3 Film Density Measurement and Fractional Free Volume	30
2.2.4 Dynamical Mechanical Analysis	31

2.2.5	Sorption and Desorption of Chloroform in FC-70-doped Teflon AF 2400 Films.....	32
2.2.6	Transport of Solutes Through Films.....	33
2.2.7	Determination of Solute Diffusion Coefficients (<i>D</i>) and Partition Coefficients (<i>K</i>).....	34
2.2.8	Recycling of Teflon AF 2400	36
2.3	RESULTS AND DISCUSSION	37
2.3.1	Characterization of FC-70-doped Teflon AF 2400 Films.....	37
2.3.2	Density and Free Volume of FC-70-doped Teflon AF 2400 Films	38
2.3.3	Sorption of Chloroform in Doped Films.....	43
2.3.4	Dependence of Permeability Coefficients (<i>P</i>), Diffusion Coefficients (<i>D</i>), and Partition Coefficients (<i>K</i>) on Film Composition	46
2.3.5	Transport Selectivity of FC-70-doped Teflon AF Films Based on Different Substitutions.....	57
2.3.6	Recycling of Teflon AF 2400	58
2.4	CONCLUSION	59
2.5	ACKNOWLEDGEMENT	60
3.0	PROPERTIES AND TRANSPORT BEHAVIOR OF TEFLON AF 2400 NANOCOMPOSITE FILMS.....	61
3.1	INTRODUCTION	61
3.2	EXPERIMENTAL.....	63
3.2.1	Materials	63
3.2.2	Surface Modification and Characterization of Silica Nanoparticles	64

3.2.3	Preparation of the Composite Films	65
3.2.4	Morphological, Mechanical, Sorption, and Transport Properties of the Composite Films.....	66
3.2.5	Film Density Measurement and Apparent Fractional Free Volume (aFFV)	70
3.2.6	Radius of Gyration (R_g) of Teflon AF 2400	71
3.3	RESULTS AND DISCUSSION	72
3.3.1	Fluorophilic Nanoparticle Characterization	72
3.3.2	Morphology of Teflon AF Composite Films.....	75
3.3.3	Density and Apparent Free Volume of Teflon AF/FNP Composite Films.....	78
3.3.4	T_g , ΔC_p at T_g , and modulus of Teflon AF/FNP Composite Films and R_g of Teflon AF	79
3.3.5	Sorption of Chloroform in Teflon AF/FNP Composite Films	82
3.3.6	Solute Permeability (P) and Selectivity through Teflon AF/FNP Composite Films.....	83
3.3.7	Mechanical Properties of Teflon AF/FNP/FC-70 Composite Films.....	86
3.3.8	aFFV _P of Teflon AF/FNP/FC-70 Composite Films	86
3.3.9	aFFV _P Characteristics Differ in 2- and 3-component Films	87
3.3.10	Transport Properties of Teflon AF/FNP/FC-70 Composite Films	89
3.4	CONCLUSION	92
3.5	ACKNOWLEDGEMENT	93
4.0	PREPARATION AND APPLICATIONS OF POROUS TEFLON AF 2400	95

4.1	INTRODUCTION	95
4.2	EXPERIMENTAL.....	98
4.2.1	Materials	98
4.2.2	Preparation and Characterization of Porous Teflon AF 2400 Films.....	98
4.2.3	Transport of Solutes through Films	100
4.2.4	Preparation, Characterization, and Transport of Fluorescent Nanoparticles Across Porous Teflon AF 2400 Films	101
4.2.5	Immobilization of Fluorous Tag on Porous Teflon AF 2400 Matrix ...	104
4.2.6	Porous Teflon AF Templated Synthesis of Porous Poly(styrene-divinylbenzene).....	104
4.3	RESULTS AND DISCUSSION	105
4.3.1	Characterization of Porous Teflon AF 2400 Films	105
4.3.2	Transport Properties of Krytox Filled Porous Teflon AF 2400 Films.	111
4.3.3	Size-based Separation of Nanoparticles.....	113
4.3.4	Porous Teflon AF 2400 Films as Microarray Substrate.....	122
4.3.5	Porous Teflon AF 2400 Templated Synthesis of Porous Hydrocarbon Polymer Matrix	125
4.4	CONCLUSION	127
4.5	ACKNOWLEDGEMENT	128
5.0	ISOTHERMAL TITRATION CALORIMETRY OF PERFLUORODECANOIC ACID WITH PYRIDINE AND QUINAZOLINE IN AN ORGANIC, A SEMI-FLUORINATED AND A PERFLUORONATED SOLVENT	129
5.1	INTRODUCTION	129

5.2	EXPERIMENTAL.....	131
5.2.1	Materials	131
5.2.2	Isothermal Titration Calorimetry (ITC)	131
5.2.3	Analysis of Isothermal Titration Calorimetry Data	132
5.3	RESULTS AND DISCUSSION.....	135
5.3.1	Effects of Solvent and Temperature on the Dimerization of PFDA.....	135
5.3.2	Thermodynamics of PFDA-quinazoline Complex Formations in FC-77, HFE-7500, and 1-chloropentane.....	138
5.3.3	Thermodynamics of PFDA-pyridine Complex Formations in FC-77, HFE-7500, and 1-chloropentane.....	144
5.3.4	Discussion.....	149
5.4	CONCLUSION	154
5.5	ACKNOWLEDGEMENT	155
6.0	SUMMARY AND FUTURE DIRECTIONS.....	156
	APPENDIX A.....	158
	APPENDIX B.....	162
	BIBLIOGRAPHY.....	179

LIST OF TABLES

Table 1-1. Properties of Teflon AFs.	4
Table 1-2. Radius of free volume elements (\AA) in Teflon AF 2400 from various methods.....	6
Table 1-3. Structures Sorption of organic liquids in Teflon AFs at 25 °C.....	15
Table 2-1. Storage Modulus of FC-70-doped Teflon AF Films at 20.0 °C.	42
Table 2-2. Summary of the Physical and Chemical Properties of FC-70-doped Teflon AF Films at 20.0 °C.....	43
Table 2-3. Comparison of Permeability Coefficients through Fresh Pure Teflon AF Film and Chloroform-soaked Pure Teflon AF Film at 20.0 °C.....	44
Table 2-4. Solute Partition Coefficients (FC-70/ CHCl_3) at 20.0 °C.	51
Table 2-5. Structures Properties of the Fresh Teflon AF 2400 Films and Recycled Teflon AF 2400 Film.....	59
Table 3-1. A summary of physical, mechanical, chemical, and transport properties of composite Teflon AF films at 20.0 ± 1.0 °C.	77
Table 4-1. Selective transport of octafluorotoluene over toluene through porous Teflon AF 2400 based supported liquid membranes at 20.0 ± 1.0 °C.	112
Table 4-2. Zeta-potential of fluorescent silica nanoparticles in ethanol.	119

Table 5-1. Thermodynamic parameters of PFDA dimer formation obtained from fitting ITC titration curves.	137
Table 5-2. Thermodynamic parameters of PFDA and quinazoline complex formations obtained from fitting ITC titration curves.	143
Table 5-3. Thermodynamic parameters of PFDA and pyridine complex formations obtained from fitting ITC titration curves.	148
Table 5-4. Stoichiometry of complex formations between PFDA and quinazoline/pyridine.....	150
Table A-1. Density analysis of Teflon AF/FNP/FC-70 films (70 wt% FNP).	158

LIST OF FIGURES

Figure 1-1. Structure of Teflon AF.....	4
Figure 1-2. Accessible free volume distributions for the positronium probe molecule ($R = 1.1 \text{ \AA}$) in Teflon AF 2400.....	7
Figure 1-3. Visualization of chain packing and free volume distribution from molecular modeling.	7
Figure 1-4. Effect of critical volume on infinite dilution gas permeability at 35 °C.....	9
Figure 1-5. The dependence of permeability coefficients through Teflon AF 2400 films on feed pressure at 35 °C.....	11
Figure 1-6. The dependence of positron lifetime on the dopant weight percentage (A); Effect of critical volume on gas permeability at 25 °C (B): $\Delta p = 3.4 \text{ atm}$ for H_2 , O_2 , N_2 , CH_4 ; $\Delta p = 0.33$ to 3.4 atm for <i>n</i> -butane.....	13
Figure 1-7. The effect of chloroform sorption by Teflon AF 2400 is shown by the thermodynamic cycles of the partitioning of benzene vapor, benzene in chloroform, and benzene in Teflon AF 2400 membranes in the gas and solution phases.....	16
Figure 1-8. Dependence of permeability coefficients on the molecular weight of solutes.....	18
Figure 1-9. Artificial molecular receptor ($R = 1\text{-propyl}$) binding with phenobarbital.	19
Figure 1-10. Proposed structure of 3:1 complex from Krytox 157 FSH and pyridine.	21

Figure 2-1. Structures of polymer and dopants: Teflon AF 2400 (n = 13 mol %, m = 87 mol %), Krytox FSH (7000-7500), and FC-70.....	28
Figure 2-2. FT-IR spectra of Teflon AF films doped with various amounts of FC-70 (wt %)..	37
Figure 2-3. Cross-section SEM micrographs of (a) a pure Teflon AF film and (b) a Teflon AF film doped with 30 wt % FC-70.	38
Figure 2-4. Cross Dependence of film density (20.0 ± 1.0 °C) on FC-70 content (wt %).	39
Figure 2-5. Cross Concentration ratio of Teflon AF 2400 polymer in the doped films over a pure film was plotted against the weight percentage of FC-70 in the film.....	40
Figure 2-6. Dependence of FFV on FC-70 content (wt %)..	41
Figure 2-7. Sorption of chloroform in FC-70-doped Teflon AF films.	45
Figure 2-8. Permeability coefficients of solutes in FC-70-doped films at 20.0 ± 1.0 °C	48
Figure 2-9. Diffusion coefficients of solutes in FC-70-doped Teflon AF 2400 films at 20.0 ± 1.0 °C.	50
Figure 2-10. Partition coefficients of solutes in FC-70-doped films at 20.0 ± 1.0 °C.....	53
Figure 2-11. Selectivity of partitioning based on different fluorine substitutions.....	55
Figure 2-12. Partitioning selectivities of octafluorotoluene over toluene in FC-70-doped (0-30 wt %) Teflon AF films were plotted against the product of partitioning selectivities of trifluoromethyl/methyl and perfluorophenyl/phenyl groups	55
Figure 2-13. Transport selectivity based on the substitution of fluorine atoms (8F, 5F, 3F) at 20.0 ± 1.0 °C.	58
Figure 3-1. (A) water contact angle of unmodified silica nanoparticles on a microscope slide; (B) water contact angle of fluoroalkylsilane-modified silica nanoparticles on a microscope slide...	72
Figure 3-2. TEM micrographs of the silica nanoparticles.	73

Figure 3-3. DSC curves of unmodified (black lines), octylsilane modified (blue lines) and fluoroalkylsilane modified (magenta lines) silica nanoparticles	74
Figure 3-4. Cross-sectional SEM images of Teflon AF 2400 films containing various weight percentages of FNP and FC-70.....	76
Figure 3-5. Tan(δ) curves of fluorophilic silica nanoparticle doped Teflon AF 2400 films.	80
Figure 3-6. Change of heat capacity at the glass transition of FNP doped Teflon AF 2400 films	80
Figure 3-7. The logarithms of the permeability coefficients of toluene, octafluorotoluene, and naphthalene through composite Teflon AF 2400 films at 20.0 ± 1.0 °C.	83
Figure 3-8. Diffusion coefficient of NPTH versus $1/aFFVP$ of the composite Teflon AF films at 20.0 ± 1.0 °C	85
Figure 3-9. The logarithms of the permeability coefficients of toluene and octafluorotoluene through composite Teflon AF 2400 films at 20.0 ± 1.0 °C.....	90
Figure 3-10. The transport selectivity of OFT over TOL through composite Teflon AF 2400 films at 20.0 ± 1.0 °C	90
Figure 3-11. Diffusion coefficients of solutes in composite Teflon AF films at 20.0 ± 1.0 °C....	91
Figure 3-12. Partition coefficients of solutes in composite Teflon AF films at 20.0 ± 1.0 °C	92
Figure 4-1. The experimental setup of nanoparticle transport across porous Teflon AF 2400 films.	103
Figure 4-2. The erosion of fluorophilic silica nanoparticles over time.....	106
Figure 4-3. SEM micrographs.....	108
Figure 4-4. N ₂ adsorption and desorption isotherms.	109
Figure 4-5. Water contact angle of a pure Teflon AF 2400 film	110

Figure 4-6. Permeability coefficients of toluene and octafluorotoluene through porous Teflon AF 2400 based supported liquid membranes at 20.0 ± 1.0 °C	112
Figure 4-7. TEM micrographs of the silica nanoparticles	114
Figure 4-8. The size distribution of nanoparticles	115
Figure 4-9. The fluorescence intensity of fluorescein tagged silica nanoparticle-100nm (1 mg/mL; excitation: 450 nm); rhodamine B tagged silica nanoparticle-128 nm (1 mg/mL; excitation: 510 nm).	116
Figure 4-10. Electroosmotic flow through porous Teflon AF 2400 film: (A) 0 h; (B) 96 h.	117
Figure 4-11. Transport of nanoparticles through porous Teflon AF films (96 hours, 3V).....	119
Figure 4-12. The fluorescence measure of nanoparticle transport through porous Teflon AF 2400 films (experimental setup: Figure 4-1; 96 hours; 3 volts; excitation: 510 nm).	120
Figure 4-13. The fluorescence measure of nanoparticle transport through porous Teflon AF 2400 films (experimental setup: Figure 4-1; 96 hours; 3 volts; excitation: 450 nm)	121
Figure 4-14. The structure of 1 ($Rf_6=(CF_2)_5CF_3$).	122
Figure 4-15. Fluorescence images (350 nm/455 nm) of Teflon AF films equilibrated with 15 μ M of 1 in ethanol (10% H ₂ O)	123
Figure 4-16. Non-covalent immobilization of 1 on porous Teflon AF 2400 films (blue) and solid Teflon AF films (black) on both film surfaces and cross sections	124
Figure 4-17. The structure of 2 ($Rf_6=(CF_2)_5CF_3$)	126
Figure 4-18. Cross-sectional SEM micrographs: (A) Poly(styrene-divinylbenzene) from bulk polymerization; (B) Poly(styrene-divinylbenzene) in porous Teflon AF 2400 matrix; (C) Poly(styrene-divinylbenzene) after the removal of Teflon AF template; (D) Elemental analysis of	

films in (A), (B), and (C). Note: the volume ratio of styrene to divinylbenzene in (A), (B), and (C) are 9:1.	127
Figure 5-1. Structures of perfluorodecanoic acid and two heterocyclic bases	131
Figure 5-2. ITC profile of PFDA dimer dissociation in FC-77 and HFE-7500 at 25, 35, and 45 °C.....	137
Figure 5-3. ITC profile of PFDA and quinazoline complex formations in FC-77, HFE-7500, and 1-chloropentane at 25, 35, and 45 °C.....	141
Figure 5-4. Enthalpy-entropy compensation of 1:1 complex between PFDA and quinazoline (black bars: ΔG° ; red bars: ΔH° ; blue bars: $-T\cdot\Delta S^{\circ}$).....	142
Figure 5-5. ITC profile of PFDA and pyridine complex formations in FC-77, HFE-7500, and 1-chloropentane at 25, 35, and 45 °C	146
Figure 5-6. Enthalpy-entropy compensation of 1:1 complex between PFDA and pyridine (black bars: ΔG° ; red bars: ΔH° ; blue bars: $-T\cdot\Delta S^{\circ}$).....	147
Figure 5-7. Heat capacity changes for association of PFDA with quinazoline/pyridine in FC-77	149
Figure 5-8. Enthalpy-entropy compensation of complex formation between PFDA and quinazoline/pyridine	151
Figure 5-9. Schematic structure of PFDA/pyridine complexes	151
Figure A-1. Low magnification cross-sectional SEM images of Teflon AF 2400 films containing various weight percentages of FNP and FC-70	159
Figure A-2. Cross-sectional SEM images of a Teflon AF 2400 film containing 15 wt% octylsilane modified silica nanoparticles.....	160
Figure A-3. Isotherm plot of pure Teflon AF 2400 and 70 wt% FNP doped Teflon AF 2400 ..	160

Figure A-4. Temperature derivative of heat capacity of FNP doped Teflon AF films.....	161
Figure A-5. New transition temperatures of Teflon AF/FC-70 system	161
Figure B-1. Contour map for the titration of PFDA with quinazoline in FC-77 at 25 °C	162

LIST OF ABBREVIATIONS

Activity coefficient (γ)

Apparent fractional free volume (aFFV)

Binding constant (K)

Change in heat capacity (ΔC_p)

Density (ρ)

Differential scanning calorimetry (DSC)

Diffusion coefficient (D)

Dipolarity (π^*)

Dynamic mechanical analysis (DMA)

Fluorophilic silica nanoparticle (FNP)

Fractional free volume (FFV)

Glass transition temperature (T_g)

Isothermal titration calorimetry (ITC)

Partition coefficient (K)

Perfluorodecanoic acid (PFDA)

Permeability (P)

Radius of gyration (R_g)

Scanning electron microscope (SEM)

Selectivity (S)

Standard enthalpy change (ΔH°)

Standard entropy change (ΔS°)

Standard free energy change (ΔG°)

Transmission electron microscope (TEM)

Viscosity (η)

Zeta potential (ξ)

PREFACE

I would like to take a moment to acknowledge the people who have contributed to my success in completing this dissertation.

First and foremost, I would like to express my gratitude to my research advisor and mentor, Professor Stephen Weber, who has given me the opportunity to grow into an independent scientist. None of this work would have been possible without his support and guidance. I am tremendously grateful for all the members in Dr. Weber's group, especially Dr. Yanhong Yang, Dr. Kristi Kauffman, Dajuan Lu, Sijia Wang, Anthony Horn, and Yiseul Cho. I really appreciate all of them for many nice help along the way.

I had the good fortune to work with a number of excellent collaborators. The research described in this dissertation would not have been possible without contributions from them. I especially would like to thank Dr. Hussam at George Mason University for the long term collaboration. I wish to thank Mr. Albert Stewart (Department of Mechanical Engineering & Materials Science) for the access and help on the SEM instrumentation, and Mr. Thomas Harper (Department of Biological Science) for access and help on the TEM. I appreciate Professor Yadong Wang and Ms. Britta Rauck (Department of Biongeering), and Professor Di Gao (Department of Chemical and Petroleum Engineering) for technical assistance, Professor Götz Vesper and Dr. Lu Whaley (Department of Chemical and Petroleum Engineering) for access to BET.

I owe special thanks to Professor Dennis Curran, Professor David Waldeck, and Professor Robert Enick, for the commitment of my doctoral committee. I really appreciate their input and invaluable advice for my training and education. In addition, I would like to thank Professor Alexander Star and Professor Tara Meyer for serving on my proposal committee. I am also very grateful to the faculty, staff, and fellow students in the Department of Chemistry. More importantly, their help and friendship make my time in Pitt a great memory. In addition, I must thank Bayer MaterialScience for 2010-2011 Graduate Student Fellowship and University of Pittsburgh for 2011-2012 Andrew Mellon Predoctoral Fellowship.

Last, but certainly not least, I appreciate all the support from my family members and friends. I extremely acknowledge my parents for their everlasting support to me. I am especially grateful to my husband, Dr. Yijun Huang, for his love and encouragement in my life. For that, I cannot thank you enough. This dissertation is also dedicated to my son, Andrew Huang. I would not be where I am today without them.

1.0 INTRODUCTION

Part of this chapter is from **Teflon AF Materials**, Zhang, H.; Weber, S. G. *Topics in Current Chemistry* **2012**, *308*, 307–337. Adapted with kind permission from Springer Science and Business Media (Licence numbers: 3278961061464 and 3278961395952). Zhang, H. wrote the paper under the guidance of Weber, S. G.

1.1 FLUOROUS MEDIA

Fluorous media are highly non-polar and notoriously poor solvents.¹ The “fluorous nature” of fluorocarbons refers to their macroscopic phase behavior. They (with few exceptions depending on temperature) exist as a third phase when in contact with water and organic solvents – widely regarded as the simultaneous hydrophobic and oleophobic nature.¹ This behavior has been explained in molecular terms based on experiment and theory. Compared to hydrocarbon analogs, fluorocarbons are more rigid and have a larger cross-sectional area, and they pack less densely and display much smaller van der Waals interaction energy per molecular contact area.^{2,3} Surfaces with fluorocarbon-containing modifications can be described as “fluorous”, for example, showing a high contact angle with water. So-called “fluorophilic” solutes, which are wholly or partly fluorocarbon, will adsorb to fluorous surfaces and preferentially partition from organic into fluorous solvents. This unique property of the fluorous media—exclusion of non-

fluorinated molecules—lead to broad applications including chemical separations in synthesis and catalysis,⁴ and novel biomaterials for biological and medical applications.⁵

Fluorous separation techniques widely used in synthetic community commonly rely on the covalently labeled fluorous tags.⁶ The phase separation strategy based on the covalent labeling of reagents or catalysts with fluorous tags has found a wide range of practical applications since 1990s.⁶⁻⁸ By taking advantage of organic reactions integrated with liquid-liquid extraction, fluorous biphasic synthesis^{9,10} and catalysis¹¹⁻¹³ as well as fluorous triphasic strategy¹⁴ were developed to facilitate product purification and the recycling of catalysts. Protocols relying on fluorous liquid-liquid extraction are particularly effective for the separation of “heavy fluorous” substances ($\geq 60\%$ w/w of fluorine content) from organics. For separating “light fluorous” compounds from hydrocarbons, fluorous liquid-solid extraction using “fluorous reverse phase silica gel” makes the ease of automation and parallel processing in combinatorial chemistry applications.^{6,10}

As a dimensionally stable fluorous matrix, perfluoropolymers are receiving increased attention in both the scientific community and industry. The most well-known property shared by perfluoropolymers is their extraordinary thermal and chemical stability due to the strong carbon-fluorine and carbon-carbon bonds.^{15,16} As an orthogonal phase to aqueous and organic media, perfluoropolymers are soluble only in perfluorinated solvents, Novec engineering liquids (hydrofluoroethers), and supercritical CO₂ under specified temperature and pressure conditions.¹⁵⁻¹⁸ These intrinsic features favor the long-term chemical and morphological stability of perfluoropolymers (e.g. as coatings, membranes, tubings, fibers, seals and etc.) in hostile environments. Notably, it is of practical importance that perfluoropolymers feature low surface energy, therefore, they display much less non-specific adsorption than other polymeric materials

when exposed to biological fluids.^{19,20} A wide range of perfluoropolymer-based materials have been designed and evaluated as anti-fouling coatings.⁵ Fluorous surfaces with patterned post-functionalization offer valuable platforms for directed cell growth, and bio-analytical assays.²¹⁻²³

1.2 TEFLON AF FAMILY

Among commercially available perfluoropolymers, the Teflon AF family (**Figure 1-1**) is an unusual class of amorphous glassy copolymers with a high fractional free volume (FFV).²⁴⁻²⁶ Teflon AFs are copolymers of tetrafluoroethylene (TFE) and 2,2-bis(trifluoromethyl)-4,5-difluoro-1,3 dioxole (BDD). Two types of Teflon AF, produced by DuPont, are now available in market: Teflon AF 2400 (TFE: 13 mol%; BDD: 87 mol%) and Teflon AF 1600 (TFE: 35 mol%; BDD: 65 mol%). Some important physical, chemical, and mechanical properties of Teflon AFs are listed in **Table 1-1**.²⁷⁻²⁹ Thin coatings and films of Teflon AFs are optically transparent over a wide range (200-2000 nm), which makes them ideal media for the investigation of intermolecular interactions.^{1,30} Moreover, Teflon AFs exhibit a lower refractive index and dielectric constant than any other solid organic polymer known.^{31,32} Thus, Teflon AFs are recognized as eligible materials for optoelectronic devices (e.g. coatings on waveguide devices),³⁰ and functional coatings allowing the manipulation of tiny amounts of liquids by electrowetting for microfluidics and microreactors.³³⁻³⁵ The most unique feature of Teflon AFs is their high free volume (size, amount, and size distribution), which pioneered their applications in the field of membrane separations.

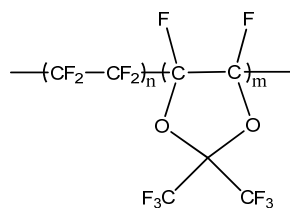


Figure 1-1. Structure of Teflon AF.

Teflon AF 2400: $n = 13$ mol%; $m = 87$ mol%; Teflon AF 1600: $n = 35$ mol%; $m = 65$ mol%.

Table 1-1. Properties of Teflon AFs^{1,27,29}

Property	Teflon AF 2400	Teflon AF 1600
Crystallinity	None	None
M_w (kDa)	300	100
T_g ($^{\circ}\text{C}$)	240 ± 10	160 ± 10
Density (g/cm^3)	1.75	1.82
FFV (%)	33.4	30.0
Refractive index	1.29	1.31
Dielectric constant	1.9	2.1
Contact angle with water ($^{\circ}$)	105	104
Critical surface energy (dyn/cm)	15.6	15.7
Permeability O_2 (barrer)	1140	170
Solubility	1.90	1.93
Common organic solvents	None	None
Perfluorinated solvents	C_6F_6 , $\text{C}_6\text{H}_5\text{CF}_3$, FC-72, etc.	C_6F_6 , $\text{C}_6\text{H}_5\text{CF}_3$, FC-72, etc.
Tensile strength (MPa, 23°C)	26.4 ± 1.9	26.9 ± 1.5
Elongation at Break (% , 23°C)	7.9 ± 2.3	17.1 ± 5.0

1.2.1 Free Volume of Teflon AFs

A polymer in amorphous form usually has significantly larger free volume than the same polymer in crystalline form because of the inefficient packing of disordered chains in the amorphous regions.²⁶ Both Teflon AF 2400 and Teflon AF 1600 are completely amorphous. The high FFV of Teflon AFs is responsible for a number of their successful applications in sensors and separations. Teflon AFs possess the two criteria for permeability according to the contemporary wisdom on highly permeable polymers, namely the presence of bulky non-polar structures and rigid main chains to create large barriers to rotation.^{36,37} As reported by Yampolskii and his coworkers, the rotation barrier for two neighboring dioxolane rings is as high as 60 kJ/mol.²⁶ These structural characteristics combined with the weak van der Waals interactions between fluorocarbon chains give Teflon AFs a high free volume.

Many experimental techniques have been designed to probe the size of free volume elements in Teflon AFs: ¹²⁹Xe NMR spectroscopy, positron annihilation lifetime spectroscopy (PALS), and inverse gas chromatography (IGC).^{24,25,38} The free volume size distributions of amorphous Teflon AFs determined by various techniques are summarized in **Table 1-2**.^{24,38,39} Teflon AF 1600 shows smaller free volume elements than Teflon AF 2400. This is probably due to the presence of fewer dioxolane rings in Teflon AF 1600. Both ¹²⁹Xe NMR spectroscopy and IGC measure the average size of free volume elements, whereas PALS is able to discover both the free volume size distribution and the amount of free volume.^{25,39} Positrons in Teflon AFs have two lifetimes, indicating two populations of free volume elements.³⁹ **Figure 1-2** shows the bimodal distribution of free volume elements in Teflon AF 2400 based on $V_{\text{connected}}$ and

R_{max} approaches.³⁹ Molecular modeling reveals a qualitative impression of the free volume distribution and morphology in Teflon AFs (**Figure 1-3**).^{26,39} Clearly, two types of qualitatively different free volume elements are present in Teflon AFs. The first type, with high segmental packing around it, resembles the free volume in conventional low free volume glassy polymers. The other type features a large size. Large, preexisting free volume elements will require much less activation energy for the diffusion and dissolution/partitioning of guest molecules in the polymeric matrix. The large free volume of Teflon AFs and for Teflon AF 2400 in particular, makes the amorphous Teflon AF materials valuable materials in the field of membrane separations. More will be discussed below on controlling the free volume in Teflon AF composite films.

Table 1-2. Radius of free volume elements (Å) in Teflon AF 2400 from various methods^{24,38,39}

Polymer	PALS				¹²⁹ Xe-NMR		IGC		
	R_{sp}		R_c		R_{sp}	R_c	$R(V_w)$	$R(V_b)$	$R(V_c)$
	R_3	R_4	R_3	R_4					
Teflon AF 2400	2.7	6.0	3.7	6.3	8.04 ^a	5.12 ^a	3.6	4.7	6.4
					7.83 ^b	5.02 ^b			
Teflon AF 1600	2.5	4.9		5.4	6.66	4.43	3.1	4.0	5.5

^a powder. ^b film. R_{sp} represents the data obtained by assuming spherical micro voids; R_c represents the data obtained by assuming cylindrical micro voids; R_3 , R_4 correspond to the radii deduced from the presence of two lifetimes. The quantitative determination of the volume of the free volume elements depends on the molecular volume of the probe solute. As the molecular volume may be determined in different ways, the measurement of the volume of the free volume elements depends on the choice of which one to use. V_w , V_b , V_c represent are the volumes of the free volume elements based on the solute's van der Waals volume, molecular volume in the liquid phase at the boiling point T_b , and the critical volume respectively.

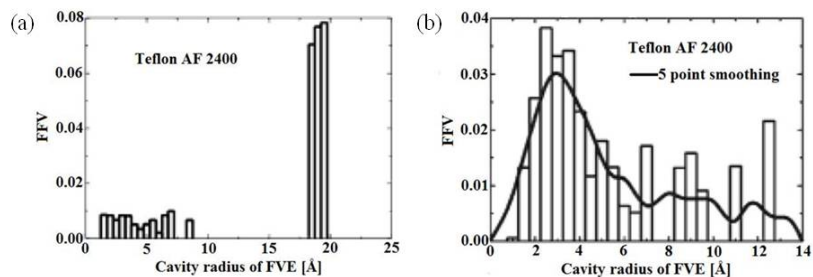


Figure 1-2. Accessible free volume distributions for the positronium probe molecule ($R = 1.1 \text{ \AA}$) in Teflon AF 2400: (a) $V_{\text{connected}}$; (b) R_{max} .³⁹ Adapted with permission from (**Molecular Modeling Investigation of Free Volume Distributions in Stiff Chain Polymers with Conventional and Ultrahigh Free Volume: Comparison between Molecular Modeling and Positron Lifetime Studies.** Hofmann, D.; Entrialgo-Castano, M.; Lerbret, A.; Heuchel, M.; Yampolskii, Y. *Macromolecules* **2003**, *36*, 8535.). Copyright (2013) American Chemical Society.

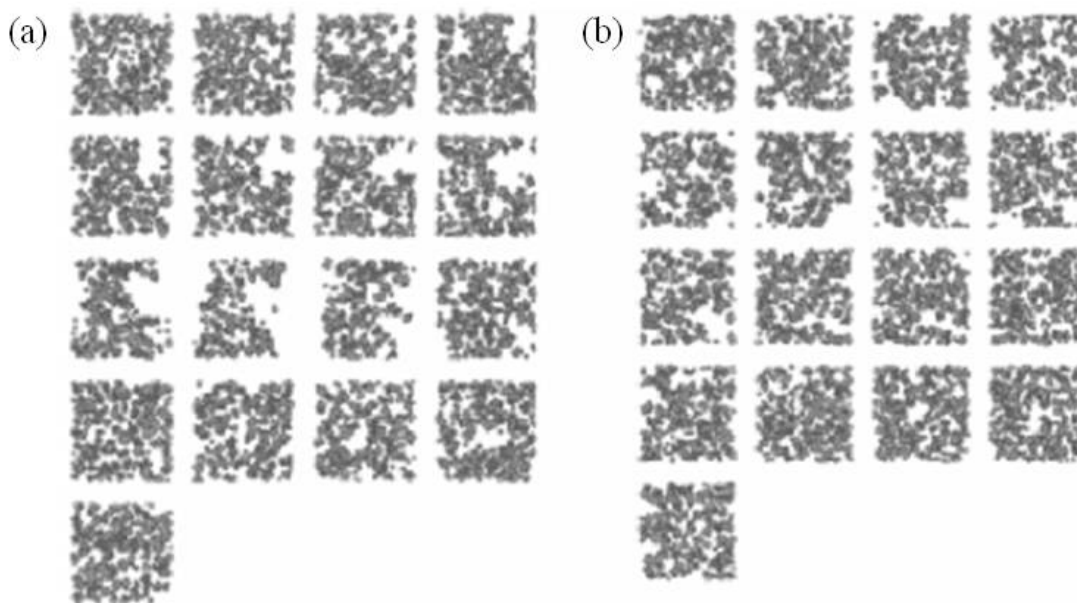


Figure 1-3. Visualization of chain packing and free volume distribution from molecular modeling (InsightII/Discover software of Accelrys Inc, COMPASS force field) by assuming cubic packing of macromolecules into the blocks: (a) Teflon AF 2400; (b) Teflon AF 1600. The average length of the sides of the blocks is between 45 \AA and 50 \AA . The figures present a series of approximately monatomic parallel planes of the block cut perpendicular to the z axis with the distance between each two continuous planes of about 3 \AA .^{26,39} Adapted with permission from (**Molecular Modeling Investigation of Free Volume Distributions in Stiff Chain Polymers**

with Conventional and Ultrahigh Free Volume: Comparison between Molecular Modeling and Positron Lifetime Studies. Hofmann, D.; Entrialgo-Castano, M.; Lerbret, A.; Heuchel, M.; Yampolskii, Y. *Macromolecules* **2003**, *36*, 8532.). Copyright (2013) American Chemical Society.

1.2.2 Gas Transport and Pervaporation

Mass transport of gaseous species across membranes depends upon the diffusion (D) and partition coefficient (S) of gases in the membrane. Penetrants (atoms or molecules in the gas phase that partition into a membrane) first dissolve into the membrane surface contacting the feed flow, and then diffuse across the membrane, finally partitioning into the permeate flow. The permeability coefficients (P) can be expressed as:⁴⁰

$$P = D \cdot S \quad (2-1)$$

The transport selectivity through membrane is defined as:^{40,41}

$$S = \frac{P_A}{P_B} = \left(\frac{D_A}{D_B} \right) \cdot \left(\frac{S_A}{S_B} \right) \quad (1-2)$$

Glassy and rubbery polymers are known to display different behavior in gas transport.⁴² The separation of gases by selective transport through rubbery polymer membranes is primarily caused by differences in the solubility whereas the separation by glassy polymer membranes is mainly by differences in the gas diffusivity.^{41,42} Therefore, glassy polymer membranes normally separate gaseous species in a size-sieving manner. Exceptions do exist for some glassy polymers with high free volume, for example, poly(1-trimethylsilyl-1-propyne) (PTMSP, FFV = 32%).^{41,43} As shown in **Figure 1-4(A)**, gas permeability through PTMSP membranes increases along with the increase of critical volume.⁴³ The more condensable gaseous species with higher molar volume are more permeable due to their higher solubility in PTMSP matrices.^{41,43} The gas

permeability through Teflon AF 2400 is second only to PTMSP.^{41,43,44} However, gas transport through Teflon AF 2400 membranes follows the general trend of size-sieving, which is similar (although permeabilities are larger) to the behavior of low free volume glassy polymers (e.g. polysulfone, polycarbonate, and etc.).^{41,43,44} Notably, the decrease in permeability as critical volume increases is much less than that for polysulfone. An interesting example shown in **Figure 1-4** is that C_3F_8 displays even higher transport rate than its homolog- C_2F_6 , which has smaller critical volume and is favored by diffusion. Therefore, gas transport behavior through Teflon AF 2400 membranes may be intermediate between PTMSP and classical low free volume glassy polymers depending on the solubility of the penetrant.^{43,44} Compared to Teflon AF 2400, Teflon AF 1600 has a lower free volume, and is less permeable to gases.

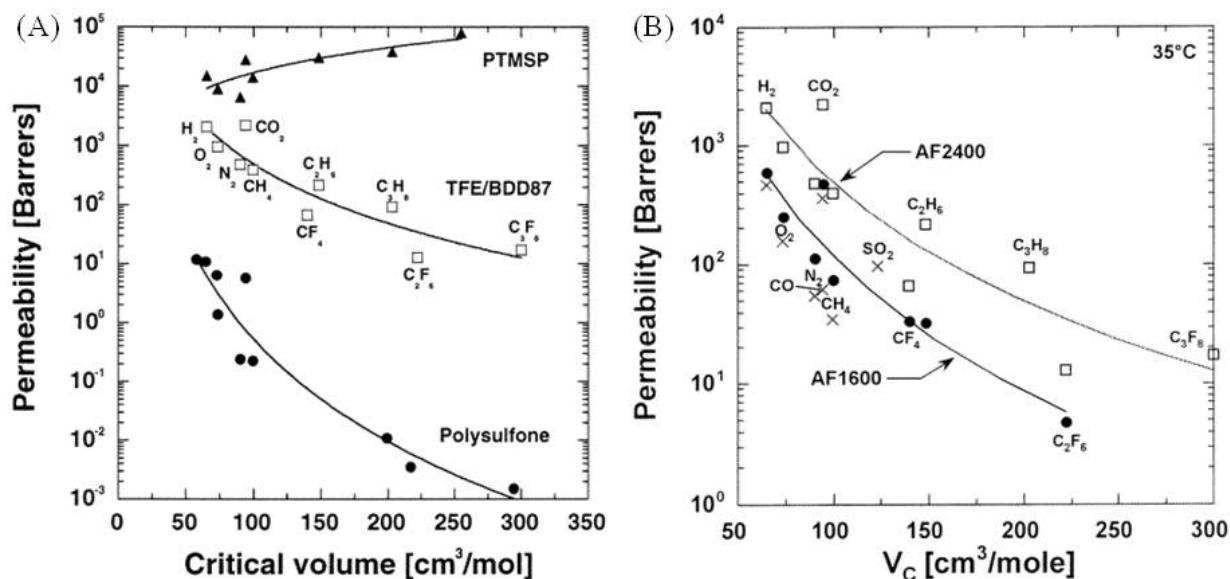


Figure 1-4. Effect of critical volume on infinite dilution gas permeability at 35 °C: (A) in PTMSP, Teflon AF 2400, and polysulfone; (B) in Teflon AF 2400 and Teflon AF 1600.^{43,44} Adapted with permission from (Gas Sorption, Diffusion, and Permeation in Poly(2,2-bis(trifluoromethyl)-4,5-difluoro-1,3-dioxole-co-tetrafluoroethylene. Merkel, T. C.; Bondar, V.; Freeman, B. D.; Yampolskii, Yu. P. *Macromolecules* **1999**, *32*, 8435. **Gas and Vapor Sorption, Permeation, and Diffusion in Glassy Amorphous Teflon AF 1600.** Alentiev, A. Y.; Shantarovich, V.

The gas permeability at a certain temperature relies not only on the nature of the penetrant and polymeric membrane, but sometimes also on the feed pressure especially when penetrants can plasticize the polymer membranes.^{41,43,44} The dissolution of gaseous species in Teflon AFs follows the non-linear dual sorption model.^{43,44} Gases dissolve in both the free volume and the condensed polymeric matrix. The former mode obeys the Langmuir sorption isotherm while the latter follows Henry's law.⁴³⁻⁴⁵ Sorption isotherms of light gases, C1–C4 hydrocarbons, and C1–C3 perfluorocarbons fit the dual sorption model very well.^{43,44} Teflon AF 2400 has a larger free volume, and displays a higher sorption capacity than Teflon AF 1600. The Henry's law constants of light gases in Teflon AFs are much larger than in other glassy polymers. This trend is similar to that observed for gas solubility in liquids, i.e., gases are generally more soluble in solvents with lower solubility parameters.⁴⁶ Interestingly, the desorption isotherms of the hydrocarbons and perfluorocarbons display hysteresis.⁴⁴ Such hysteresis is more significant for the more soluble penetrants, which are better plasticizers.⁴⁴ The penetrant-induced changes in glassy polymers by plasticization can be ascribed to long-lived increases in free volume and therefore the Langmuir capacity parameter, which thermodynamically favors the accommodation of more penetrants.^{44,47} Therefore, the selective solubilization of the more soluble penetrants in Teflon AF membranes can be further improved by increasing the pressure of feed flow.

Because plasticization can effectively increase the polymer chain mobility, not only the gas solubility but also the diffusion coefficients will be feed-pressure dependent. The dependence of diffusion coefficients on feed pressure for poorly absorbed gases (e.g. O₂, N₂,

CO₂, CH₄, CF₄) and highly absorbed gases (e.g. C₂H₆, C₃H₈, C₂F₆, C₃F₈) exhibit different behaviors.⁴³ The concentration dependence of diffusion coefficients is more pronounced for fluorocarbons than hydrocarbons, indicating better plasticization by the former. Because permeability coefficients are products of partition coefficients and diffusion coefficients, and certain penetrants have higher partition coefficients and diffusion coefficients at higher pressures, gas transport rates can display dramatic concentration dependent effects. Furthermore, the selectivity of gas transport can be tuned by controlling the pressure of feed flow. For example, as shown in **Figure 1-5**,⁴¹ Teflon AF 2400 membranes become more selective for propane over nitrogen when the feed pressure is higher than 80 psi.

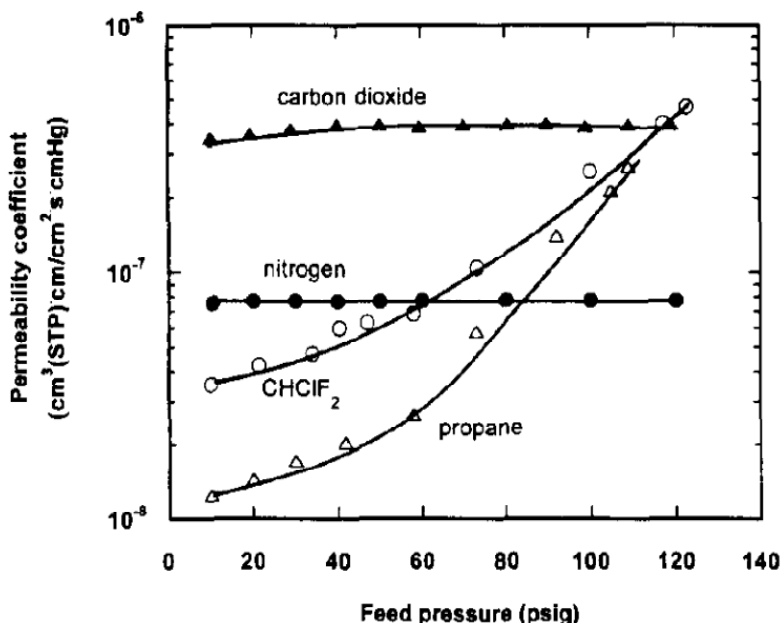


Figure 1-5. The dependence of permeability coefficients through Teflon AF 2400 films on feed pressure at 35 °C.⁴¹ Adapted with permission from (Gas and vapor transport properties of amorphous perfluorinated copolymer membranes based on 2,2-bistrifluoromethyl-4,5-1,3-dioxole/tetrafluoroethylene. Pinnau, I.; Toy, L. G. *Journal of Membrane Science* **1996**, *109*, 130.). Copyright (2013) Elsevier (License number: 3278990466500).

Nanocomposite membranes based on Teflon AFs and fumed silica display distinctive transport behavior in comparison to both conventional polymeric membranes containing nonporous nano-scale fillers and pure Teflon AFs.^{48,49} Nonporous nanoparticles as dopants in polymers are known to increase the diffusion pathway and block the effective area of transport.⁵⁰ Gas solubility (measured as moles per total material volume) in a polymer/nanoparticle hybrid material is lower than in the pure polymer due to the negligible gas solubility in the nonporous nanoparticles. Therefore, introducing nanoparticles into polymeric membranes was until recently found to decrease permeability coefficients. Surprisingly, Merkel and coworkers found that fumed silica (smaller than 50 nm) can disrupt the molecular packing of amorphous poly(4-methyl-2-pentyne) (PMP) leading to increased gas permeability.⁵⁰ Interestingly, fumed silica (13 nm)-doped Teflon AF 2400 membranes behave similarly.^{48,49} Merkel and coworkers discovered by positron annihilation lifetime spectroscopy that fumed silica nanoparticle as dopants in Teflon AF 2400 membranes lead to a systematic increase of fractional free volume in the membrane.⁴⁸ As shown in **Figure 1-6(A)**, the longer positron lifetime, which corresponds to larger free volume elements in the composite membrane, shows a general trend of increasing along with the weight percentage of fumed silica.⁴⁹ In contrast, the shorter positron lifetime, which corresponds to small free volume elements, appears to be independent of the filler amount. Teflon AF 2400 membranes containing higher loadings of fumed silica nanoparticles become more permeable to gases, as shown in **Figure 1-6(B)**.⁴⁹ Surprisingly, the dependence of the permeability on the feed pressure of highly absorbed gases in Teflon AF 2400 membranes containing large loadings of fumed silica is reversed compared to that in pure Teflon AF 2400 membranes.⁴⁹ The saturation of non-equilibrium excess free volume sorption sites at high feed pressure is responsible for the observed decrease of gas solubility in the composite membranes.⁴⁹ Later, De Sitter and

coworkers investigated the gas phase transport of poly(4-methyl-2-pentyne) (PMP)/silica nanocomposites and pointed out that a single fumed silica nanoparticle is composed of smaller silica aggregates, and the interstitial cavities situated in the aggregates may contribute to the change of free volume and transport behavior.⁵¹

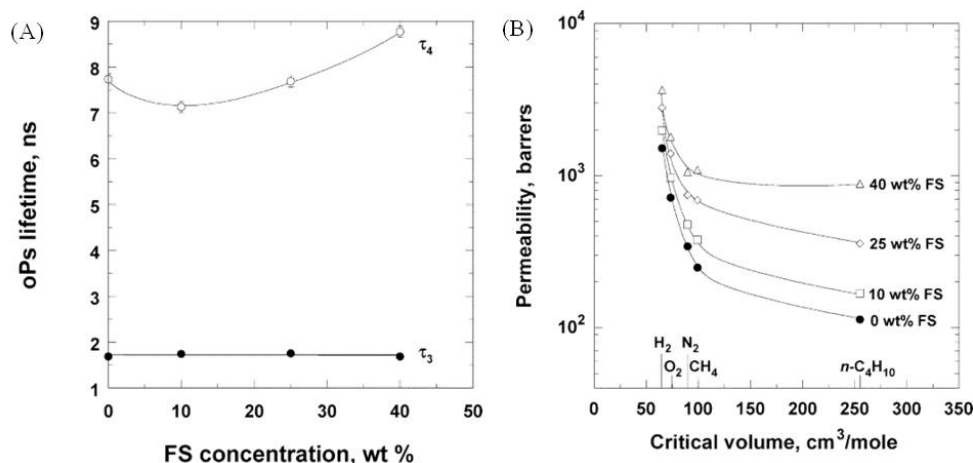


Figure 1-6. The dependence of positron lifetime on the dopant weight percentage (A); Effect of critical volume on gas permeability at 25 °C (B): $\Delta p = 3.4$ atm for H₂, O₂, N₂, CH₄; $\Delta p = 0.33$ to 3.4 atm for *n*-butane.⁴⁹ Adapted with permission from (Sorption and Transport in Poly(2,2-bis(trifluoromethyl)-4,5-difluoro-1,3-dioxole-co-tetrafluoroethylene Containing Nanoscale Fumed Silica. Merkel, T. C.; He, Z.; Pinnau, I.; Freeman, B. D.; Meakin, P.; Hill, A. J. *Macromolecules* **2003**, *36*, 8408.). Copyright (2013) American Chemical Society.

In view of the attractive combination of gas permeability, selectivity, and stability, Teflon AFs are potentially useful membrane materials in pervaporation, a method in which components of a solution are transported selectively through a membrane into a vapor phase.^{29,52,53} Yampolskii and co-workers systematically investigated the pervaporation and solubility of some common organic solvents (chloromethanes, acetone, alcohols, benzene, fluorobenzene, and cyclohexane) in Teflon AFs.^{29,52} **Table 1-3** shows the solubility of some solvents in Teflon AFs. Both Teflon AFs absorb organic solvents significantly.⁵² The fractional free volume of Teflon

AF 2400 is higher than Teflon AF 1600. Therefore, Teflon AF 2400 displays higher sorption capacity than Teflon AF 1600. Interestingly, the dependence of the permeability coefficient on the composition of the solution varies for different species.⁵³ For example, the permeability coefficient of acetone increases with the increase of acetone fraction in the liquid feed whereas the permeability coefficient of methanol decreases with the increase of methanol fraction in the liquid feed.⁵³ The shift of IR vibrational bands and quantum chemical calculations indicate the existence of effective hydrogen bonding of both acetone and methanol with the dioxole rings in Teflon AF 2400.⁵³ However, the significant self-association of methanol molecules leads to higher activation energy of diffusion, and consequently lower diffusion coefficients compared to non-associated monomers.⁵³ Recently, both the dimeric and trimeric forms of methanol have been visualized in methanol vapor transport through Teflon AF 2400 by quantitative analysis of penetrant pressure over time.⁵⁴ The experimentally determined diffusion coefficient of methanol dimer is about one tenth of the value for methanol monomer while the diffusion coefficient of the methanol trimer is about one hundredth of that of the methanol monomer.⁵⁴ The decrease in diffusion coefficients for self-associated species is much greater than expected based on estimation from Stokes-Einstein equation. Interestingly, the molecular radius of the methanol monomer based on its critical volume is about 6.6 Å, which is similar to the feature radius of the large free volume elements in Teflon AF 2400 (**Table 1-2**). Therefore, the diffusion of the larger, self-associated species will be much slower due to a sieving effect. High concentrations of methanol shift the self-association to the dimer and trimer states which have significantly lower permeabilities than the monomer, and result in a decreased average transport rate.⁵⁴

Table 1-3. Sorption of organic liquids in Teflon AFs at 25 °C.⁵²

Solvent	Sorption in Teflon AFs (g/100 g polymer)	
	Teflon AF 2400	Teflon AF 1600
CH ₂ Cl ₂	5.15	4.36
CHCl ₃	9.11	8.14
CCl ₄	16.94	11.90
CH ₃ OH	1.84	0.54
C ₂ H ₅ OH	2.81	1.12
(CH ₃) ₂ CO	2.43	2.38
C ₆ H ₆	4.65	4.25
C ₆ H ₁₂	6.75	4.21

1.2.3 Liquid Phase Transport

Fluorous liquids are selective solvents for fluorous tagged and F-substituted compounds, and are valuable platforms for the synthetic community.^{1,13,55} With an eye on separation, extraction, and synthetic applications, our lab initiated the investigation of Teflon AF 2400 as a dimensionally stable fluorous solvent for liquid phase transport about ten years ago.⁵⁶⁻⁵⁹ A thorough study on the thermodynamic cycle of vapor benzene, benzene in chloroform solution, and Teflon AF 2400 membrane reveals dramatically different behaviors of benzene permeating a Teflon AF 2400 membrane in contact with the liquid phase and benzene permeating a Teflon AF 2400 membrane in the gas phase.⁵⁶ As shown in **Figure 1-7**, the diffusion coefficient of the solute benzene in a

Teflon AF 2400 membrane in equilibrium with a chloroform solution of benzene is about three orders of magnitude larger than the value obtained from the gas transport study.⁵⁶ Meanwhile, the partition coefficient of benzene from chloroform to a Teflon AF 2400 membrane in equilibrium with chloroform is about one tenth of the value deduced from the thermodynamic cycle for partitioning from the gas phase.⁵⁶ The assessment of both diffusion and partition coefficients, combined with the fact that Teflon AF 2400 absorbs a significant amount of chloroform, indicates that chloroform fills the free volume and leads to the decrease of the benzene partition coefficient.^{56,57} At the same time, the high chloroform concentration in Teflon AF 2400 can plasticize the membrane and makes the diffusion of benzene much easier in the membrane where polymer chains have relatively high mobility.^{56,57} As a result, organic solutes with similar size display much higher permeability through Teflon AF 2400 membranes in liquid phase transport compared to gas permeation.^{56,57}

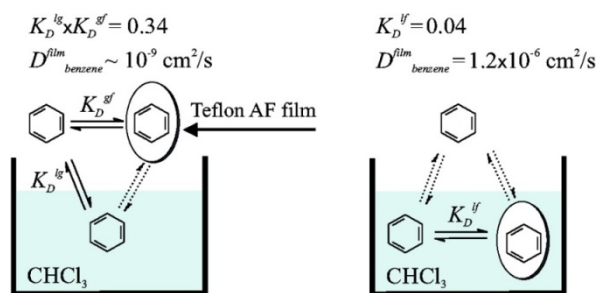


Figure 1-7. The effect of chloroform sorption by Teflon AF 2400 is shown by the thermodynamic cycles of the partitioning of benzene vapor, benzene in chloroform, and benzene in Teflon AF 2400 membranes in the gas and solution phases.⁵⁶ Adapted with permission from (How Fluorous Is Poly(2,2-bis(trifluoromethyl)-4,5-difluoro-1,3-dioxido-co-tetrafluoroethylene) (Teflon AF)?). Zhao, H.; Ismail, K.; Weber, S. G. *Journal of the American Chemical Society* **2004**, *126*, 13184.). Copyright (2013) American Chemical Society.

Although Teflon AF 2400 membranes are highly permeable in liquid phase transport, solute transport through Teflon AF 2400 membranes displays a similar size-sieving characteristic for a homologous series of compounds as observed in the gas permeation.⁵⁷ **Figure 1-8** shows the dependence of permeability coefficients on the molecular weight of solutes. The regression of $\log(\text{Permeability})$ of the neutral aromatic solutes (red dots) versus the logarithm of molecular weight yields a linear relationship.⁵⁷ The permeability coefficient of benzene is 74 times that of anthracene, which is about twice the molar volume of benzene. The size sieving effect is much less significant in gas phase. For example, in **Figure 1-6** (0% nanoparticles), the rate of change of permeability over critical volume (slope) becomes less steep when the critical volume increases due to the plasticization effect of organic vapors with large critical volume.⁴⁴ Even though increasing the size of a penetrant makes its diffusion less favorable, increased polymeric chain mobility due to plasticization is beneficial for diffusion through the polymer. Polar hydrocarbons have lower permeability coefficients (below the line) due to the unfavorable partitioning to Teflon AF membranes. Transport of solutes that are able to dimerize shows concentration dependent permeability (e.g. benzoic acid and pentafluorobenzoic acid) due to the lower transport rate of the dimer compared to the monomer.^{54,57} Notably, fluorinated solutes show higher permeability than their hydrocarbon analogues, even though the diffusion of fluorinated analogs of hydrocarbons is less favorable because of their larger molar volume.⁵⁷ In fact, the effect is quite significant. For example, the permeability of octafluorotoluene is about 103 larger than would be predicted from the linear correlation based on hydrocarbons. Therefore, Teflon AFs are potentially useful materials in liquid phase membrane separation and solid phase extraction.

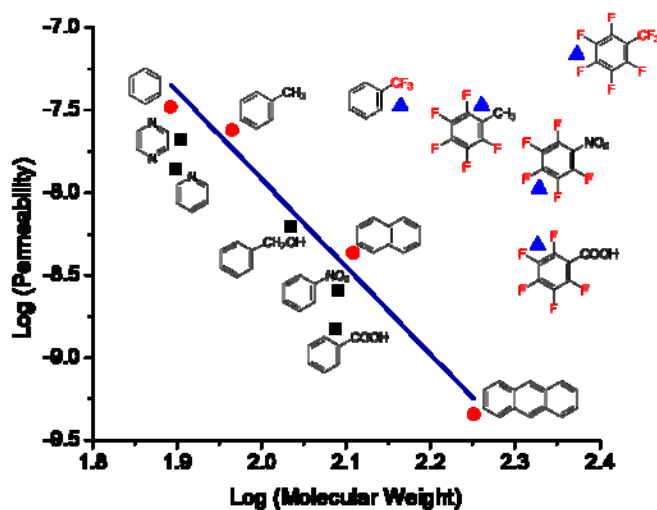


Figure 1-8. Dependence of permeability coefficients on the molecular weight of solutes.^{57,58} Red circles: aromatic hydrocarbons (and used to establish the regression line shown); black squares, aromatic hydrocarbons with polar functional groups; blue triangles, solutes with C-F substituted for C-H.

1.3 MOLECULAR RECOGNITION

Molecular recognition is a fundamental process in chemical and biological events. The classical “lock-and-key” model describes the recognition of a molecular receptor and a substrate at binding sites that are complementary in size, shape and spatial arrangement of functional groups.⁶⁰ Molecular recognition is usually driven by non-covalent interactions, including hydrogen bond, hydrophobicity, ionic, and π - π stacking.¹ Our group is interested in combining molecular recognition processes with analytical applications, specifically on chemical separations and sample preparation methods (liquid and solid phase extractions and liquid phase transports). In these processes, the selectivity of the extraction/transport is almost completely defined by the selectivity of the molecular receptor and the partition coefficients of the formed

complex.¹ Thus, the appropriate selection of a molecular receptor can add selectivity and specificity to analytical applications. For example, compared with the receptor-free system, Valenta and coworkers observed a 40-fold increase in the extraction of phenobarbital from human control serum when an artificial molecular receptor (**Figure 1-9**) is incorporated into the receiving phase (chloroform).⁶¹

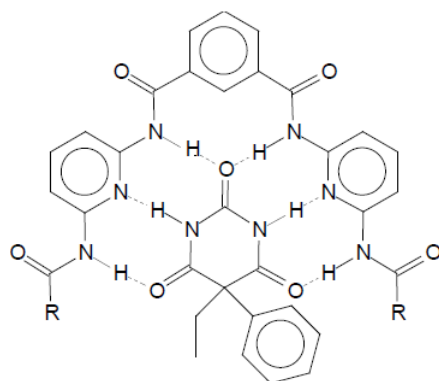


Figure 1-9. Artificial molecular receptor (R = 1-propyl) binding with phenobarbital.⁶¹ Adapted with permission from (**Enhanced Extraction of Phenobarbital from Serum with a Designed Artificial Receptor**. Valenta, J. N.; Dixon, R. P.; Hamilton, A. D.; Weber, S. G. *Analytical Chemistry* **1994**, *66*, 2398.). Copyright (2013) American Chemical Society.

In molecular recognition-based extraction and transport, selectivity for a target is high if non-covalent intermolecular interactions between receptor and target dominate the standard-state free energy change for the extraction process.¹ The most selective systems are those in which the receptor is completely responsible for the partitioning or distribution of the target into the extracting phase. Thus a matrix that is a poor solvent will provide the most selective environment for molecular recognitions. As a pioneering demonstration by O'Neal and coworkers, Krytox 157 FSH (a carboxylic acid terminated perfluoropolyether) interacts with pyridines, and

facilitates the extraction of pyridines from CHCl_3 to FC-72 (perfluorohexanes). For example, 72% of the pyridine (2.0 mM) is extracted from an equal volume of CHCl_3 to FC-72 (2.0 mM Krytox 157 FSH). The pyridine forms hydrogen bonded complexes with the molecular receptor accounting for the high extraction yield (**Figure 1-10**)^{62,63} In comparison, the extraction efficiency of phenol is only 1%, indicating non-effective interaction with Krytox 157 FSH. Remarkably, with molecular receptor (2.0 mM Krytox 157 FSH), the extraction of a highly polar substituted pyridine – nicotinamide (2.0 mM) – from an equal volume of CHCl_3 to FC-72 is 9%.⁶² O'Neal further demonstrated that porphyrins can be successfully extracted into FC-72 through non-covalent interaction with Krytox 157 FSH salt.⁶⁴ Based on hydrogen bond formation in the fluorosolvant, Shimizu and coworkers reported encapsulation of benzenes in hexameric hydrogen bonded supramolecular assembly.⁶⁵ Taking the halogen bond (e.g. I \cdots I-PFCs) as foothold, Parisi and coworkers successfully extracted CsI from aqueous to fluorosolvant phase with the assistance of a crown ether to bind to Cs^+ .⁶⁶ The coordination between a fluorosolvant copper(II)-carboxylate and pyridyl-tagged porphyrins effectively extracted the latter into fluorosolvant phase.⁶⁷ Furthermore, the enhanced ion pair interactions in the extremely non-polar, non-coordinating and poorly solvating fluorosolvant media provide opportunities for ion-selective electrodes (ISEs).^{20,68-70} Bühlmann and coworkers developed the first generation of such fluorosolvant membrane-based ISEs from a fluorosolvant bulk membrane containing ionophore (sodium tetrakis[3,5-bis(perfluorohexyl)phenyl]-borate) in perfluoroperhydrophenanthrene as the sensing phase.²⁰ This ion-selective electrode showed remarkably high potentiometric selectivity, K_{ip} , which exceeds previously reported values in the conventional plasticized PVC membranes by more than 5 orders of magnitude.²⁰ Recently, Bühlmann's group developed the second generation of fluorosolvant membrane ISEs for pH measurements by using Teflon AF 2400

membranes containing a linear perfluorooligoether (14.3 ether groups per molecule) as a plasticizer,⁷¹ sodium tetrakis[3,5-bis(perfluorohexyl)phenyl]borate as ionic sites, and bis[(perfluorooctyl)propyl]-2,2,2-trifluoroethylamine as an H⁺ ionophore.⁷⁰ Such amorphous fluoruous polymer-based electrodes exhibited high potentiometric selectivities, Nernstian responses to H⁺ over a wide pH range, and enhanced mechanical stability compared to the bulk membranes.⁷⁰ In summary, hydrogen bonding-, halogen bonding-, coordination-, and charge-based fluorinated receptors have shown high molecular recognition potency in the poorly solvating fluoruous media and lead to prospective applications. However, the field still lacks a comprehensive understanding of the thermodynamics of molecular recognition in fluoruous media.

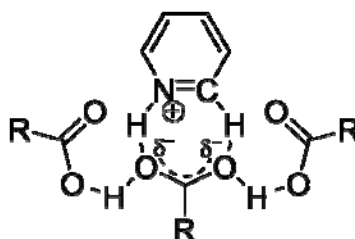


Figure 1-10. Proposed structure of 3:1 complex from Krytox 157 FSH and pyridine.

R = CF₃CF₂CF₂O[CF(CF₃)CF₂O]₃₃CF(CF₃).⁶² Adapted with permission from (**Extraction of Pyridines into Fluorous Solvents Based on Hydrogen Bond Complex Formation with Carboxylic Acid Receptors**. O’Neal, K. L.; Geib, S.; Weber, S. G. *Analytical Chemistry* **2007**, 79, 3132.). Copyright (2013) American Chemical Society.

1.4 OBJECTIVE AND MOTIVATION

This thesis is aimed at gaining fundamental understanding of *the liquid phase transport through fluoropolymer thin films, fluoropolymer/liquid interface behaviors, and the thermodynamics of*

molecular interactions in fluorous media. Specific questions that motivated this work include: (1) How to modulate the chemical environment (e.g. fluorophilicity) within Teflon AF 2400 films? (2) What are the impacts of dopants (liquid- and nano- components) to the physical properties (e.g. free volume, polymeric chain mobility, morphology, etc.) of Teflon AF 2400 composite films, and how do such properties influence the transport behavior (permeability, diffusivity, partition coefficients, and selectivity) through these films? (3) Wetting is a key issue with Teflon AF 2400 due to its inherent hydrophobic and oleophobic nature. How can we modulate the wettability of porous Teflon AF 2400 to render its potential applications in chemical separations, sensing, and templated synthesis? (4) What are the impacts of solvent strength (fluorous, semi-fluorous, and organic solvents) to the thermodynamics (ΔG° , ΔH° , and ΔS°) and stoichiometry of molecular interaction? What is the origin of the enhanced molecular interaction in fluorous media?

Chapter 2.0 details a study on the properties and transport behavior of perfluorotriptylamine (FC-70) doped Teflon AF 2400 films. We found that doping FC-70 restores the fluorophilicity of Teflon AF 2400, resulting in improved transport selectivity for fluorinated compounds compared to their hydrocarbon analogues. Surprisingly, we observed an interesting antiplasticization/plasticization behavior: less than 12 wt% FC-70 accommodates the large free volume elements in Teflon AF 2400 to antiplasticize the polymer; more than 12 wt% FC-70 dilutes Teflon AF 2400 to plasticize the polymer. The distinctive function of FC-70 signifies a sharp transition of the physical properties and transport behavior of Teflon AF 2400. Chapter 3.0 focuses on Teflon AF nanocomposite films in aim to develop highly permeable and selective polymeric fluorous matrix. We observed astonishingly high fractional free volume (~50%) while distinctive morphologies from glassy Teflon AF 2400/fluorophilic silica

nanoparticles and plasticized Teflon AF 2400/fluorophilic silica nanoparticles systems. This is an unprecedented example demonstrating the effect of a plasticizer to create structurally different polymer nanocomposites. The film composition dictates nanoscale morphology. The nanoscale morphologies dictate the transport behavior. In chapter 4.0, we developed porous Teflon AF 2400 material and extended its application in separations (fluorocarbon vs. hydrocarbon, and fractionation of nanoparticles), sensing, and templated synthesis. The challenge and demand remain in the separation and purification of nanoparticles because size does matter in practical applications (e.g. SERS, imaging, mobility, etc.). According to the feature pore size of porous Teflon AF 2400 films, nanoparticles can be separated by size when transporting through the films driven by electrophoresis. This application should lead to the development of more robust and high performance nanoparticle separation device that can function in aggressive aqueous and organic environments. As a preliminary step to evaluate the potential signal enhancement of porous Teflon AF 2400 thin film for microarray substrate, this chapter examined the immobilization of a fluorescent molecule with fluorous tag on the porous Teflon AF 2400. The signal to noise ratio is more than 30 times than the traditional fluorous glass slides. With the assistance of a semi-fluorous molecule, porous Teflon AF 2400 can serve as a template for the synthesis of porous organic polymer matrix. And finally, in Chapter 5.0, we quantitatively investigated the thermodynamics of molecular interactions (pyridine and perfluorodecanoic acid; quinazoline and perfluorodecanoic acid) in solvents with different strength (FC-77, HFE-7500, and 1-chloropentane) by isothermal titration calorimetry. Experimental data on complexes between N-heterocyclic bases and perfluorodecanoic acid in the three solvents were compiled to compare solvent effects on the behavior of complex formation. It becomes clear that polar solvents support the 1:1 complex while nonpolar poor solvents lead to complexes with 1:2 and

1:3 (base/acid) stoichiometries. To our knowledge, this is the first quantitative and thorough study on the thermodynamics of hydrogen bonding in fluorous solvents.

The profound understanding of the transport behavior of Teflon AF 2400 and its composite materials, the Teflon AF/liquid interface, and the specific interactions between a molecular receptor and targets in fluorous matrices will add knowledge and predictability to film-based extractions, membrane separations, and sensor technologies and thus lead to greater advances in the related fields.

2.0 PROPERTIES AND TRANSPORT BEHAVIOR OF PERFLUOROTRIPENTYLAMINE (FC-70)-DOPED AMORPHOUS TEFLON AF 2400 FILMS

Reprinted from **Properties and Transport Behavior of Perfluorotripentylamine (FC-70)-Doped Amorphous Teflon AF 2400 Films**, Zhang, H.; Hussam, A.; Weber, S. G. *Journal of the American Chemical Society*, **2010**, *132*, 17867–17879. Adapted with permission from American Chemical Society. Weber, S. G. conceived the study. Hussam, A. performed the measurement of activity coefficients by head space gas chromatography (HSGC) and contributed to the experimental section on HSGC. Zhang, H. performed the rest of the experimental work and wrote the paper under the guidance of Weber, S. G.

2.1 INTRODUCTION

Polymer membranes and films are widely applied in gas separations,⁷²⁻⁷⁶ ion separation/ion exchange,^{77,78} liquid-phase extraction/separation of organic compounds of biological and environmental interest,⁷⁹ sensor materials,^{30,80,81} and as coatings to improve or create functionality such as electrowetting,⁸² avoidance of biofouling,⁸³ improving biocompatibility,⁸⁴ and growing stem cells⁸⁵ and as composites with nanomaterials.^{86,87} Fluorocarbon polymers are well represented in several of these applications. The development of fluorous media is of

special interest for the selective partitioning of fluorinated substances.^{4,88} Highly fluorinated hydrogen bonding,^{62-65,89} coordination,⁶⁷ and ionic receptors⁷⁰ have been shown to impart selectivity to fluorous phases for complementary target species. Notably, the partitioning of fluorinated solutes into fluorous media is preferred even without specific interactions, due to weak van der Waals interactions per molecular contact area.³ This unique property renders fluorocarbons to be the basis of a distinctive platform for selective extraction and transport.^{3,55} In many cases, covalent modification of reaction participants with fluorous tags facilitates product purification and catalyst recycling in synthetic chemistry.^{7,8,12,13} Fluorous-supported liquid membranes have been recognized as promising platforms for sensors and separations.^{20,69,90,91} As alternative fluorous media, perfluoropolymers attracted our attention given their potential value for selective transport. Dimensionally stable perfluoropolymers are promising matrices for membrane separations due to their low activation energy of diffusion and unique solubility/partitioning behavior.¹⁵ In addition, strong carbon-fluorine and carbon-carbon bonds give perfluoropolymers extraordinary thermal and chemical stability, thereby yielding a long lifetime in hostile environments.^{15,16}

Among commercially available perfluoropolymers, Teflon AF 2400 is an unusual amorphous glassy copolymer with a high fractional free volume (FFV).²⁴⁻²⁶ This intrinsic feature is probably due to the rigid structure of the dioxolane ring in Teflon AF 2400 and the weak van der Waals interactions between fluorous polymeric chains, **Figure 2-1**.²⁶ The free volume size distributions of amorphous Teflon AF 2400 determined by various techniques are in substantial agreement (radius ranges from 3 to 8 Å) based on spherical or cylindrical assumptions of microcavity geometry.^{24,25,38} Theoretical modeling indicates the bimodal distribution of microvoids and their partial connectivity in Teflon AF 2400.³⁹ Due to the significant free

volume, the gas permeability of Teflon AF 2400 is second only to poly(1-trimethylsilyl-1-propyne) (PTMSP).^{25,92} Thus, Teflon AF 2400 has been widely investigated as the matrix for gas transport (light gases, C1–C4 hydrocarbons, and C1–C3 fluorocarbons),^{41,43,44,93-95} pervaporation (acetone, chlorinated hydrocarbons, hydrocarbons, and lower alcohols),^{29,52,53,96} and gas sensors (H₂S, NO₂, Cl₂, and CO₂).^{30,97,98}

We initiated an investigation of Teflon films as matrices for liquid-phase selective transport with an eye on extraction, separations, and applications in synthesis and analysis.^{56,57} Teflon AF 2400's high FFV and large Henry's constant⁴⁵ for chloroform result in strong sorption of chloroform, which decreases free volume and enhances segmental movement plasticizing the polymer.⁵⁶ Thus, the permeability of a solute (dissolved in chloroform) across the film deviates from the ideal prediction from the reported pervaporation results.⁵⁶ In this sense, Teflon AF 2400 films in contact with organic liquids become less fluororous and more "organic like". In order to maintain the fluororous nature of Teflon AF 2400 (π^* : -0.28), we tried to dope the films with perfluorinated compounds. Attempts to dope 50 wt % Krytox 157FSH (MW 7000–7500) in Teflon AF 2400 lead to significantly decreased solute permeability, even though the film was plasticized by the dopant.^{56,57} This was attributed to a trade-off between the enhancement of segmental movement and the viscous environment.⁵⁷ Therefore, we attempted to modulate the chemical environment within Teflon films by doping them with a lower molecular weight perfluorinated liquid, which is much less viscous yet has a high boiling point. Perfluorotripropylamine (Fluorinert FC-70, bp 215 °C, π^* : -0.23) was chosen as a dopant due to its considerable stability, compatibility, and solvophobicity.

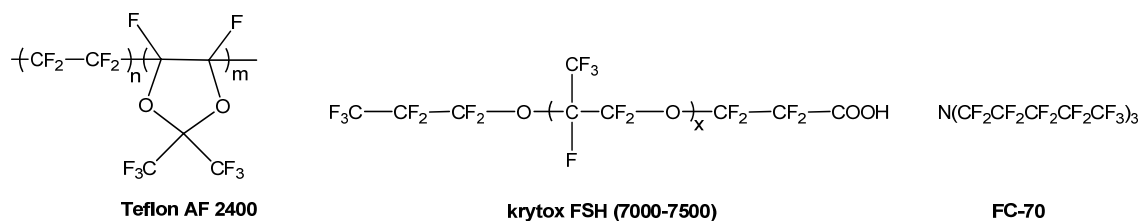


Figure 2-1. Structures of polymer and dopants: Teflon AF 2400 ($n = 13$ mol %, $m = 87$ mol %), Krytox FSH (7000–7500), and FC-70.

In this context, we systematically investigated the physical and chemical properties of Teflon AF 2400 films doped with various amounts of FC-70. We provide experimental evidence on the “FC-70-like” property of Teflon AF 2400 films doped with a large weight percentage of FC-70 (>20 wt %). Antiplasticization and plasticization effects were observed, respectively, for Teflon films doped with low and high weight percentages of FC-70. Transport behavior of solutes can be related to the independently established film properties.

2.2 EXPERIMENTAL

2.2.1 Materials

Teflon AF 2400 was purchased from DuPont (Wilmington, DE). Fluorinert FC-72 (a mixture of perfluorohexanes, bp 56 °C) and Fluorinert FC-70 (perfluorotripentylamine, bp 215 °C) were purchased from 3M (Minneapolis, MN). Probe solutes used in transport experiments (toluene, α,α,α -trifluorotoluene, 2,3,4,5,6-pentafluorotoluene, octafluorotoluene, nitrobenzene, and pentafluoronitrobenzene) were purchased from Sigma-Aldrich (St. Louis, MO). Chloroform was obtained from Fisher Scientific and used as received. Water was purified with a Milli-Q

Synthesis A10 system (Millipore, Bedford, MA). Tygon Chemfluor FEP tubing, resistant to vapor chloroform, was purchased from United States Plastic Corp. (Lima, OH).

2.2.2 Film Preparation and Morphological Characterization

Pure films of Teflon AF 2400 were cast from a 12 mg/mL solution of amorphous Teflon AF 2400 polymer dissolved in FC-72. A defined amount of solution was transferred into an optical flat-bottomed glass Petri dish with an i.d. of 6.0 cm. The dish was covered with a piece of weighing paper and a glass cover. The solvent, FC-72, was allowed to evaporate at room temperature until a constant weight of the film was reached. Three milliliters of Milli-Q water were added to the Petri dish to enable the film to float on top of the water within several minutes. The film was then oven dried at 110 °C for 2 h to remove water residue and stored at room temperature.

To prepare FC-70-doped Teflon AF 2400 films for both density measurement and dynamic mechanical analysis (DMA), FC-70 was weighed and mixed with a 12 mg/mL solution of Teflon AF 2400 polymer in FC-72 in the calculated proportions. Doped Teflon films were formed under the same conditions as described above for the pure films with one difference. They were readily peeled off using a scalpel with the addition of 0.4 mL of ethanol rather than using water for this step. The doped films were not oven dried because FC-70 could be lost. They were stored in a covered container with an FC-70-saturated atmosphere.

The FC-70-doped Teflon AF 2400 films used in the transport experiments were prepared by soaking a piece of pure Teflon AF 2400 film in a chloroform solution containing a defined amount of FC-70 (including 0 wt %) with stirring (200 rpm) at 20.0 ± 1.0 °C. The FC-70 content in the film was evaluated by FT-IR absorbance analysis to determine when the two phases

reached equilibrium. The resulting chloroform solution containing FC-70 was used as the receiving phase and to prepare the source phase solution in the transport experiments. The equal chemical potential of FC-70 in the source phase, polymer phase, and receiving phase prevented the potential loss or gain of FC-70 in doped films during the transport experiments. There is no significant difference of solute permeabilities in oven-dried pure Teflon AF films compared to pure Teflon AF films that were not oven dried. Thus, differences between pure Teflon AF films and FC-70-doped films are not caused by the difference in preparation procedures.

For all FC-70-doped Teflon AF 2400 films, the amount of dopant in the film was evaluated by FT-IR absorbance analysis. Films were cut into small pieces (0.8 cm × 0.8 cm) for both density measurement and transport experiments. A Starrett micrometer (Athol, MA) with an accuracy of ±1 μm was used to measure film thickness.

The morphology of the films was investigated using a Philips XL-30 field emission SEM. FC-70-doped Teflon AF 2400 films were fractured in liquid nitrogen and sputter coated with palladium to enhance surface conductivity.

2.2.3 Film Density Measurement and Fractional Free Volume

The hydrostatic weighing method was used to determine film density (ρ). A film (mass, m) was hung on the hook of a suspension system in silicon oil (ρ_s), which was chosen because of its high boiling point. The mass change of the suspension system with and without the film ($W - W_0$) was recorded by a XS105 DualRange analytical balance (Mettler Toledo, Columbus, OH). The hydrostatic density after correction (the density of air at 20 °C, $\rho_A = 0.00129 \text{ g/cm}^3$) is given by eq 2-1:^{99,100}

$$\rho = \frac{m}{(W - W_0) / \rho_S} + \rho_A \quad (2-1)$$

On the basis of measured densities, the FFV of the FC-70-doped Teflon films can be calculated according to **eq 2-2**:¹⁰¹

$$FFV = \frac{V_F}{V} = \left(\frac{V - V_0}{V} \right) = 1 - \rho \cdot V_0 \quad (2-2)$$

where the specific free volume (V_F) is the difference between the experimentally determined specific volume (V) and the estimate of specific volume at absolute zero (V_0). V equals the reciprocal of measured film density (ρ). As suggested by Lee, V_0 is 1.3 times the van der Waals specific volume,¹⁰² which can be obtained according to a group contribution method.¹⁰³ For a polymer-dopant system, V_0 can be estimated based on the weight fraction of each component:¹⁰⁴

$$V_{0,mixture} = V_{0,polymer} \cdot wt\%_{polymer} + V_{0,additive} \cdot wt\%_{additive} \quad (2-3)$$

2.2.4 Dynamical Mechanical Analysis

Dynamical mechanical analysis was carried out using a Q800 DMA (TA Instruments, New Castle, DE). DMA was performed on a piece of film cut and mounted between the tensile mode clamps of the instrument. The dimensions of films were approximately 9 mm long by 0.53 mm wide by 0.02 mm thick. The sample was prestretched under a preload force of 0.01 N. A sinusoidal strain deformation (0.3%) of 1 Hz was applied during a temperature sweep from -100 to 300 °C at a rate of 3 °C/min.

2.2.5 Sorption and Desorption of Chloroform in FC-70-doped Teflon AF 2400 Films

A FT-IR gas flow cell was utilized to measure the sorption of chloroform in the FC-70-doped Teflon AF 2400 films. Saturated chloroform vapor was carried into the IR flow cell (containing two lead spacers sandwiched between two KBr windows) by nitrogen gas with a pressure of 15 psi (20 °C) at a flow rate of 0.1 LPM. The tail gas was absorbed by n-butanol. IR absorbance of chloroform in the flow cell was continuously monitored by an FT-IR spectrometer (Bio-Rad Excalibur FTS 3000 Spectrometer, DigiLab, Randolph, MA). In order to measure the sorption of chloroform in an FC-70-doped Teflon AF film, a piece of the film with the same diameter as the KBr window was placed between the two lead spacers in the flow cell for IR measurement (after 30 min equilibrium had been reached). The IR absorbance of the flow cell without a film was monitored as the control experiment. The net sorption of chloroform in the film was obtained from the difference between the IR absorbance with and without the film. Since the C-Cl vibration shifted from 772 cm⁻¹ for the vapor chloroform to 768 cm⁻¹ for the chloroform saturated in the film, the peak area of the C-Cl vibration was used for IR quantification.

To determine the diffusion coefficient of chloroform in FC-70-doped Teflon AF 2400 film, a film in equilibrium with liquid chloroform was set in the FT-IR window for kinetic measurement. The FT-IR absorbance (3025 cm⁻¹, C-H stretch) was continuously acquired with a time interval of 1 min. Assuming that the concentration of chloroform on the film surfaces is zero ($D_{\text{chloroform in film}} \ll D_{\text{chloroform in air}}$), the portion of chloroform remaining in the film can be theoretically described by eq 2-4:^{105,106}

$$\frac{M_t}{M_0} = \frac{A_t}{A_0} = \frac{8}{\pi^2} \cdot \sum_{k=0}^{\infty} \left(\frac{1}{2 \cdot k + 1}\right)^2 \cdot e^{-(2 \cdot k + 1)^2 \cdot \pi^2 \cdot D \cdot t / l^2} \quad (2-4)$$

where M_0 is the initial total amount of chloroform inside the film, M_t is the amount of chloroform remaining in the film at time t , A_0 corresponds to the initial IR absorbance, whereas A_t is the absorbance at time t . l is the film thickness. D denotes the diffusion coefficient of chloroform in the film, which can be obtained from nonlinear fitting by Mathcad 14 (“infinity” in the sum was set to 100).

2.2.6 Transport of Solutes through Films

Transport experiments were conducted with a homemade, three-phase transport device at 20.0 ± 1.0 °C.¹⁰⁷ The film was mounted between two quartz cuvettes (path length = 1.0 cm, Starna Cells, Atascadero, CA) with holes (0.5 cm in diameter) to define the effective transport area. Two pieces of Viton gasket were placed in between the film and the cuvettes to prevent leaking. The eight-position multicell transport holder was used to hold eight cells (four pairs) in a rack, which were kept at constant temperature by water circulation from a thermostatic water bath. The stirring module for the multicell transport holder could control the stirring speed at the same rate for the eight cells. The volume of the source phase containing the solute and receiving phase was 3.00 mL in all the transport experiments. Solute concentration in the receiving phase was continuously monitored by a UV spectrophotometer (Hewlett-Packard 8452A UV-visible diode array spectrophotometer, Palo Alto, CA). The steady-state flux, J , of a solute through the film is given by eq 2-5:⁵⁷

$$J = \frac{dC_r}{dt} \cdot \frac{V}{A} (\text{mol} \cdot \text{cm}^{-2} \cdot \text{s}^{-1}) \quad (2-5)$$

where dC_r/dt is the accumulation rate of solute in the receiving phase, V is the volume of the receiving phase (3.00 mL), and A is the effective transport area (0.196 cm²). The permeability coefficient, P , can be deduced from the flux:⁵⁷

$$P = \frac{J \cdot l}{C_s - C_r} \approx \frac{J \cdot l}{C_{sl}} (\text{cm}^2 \cdot \text{s}^{-1}) \quad (2-6)$$

where l is the film thickness and C_s and C_r represent the concentration of the solute in the source phase and receiving phase, respectively. In our experimental duration, C_r is negligible compared to C_s . Thus, $C_s - C_r$ can be simplified to the initial concentration of the solute in the source phase, C_{sl} . Selectivity of a film is defined as the permeability ratio of a fluorinated compound over its hydrogen-containing control:

$$S = \frac{P_F}{P_H} \quad (2-7)$$

2.2.7 Determination of Solute Diffusion Coefficients (D) and Partition Coefficients (K)

In order to clearly observe the lag phase prior to the solute flux reaching the steady state, FC-70-doped Teflon AF films with various thicknesses (36–127 μm) were employed in the transport experiments. The concentration of source phase solutions (e.g., toluene, 1.0 M; α,α,α -trifluorotoluene, 0.3 M; 2,3,4,5,6-pentafluorotoluene, 0.5 M; octafluorotoluene, 0.1 M; nitrobenzene, 0.5 M; pentafluoronitrobenzene, 0.2 M) was chosen based on solute absorptivity. UV absorbance of the receiving phase was recorded continuously at a time interval of 20 s in order to measure the solute accumulation. For a transport system that starts with “zero” solute concentration in both the film and the receiving phase, the accumulation of solute molecules can be theoretically described by eq 2-8:¹⁰⁵

$$Q_t = K \cdot C_s \cdot l \cdot \left(\frac{D \cdot t}{l^2} - \frac{1}{6} - \frac{2}{\pi^2} \cdot \sum_{n=1}^{\infty} \frac{(-1)^n}{n^2} \cdot e^{-D \cdot n^2 \cdot \pi^2 \cdot t / l^2} \right) (\text{mol} \cdot \text{cm}^{-2}) \quad (2-8)$$

where Q_t denotes the accumulation of the solute in the receiving phase (substance passed through the film) per transport area within the time range t . K is the partition coefficient of the solute from chloroform to the film. C_s is the concentration of the solute in the source phase solution. l represents the thickness of film. D is the average diffusion coefficient of the solute in the film. Thus, the diffusion coefficients and partition coefficients can be obtained by nonlinear fitting **eq 2-8** to experimental data using Mathcad 14 (“infinity” in the sum was set to 100).

The partition coefficients of octafluorotoluene and 2,3,4,5,6-pentafluorotoluene from chloroform to pure FC-70 were determined from the liquid-liquid partitioning experiments. The solution of 1 mM octafluorotoluene or 5 mM 2,3,4,5,6-pentafluorotoluene in chloroform (750 μL /500 μL) mixed with FC-70 (750 μL /1 mL) was placed in a VWR GC-autosampler vial (1.8 mL, West Chester, PA) and shaken at 1300 rpm for 30 min at 20 °C (Bioshaker, BIONEXUS Inc., Oakland, CA). The chloroform layers were then quantitatively analyzed by UV spectrophotometry at 267 and 258 nm.

The partition coefficients of toluene, α,α,α -trifluorotoluene, nitrobenzene, and pentafluoronitrobenzene from chloroform to pure FC-70 were determined from head space gas chromatography (HSGC). The instrument combines the inherent sensitivity of modern capillary gas chromatography with computer-controlled gas sampling, injection, sample equilibration, and data handling techniques. The details of a custom-built HSGC have been described elsewhere.¹⁰⁸ The instrument was used to precisely sample the vapor phase in equilibrium with the solution phase and analyze the vapor phase by a gas chromatographic technique.

In a typical experiment, a standard mixture of four solutes was added to 10.0 mL of FC-70 solvent by using a calibrated auto syringe into a thermostatic (± 0.1 °C) glass cell. The

solute's mole fraction range was toluene: 0.001–0.007, α,α,α -trifluorotoluene: 0.001–0.005, nitrobenzene: 0.001–0.009, and pentafluoronitrobenzene: 0.001–0.004, each added over 10–20 increments.

Once the vapor-liquid equilibrium is established, 50 μL of the vapor was sampled and injected by using the automated valve system on-column into a capillary GC for analysis. This procedure was continued after each aliquot addition to obtain a series (10–20 additions) of concentration-dependent vapor pressures. Assuming ideal gas, the response peak areas can be used to calculate the activity coefficients of the solute, γ_i , in a solvent by the equation:

$$\gamma_i = A_i / (A_i^\circ \cdot x_i) \quad (2-9)$$

where A_i is the peak area for the solute, A_i° is the peak area for pure solute (measured separately), and x_i is the mole fraction of the solute in the solvent. The γ_i values are therefore referenced to the pure solute as the standard state. The infinite dilution activity coefficient was obtained from extrapolation of γ_i vs x_i curve to $x_i = 0$, and the mole-fraction-based partition coefficient was determined from the vapor-liquid composition.

2.2.8 Recycling of Teflon AF 2400

FC-70-doped Teflon AF 2400 films after usage have been recycled as follows. First, small pieces of used films were dissolved in FC-72 to cast large films in order to allow the IR quantification of remaining FC-70 conveniently. Second, the film was heated to approximately 160 °C in an oven with vacuum for several days until the characteristic peak of FC-70 (891 cm^{-1}) could no longer be observed by IR. After treatment, the films were redissolved in FC-72. Filtration was carried out to remove the dust attracted by static electricity. Finally, clean Teflon AF 2400 was recovered after evaporation of FC-72.

2.3 RESULTS AND DISCUSSION

2.3.1 Characterization of FC-70-doped Teflon AF 2400 Films

FC-70 (0-40 wt %) doped Teflon AF 2400 films were prepared as transparent and homogeneous films. As shown in **Figure 2-2**, FT-IR spectra of FC-70-doped Teflon films show the characteristic peak of FC-70 at 891 cm^{-1} . The peak magnitude is dependent on the weight percentage of FC-70; thus, it is used to verify the composition of FC-70-doped Teflon films.

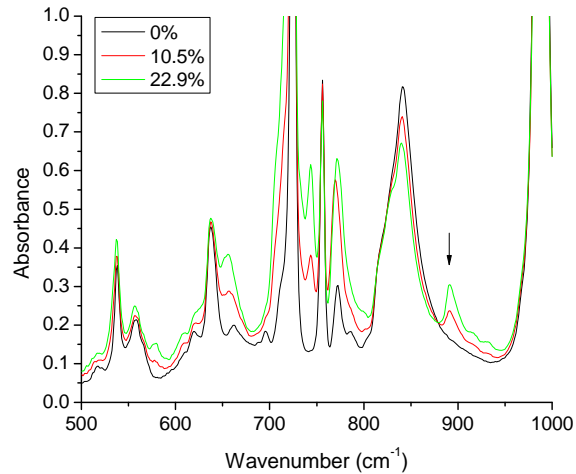


Figure 2-2. FT-IR spectra of Teflon AF films doped with various amounts of FC-70 (wt %).

SEM was used to determine the macroscopic homogeneity of FC-70-doped Teflon films. Both films display satisfactory homogeneity through the cross-section, as shown in **Figure 2-3**. The morphology of 30 wt % FC-70-doped Teflon is very similar to that of the pure Teflon film. As confirmed by SEM, the films are free from detectable pinholes or cracks.

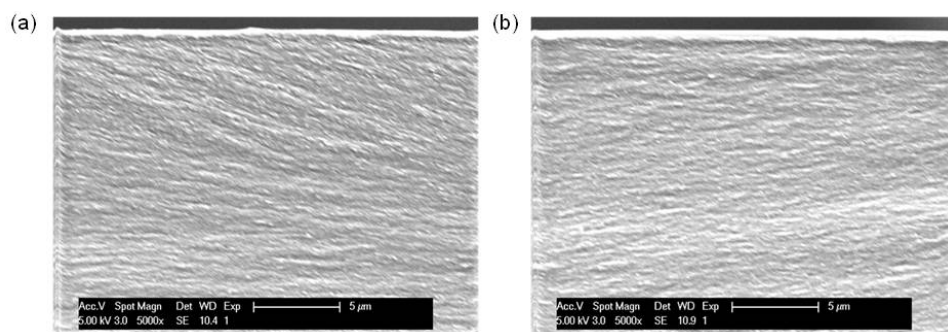


Figure 2-3. Cross-section SEM micrographs of (a) a pure Teflon AF film and (b) a Teflon AF film doped with 30 wt % FC-70.

2.3.2 Density and Free Volume of FC-70-doped Teflon AF 2400 Films

Doping miscible low molecular weight additives in a polymer film should result in the change of both physical and chemical properties of the film.¹⁰⁹ Dopants may decrease FFV and substantially reduce gas permeabilities.^{104,110} The effect of FC-70 content on the film's free volume can be seen in **Figure 2-4**, showing the density of Teflon AF 2400 films containing various amounts of FC-70. The film density increases significantly (in the range of 0-12 wt % dopant) and then decreases gradually along with the FC-70 content (12-40 wt %) in the film. Interestingly, the peak density of the doped film (2.06 g/cm³) is significantly higher than both pure Teflon film (1.82 g/cm³) and pure FC-70 liquid (1.94 g/cm³). This indicates the volumetric shrinkage of FC-70-doped Teflon AF 2400 film, usually a phenomenon accompanying antiplasticization.¹¹¹

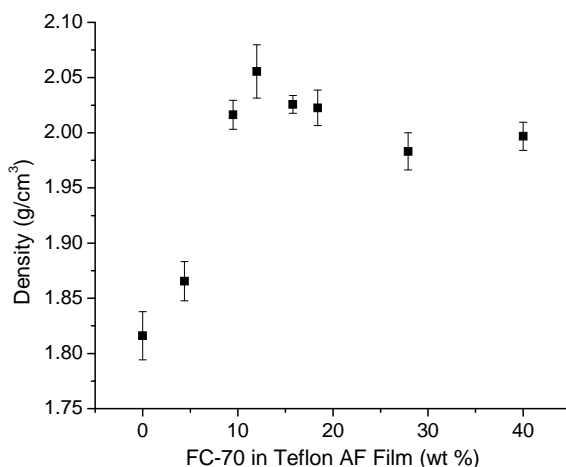


Figure 2-4. Cross Dependence of film density (20.0 (1.0 °C) on FC-70 content (wt %). The number of measurements for each data point are: 5 (0 wt %), 8 (4.4 wt %), 8 (9.5 wt %), 9 (12.0 wt %), 11 (15.8 wt %), 9 (18.4 wt %), 6 (27.9 wt %), and 10 (40.0 wt %). The error bars represent the standard error of the mean. Pure films were oven dried to remove water residue, while doped films were air dried to remove ethanol residue.

To understand the role of the dopant, the concentration of Teflon AF 2400 in the doped films (C) over a pure film (C_0) was plotted against FC-70 content (**Figure 2-5**). Teflon AF 2400 concentration is almost a constant in films containing 0–12 wt% FC-70. This observation indicates that FC-70 mainly fills in the existing free volume of the Teflon polymer in this range of compositions. Having 12 wt % FC-70 in 88 wt % Teflon AF 2400 requires that 44.6% of the free volume in Teflon is occupied by FC-70. Hofmann and co-workers³⁹ used two models to describe the experimentally determined free volume distribution in Teflon AF 2400. In one, called R_{max} , the measured sizes correspond to the size of a feature in what may be a larger, irregular void. In the other, called $V_{connect}$, the measured size corresponds to the size of the complete void. An analogy may help. In a simple image of a flower, the R_{max} approach would characterize the flower by the size of the petals, whereas the $V_{connect}$ would characterize the size of the void by the size of the whole flower. According to Hofmann and co-workers, 44.6%

of the free volume in Teflon AF 2400 corresponds to cavities with a feature size larger than 8–9 Å in the R_max approach. Interestingly, the critical diameter is equal to the length of the side chain (r) in FC-70 calculated by Gaussian.⁶⁸ In contrast, according to V_connect approach, 75% of the free volume can accommodate FC-70. We would have observed the transition from filling the void volume to dissolving the polymer (**Figure 2-5**) at 20 wt %, which is significantly larger than the experimentally determined value.³⁹ Such inconsistency could be due to the topological complexity of free volume elements which cannot accommodate FC-70, even though those elements have larger feature size than FC-70. In summary, the data for the FC-70/Teflon AF 2400 system shows that the accessible free volume distribution based on the R_max approach is more appropriate than the V_connect approach.

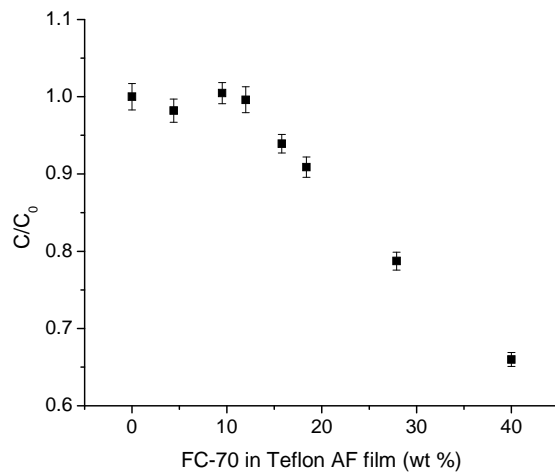


Figure 2-5. Cross Concentration ratio of Teflon AF 2400 polymer in the doped films over a pure film was plotted against the weight percentage of FC-70 in the film. Error bars represent the standard error of the mean. Pure films were oven dried to remove water residue, while doped films were air dried to remove ethanol residue. Note: C/C_0 also equals the ratio of volume of the pure film (V_0) to the volume of the doped film (V) containing the same amount of Teflon AF 2400.

The FFV of FC-70-doped Teflon AF 2400 films was calculated from the measured film densities based on empirical methods (**Figure 2-6**). The FFV of doped films decreases in the range of 0-12 wt % dopant and then increases gradually to approach the FFV of pure FC-70. Similar phenomena have been reported in other polymeric materials doped with small molecule additives.^{104,112-114} A turning point of the FFV change is probably due to the transition of the chemical environment of FC-70-doped Teflon AF 2400 films. Since FC-70 (0-12 wt %) fills in the existing microvoids within the Teflon AF 2400 polymer, the decrease of free volume will lead to subsequently reduced polymeric chain mobility. When the microvoids in the polymeric matrix are saturated with FC-70 (12–40 wt %), adding more FC-70 will dilute the polymer chains. Thus, a polymeric chain unit of Teflon AF 2400 has fewer polymeric segments and more FC-70 molecules in its vicinity. Its local friction may be significantly reduced, which results in easier thermal motion of polymeric segments. Overall, changes in FFV would lead one to predict an antiplasticization effect on the films with less than 12 wt% dopant due to void filling by FC-70 and a plasticization effect on the films with more than 12 wt % dopant due to chain dilution.

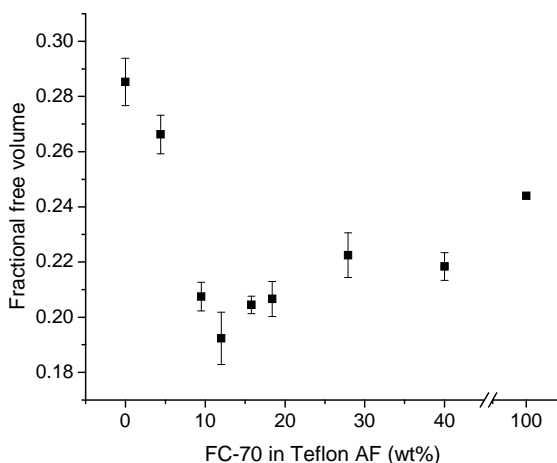


Figure 2-6. Dependence of FFV on FC-70 content (wt %). Error bars are the standard error of the mean. Pure films were oven dried to remove water residue, while doped films were air dried to remove ethanol residue.

In order to determine the influence of FC-70 on antiplasticization/plasticization effects, we monitored the viscoelastic properties of FC-70-doped Teflon AF films by dynamic mechanical analysis (DMA). **Table 2-1** shows the storage modulus (E') of FC-70-doped Teflon AF films at the temperature for transport experiments (20 °C). The 10 wt % FC-70 shows the antiplasticization effect, with the storage modulus E' 1.3 times higher than that of pure Teflon AF. Further increase of FC-70 content leads to a decrease of the storage modulus, indicating plasticization. This is confirmed by the emergence of two low temperature transitions in the DMA for 26 (4 and 134 °C) and 35 wt % (-10 and 117 °C) FC-70-doped Teflon AF 2400 films that are not present in films that contain 0, 10, and 18 wt % FC-70. The presence of two low-temperature transitions was also observed by Lugert and co-workers⁷¹ while studying the plasticization of Teflon AF 2400 by perfluoroperhydrophenanthrene, perfluoro(1-methyldecalin), and 2H-perfluoro-5,8,11-trimethyl-3,6,9,12-tetraoxapentadecane. The extent of polymeric chain mobility indicated by the antiplasticization/plasticization effect is an important influencing factor for solute transport through films.

Table 2-1. Storage Modulus of FC-70-doped Teflon AF Films at 20.0 °C^a

FC-70 (wt %)	Storage Modulus (MPa)
0	1122
10	1439
18	1085
26	836
35	593

^a Pure films were oven dried to remove water residue, while films were air dried to remove ethanol residue.

In what follows, we present a considerable number of experimental data showing how the physical changes just described influence the thermodynamic (partitioning) and transport properties of these films. As a guide, we present a broad overview of the results in **Table 2-2**.

Table 2-2. Summary of the Physical and Chemical Properties of FC-70-doped Teflon AF Films at 20.0 °C^a

Properties	Teflon AF 2400 doped with FC-70	
	0–12 wt% FC-70 content	>12wt% FC-70 content
Free Volume	Decreasing, FC-70 fills the free volume of Teflon AF 2400	Increasing, FC-70 dilutes Teflon AF 2400
Storage Modulus	Increasing	Decreasing
Sorption of CHCl ₃	Decreasing and approaching the solubility of CHCl ₃ in FC-70	
Permeability Coefficients	Decreasing	Increasing
Diffusion Coefficients	Decreasing	Increasing
Partition Coefficients	Decreasing trend in general	
Partitioning Selectivity (8F/8H, 5F/5H) ^a	Increasing trend in general	
Partitioning Selectivity (3F/3H) ^a	No increase	

^a Partition coefficient of a fluorous compound with the stated number of F atoms divided by the partition coefficient of the analogous hydrogen-containing compound.

2.3.3 Sorption of Chloroform in Doped Films

Our previous study found that pure Teflon AF 2400 films in equilibrium with chloroform contain 1.13 M chloroform.⁵⁶ There is ongoing interest in the analysis of how chloroform may influence solute transport. We compared the permeability coefficients of nitrobenzene and pentafluoronitrobenzene through a fresh pure Teflon AF film (P_f) and a film from the same batch soaked in fresh chloroform for 4 days (P_s). As shown in **Table 2-3**, P_s is significantly larger than P_f for each solute. This could be interpreted as enhanced solute diffusivity due to the

plasticization of Teflon by chloroform.⁵⁶ Moreover, the ratio of permeability coefficients (P_s/P_f) for nitrobenzene is slightly higher than pentafluoronitrobenzene. Obviously, the Teflon film in equilibrium with chloroform becomes more “organic like”, which is less favorable for the selective partitioning of fluorocarbons than the corresponding hydrocarbon counterparts.

Table 2-3. Comparison of Permeability Coefficients through Fresh Pure Teflon AF Film and Chloroform-soaked Pure Teflon AF Film at 20.0 °C

Solutes	Permeability through fresh Teflon AF film (P_f , cm ² /s) ^a	Permeability through soaked Teflon AF film (P_s , cm ² /s) ^a	P_s/P_f
Nitrobenzene	$(1.05 \pm 0.003) \times 10^{-9}$	$(2.53 \pm 0.10) \times 10^{-9}$	2.4 ± 0.10
Pentafluoronitrobenzene	$(4.98 \pm 0.05) \times 10^{-9}$	$(1.06 \pm 0.002) \times 10^{-8}$	2.1 ± 0.20

^a The permeability coefficients are the mean values of duplicate experiments. Errors indicated in the table are the standard error of the mean.

We doped films with FC-70 to reduce the sorption of organic solvents in the Teflon matrix for the purpose of achieving selective transport of fluorocarbons over hydrocarbons. The chloroform sorption in Teflon AF films doped with FC-70 was investigated by means of gas-phase IR experiments. As shown in **Figure 2-7**, the amount of chloroform absorbed in doped films decreases along with the increase of FC-70 wt % and then levels off. This phenomenon could be a result of the free volume change inside the film and the enhanced fluorophilicity of the Teflon matrix doped with FC-70. According to the dual-sorption model, sorption of chloroform in FC-70-doped Teflon AF films contains the sorption into both the free volume and the polymeric matrix.^{43,45} The variation of sorption into free volume is roughly parallel to the change of FFV, whereas the matrix sorption would decrease in Teflon films doped with FC-70 because of the increased fluorophilicity. The amount of chloroform absorbed in Teflon films

doped with more than 20 wt % FC-70 approaches the solubility of chloroform in pure FC-70 (4.06 g of chloroform per 100 g of FC-70). Therefore, Teflon AF 2400 films doped with more than 20 wt % FC-70 appear to behave more “FC-70 like”.

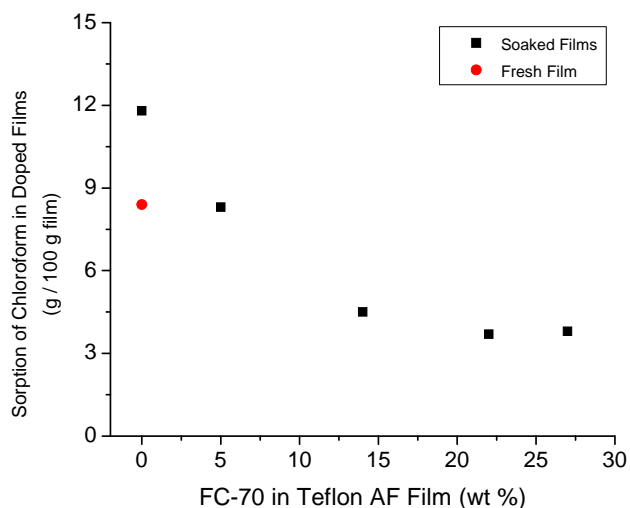


Figure 2-7. Sorption of chloroform in FC-70-doped Teflon AF films.

We noticed that the amount of chloroform absorbed by a fresh pure Teflon film is significantly lower than in a soaked pure film. This indicates that the chloroform imbibed by the film during the soaking process could change the film’s properties and then enhance its sorption capacity. Similar effects were reported for the sorption and desorption isotherms of some gaseous hydrocarbons and fluorocarbons in Teflon AFs.⁴⁵ Gas desorption isotherms were found to be higher than sorption isotherms in Teflon AFs. This effect is especially pronounced for gases which are more soluble in the Teflon matrices.⁴⁵ It could be attributed to the plasticization of Teflon film caused by the sorption of molecules in high concentration, which may effectively decrease the matrix cohesive energy to more easily accommodate more molecules.¹

The desorption of chloroform from FC-70-doped Teflon AF films in equilibrium with liquid chloroform was also observed by FT-IR. The diffusion coefficient of chloroform in a 5 wt % FC-70-doped film was determined to be $9.3 \times 10^{-9} \text{ cm}^2 \cdot \text{s}^{-1}$ at $20.0 \pm 1.0 \text{ }^\circ\text{C}$. This value is about 20% of the diffusion coefficient of chloroform in pure Teflon AF film from a pervaporation study ($4.22 \times 10^{-8} \text{ cm}^2 \cdot \text{s}^{-1}$ at $25 \text{ }^\circ\text{C}$),⁵² indicating the restricted mobility of chloroform in the Teflon film antiplasticized by FC-70.

2.3.4 Dependence of Permeability Coefficients (*P*), Diffusion Coefficients (*D*), and Partition Coefficients (*K*) on Film Composition

The dependence of permeability coefficients on film composition was investigated using aromatic compounds as probe molecules. Recall that permeability coefficients are products of partition coefficients and diffusion coefficients. As shown in **Figure 2-8**, solute permeability coefficients are sensitive to FC-70 content in Teflon AF films. Six probe solutes (toluene (TOL), α,α,α -trifluorotoluene (TFT), 2,3,4,5,6-pentafluorotoluene (PFT), octafluorotoluene (OFT), nitrobenzene (NB), and pentafluoronitrobenzene (PFNB)) show similar trends in the plots. The permeability coefficients decrease as FC-70 content increases when films are doped with less than 15 wt % FC-70. The permeability coefficient of each solute through the pure Teflon AF films is around 10 times larger than through the films doped with 15 wt % FC-70. The trend of the permeability coefficient is reversed when films are doped with more than 15 wt % FC-70. Films containing more than 30 wt % FC-70 can transport solutes as effectively as the pure film. The SEMs of permeability coefficients through pure Teflon films of different thicknesses is never greater than 6% for each solute. Thus, film thickness has no measurable influence on permeabilities.

A plot of $\log P$ versus $\log MW$ of aromatic hydrocarbon solutes is linear with a negative slope-larger homologues permeate more slowly than smaller homologues.⁵⁷ Among six probe solutes in the present work, toluene and nitrobenzene contain no fluorine and fit the linear relationship well. However, the fluorinated solutes with a higher weight percentage of fluorine have logarithmic values of permeability (through pure Teflon AF film) which depart positively (higher P) from the hydrocarbon line. This is consistent with the preferred transport of fluorocarbons through pure Teflon AF 2400 films. For each composition of FC-70 (0–30 wt %) doped Teflon AF 2400 film, the permeability coefficients of the toluene series can be arranged in decreasing order $P_{\text{OFT}} > P_{\text{PFT}} > P_{\text{TFT}} > P_{\text{TOL}}$, despite the fact that the molar mass/critical volumes decrease in the same order. This observation demonstrates that the increase in partition coefficient that accompanies the replacement of a hydrogen atom by a fluorine atom in a solute is greater than the decrease of the diffusion coefficient of the solute. We decided to investigate this in a little more detail.

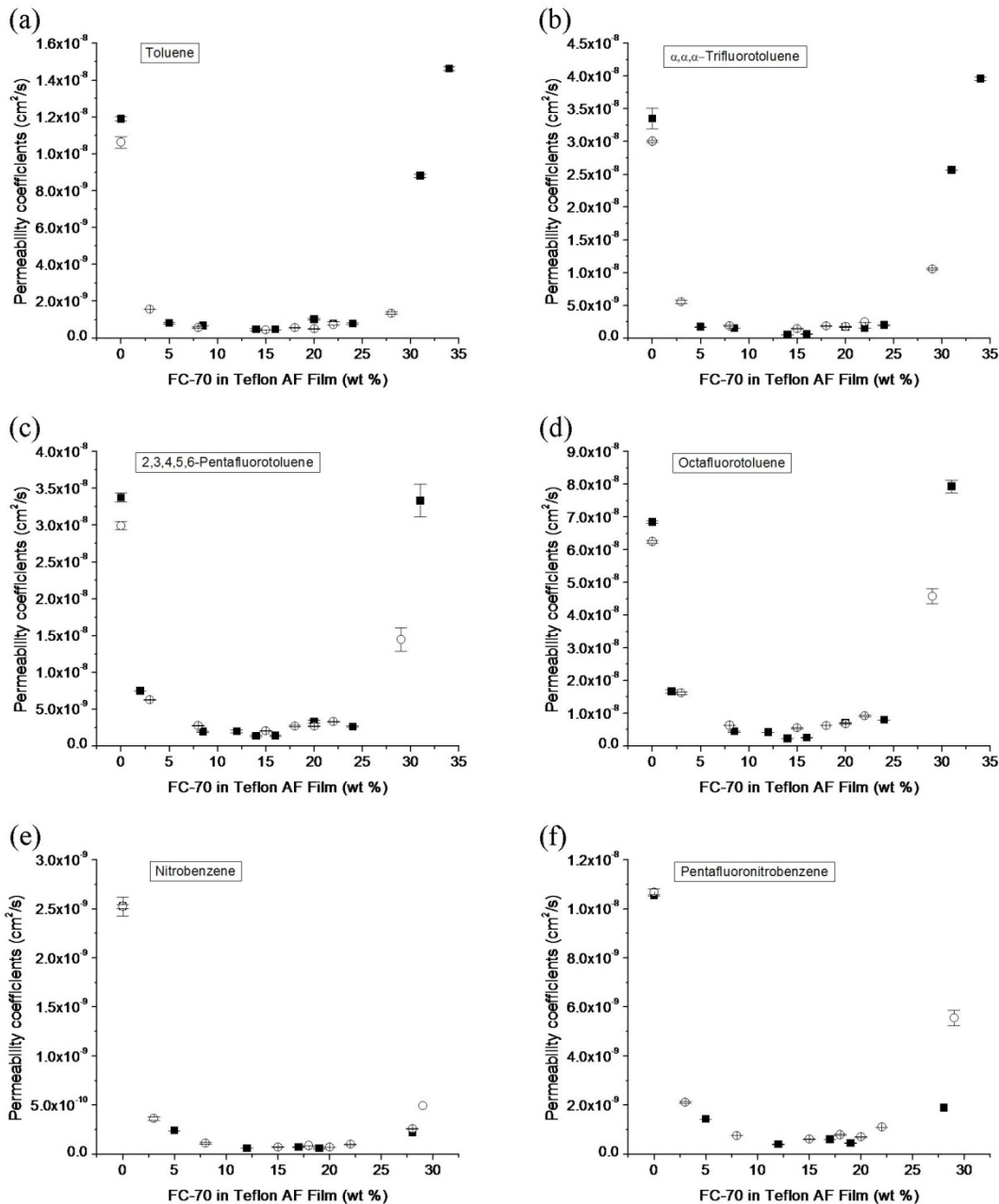


Figure 2-8. Permeability coefficients of solutes in FC-70-doped films at 20.0 ± 1.0 °C: (a) toluene; (b) α,α,α -trifluorotoluene; (c) 2,3,4,5,6-pentafluorotoluene; (d) octafluorotoluene; (e) nitrobenzene; (f) pentafluoronitrobenzene. For all dark squares (■), the source phase concentration is 0.1 M; the film thickness is between 18 and 33 μm. (○) Film thickness ranges from 36 to 127 μm and the source phase concentration varies: (a) 1.0, (b) 0.3, (c) 0.5, (d) 0.1, (e) 0.5, (f) 0.2 M. The error bars represents the standard error of the mean for two measurements.

The diffusion coefficients of six solutes in FC-70-doped Teflon AF 2400 films are plotted against the film composition, as shown in **Figure 2-9**. For all the solutes, the diffusion coefficients decrease as the amount of FC-70 is increased in the low weight percentage range (0–10 wt %), and then the trend is reversed at the high FC-70 content (10–30 wt %). Factors that influence the diffusion in the doped films include (1) the local viscosity, (2) the tortuosity of the diffusion path which is directly related to the concentration of amorphous Teflon in the film,¹¹⁵ and (3) the polymeric chain mobility. We showed above that chloroform sorption decreased in Teflon films with more FC-70 dopant. Because chloroform (dynamic viscosity at 20 °C, 0.573 cP)¹¹⁶ is less viscous than FC-70 (dynamic viscosity at 25 °C, 24 cP), solute diffusion will be slower in the more viscous environment created by FC-70. According to the Teflon concentration in doped films (refer to **Figure 2-5**), the tortuosity is similar in films doped with less than 12 wt % FC-70 and then significantly decreases with a further increase of FC-70 content. Thus, solutes would experience a shorter pathway when diffusing across the films doped with more than 12 wt % FC-70. In addition, the mobility of the polymer chain decreases first at the low FC-70 content (<12 wt %) and then increases at the high FC-70 content (>12 wt %). Solute diffusion through a polymer is easier when the chain mobility increases, and becomes more difficult when the chain mobility decreases. Therefore, in the range of compositions with FC-70 less than 12 wt %, all three factors become less favorable for diffusion as the FC-70 concentration increases. Thus, diffusion coefficients show a decreasing trend in this range. Meanwhile, diffusion coefficients increase along with the increased dopant amount in films containing more than 12 wt % FC-70. This indicates that the influence of the tortuosity and polymer chain mobility are more important than the viscosity of the additive on solute diffusivity in this system. The diffusion coefficients in films containing approximately 30 wt % FC-70 are

larger than in a pure Teflon film, showing the possibility to improve the transport efficiency by doping a large amount of FC-70.

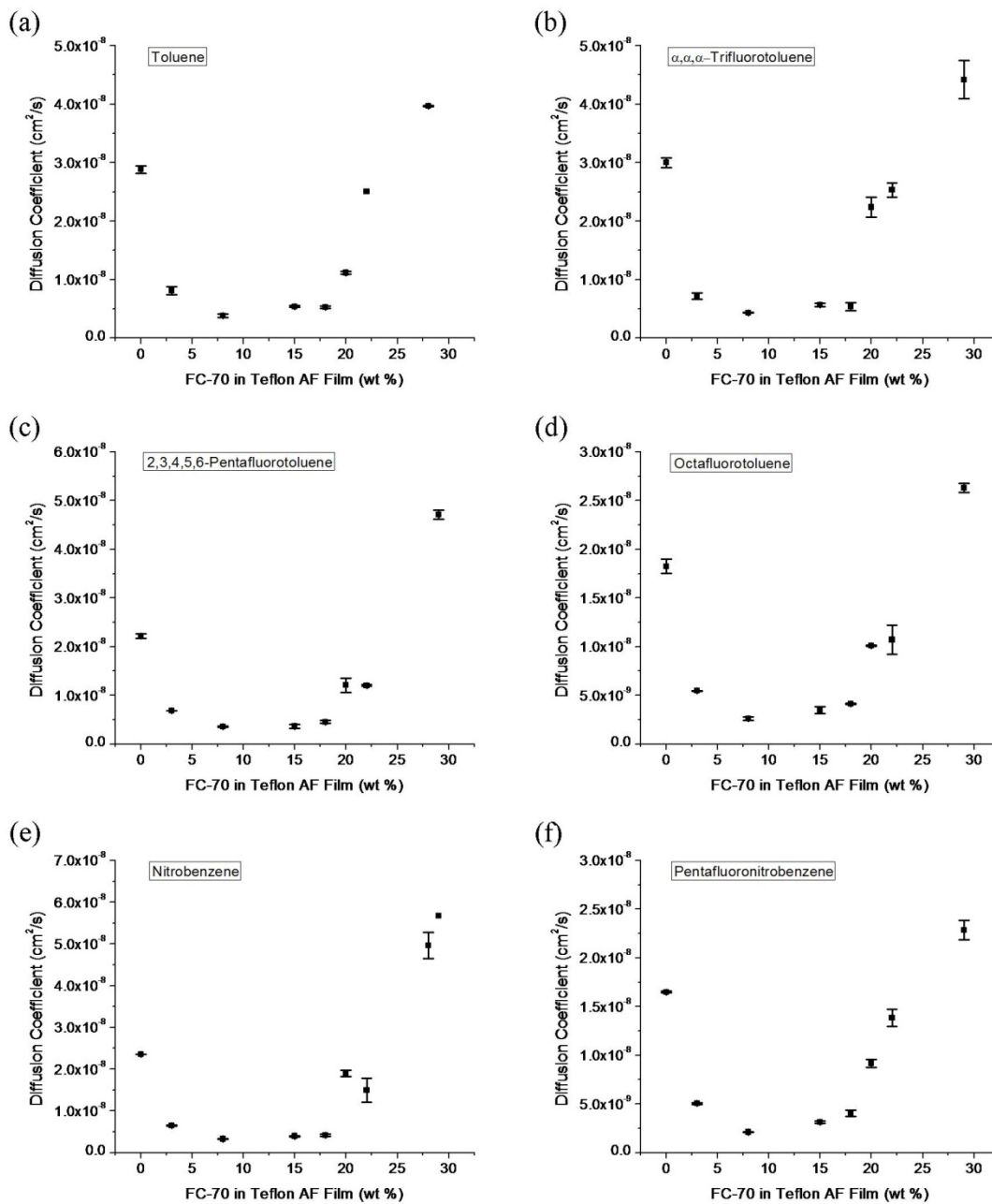


Figure 2-9. Diffusion coefficients of solutes in FC-70-doped Teflon AF 2400 films at 20.0 ± 1.0 °C:

- (a) toluene, $C_s = 1.0$ M; (b) α,α,α -trifluorotoluene, $C_s = 0.3$ M; (c) 2,3,4,5,6-pentafluorotoluene, $C_s = 0.5$ M;
 (d) octafluorotoluene, $C_s = 0.1$ M; (e) nitrobenzene, $C_s = 0.5$ M; (f) pentafluoronitrobenzene, $C_s = 0.2$ M.

It is helpful to understand the partitioning of solutes from chloroform to pure FC-70 before we investigate solute partitioning from chloroform into FC-70-doped Teflon AF films. Octafluorotoluene and 2,3,4,5,6-pentafluorotoluene have relatively large partition coefficients and thus can be accurately measured by the liquid-liquid partitioning experiment. The partition coefficients of the other four solutes were obtained from the measurement of activity coefficients by head space gas chromatography (HSGC). The partition coefficients (based on molar concentration ratio) are summarized in **Table 2-4**. In general, substitution of fluorine increases the partition coefficients from chloroform to FC-70. Compared with the methyl group, the nitro group is more polar. Therefore, the nitrobenzene series exhibits lower partition coefficients than the analogous toluenes.

Table 2-4. Solute Partition Coefficients (FC-70/CHCl₃) at 20.0 °C

Solutes	$K_{F,C}$
Toluene ^a	0.011 ± 0.001
α,α,α -Trifluorotoluene ^a	0.060 ± 0.004
2,3,4,5,6-Pentafluorotoluene ^b	0.108 ± 0.002
Octafluorotoluene ^b	0.616 ± 0.006
Nitrobenzene ^a	0.006
Pentafluoronitrobenzene ^a	0.045

^a Data were obtained from HSGC. ^b Data were obtained from solute partitioning (triplicate measurements). The errors indicated in table are the standard error of the mean.

The partition coefficients and diffusion coefficients of the solutes from chloroform to FC-70-doped Teflon films have been determined simultaneously from the transport experiments with thick films. As shown in **Figure 2-10**, the partition coefficients of all the solutes show a

decreasing trend in general along with the increase of FC-70 wt % and eventually approach their partition coefficients from chloroform to pure FC-70. Therefore, Teflon films doped with larger amounts of FC-70 behave more “FC-70 like”. A descending order of partition coefficients ($K_{\text{OFT}} > K_{\text{PFT}} > K_{\text{TFT}} > K_{\text{PFNB}} > K_{\text{TOL}} > K_{\text{NB}}$) is common for the Teflon films with different amounts of dopant.

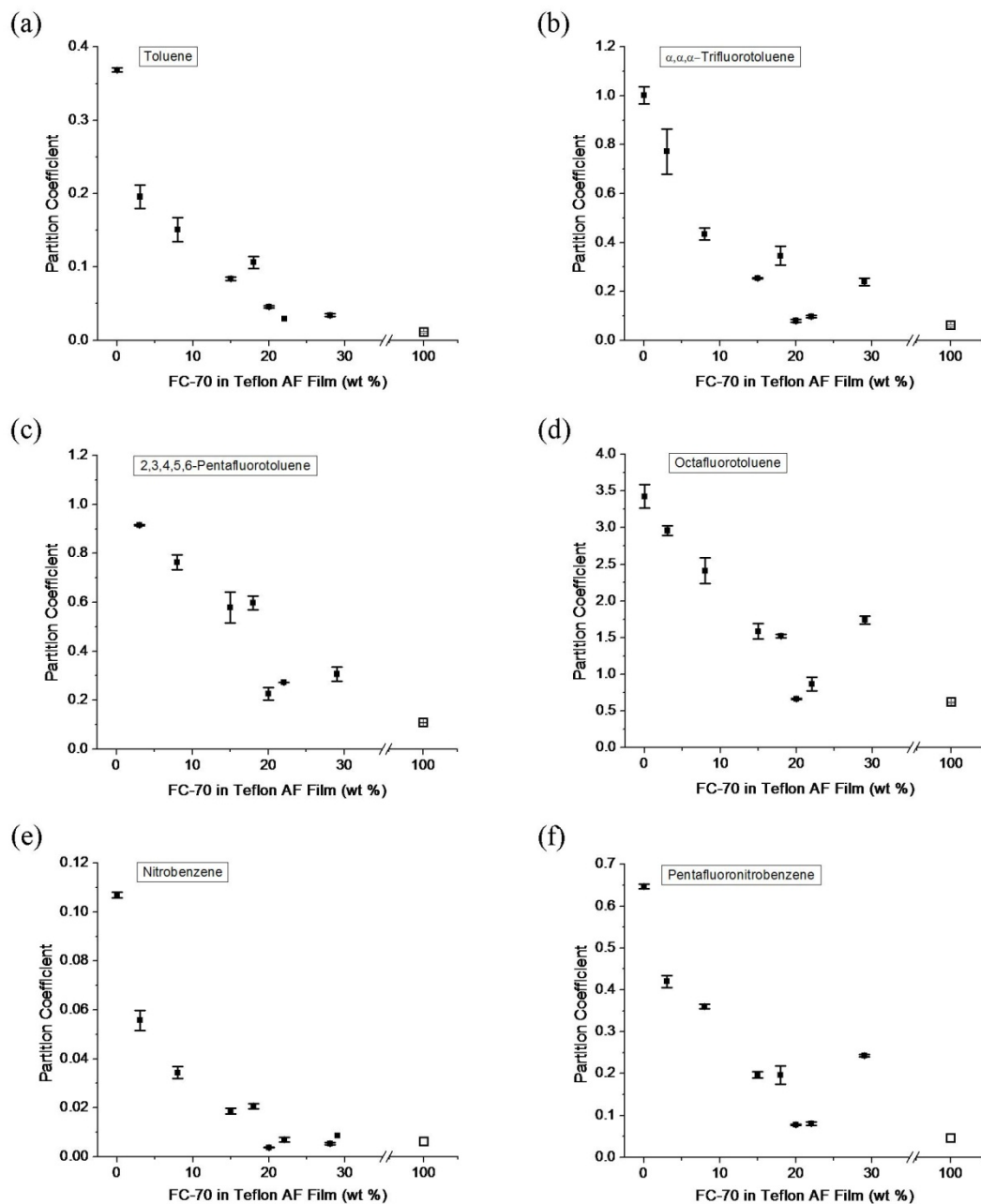


Figure 2-10. Partition coefficients of solutes in FC-70-doped films at 20.0 ± 1.0 °C: (a) toluene, $C_s = 1.0$ M; (b) α,α,α -trifluorotoluene, $C_s = 0.3$ M; (c) 2,3,4,5,6-pentafluorotoluene, $C_s = 0.5$ M; (d) octafluorotoluene, $C_s = 0.1$ M; (e) nitrobenzene, $C_s = 0.5$ M; (f) pentafluoronitrobenzene, $C_s = 0.2$ M. Partition coefficients of toluene, α,α,α -trifluorotoluene, nitrobenzene, and 2,3,4,5,6-pentafluorotoluene from chloroform into pure FC-70 were obtained from head space gas chromatography. Liquid-liquid partitioning experiments were performed to get those values for 2,3,4,5,6-pentafluorotoluene and octafluorotoluene.

Since fluorine substituents contribute to the selective partitioning from chloroform to FC-70-doped Teflon films, it is worthwhile to compare the outcomes of the solutes with different substitutions. Six solutes were classified into three categories: substitution of three methyl hydrogen atoms with fluorine (3F/3H), substitution of five phenyl hydrogen atoms with fluorine (5F/5H), and substitution of eight hydrogen atoms with fluorine (8F/8H). On the basis of different substitutions with fluorine, the selectivities of partitioning from chloroform to doped Teflon films are plotted in **Figure 2-11**. Interestingly, the partitioning selectivities of 2,3,4,5,6-pentafluorotoluene/toluene are close to those of octafluorotoluene/ α,α,α -trifluorotoluene. In addition, α,α,α -trifluorotoluene/toluene and octafluorotoluene/2,3,4,5,6-pentafluorotoluene pairs also have similar partitioning selectivities. If indeed the effects of a particular substitution pattern, e.g., 3F/3H, on partition coefficients is independent of the remainder of the molecule, then the product of the selectivities for the substitutions 3F/3H and 5F/5H should predict the selectivity for the substitution 8F/8H. Thus, partitioning selectivities, $S_{k-CF_3/-CH_3}$ and $S_{k-C_6F_5/-C_6H_5}$, were calculated from the average of the partitioning selectivities of the solute pairs with the corresponding substitutions. The product of the two partitioning selectivities is very close to the partitioning selectivity of the octafluorotoluene/toluene pair ($S_{kC_6F_5CF_3/C_6H_5CH_3}$) at each film composition. A linear relationship ($R^2 = 0.9964$) was obtained with a slope of 1.009 ± 0.025 and an intercept of -0.368 ± 0.444 , when $S_{kC_6F_5CF_3/C_6H_5CH_3}$ is plotted against $S_{k-CF_3/-CH_3} \times S_{k-C_6F_5/-C_6H_5}$ (**Figure 2-12**). Statistical analysis shows no significant difference between the slope and the ideal value of unity ($p = 0.723$). The difference between the intercept and the ideal value of zero is not significant either ($p = 0.446$). This correlation in the toluene series indicates that neither the substitution of fluorine on the methyl group nor that on the phenyl group will significantly change the partitioning properties of other substructures in the solutes.

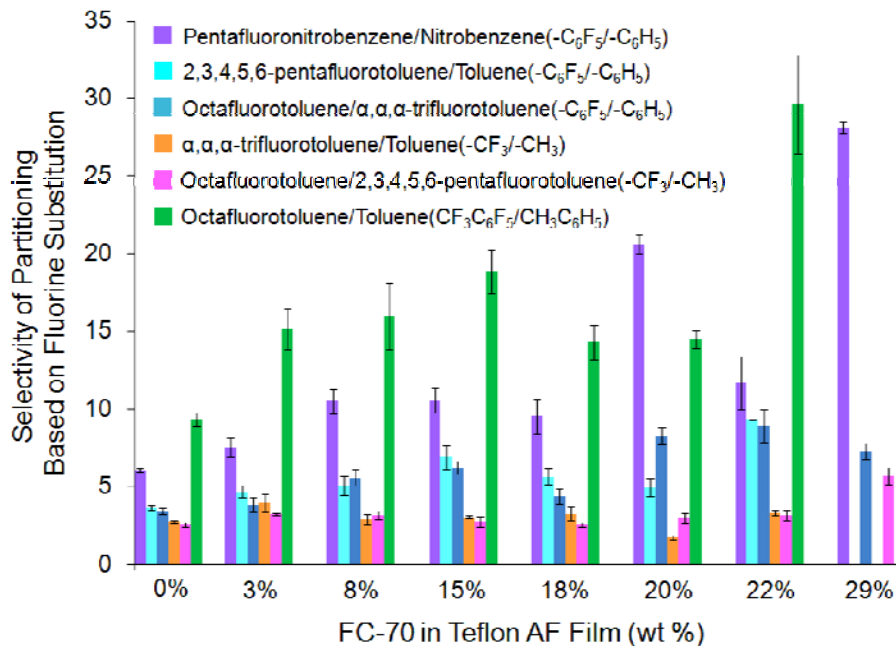


Figure 2-11. Selectivity of partitioning based on different fluorine substitutions. The error bars are the standard error of the mean.

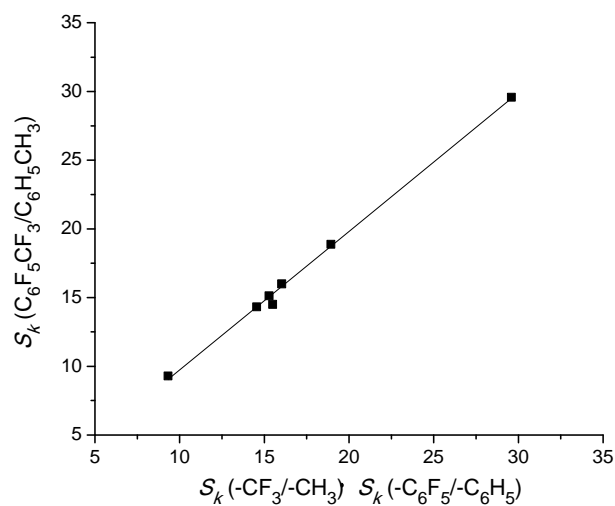


Figure 2-12. Partitioning selectivities of octafluorotoluene over toluene in FC-70-doped (0–30 wt %) Teflon AF films were plotted against the product of partitioning selectivities of trifluoromethyl/methyl and perfluorophenyl/phenyl groups ($y = 1.009x - 0.368$, $R^2 = 0.9964$).

For the nitrobenzene pair, the partition ratio of pentafluoronitrobenzene over nitrobenzene is much higher than the ratios of toluene pairs with the same substitution. This probably results from the strong electron-withdrawing effect of the F/H substitution on the nitro group. Nitrobenzene is not only highly polar but also highly polarizable.¹¹⁷ Substitution of five hydrogen atoms on the phenyl group with fluorine atoms may significantly decrease the electron density on the nitro group, thus decreasing its polarizability. Recently, Amemiya's group reported that the lipophilic nature of perfluoroalkyl surfactants originates from the electron-withdrawing effect of a perfluoroalkyl group on its adjacent oxoanion groups.¹¹⁸ The decrease in the charge density on the carboxylate functional group is responsible for the significant solubility of perfluorooctanoate in octanol. In a similar way, therefore, the intermolecular interactions between pentafluoronitrobenzene and solvent are weaker than those of nitrobenzene. Confirmation of this notion can be seen in the relatively large difference of the boiling points of the two liquids (52 °C). In comparison, the differences of boiling point between the toluene and 2,3,4,5,6-pentafluorotoluene pair as well as the α,α,α -trifluorotoluene and octafluorotoluene pair are 6 and 2 °C, respectively. In addition, an FT-IR study of nitrobenzene in chloroform indicates a strong hydrogen-bond formation.¹¹⁹ However, the nitro group in pentafluoronitrobenzene will be a much weaker hydrogen-bond acceptor due to the decreased electron density. Thus, the 5F/5H substitution on the phenyl group significantly changes the electronic properties of the nitro group.

2.3.5 Transport Selectivity of FC-70-doped Teflon AF Films Based on Different Substitutions

The transport selectivities based on different substitutions (3F, 5F, 8F) are plotted against the composition of FC-70-doped films (**Figure 2-13**). Usually, longer fluororous ponytails, more ponytails, and/or a higher weight percentage of fluorine lead to larger partition coefficients into fluororous media and thus better selectivity in partitioning dominated selective transport. There is a general increasing trend for the selectivities of 8F- and 5F-substituted pairs. Among all the solute pairs we studied, the octafluorotoluene and toluene pair has the largest difference in fluorine content; thus, the partitioning of octafluorotoluene compared with toluene ($K_{\text{OFT}}/K_{\text{TOL}}$) into doped film is more favorable than into the pure Teflon AF film. However, the relatively large size of octafluorotoluene leads to slower diffusion. Nonetheless, the selectivity of this pair increased using Teflon AF films doped with larger FC-70 content. For the solute pairs with the same substitution of five fluorine atoms on the phenyl ring, the selectivity increased most significantly for the pentafluoronitrobenzene/nitrobenzene pair followed by the octafluorotoluene/ α,α,α -trifluorotoluene and 2,3,4,5,6-pentafluorotoluene/toluene pairs. For the solute pairs with substitution of three fluorine atoms, no obvious increase on selectivity was observed using FC-70 (≤ 30 wt %) doped Teflon AF film. Further increase of the FC-70 wt % in Teflon film can be beneficial to increase the transport selectivity. However, a Teflon AF 2400 film containing FC-70 larger than a weight percentage of 35 wt % is difficult to handle practically due to the reduced mechanical properties.

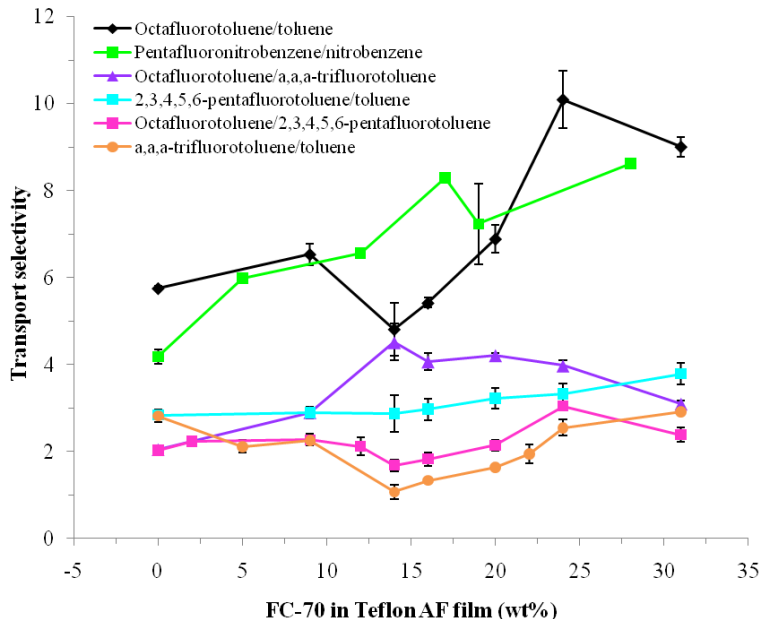


Figure 2-13. Transport selectivity based on the substitution of fluorine atoms (8F, 5F, 3F) at 20.0 ± 1.0 °C. The error bars represent the standard error of the mean.

2.3.6 Recycling of Teflon AF 2400

Teflons are normally not considered to be easily degraded. The recycling of Teflons can reduce not only the production of waste but also the cost of our separation system. As shown in **Table 2-5**, the recycled Teflon AF 2400 films have a similar film density to that of the fresh films with no significant difference ($p = 0.553$). The practicality of the recycled Teflon AF 2400 for the transport application has been verified. The relative errors of permeability coefficients for toluene and α,α,α -trifluorotoluene through recycled films and fresh films are 22% and 13%, respectively, which fall within the margin of error in our long-term study.⁵⁷ The selectivity of α,α,α -trifluorotoluene over toluene has 9% relative error through the recycled Teflon films and fresh ones. Therefore, the FC-70-doped Teflon AF 2400 used in this work could be recycled for practical use.

Table 2-5. Properties of the Fresh Teflon AF 2400 Films and Recycled Teflon AF 2400 Film

	Fresh Teflon AF 2400 Film	Recycled Teflon AF 2400 Film
Density (g/cm ³)	1.816 ± 0.022 (<i>n</i> ^a = 5)	1.822 ± 0.017 (<i>n</i> ^a = 10)
<i>P</i> _{toluene} (cm ² /s)	(1.19 ± 0.01) × 10 ⁻⁸	(0.953 ± 0.040) × 10 ⁻⁸
<i>P</i> _{α,α,α-Trifluorotoluene} (cm ² /s)	(3.35 ± 0.16) × 10 ⁻⁸	(2.94 ± 0.02) × 10 ⁻⁸
Selectivity	2.82 ± 0.14	3.08 ± 0.13

^a *n* is the number of measurements.

2.4 CONCLUSION

Perfluorotripropylamine-doped Teflon AF 2400 matrices transport fluorinated organic compounds with considerable selectivity compared to their organic counterparts. Less chloroform partitions into Teflon AF films containing FC-70 than into undoped films. The amount of chloroform absorbed in Teflon films with larger than 20 wt % FC-70 is close to the solubility of chloroform in FC-70. Moreover, solute partition coefficients from chloroform to Teflon films doped with more FC-70 approach the partition coefficients from chloroform to pure FC-70. Both the sorption behavior of chloroform and the solute partitioning pattern indicate that doped Teflon films have FC-70-like properties. The permeabilities of six solutes through Teflon films doped with various amounts of FC-70 (0–30 wt%) show a similar pattern as FC-70 content is changed due to the integrated effect of solute diffusion and partitioning. FC-70-doped films show increasing selectivity for transport of 8F/8H- and 5F/5H-substituted solute pairs as FC-70 content increases.

2.5 ACKNOWLEDGEMENT

We thank the National Science Foundation for support through grants CHE-0957038 and CHE-0615952. We thank Jie Zhang for preliminary experimental work. Hong Zhang thanks Bayer MaterialScience for a 2010–2011 Graduate Student Fellowship.

3.0 PROPERTIES AND TRANSPORT BEHAVIOR OF TEFLON AF 2400 NANOCOMPOSITE FILMS

Parts of this chapter are from **Nanocomposite Teflon AF 2400 films as tunable platforms for selective transport**, Zhang, H.; Wang, S.; Weber, S. G. *Analytical Chemistry*, **2012**, *84*, 9920–9927; and **Morphology and free volume of nanocomposite Teflon AF 2400 films and their relationship to transport behavior**, Zhang, H.; Wang, S.; Weber, S. G., *Journal of Membrane Science*, **2013**, *443*, 115–123. Adapted with permission from American Chemical Society and Elsevier (License number: 3278960661775). Weber, S. G. and Zhang, H. conceived the study. Zhang, H. performed all the experimental work with the help of Wang, S., and wrote the paper under the guidance of Weber, S. G.

3.1 INTRODUCTION

Nanocomposite materials produced by embedding nanoparticles in polymer matrices exhibit unique and promising properties that are of interest in many fields, including sensors,¹²⁰ separations,^{49,50} fuel cells,¹²¹ drug delivery,¹²² regenerative medicine,¹²³ and smart materials.¹²⁴ In some cases, the macroscopic properties that lead to the foregoing applications are controlled by the microscopic structure and morphology of the materials. However, creating a particular morphology is a challenge.¹²⁵ Nanoparticle patterns can be created by external means and by

tailoring nanoparticle-nanoparticle and nanoparticle-polymer matrix interactions.¹²⁵ Recently, several investigators have developed an understanding of the phase behavior of nanoparticle-polymer melts.¹²⁶⁻¹²⁸ Of course, the phase behavior depends on thermodynamics.^{125,129} The recent work is interesting because it shows how subtle changes, e.g., in brush length on polymer-modified nanoparticles,¹²⁶ entropic contributions from the number of polymer contacts with a particle,¹²⁷ or the relative sizes of polymer chains and nanoparticles^{126,128} can control phase behavior.

Applications of fluorinated materials are growing. These robust, transparent materials offer the potential for selective chemical separations and sensors.^{1,130,131} Introducing receptors complementary to targets will improve sensitivity and specificity of the separation/measurement.^{62,64,132,133} Fluorinated materials are ideal matrices for molecular recognition due to weak van der Waals interactions per molecular contact area.³ Teflon AF is a family of amorphous glassy copolymers of tetrafluoroethylene (TFE) and 2,2-bis(trifluoromethyl)-4,5-difluoro-1,3-dioxole (PDD). Teflon AF 2400 exhibits a high fractional free volume (FFV)²⁶ stemming from the rigid structure of the dioxolane ring and the weak van der Waals interactions between chains.²⁶ Theoretical studies predict a bimodal distribution of free volume elements and their partial connectivity in Teflon AF 2400.³⁹ The high FFV and weak inter chain interactions lead to a low activation energy of diffusion as well as distinctive solubility/partitioning behavior of gaseous permeants in Teflon AF 2400.¹⁵ This material provides unique opportunities for transport-based processes, including gas separation, pervaporation, permeation-based sensors, ion sensing, and flow chemistry.²⁸

We are not aware of investigations that probe the effect of plasticizer on the nanoscale morphology of composite materials, nor are we aware of work that relates the control of

composition (plasticizer) to the amount and character of the material's free volume and its impact on molecular transport. There is only a handful of studies that include a plasticizer in polymer-nanoparticle composites,¹³⁴⁻¹³⁶ chiefly to increase conductivity in electrolyte material applications for lithium batteries. Thus, we have developed a system with up to four components: polymer (Teflon AF 2400), nanoparticles (solid silica modified with a fluoroalkylsilane monolayer), plasticizer (perfluorotripropylamine), and casting solvent that all have very low and similar cohesive energy densities. The resulting stable suspensions allow for casting films by slow solvent evaporation leading to reproducible creation of polymer films with both nanoparticles and plasticizer. We find that the films' morphologies are controlled by the presence of plasticizer. The morphological differences translate directly into very different molecular transport properties. We conclude that the presence of a plasticizer is one more tool to consider in the attempt to control polymer nanocomposite architecture and properties.

3.2 EXPERIMENTAL

3.2.1 Materials

Teflon AF 2400 was purchased from DuPont (Wilmington, DE). HFE-7100 (a mixture of methoxynonafluoroisobutane, and methoxynonafluorobutane), PF-5080 (a mixture of perfluoro compounds comprising primarily compounds with 8 carbons), FC-77 (primarily a mixture of C₈F₁₈ and cyclic C₈F₁₆O), and Fluorinert FC-70 (perfluorotripropylamine, bp 215 °C) were purchased from 3M (Minneapolis, MN). The suspension of silica nanoparticles in isopropanol (IPA-ST-ZL) was kindly supplied by Nissan Chemical Industries Ltd. (Houston, TX).

1H,1H,2H,2H-perfluorooctyltriethoxysilane, triethoxy(octyl)silane, and probe solutes used in transport experiments (toluene (TOL), octafluorotoluene (OFT), naphthalene (NPTH), and Reichardt's dye) were purchased from Sigma-Aldrich (St. Louis, MO). Ammonium hydroxide (28.0–30.0%) was purchased from J. T. Baker (Phillipsburg, NJ). Ethanol, isopropanol and chloroform were obtained from Fisher Scientific and used as received. Water was purified with a Milli-Q Synthesis A10 system (Millipore, Bedford, MA).

3.2.2 Surface Modification and Characterization of Silica Nanoparticles

A colloidal suspension of silica nanoparticles (IPA-ST-ZL, 10 mL) was added to a vigorously stirred solution of isopropanol (25 mL) and HFE-7100 (25 mL) at room temperature. Then 1H,1H,2H,2H-perfluorooctyltriethoxysilane (2.0 g, 1.5 mL) was added and the resulting mixture was stirred until a homogeneous suspension was obtained. A solution of ammonium hydroxide (28.0–30.0%, 10 mL) in isopropanol (25 mL) was added dropwise with stirring over 10 minutes. Finally, the mixture was refluxed at 70–80 °C for 3 days. The modified nanoparticles were centrifuged at 6,000 rpm for 30 min and then resuspended in ethanol/HFE-7100 (30 mL/15 mL) for three cycles to remove excess silane reagent. The organosilane-modified silica nanoparticles were obtained under the same conditions as described above for the fluoroalkylsilane modification with only one difference. Instead of using the ethanol/HFE-7100 mixture, pure ethanol was used as the solvent in both the reaction and washing processes.

The modified nanoparticles were characterized by elemental analysis, transmission electron microscopy (TEM), differential scanning calorimetry (DSC), and water contact angle. Elemental analysis (C, H, F %) was conducted by Atlantic Microlab Inc. (Norcross, GA).

Nanoparticle samples for TEM measurements were prepared by adding a droplet of dilute nanoparticle suspension (in ethanol) on a carbon-coated Cu grid (Ted Pella, Inc., CA). The grid was allowed to dry, and the measurement was performed with a Philips Mogagni 268 TEM. Differential scanning calorimetry (DSC) analysis was performed with a Shimadzu DSC-60 Differential Scanning Calorimeter. Samples (unmodified and modified silica nanoparticles) were freeze-dried for 17 hours before measurement. The experimental program for each measurement includes two cycles. Each cycle contains four steps: stabilizing at 30 °C for 5 minutes, heating to 380 °C at a rate of 5 °C/min, stabilizing at 380 °C for 5 minutes, and cooling down to 30 °C at a rate of 5 °C/min. The hydrophobicity of modified and unmodified silica nanoparticles was characterized by water contact angle measurements. Colloidal suspensions of nanoparticles (5 mg/mL) in ethanol were dropped on an ethanol-cleaned microscope slide. The solution was allowed to spread out and dry to form a thin nanoparticle layer. The water contact angle on the nanoparticle-covered slide was measured with a VCA 2000 Video Contact Angle System (Billerica, MA).

3.2.3 Preparation of the Composite Films

To prepare FNP-doped Teflon AF 2400 films, the nanoparticles were added to a 10 mg/mL solution of Teflon AF 2400 in HFE-7100/PF5080 (volume ratio = 2:1) in the desired proportions. Sonication gives homogeneous and stable suspensions of FNPs in Teflon AF 2400 solution. Suspensions were transferred into an optical-flat-bottomed glass Petri dish with an i.d. of 6.0 cm. The dish was covered with a piece of weighing paper and a glass cover. The solvent was allowed to evaporate slowly at room temperature until a constant weight of the film was reached (about 4 days). Films were readily peeled off with forceps after adding 2 mL of ethanol to the dish. FNP-

doped Teflon AF 2400 films were equilibrated in pure chloroform (stirred at 200 rpm at 20.0 ± 1.0 °C) for 48 hours before transport experiments.

To prepare a Teflon AF 2400 film containing FNP and FC-70 (typical weight of a film \approx 200 mg), the nanoparticles, FC-70, and Teflon AF 2400 were introduced in the desired proportions and sonicated in HFE-7100/PF5080 (volume ratio = 2:1, total volume: 5 mL) to form a homogeneous suspension. Three-component films were obtained under the same conditions as described above with one difference. They were peeled off using a scalpel with the addition of 3mL FC-70 saturated EtOH/10% H₂O. These films were stored in a covered container with an FC-70-saturated atmosphere, then were equilibrated in chloroform containing a defined concentration of FC-70 before transport experiments to ensure equal chemical potential of FC-70 in the source phase, polymer phase, and receiving phase.¹³⁷

3.2.4 Morphological, Mechanical, Sorption, and Transport Properties of the Composite Films

All the composite Teflon films were characterized by scanning electron microscopy (SEM) and dynamic mechanical analysis (DMA).¹³⁷ For the investigation of film morphology and homogeneity, the cross-sectional images of composite Teflon AF 2400 films were captured using a Philips XL-30 field emission SEM (Hillsboro, OR). Films for SEM studies were fractured in liquid nitrogen and sputter-coated with palladium to enhance surface conductivity. Dynamic mechanical analysis was carried out using a Q800 DMA (TA Instruments, New Castle, DE). DMA was performed on a rectangular shaped film mounted between the tensile mode clamps of the instrument. Thin Teflon AF gaskets were used between a three component film (Teflon AF/FNP/FC-70) and a clamp to prevent mechanical damage to the film. The sample was pre-

stretched under a preload force of 0.01 N. The storage modulus at 20 °C for all films was measured under a sinusoidal strain deformation (0.3% strain amplitude) of 1 Hz. The glass transition temperature of Teflon AF films doped with FNPs was determined using a sinusoidal strain deformation (0.3% strain amplitude) of 1 Hz during a temperature sweep from –100 to 300 °C at a rate of 3 °C/min. Three component films (Teflon AF/FNP/FC-70) display much higher stiffness at low temperatures. Therefore, the glass transition temperature of three-component films was measured under a sinusoidal strain deformation (0.1% strain amplitude) of 1 Hz during a temperature sweep from –50 to 300 °C at a rate of 3 °C/min to ensure the film integrity.

DSC was used to determine the change in heat capacity at T_g for FNP-containing Teflon AF films. Differential scanning calorimetry (DSC) analysis of fluorophilic silica nanoparticle doped Teflon AF 2400 films was performed with a Shimadzu DSC-60 Differential Scanning Calorimeter. Small pieces of films with dimension $\sim 2\text{mm} \times 2\text{mm}$ (total mass: 10–17 mg) were applied in measurement. The experimental program for each sample includes many cycles: 0 wt%: 3; 5 wt%: 3; 15 wt%: 4; 30 wt%: 4; 50 wt%: 10; 70 wt%: 10. Each cycle contains four steps: stabilizing at 100 °C for 5 minutes, heating to 300 °C at a rate of 5 °C/min, stabilizing at 300 °C for 1 minutes, and cooling down to 100 °C at a rate of 10 °C/min. Curve fits to obtain the change of heat capacity was performed by PeakFit (Systat, San Jose, CA, USA).

Pure Teflon AF and 70 wt% FNP doped Teflon AF films were subjected to BET analysis. Nitrogen sorption analysis was performed at $(77.06 \pm 0.03)\text{K}$ with a Micromeritics ASAP 2010 gas adsorption analyzer. Before each measurement, the film was outgassed overnight at 60 °C to remove dissolved and adsorbed gases.

The sorption of chloroform in all composite Teflon AF films was measured by FT-IR in a gas flow cell.¹³⁷ Saturated chloroform vapor was carried into the IR flow cell by nitrogen gas

with the pressure of 15 psi (20 °C) at a flow rate of ~0.1 LPM. The tail gas was absorbed by *n*-butanol. IR absorbance of chloroform in the flow cell was continuously monitored by an FT-IR spectrometer (Bio-Rad Excalibur FTS 3000 Spectrometer, DigiLab, Randolph, MA) to ensure equilibrium (typically 30 minutes). In order to measure the sorption of chloroform in a hybrid film, a piece of the film with the same diameter as the KBr window was placed between the two lead spacers in the flow cell for IR measurement. The IR absorbance of the flow cell without a film was monitored as the control experiment. The chloroform sorption was quantified based on the difference of IR absorbance with and without a film. Since the characteristic vibrational peak shifted from 772 cm⁻¹ for the vapor chloroform to 768 cm⁻¹ for the chloroform in Teflon film, the peak area was used for IR quantification.^{56,137}

Permeabilities, diffusion coefficients, and partition coefficients of solutes through composite Teflon AF films were determined using a three-phase transport device at 20 ±1.0 °C.¹³⁷ A film was mounted between two quartz cuvettes (path length equals 1.0 cm, Starna Cells, Atascadero, CA) with holes (0.5 cm in diameter) to define the effective transport area. Two pieces of Viton gasket were placed in between the film and cuvettes to prevent leaking. The eight-position multi-cell transport holder was used to hold eight cells (four pairs) in a rack, which were kept at constant temperature by water circulation from a thermostatic water bath. The stirring module for the multi-cell transport holder controlled the stirring speed at the same rate for the eight cells. The volume of the source phase containing the analyte and receiving phase was 3.00 mL in all the transport experiments. The concentration of probe solute in the source phase is 0.10 M for all transport experiments. Solute concentration in the receiving phase was continuously monitored by a UV spectrophotometer (Hewlett-Packard 8452A UV-visible diode

array spectrophotometer, Palo Alto, CA). The steady-state flux, J , of a solute through the film is given by **eq. 3-1**:⁵⁷

$$J = \frac{dC_r}{dt} \cdot \frac{V}{A} (\text{mol} \cdot \text{cm}^{-2} \cdot \text{s}^{-1}) \quad (3-1)$$

dC/dt is the accumulation rate of solute in the receiving phase. V is the volume of the receiving phase (3.00 mL). A is the effective transport area (0.196 cm²). The permeability coefficient, P , can be deduced from the flux:⁵⁷

$$P = \frac{J \cdot l}{C_s - C_r} \approx \frac{J \cdot l}{C_{st}} (\text{cm}^2 \cdot \text{s}^{-1}) \quad (3-2)$$

where l is the film thickness determined by micrometer measurements. C_s and C_r represent the concentration of the solute in the source phase and receiving phase, respectively. In our experimental duration, C_r is negligible compared to C_s . Thus $C_s - C_r$ can be simplified as the initial concentration of the solute in the source phase, C_{st} .

In order to clearly observe the lag phase prior to the solute flux reaching the steady state, thick films (77 μm to 235 μm) were employed in the transport experiments. The thick films were prepared by firmly stacking multiple thin films (20-40 μm) together. The concentrations of source phase solutions (toluene: 0.9 M, octafluorotoluene: 0.1 M, naphthalene: 1.0 M) were chosen based on solute absorptivity. UV absorbance of the receiving phase was recorded continuously at a time interval of 20 s in order to measure the solute accumulation. For a transport system that starts with “zero” solute concentration in both the film and the receiving phase, the accumulation of solute molecules can be theoretically described by **eq. 3-3**:¹³⁷

$$Q_t = K \cdot C_s \cdot l \cdot \left(\frac{D \cdot t}{l^2} - \frac{1}{6} - \frac{2}{\pi^2} \cdot \sum_{n=1}^{\infty} \frac{(-1)^n}{n^2} \cdot e^{-D \cdot n^2 \cdot \pi^2 \cdot t / l^2} \right) (\text{mol} \cdot \text{cm}^{-2}) \quad (3-3)$$

Q_t denotes the accumulation of the solute in the receiving phase (substance passed through the film) per transport area within the time range t . K is the partition ratio of the solute from chloroform to the film. C_s is the concentration of the solute in the source phase solution. l represents the thickness of film. D is the average diffusion coefficient of the solute in the film. Thus, the diffusion coefficients and partition coefficients can be obtained by nonlinear fitting **eq. 3-3** to experimental data using Mathcad 14 (“infinity” in the sum was set to 100).

3.2.5 Film Density Measurement and Apparent Fractional Free Volume (aFFV)

The hydrostatic weighing method was used to determine film density (ρ).¹³⁷ Based on measured densities, the aFFV of the Teflon films containing dopants (FNP alone or both FNP and FC-70) can be calculated according to **eq. 3-4**:

$$aFFV = 1 - \rho \cdot \left(1 - \sum_i wt_i \%\right) \cdot \frac{(1 - f_T)}{\rho_T} - \sum_i \rho \cdot wt_i \% \cdot \frac{(1 - f_i)}{\rho_i} \quad (3-4)$$

where ρ_T and f_T correspond to the density and FFV of pure Teflon AF 2400, respectively. ρ_i is the density of a dopant, while f_i is the FFV of the dopant. $wt_i \%$ is the weight percentage of a dopant in the film. The second term, $\rho \cdot \left(1 - \sum_i wt_i \%\right) \cdot \frac{(1 - f_T)}{\rho_T}$, represents only the volume occupied by

the Teflon AF 2400 (excluding free volume) per unit volume of the hybrid film. The third term, $\rho \cdot wt_i \% \cdot \frac{(1 - f_i)}{\rho_i}$, is the volume of the dopant (excluding free volume) per unit volume of the

hybrid film. We assume that the fluoros surface modification has a negligible impact on the density and free volume of the solid silica particles. The density of FNP is taken to be the same as unmodified nanoparticles, and the FFV of FNPs is 0.

The apparent fractional free volume of the permeable component in the film ($aFFV_p$) is calculated according to **eq. 3-5**:

$$aFFV_p = \frac{aFFV}{1 - \rho \cdot wt_{FNP} \% / \rho_{FNP}} \quad (3-5)$$

where $wt_{FNP}\%$ and ρ_{FNP} correspond to the weight fraction and density of FNP, respectively.

3.2.6 Radius of Gyration (R_g) of Teflon AF 2400

Viscosity measurements of a series of dilute Teflon AF 2400 solutions in FC-77 (1, 2, 3, 4, 5 mg/mL) were performed with an AR 2000ex rheometer at 20 °C. Over this range of low concentrations (1–5 mg/mL), the reduced viscosity (η_{re}) and inherent viscosity (η_{in}) change linearly with Teflon AF 2400 concentration, and therefore, follow the Huggins and Kraemer equations:¹³⁸

$$\frac{\eta - \eta_s}{\eta_s \cdot c} = \eta_{re} = [\eta] + K_H \cdot [\eta]^2 \cdot c \quad (3-6)$$

$$\frac{\ln\left(\frac{\eta}{\eta_s}\right)}{c} = \eta_{in} = [\eta] + K_K \cdot [\eta]^2 \cdot c \quad (3-7)$$

where η and η_s correspond to the viscosity of the Teflon AF 2400 solution and pure solvent (FC-77), respectively. K_H and K_K are the Huggins and Kraemer constants. The intrinsic viscosity ($[\eta]$) of Teflon AF 2400 was determined by plotting η_{re} and inherent viscosity η_{in} versus the solution concentration (c). The radius of gyration of Teflon AF 2400 in FC-77 was determined from the intrinsic viscosity according to **eq. 3-8**:¹³⁸

$$R_g = \sqrt[3]{\frac{[\eta] \cdot M_w}{6.2 \cdot N_A}} \quad (3-8)$$

where M_w is the weight-average molecular weight of Teflon AF 2400. N_A is the Avogadro constant.

3.3 RESULTS AND DISCUSSION

3.3.1 Fluorophilic Nanoparticle Characterization

From elemental analysis, the surface coverage of the fluoruous moiety was $(3.2 \pm 0.1) \mu\text{mol}/\text{m}^2$ ($n=3$), which is approximately 40% of the surface silanol concentration $[(8 \pm 1) \mu\text{mol}/\text{m}^2]$.¹³⁹ This surface coverage is comparable to that of (1H,1H,2H,2H-perfluorodecyl)dimethylchlorosilane-modified silica ($3.45 \mu\text{mol}/\text{m}^2$).¹⁴⁰ The contact angle of a water droplet on a surface with these particles exceeds 150° (**Figure 3-1**). We also modified silica nanoparticles with triethoxy(octyl)silane under the same conditions except for the solvent (ONPs). As revealed by elemental analysis, we obtained a surface coverage of $4.76 \mu\text{mol}/\text{m}^2$.

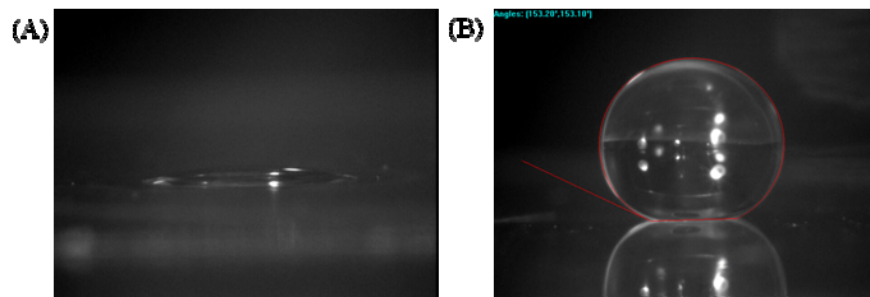


Figure 3-1. (A) water contact angle of unmodified silica nanoparticles on a microscope slide; (B) water contact angle of fluoroalkylsilane-modified silica nanoparticles on a microscope slide.

TEM was used to further characterize unmodified and modified silica nanoparticles (**Figure 3-2**). The mean diameters (d_i , $i = A, B$, or C) of unmodified (number counted: $n_A = 1056$), fluoroalkylsilane modified ($n_B = 845$), and octylsilane modified ($n_C = 1183$) silica nanoparticles determined by Simple PCI 6 are (114.69 ± 0.21) nm, (115.90 ± 0.24) nm, and (116.10 ± 0.20) nm, respectively. Statistical analysis shows a significant difference between d_A and d_B/d_C ($p_{A,B} = 1.13 \times 10^{-4}$, $p_{A,C} = 8.22 \times 10^{-7}$), while the difference between d_B and d_C is not significant ($p_{B,C} = 0.525$). Interestingly, the diameter difference between unmodified and fluoroalkylsilane modified silica nanoparticles (~ 12 Å) is close to twice the value of the thickness of the inclined fluorosilane monolayer determined from chemical vapor surface modification on a hydroxylated oxide surface – 6.0 Å.¹⁴¹ This indicates monolayer coverage on the modified silica nanoparticle surface. Overall, the fluorosilane modification of silica nanoparticles is satisfactory.

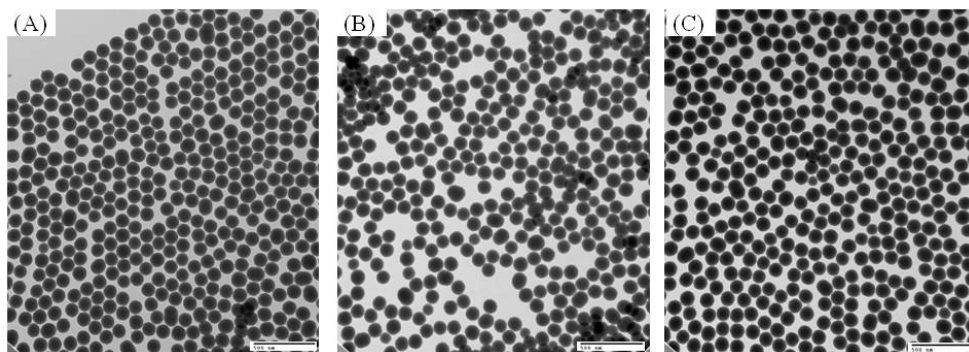


Figure 3-2. TEM micrographs of the silica nanoparticles: (A) unmodified; (B) fluoroalkylsilane modified; (C) octylsilane modified (scale bar = 500 nm). Obvious overlapping particles were manually identified for exclusion from the analysis by the image analysis software (Simple PCI 6).

The thermal properties of unmodified, O-, and FNP were determined by DSC (**Figure 3-3**). Dehydration gives a broad endothermic peak with an onset temperature at 30 °C. ONPs show

a single exothermic peak with the onset temperature at 231 °C from the decomposition the modification.¹⁴² FNPs display more complicated thermal behavior. The dehydration process is attenuated in comparison to the other two materials. Thus, little weakly bound water exists on these particles. A sharp endothermic phase transition at 273–278 °C can be ascribed to the chain melting transition of the fluorocarbon moiety.¹⁴³ The decomposition of the hydrocarbon linker starts at 318 °C. Immediately following the exothermic transition from linker degradation, the evaporation of the fluorocarbon residue (thermally stable at temperatures less than 500 °C) gives rise to an endothermic transition.¹⁴⁴ FNPs feature a higher degradation temperature than the glass transition temperature (T_g) of Teflon AF 2400 (240 °C). Therefore, composite films of Teflon AF 2400 and FNPs will display high thermal stability below Teflon AF 2400's T_g .

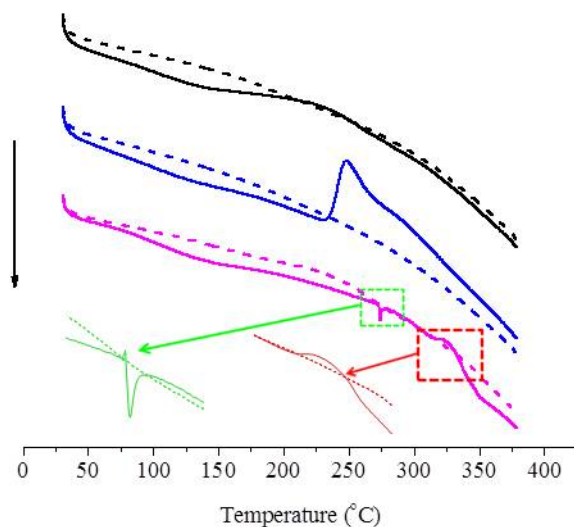


Figure 3-3. DSC curves of unmodified (black lines), octylsilane modified (blue lines) and fluoroalkylsilane modified (magenta lines) silica nanoparticles. Solid lines represent the first heating cycle and dashed lines are the second heating cycle.

3.3.2 Morphology of Teflon AF Composite Films

Notably, a stabilizer-free FNP suspension in HFE-7100 has been stable for 2 years at the time of writing. The slow evaporation of solvent from an FNP suspension containing Teflon AF 2400 leads to homogeneous thin Teflon films incorporating FNPs (see **Figure A-2**). **Figure 3-4** shows cross sections (fracture in liquid nitrogen) of Teflon AF films containing FNP alone, as well as Teflon AF containing both FNP and FC-70. In the Teflon AF 2400 film containing 15 wt% (12 volume % (v%)) FNPs, the majority of the nanoparticles exist as individual entities surrounded by the Teflon matrix. Individual nanoparticles are attached to a web-like Teflon AF matrix. Higher (50 wt% (40 v%) and 70 wt% (53 v%)) concentrations of FNPs in Teflon AF 2400 films display Teflon AF threads that terminate at feet on individual FNPs. It is worth pointing out that a Teflon AF 2400 film containing 15 wt% ONPs shows that phase separation occurred during the film formation(see **Figure A-3**). The composite films containing Teflon AF 2400, FNPs, and FC-70, display a very different morphology in comparison to films containing only Teflon AF 2400 and FNPs. All the three-component films are composed of nanoparticles with non-ideal spherical shape that show a broader size range than the FNPs themselves. Therefore, we believe that the three-component films are packed core-shell type nanoparticles with FNPs as the core and a shell of FC-70-plasticized Teflon AF 2400. The intertwining of the polymer chains of adjacent shells results in good film integrity although the films contain only 10–25 wt% Teflon AF 2400.

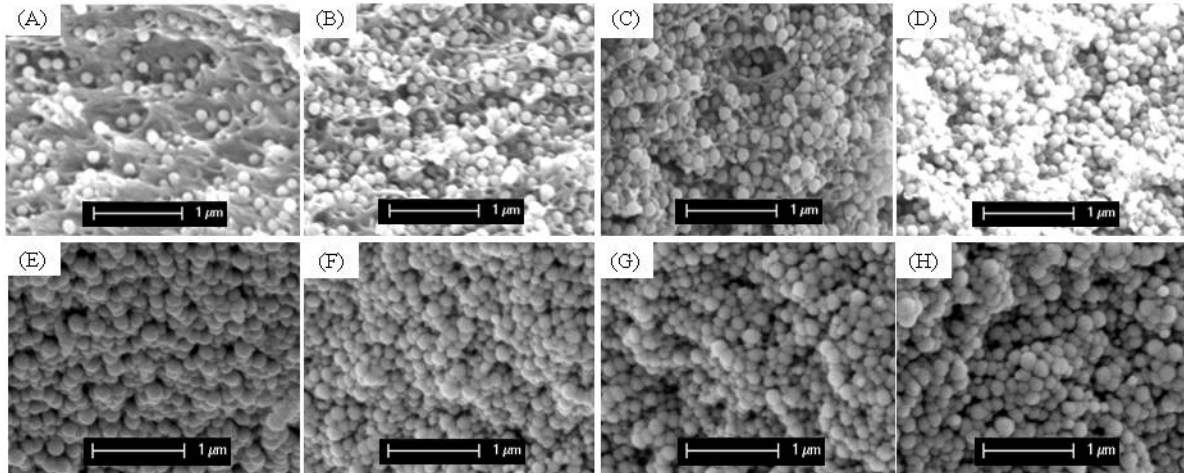


Figure 3-4. Cross-sectional SEM images of Teflon AF 2400 films containing various weight percentages of FNP and FC-70: (A) 15 wt% (12 v%) FNPs; (B) 30 wt% (25 v%) FNPs; (C) 50 wt% (40 v%) FNPs; (D) 70 wt% (53 v%) FNPs; (E) 70 wt% FNPs and 5 wt% FC-70; (F) 70 wt% FNPs and 10 wt% FC-70; (G) 70 wt% FNPs and 15 wt% FC-70; (H) 70 wt% FNPs and 20 wt% FC-70.

Teflon AF 2400 with different states (glassy and plasticized) leads to structurally different polymer nanocomposites. In what follows, we present a systematic study showing how the changes in film composition and morphology just described influence physical, mechanical and chemical properties of these films, and render distinctive transport behaviors. As a guide, we present a broad overview of the results in **Table 3-1**.

Table 3-1. A summary of physical, mechanical, chemical, and transport properties of composite Teflon AF films at 20.0 ± 1.0 °C

Properties	Composite Teflon AF 2400 Films								
	Pure Teflon AF	Teflon AF/FNP				FC-70 plasticized Teflon AF/FNP			
FNP (wt%)	0	15	30	50	70	70	70	70	70
FC-70 (wt%)	0	0	0	0	0	5	10	15	20
Density (g/cm^3) ^a	1.772±0.005 ^b	1.909±0.013	1.904±0.010	1.842±0.010	1.761±0.007	1.875±0.009	1.863±0.010	1.818±0.010	1.878±0.014
aFFV _p ^c	0.303±0.002	0.272±0.006	0.305±0.005	0.400±0.007	0.558±0.007	0.494±0.009	0.502±0.010	0.530±0.010	0.495±0.014
Distribution of aFFV _p (shell/void)	—	—	—	—	—	0.131/0.363	0.140/0.362	0.138/0.392	0.153/0.342
Transition temperature (oC) d(Tan δ)/dT=0	261	271	272	276	271	267, 121, -7	265, 120, -12	260, 103, -19	259, 98, -24
ΔC_p at T_g ($\text{J}\cdot\text{g}^{-1}\cdot\text{K}^{-1}$)	0.063	0.050	0.034	0.013	0.00	—	—	—	—
Storage modulus (MPa)	1072	1625	1603	1675	1317	1240	934	738	454
Interparticle distance (nm) ³⁶	—	84.7	43.4	20.0	7.4	—	—	—	—
Sorption of CHCl ₃ (g/100 g soft matrix in the film)	8.00	7.24	8.27	10.08	11.83	6.77	5.70	3.50	1.53
Log (Permeability/cm ² /s) (NPTH)	-9.076	-9.118±0.098	-9.014±0.25	-8.561±0.061	-8.187±0.280	—	—	—	—
Partition coefficient (NPTH)	0.054	0.038±0.001	0.055±0.006	0.097±0.003	0.156±0.027	—	—	—	—
Log (Permeability/cm ² /s) (TOL)	-7.763±0.008	-7.781±0.009	-7.742±0.031	-7.368±0.006	-6.977±0.003	-8.348±0.017	-8.251±0.002	-8.223±0.029	-8.023±0.054
Log (Permeability/cm ² /s) (OFT)	-7.011±0.003	-7.025±0.005	-6.982±0.001	-6.682±0.002	-6.425±0.001	-7.358±0.004	-7.225±0.007	-7.020±0.032	-6.785±0.014
Transport selectivity (OFT/TOL)	5.64±0.12	5.71±0.14	5.75±0.41	4.86±0.08	3.57±0.03	9.77±0.39	10.60±0.17	15.95±1.60	17.30±2.23

^a The number of density measurements for each film are: 8 (0 wt% FNP), 9 (15 wt% FNP), 10 (30 wt% FNP), 9 (50 wt% FNP), 10 (70 wt% FNP), 10 (70 wt% FNP, 5 wt% FC-70), 10 (70 wt% FNP, 10 wt% FC-70), 10 (70wt% FNP, 15 wt% FC-70), 10 (70 wt% FNP, 20 wt% FC-70). Interparticle distance in Teflon AF/FNP films is calculated according to a published method.¹⁴⁵ The data shown for transport studies are the mean values of two duplicate experiments.

^b All errors in the table are standard deviations of the mean. ^c Fractional free volume for the non-nanoparticle matrix alone.

3.3.3 Density and Apparent Free Volume of Teflon AF/FNP Composite Films

Film density increases first and then decreases as the weight fraction of FNPs increases in Teflon AF films containing FNP alone. The 70 wt% FNP-containing films have even lower density than the pure Teflon AF 2400 films. It is remarkable that the replacement of Teflon AF 2400 by the higher density modified silica nanoparticles leads to a decrease in the film density.

Knowledge of the film densities leads directly to the films' apparent fractional free volumes (aFFV).¹⁰⁴ Because of the observed morphology of the Teflon/FNP materials which include the free volume within the polymer matrix itself and void volumes at the Teflon/FNP interface, we use the term “apparent fractional free volume” (aFFV) to represent more accurately the unoccupied volumes in the films. The free volume elements at the interface of the nanoparticles and Teflon AF 2400 and within the bulk of the polymer are keys to solute transport because of the non-permeable nature of nanoparticles themselves. Thus, we focus on the aFFV of the matrix not occupied by FNPs (aFFV_p). Interestingly, the polymeric chains become more compact than pure Teflon AF 2400 in films containing 15 wt% FNPs. This observation indicates the presence of tight interface between FNPs and Teflon AF 2400 at low dopant amount. With more than 15 wt% FNPs in Teflon AF films, there is an increase in aFFV_p which can reach over 50%.

To understand further the aFFV in Teflon AF composite films containing high nanoparticle content, N₂ adsorption (BET) was performed on 70 wt% FNP-doped Teflon AF films and pure Teflon AF films, respectively. In addition to the known microporosity of Teflon AF (1–20 Å),³⁹ BET reveals mesoporous free volume elements in the composite film (see **Figure A-4**). The pore width by BJH analysis on both adsorption and desorption branches for the

composite film is no larger than 5 nm, indicating that the small mesopores are not due to nanoparticle aggregates, which would in close-packed form accommodate spheres with ~13 nm radius. The non-effective packing of Teflon AF molecules and FNPs could be the main reason of the large fraction and small size of apparent free volume elements. For deeper understanding, we have looked at T_g and mechanical properties of the Teflon AF/FNP system.

3.3.4 T_g , ΔC_p at T_g , and modulus of Teflon AF/FNP Composite Films and R_g of Teflon AF

T_g (based on DMA) increases for films containing less than 50 wt% nanoparticles, and then decreases (**Table 3-1**). The maximum T_g (276 °C) is seen in films with 50 wt% FNPs. The broadening and the decrease in peak height of the $\tan(\delta)$ -T plot indicate an increasing heterogeneity of Teflon AF in the composite films as FNP content increases (**Figure 3-5**).¹⁴⁶ The modulus of the film is maximal at intermediate FNP content, but in all cases tested is greater than that for pure Teflon AF films. The trend of T_g values obtained from DSC measurements agrees well with that obtained from DMA measurements (see **Figure A-5**). Notably, the sharp chain melting transition of the fluorocarbon moiety on the FNPs (recall **Figure 3-3**) is absent in the composite materials, indicating the non-crystalline nature of the fluoroalkane of the FNPs when in contact with Teflon AF. **Figure 3-6** shows the change of heat capacity (ΔC_p) at T_g . Since FNPs do not contribute to ΔC_p , it is reasonable to expect that ΔC_p will decrease proportionally with the increase of FNP loading (to 0 for 100 wt% FNP), if the FNP/Teflon AF interface does not contribute. However, ΔC_p displays a significant negative deviation from the linear trend. The 70 wt% FNP films show no thermal transition around T_g by DSC. Teflon AF 2400's R_g (in FC-77) is 22.69 ± 0.04 nm, which is close to the value of poly(tetrafluoroethylene) (PTFE in *n*-

$C_{24}F_{50}$ at $325\text{ }^{\circ}\text{C}$, $R_g = 20 \pm 5\text{ nm}$) with similar weight-average molecular weight (PTFE: 260 kDa; Teflon AF 2400: 300 kDa).¹⁴⁷

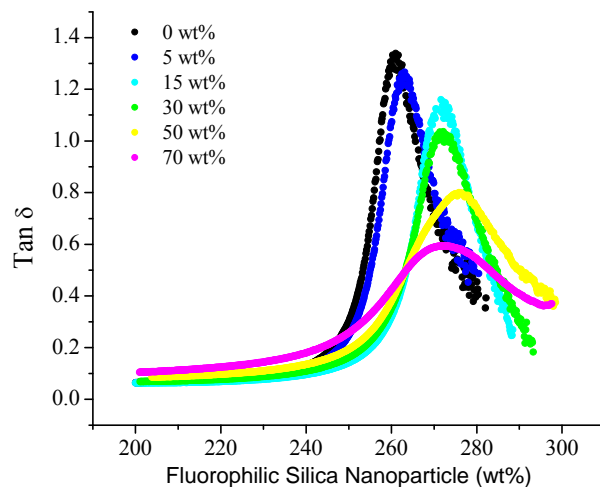


Figure 3-5. Tan(δ) curves of fluorophilic silica nanoparticle doped Teflon AF 2400 films.

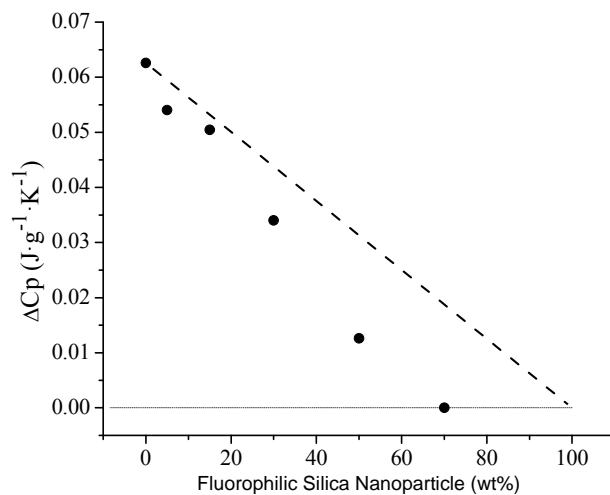


Figure 3-6. Change of heat capacity at the glass transition of FNP doped Teflon AF 2400 films.

All of the foregoing observations are consistent with the following picture. Teflon AF associates noncovalently with the FNPs (modulus increase, loss of fluoroalkane monolayer chain melting transition, SEM). However, the size of the interstitial space¹⁴⁵ for high wt% FNPs is smaller than R_g of the polymer (**Table 3-1**). This leads to chain confinement and entropic restrictions on the polymer molecules. The increase in T_g and loss of ΔC_p is a result of these factors. As He et al. have described,¹⁴⁸ more than one population of polymer molecules can exist in a composite. The configurational restriction of the confined Teflon AF molecules leads to relaxation times that are longer than the experimental time scale¹⁴⁹ with the result that this fraction does not contribute to ΔC_p at T_g .¹⁴⁸ An extreme example is the 70 wt% FNP doped Teflon AF film, in which the large fraction of the slow-moving FNPs and small interparticle dimension effectively restricts most of the Teflon AF molecules, resulting in no observable change in heat capacity at T_g . The material is somewhat like a solution envisaged by Mackay and coworkers: Teflon AF 2400 as the solute dissolves in a solid solvent (FNPs).¹²⁸ The geometric confinement of stretched polymeric chains (entropically unfavorable) could be the main reason for the exceptionally high aFFV in the composite Teflon films containing high weight fractions of FNPs.

Corroboration comes from looking at the data at low wt% FNPs. We calculate that a hypothetical material with a monolayer of polymer in its solution conformation (i.e., the monolayer thickness is R_g) on each particle occurs at a weight percentage of 21.9%. This value is close to the composition at which we observed the tightest interface between FNPs and Teflon AF 2400 (15 wt% based on the density measurements). From 0 to ~20 wt%, the polymer is titrated by the FNP surface. At higher composition (50–70 wt%), there is not enough Teflon AF polymer to effectively wet the surface of nanoparticles without taking on low probability

conformations. We speculate that the vines seen in the SEMs correspond to an entropically favored state.

3.3.5 Sorption of Chloroform in Teflon AF/FNP Composite Films

We have found earlier that chloroform sorption is a good measure of free volume that is accessible to solutes. CHCl_3 vibrations are also modestly solvatochromic which helps us to understand the free volume.^{56,137} In prior work,¹³⁷ we reduced the FFV (as determined by density measurements) of pure Teflon AF films (no NPs) by adding a compatible plasticizer, FC-70, the molecular volume of which is consonant with the population of large free volume elements. This reduction in FFV was clearly diagnosed by chloroform sorption.

It has been reported that gas sorption in a filler-containing polymer composite occurs in the polymer matrix when the filler is solid and is wet by the polymer matrix.^{150,151} For clarity, we will refer to the non-particle portion of composites as the “matrix”. The aFFV of this polymeric portion of the film will be designated as the aFFV_p. Thus, we hypothesized that chloroform sorption in the matrix will be the same as in a pure Teflon AF film regardless of the FNP weight percent. As shown in **Table 3-1**, experimental results disagree with expectations. The Teflon AF 2400 film containing 15 wt% FNPs displays a negative deviation while films with 50 and 70 wt% FNPs show positive deviations. Both results can be explained based on the aFFV_p of the film (**Table 3-1**). The 15 wt% FNP films have a lower aFFV_p as discerned from the density measurements. Similarly, the positive deviation of chloroform sorption from the hypothesized value observed in films containing 50 wt% and 70 wt% FNPs is consistent with the increased aFFV_p of the Teflon AF.

3.3.6 Solute Permeability (P) and Selectivity through Teflon AF/FNP Composite Films

The permeability coefficients of toluene (TOL), octafluorotoluene (OFT), and naphthalene (NPTH) through FNP doped Teflon AF 2400 films are listed in **Table 3-1**. The three probe solutes show similar trends versus the wt% of FNPs (**Figure 3-7**). When wt% of FNPs is greater than 15 wt%, a significant increase of P is observed along with the increased nanoparticle content. For example, the permeability of octafluorotoluene through a 70 wt% FNP doped Teflon AF 2400 film is 3.9 times that through a pure Teflon AF film, while the permeability of its hydrocarbon counterpart (toluene) through a 70 wt% FNP doped film is 6.1 times that through a pure Teflon AF film. The significant increase of $aFFV_P$ leads to the increase in transport rates.

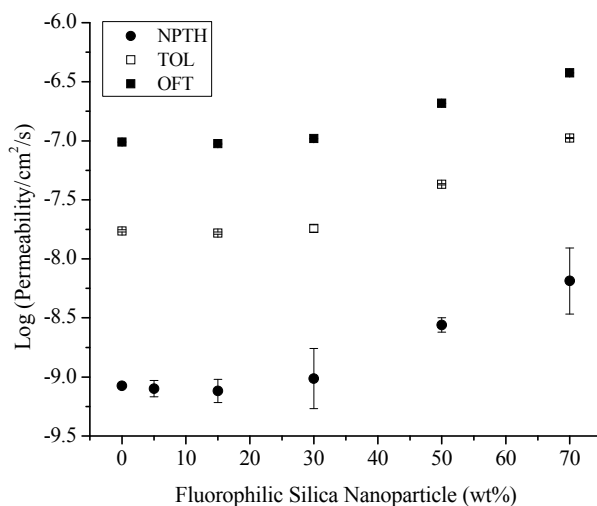


Figure 3-7. The logarithms of the permeability coefficients of toluene, octafluorotoluene, and naphthalene through composite Teflon AF 2400 films at 20.0 ± 1.0 °C.

To understand how FNPs affect permeability, we investigated the diffusion and partition coefficients of NPTH. **Table 3-1** shows the partition coefficients of NPTH from chloroform to

the matrix of FNP doped Teflon AF films. The increasing trend of partition coefficients parallels the changes in both aFFV_P and chloroform sorption. In fact, the partition coefficient of NPTH, the sorption of chloroform and the aFFV are remarkably highly correlated ($r^2 > 0.98$ for each of the three pairs).

Figure 3-8 plots the diffusion coefficients corrected for particle-induced tortuosity ($\tau = 1 + \phi_{\text{FNP}}/2$; ϕ_{FNP} is the volume fraction of particles)¹⁵² against the reciprocal of the aFFV_P of the film (**Table 3-1**). The theoretical equation ($D = e^{(A-B/FFV)}$),¹⁵³ which correlates solute diffusion in polymer with the fractional free volume gives a fine fit to the experimental data points with $r^2 = 0.873$. The B value is related to the size of the molecule and the size distribution of the FFV.¹⁵³ In the Teflon AF/FNP system, B is 0.96, which is close to the that for solutes with similar size in different polymers ($B_{\text{benzene in polymethyl acrylate, 25 }^\circ\text{C}} = 0.64$; $B_{n\text{-hexane in semicrystalline polyethanene, 25 }^\circ\text{C}} = 0.8$; $B_{\text{cyclohexane in semicrystalline polyethanene, 25 }^\circ\text{C}} = 0.85$; $B_{n\text{-octane in semicrystalline polyethanene, 25 }^\circ\text{C}} = 1.0$). The general trend of diffusion coefficient versus aFFV_P supports the disturbed chain-packing hypothesis.⁴⁹ However, there is one anomaly. The film containing 15 wt% FNP with a lower aFFV_P than the pure film, yields an increased diffusion coefficient for NPTH over that of the pure Teflon AF film. This has been observed in the Teflon AF/organosilane-modified fumed silica system.⁴⁹ It is likely that diffusion in composite Teflon AF materials depends not only on aFFV, but depends also on the size distribution of the free volume elements and their connectivity. Thus, in these materials, diffusion is not only sensitive to the free volume elements in the bulk Teflon AF but also to those that are created at the Teflon/FNP interface (the amount of which is related to interface area). The importance of the latter has been pointed out by Shen and coworkers.¹⁵⁴

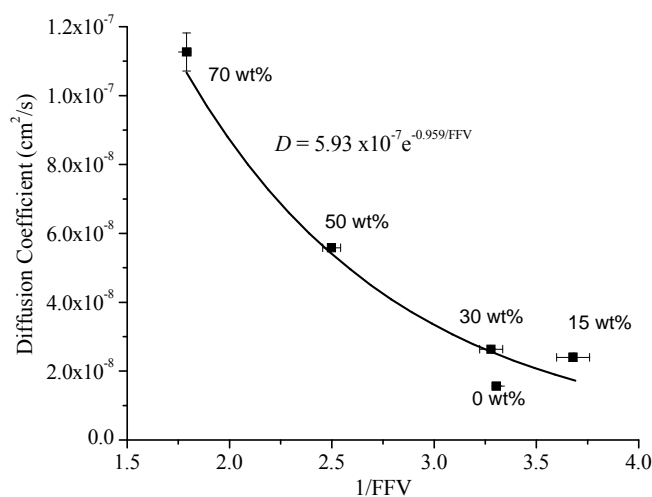


Figure 3-8. Diffusion coefficient of NPTH versus $1/aFFV_p$ of the composite Teflon AF films at 20.0 ± 1.0 °C.

As shown in **Table 3-1**, transport selectivity drops as FNP content and permeability increase. The selectivity of the OFT/TOL pair through a 70 wt% FNP doped Teflon AF 2400 films is 64% of the value of the pure Teflon AF film. This type of Teflon AF/FNP composite material could benefit applications in which the permeability, but not selectivity, of the coating is one of the key performance properties, for example, binary gas sensors and flow reactor, as the films are thermally stable and relatively unreactive.²⁸

Can the transport selectivity of the nanocomposite system be improved? Inspired by our previous study on Teflon AF 2400/FC-70 composite films, we hypothesize that high transport selectivity of the nanocomposite Teflon AF films can be approached by using FC-70 plasticized Teflon AF as the soft material in the nanocomposite films. These composite films, as revealed in **Figure 3-4**, are composed of nano-scale particles with FNPs as the core and a shell of FC-70-plasticized Teflon AF 2400. They display very different behavior compared to the composite films from glassy Teflon AF.

3.3.7 Mechanical Properties of Teflon AF/FNP/FC-70 Composite Films

The replacement of Teflon AF by FC-70 while keeping the FNP amount unchanged (70 wt%) leads to a decreasing trend of storage modulus due to the plasticization of Teflon AF 2400 by FC-70.¹³⁷ In the presence of FNPs, all three-component films display satisfactory mechanical strength even though the ratio of FC-70 to Teflon reaches 2:1, which is not a realistic composition for dimensionally stable Teflon AF/FC-70 films without FNP. As shown in **Table 3-1**, for all three-component films, the emergence of two new transitions ($\tan \delta$) at low temperatures confirms the plasticization effect of FC-70. This is consistent with our previously investigated FC-70-doped Teflon AF 2400 films¹³⁷ as well the plasticized Teflon AF system observed by Lugert and coworkers.⁷¹ As described above, FNPs restrict the number of likely configurations of the Teflon AF molecules leading to slower relaxation of Teflon AF chains and a shift of T_g to higher temperatures. In contrast, FC-70 plasticizes Teflon AF, decreasing conformation relaxation times, and permits the wetting of FNPs by Teflon AF/FC-70. Therefore, the presence of FNPs in three-component films does not significantly impact the T_g of the film: the glass transition temperatures of Teflon AF/FC-70 films (no FNPs) and three-component Teflon/FNP/FC-70 films are close at similar FC-70 volume percentages (see **Figure A-6**).

3.3.8 $aFFV_p$ of Teflon AF/FNP/FC-70 Composite Films

Table 3-1 shows that all three-component films display higher film density than the 70 wt% FNP-containing Teflon film, indicating a decrease of $aFFV_p$ by replacing Teflon AF with FC-70. This is not surprising given what we know about the plasticization of Teflon AF 2400 by FC-70 (> 12 wt%). Teflon AF 2400 plasticized by FC-70 is less rigid than Teflon AF 2400 itself and

allows better wetting of the FNP surface. Consequently, the free volume created due to the ineffective contact between FNPs and rigid Teflon AF chains in the two-component films shrinks. We believe that the $aFFV_P$ has two main contributions. One is the molecular-scale FFV of the FC-70-plasticized Teflon AF 2400 shell and the other is from small voids between core-shell particles. With regard to the former, we estimated the density (see **Table A-1**) and $aFFV$ of the Teflon/FC-70 shells from our previous work. If all of the Teflon AF/FC-70 forms shells on FNPs the shell thickness is about 8 nm. The contribution of this shell's FFV to the $aFFV_P$ is less than 1/3 in all three-component films (**Table 3-1**). Thus, the contribution of voids between particles is more than 2/3. Referring now to the entire film including FNPs, the maximum void fraction corresponding to a randomly packed bed is 0.36. The actual $aFFV$ from voids is 0.15–0.18. This is consistent with a system of soft particles which have larger packing densities than fcc or hcp packings.^{155,156}

3.3.9 $aFFV_P$ Characteristics Differ in Two- and Three-component Materials

The $aFFV_P$ values in the 70 wt% FNP-containing Teflon AF 2400 films with or without FC-70 are remarkably high, around 50%. These remarkably high fractional free volumes are rare among polymeric materials. We are not aware of any published values this high. There is data on composites of organosilane-modified fumed silica (OS) with Teflon AF 2400 and PTMSP that allows us to infer approximate $aFFVs$. These two composites exhibit similarly high $aFFV$ (40 wt% OS/Teflon AF 2400: 43% FFV; 50 wt% OS/PTMSP: 62 % FFV).^{49,152} This also points to the interesting possibility of creating light materials by mixing dense components.

In the fluororous polymer nanocomposites described here, the origins of the high $aFFV_P$ differ microscopically in the unplasticized and plasticized materials. The ineffective polymeric

chain packing caused by FNPs is the primary reason for the presence of extra small mesopores (recall BET) and high aFFV in the two-component films. In the three-component films, large aFFV_P comes from the free volume within the Teflon AF/FC-70 shell as well as the relatively large void volumes between packed nano scale particles. (Unfortunately, the boil-off of FC-70 prevents BET analysis).

The differences are not simply geometrical – there is a profound chemical consequence arising from plasticization of the polymer. FC-70 is known to occupy existing free volume of Teflon AF, which decreases chloroform sorption,¹³⁷ but the free volume in the Teflon AF itself is only about 1/3 of the total. About 2/3 of the aFFV in the FC-70-containing films arises from interstitial domains, yet the chloroform sorption capacity is remarkably low compared to the pure film (**Table 3-1**). Examination of the sorbed CHCl₃ vibrational spectra provides important information. The wavenumber of the ν_5 band in pure Teflon AF phase is 768 cm⁻¹. This peak occurs at 772 cm⁻¹ in the gas phase. In the two-component film with 70 wt% FNPs the frequency is 766 cm⁻¹, i.e., more liquid-like. The IR peak of chloroform in a three-component film containing 10 wt% Teflon AF/70 wt% FNP/20 wt% FC-70 is 771 cm⁻¹, indicating that the adsorbed chloroform is more gas-like. Our unpublished work on mesoporous Teflon AF materials is consistent with this observation. Remarkably, chloroform does not wet mesoporous Teflon AF 2400 films even though the polymer matrix itself is known to absorb chloroform.

We decided to test directly the just-stated hypothesis that the interstitial voids are virtually solvent free. Thus, we tested the transport of Reichardt's dye (551.68 Da), a chloroform-soluble molecule through a three-component film containing 20 wt% FC-70. If a continuous, solvent accessible, mesoporous volume existed in the three-component materials, transport of the highly optically absorbing dye would be obvious. However, no measurable

absorbance of Reichardt's dye (permeability $\leq 6.8 \times 10^{-12}$ cm²/s according to the limit of detection) in the receiving phase was observed after 5000 seconds (typical time for transport experiments). This indicates that the material does not have a mesoporous structure which allows solutes to pass through without partitioning into the polymeric matrix.

The picture that emerges for the three-component films is quite simple. The shell, composed of Teflon AF and FC-70, forms a continuous fluororous medium about 8 nm thick. The interstitial space, walled by fluororous materials, is not wet by the solvent chloroform. If this is true, then we should expect molecular transport to occur through this film. This should result in a high selectivity for a fluorine-substituted solute over its hydrogen-containing counterpart, and the selectivity should be dominated by partitioning.

3.3.10 Transport Properties of Teflon AF/FNP/FC-70 Composite Films

The permeabilities of probe solutes (TOL, OFT) are shown in **Table 3-1**. In the three-component films replacement of 5% of the remaining Teflon AF with FC-70 causes permeabilities to drop (**Figure 3-9**). Further replacement of Teflon by FC-70 creates higher permeabilities. We observed a 1.7-fold increase of octafluorotoluene permeability through a three component film containing 70 wt% FNP and 20 wt% FC-70 compared to a pure film. The three-component films all have markedly higher fluororous selectivities compared to either the pure Teflon AF films or the two-component films (**Figure 3-10**). The OFT/TOL transport selectivity of the three-component film with 20 wt% FC-70 is 17.3, more than three times the value in a pure Teflon AF film.

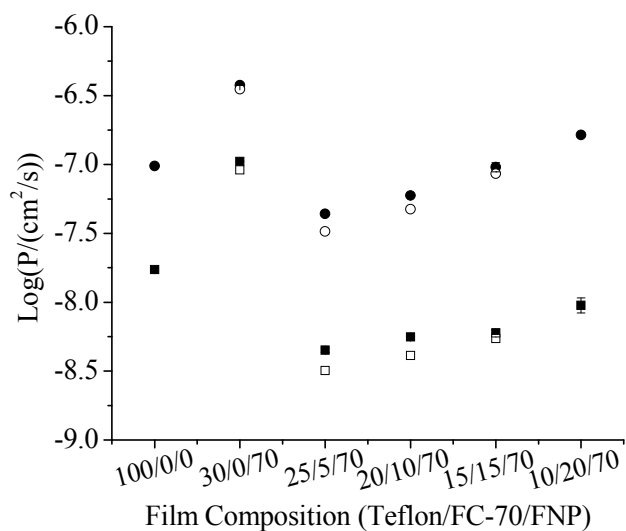


Figure 3-9. The logarithms of the permeability coefficients of toluene (TOL, ●: a thin single layer film; ○ a thick film from stacked thin films) and octafluorotoluene (OFT, ■: a thin single layer film; □ a thick film from stacked thin films) through composite Teflon AF 2400 films at 20.0 ± 1.0 °C.

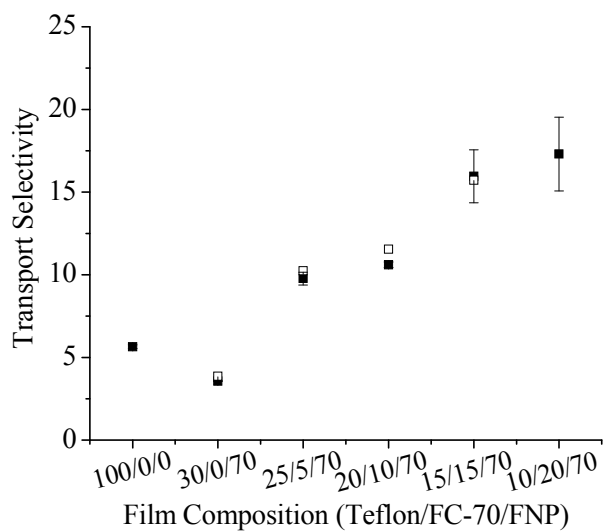


Figure 3-10. The transport selectivity of OFT over TOL through composite Teflon AF 2400 films at 20.0 ± 1.0 °C. The solid squares represent the data from single layer film transport, and the hollow squares represent the data from stacked films.

In order to understand the origin of the selectivity of the three-component films, we determined diffusion and partition coefficients. We note (**Figure 3-11**) that the ratio of the diffusion coefficients in the three-component films and in pure Teflon AF films is similar. Thus the transport selectivity does not derive from diffusion. Interestingly, plasticizing the film leads to slower diffusion. This runs counter to the normal result of plasticization - increasing diffusion rate, e.g. improving conductivity in electrolyte films for fuel cells.^{134,136} This observation corroborates the idea that the void volumes in three-component films do not play a significant role in transport, and further points out the importance of free volume morphology in composite materials for molecular transport.

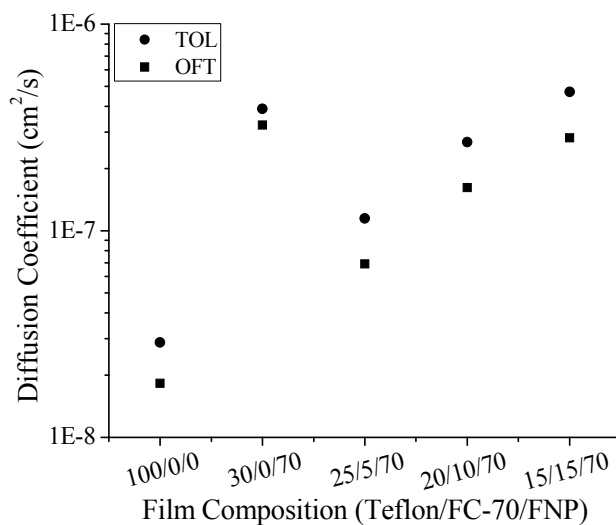


Figure 3-11. Diffusion coefficients of solutes in composite Teflon AF films at 20.0 ± 1.0 °C.

In contrast (**Figure 3-12**), the CHCl_3 /matrix partition coefficients of TOL and OFT both decrease with increasing fraction of FC-70, but the OFT partition coefficient decreases less. The partition coefficients approach their values from chloroform to pure FC-70. These three-component films act like a supported liquid membrane in the partitioning process and display

significantly increase transport selectivity compared to the pure Teflon AF films (**Table 3-1**). The OFT/TOL selectivity of a 10 wt% Teflon AF 2400/ 70 wt% FNP/20 wt% FC-70 film reached 17.3, which is 3.1 times the value through a pure Teflon AF 2400 film.

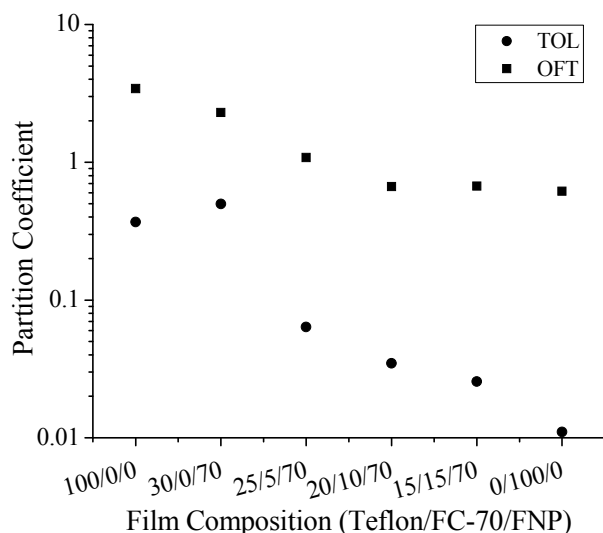


Figure 3-12. Partition coefficients of solutes in composite Teflon AF films at 20.0 ± 1.0 °C. The partition coefficient data of pure Teflon AF films and pure FC-70 are from our previous work.¹³⁷

3.4 CONCLUSION

In aiming to tailor materials properties towards high permeability with fluororous selectivity, we initiated a study of creating Teflon AF nanocomposite films with controlled structure and morphology. Glassy Teflon AF and plasticized Teflon AF nanocomposites with FNPs exhibit different morphological features. In the former, especially at high FNP wt%, the polymer forms vines with attachments to the particles. In the latter, plasticized polymer forms a shell around the FNPs. The $aFFV_p$ in both types of composite films is high $\geq 50\%$. However, the origins of the apparent free volume elements are different. The non-effective polymeric chain packing confined

by FNPs is the primary reason for the high apparent free volume in Teflon AF/FNP films, while the free volume elements in Teflon AF/FNP/FC-70 films come from the free volume in FC-70 plasticized Teflon AF shell (~1/3) and the interstitial volume (~2/3).

The wetting of low mobility FNPs by plasticized Teflon AF as well as the intertwining of the adjacent shells makes it possible to create mechanically satisfactory films with only 10 wt% of Teflon AF. These three-component films show decreased sorption of chloroform and increased transport selectivity as FC-70 content increases. Interestingly, it seems that the void volume in the matrix of three-component films, the major component of the apparent free volume, does not contribute to the chloroform sorption or solute transport. The effective medium for transport in three-component films is the connected Teflon AF 2400/FC-70 shell on the FNP skeleton. Highly selective transport of OFT/TOL is achieved without sacrificing permeation rates by using Teflon AF/FC-70/FNP composite films.

We are not aware of another case in which structurally different polymer nanocomposites result from a polymer with different states (glassy and plasticized). Our work suggests the possibility of rationally creating/optimizing polymer nanocomposites with tailored properties for applications. As an ideal medium (poor solvent) for non-covalent interaction based separations and sensors, an extension of the presented Teflon AF composite films is currently in development.

3.5 ACKNOWLEDGEMENT

We thank the National Science Foundation for support through grant CHE-0957038. We thank (all at the University of Pittsburgh) Mr. Albert Stewart (Mechanical Engineering & Materials

Science) for the access and help on the SEM instrumentation, Mr. Thomas Harper (Biological Science) for access to and help on the TEM, Prof. Yadong Wang and Ms. Britta Rauck (Biongeneering) for assistance in determining R_g , and Prof. Götz Vesper and Dr. Lu Whaley (Chemical Engineering) for access to BET measurements.

4.0 PREPARATION AND POTENTIAL APPLICATIONS OF POROUS TEFLON AF

2400

4.1 INTRODUCTION

Porous materials are receiving an increasing interest due to their widespread applications in chemical separation, catalysis, biosensor devices, drug delivery, photonics, energy-relevant processes such as gas storage and fuel cell technology, and so on.¹⁵⁷⁻¹⁶¹ In previous decades, remarkable progress has been made on the preparation and application of porous inorganic motifs including zeolites, carbon, silicon and metal-organic frameworks.¹⁶²⁻¹⁶⁷ Noticeably, porous soft materials have been a fast growing replacement for inorganic materials due to the improved chemical stability, shapeability and functionality.^{158,161} To date, the design and preparation of porous polymer materials are mainly focused on organic polymers. Stiff organic polymers are typically employed in order to overcome the thermodynamically driven pore-collapse in porous matrices.^{158,168,169} Emerging as a class of dimensionally stable fluorocarbons, fluoropolymers are featured by excellent thermal, chemical and mechanical stability.^{170,171} Fluoropolymers with inner porosity are particularly useful in separations, biomedical applications, and engineering technologies. Nafion, one of the most famous fluoropolymers based on a tetrafluoroethylene (TFE) backbone, has been serving as proton-conductive membranes in fuel cells due to its interconnected hydrophilic microchannels.^{172,173} Further

improvement of porosity in Nafion was achieved by in-situ creation of CO₂ (sulfonic acid groups of the Nafion catalyze the hydrolysis of propylene carbonate in water at 100 °C to yield CO₂) expanding inside the polymer matrix.¹⁷⁴ Such Nafion membranes with enhanced porosity have been successfully applied in two-phase emulsion separations with satisfactory fluxes.¹⁷⁴ Porous fluoropolymer membranes prepared via UV photo-polymerization of perfluoropolyether-dimethacrylate monomers show excellent permeability to glucose, insulin and albumin.¹⁷⁵ Combined with the well known properties of perfluoropolyethers— excellent stability, high oxygen permeability, and long-term biocompatibility, this type of porous fluoropolymer is used in health care applications (for example, contact lenses).¹⁷⁵⁻¹⁷⁷ In addition, the specific electrical property of porous poly-TFE allows its usage as the active layer in electrostatic transducers.¹⁷⁸ Therefore, there is a need for general approaches for creating porous fluoropolymers with different functionalities.

In a broad sense, the strategy to prepare porous polymers usually employs the pore-forming component—removable gas-generating, liquid, supercritical or solid porogens.¹⁷⁹⁻¹⁸¹ Generally, a solid porogen which acts as endo- or exo-template offers not only better control of the porous structure and porosity but also improved reliability.^{158,181} The most frequently used templates are silica nanoparticles, polymer nano-spheres, zeolites, mesoporous silica and porous alumina membranes.¹⁵⁸ Three-dimensional long-range ordered pore structure in polymers can be easily achieved by utilizing spherical colloidal crystals or periodic mesoporous silica as the template.^{158,182,183} However, it is noteworthy that a compatible surface chemistry is required for the template to be intermingled with the target polymer.¹⁸⁴

Previous attempts at fluorine modification of silica nanoparticles tune the surface wettability from hydrophilic to fluorophilic.¹⁸⁵ Therefore, hybrid materials containing

fluorophilic silica nanoparticles and Teflon AF 2400 can be easily created with satisfactory homogeneity.¹⁸⁵ Herein, our approach to prepare porous Teflon AF 2400 is to employ the fluorinated modified silica nanoparticle as the endo-template. This strategy can be readily extended to the preparation of other porous fluoropolymers. We further performed some preliminary study to demonstrate the versatility of the porous Teflon AF 2400 materials in liquid phase separations, sensor arrays, and template-directed preparation of a porous hydrocarbon polymer. Previous efforts in our lab demonstrated that: (1) Teflon AF 2400 films are able to selectively transport fluorinated solutes compared to their hydrogen-containing counterparts;^{1,56,57} (2) doping FC-70 in Teflon AF 2400 films can improve transport selectivity by diminishing the sorption of the organic solvent-chloroform;^{1,58,59} (3) fluorinated nanosilica doped Teflon AF 2400 films show significantly increased transport rate in liquid phase;^{185,186} (4) fluorinated modified porous alumina membranes filled with fluorinated liquids exhibit both high permeabilities and selectivities.^{90,91} We envisioned that a fluorinated supported liquid membrane based on porous Teflon AF 2400 matrix may exhibit both improved fluxes and selectivities. The relatively homogeneous pores of the porous Teflon AF 2400 provide features to facilitate size based separations. More significantly, the porous structure of Teflon AF 2400 matrix provides large surface area for the immobilization of fluorinated targets, which could lead to highly sensitive detection.^{187,188} As a result, porous Teflon AF 2400 matrix brings an opportunity to replace the fluorinated glass slides, which are in used in fluorinated microarray technology targeting protein-small molecule binding.¹⁸⁹⁻¹⁹³

4.2 EXPERIMENTAL

4.2.1 Materials

Teflon AF 2400 and Krytox alcohol (MW~2000) were from DuPont (Wilmington, DE). Krytox 157 FSH (MW~7500) and Krytox 157 FSL (MW~2500) were from Miller-Stephenson Chemical Company Inc. (Danbury, CT). Linear perfluoropolyether (MW~4500) was purchased from Alfa Aesar (Ward Hill, MA). HFE-7100 and PF-5080 were purchased from 3M (Minneapolis, MN). Silica nanoparticles dispersed in 1-propanol (IPA-ST-ZL) were kindly supplied by Nissan Chemical Industries Ltd. (Huston, TX). 1H,1H,2H,2H-perfluorooctyltriethoxysilane, probe solutes used in transport experiments (toluene and octafluorotoluene), sodium hydroxide, pyridine, tetraethyl orthosilicate (TEOS), (3-aminopropyl) triethoxysilane (APTEOS), fluorescein isothiocyanate, rhodamine B isothiocyanate, and Fmoc isothiocyanate were purchased from Sigma-Aldrich (St. Louis, MO). Ammonium hydroxide (28.0–30.0%) was purchased from J. T. Baker (Phillipsburg, NJ). Ethanol, 1-propanol, and chloroform were obtained from Fisher Scientific and used as received. Water was purified with a Milli-Q Synthesis A10 system (Millipore, Bedford, MA).

4.2.2 Preparation and Characterization of Porous Teflon AF 2400 Films

The surface modification of silica nanoparticles by 1H,1H,2H,2H-perfluorooctyltriethoxysilane was achieved by the sol-gel process. The detailed protocol for the fluorinated surface modification of silica nanoparticle is described in Chapter 3.0. Hybrid films containing fluorophilic silica nanoparticles and Teflon AF 2400 were prepared by the solution casting method. Fluorophilic

silica nanoparticle was weighed and mixed with a 10 mg/mL solution of Teflon AF 2400 in HFE-7100/PF5080 (volume ratio = 2:1) in the calculated proportions. Sonication was employed to form a homogeneous dispersion. The mixture was then transferred into an optical flat-bottomed glass Petri dish with an i.d. of 6.0 cm. The dish was covered with a piece of weighing paper and a glass cover. The solvent was allowed to evaporate at room temperature until a constant weight of the film was reached. Films were peeled off using forceps with the addition of 2 mL of ethanol. To prepare porous Teflon AF 2400 films, a piece of fluorophilic silica nanoparticle-doped Teflon AF 2400 film was fixed on a home-made copper frame in order to be immersed in 5 M NaOH. The solution was stirred at 60~70 °C for 24 hours. The treated film was then washed with water three times. The resulting porous film was allowed to dry at room temperature. Porous Teflon AF 2400 films used in nanoparticle transport experiments were prepared with both surfaces polished by 400 grit sand paper before the erosion of nanoparticles in order to remove the regular Teflon AF 2400 structure on surface.

Water contact angles for porous Teflon AF 2400 films were measured with a VCA 2000 Video Contact Angle System (Billerica, MA). For the investigation of film morphology and the erosion kinetics, fluorophilic silica nanoparticle-containing Teflon AF 2400 films immersed in 5 M NaOH solution (60~70 °C) for various reaction times were washed with water and fractured in liquid nitrogen. Films were sputter-coated with palladium before SEM imaging. Film cross-section and surface images were captured using a Philips XL-30 field emission SEM (Hillsboro, OR). The weight percentage of Si was obtained by SEM/EDX. It is worth mentioning that e-beam burns up the porous Teflon films much easier than the pure Teflon films. Images with acceptable damage can be obtained with accelerating voltages no higher than 5 keV. Nitrogen sorption analysis was performed at (77.06 ± 0.03) K with a Micromeritics ASAP 2010 gas

adsorption analyzer. Before each measurement, the film was outgassed overnight at 60 °C to remove dissolved and adsorbed gases.

4.2.3 Transport of Solutes through Films

Transport experiments were conducted with a home-made, three-phase transport device at 20.0 ±1.0 °C.¹⁰⁷ A fluoros supported liquid membrane was prepared by immersing a porous Teflon AF 2400 film in a fluoros oil until the film became clear. The obtained film then was mounted between two quartz cuvettes (path length 1.0 cm, Starna Cells, Atascadero, CA) with holes in the side walls (0.5 cm in diameter) to define the effective transport area. Two pieces of viton gasket were placed in between the film and cuvettes to prevent leaking. The eight-position multi-cell transport holder was used to hold eight cells (four pairs) in a rack, which were kept at constant temperature by water circulation from a thermostatic water bath. The stirring module for the multi-cell transport holder led the stirring speed at the same rate for the eight cells. The volume of the source phase containing the analyte and receiving phase was 3.00 mL in all the transport experiments. Solute concentration in the receiving phase was continuously monitored by a UV spectrophotometer (Hewlett-Packard 8452A UV-visible diode array spectrophotometer, Palo Alto, CA). The steady-state flux, J , of a solute through the film is given by eq 4-1:⁵⁷

$$J = \frac{dC_r}{dt} \cdot \frac{V}{A} (\text{mol} \cdot \text{cm}^{-2} \cdot \text{s}^{-1}) \quad (4-1)$$

dC_r/dt is the accumulation rate of solute in the receiving phase. V is the volume of the receiving phase (3.00 mL). A is the effective transport area (0.196 cm²). The permeability coefficient, P , can be deduced from the flux:⁵⁷

$$P = \frac{J \cdot l}{C_s - C_r} \approx \frac{J \cdot l}{C_{sI}} (\text{cm}^2 \cdot \text{s}^{-1}) \quad (4-2)$$

where l is the film thickness. C_s and C_r represent the concentration of the solute in the source phase and receiving phase, respectively. In our experimental duration, C_r is negligible compared to C_s . Thus $C_s - C_r$ can be simplified as the initial concentration of the solute in the source phase, C_{sI} . Selectivity of a film is defined as the permeability ratio of a fluorinated compound over its hydrogen-containing control.⁵⁷

$$S = \frac{P_F}{P_H} \quad (4-3)$$

4.2.4 Preparation, Characterization, and Transport of Fluorescent Nanoparticles Across Porous Teflon AF 2400 Films

To grow silica nanoparticles (~100 nm) with narrow size distribution, a colloidal suspension of silica nanoparticles (IPA-ST-Z, 50 nm, 2 mL) was added to a vigorously stirred solution of isopropanol (20 mL) containing TEOS (1 mL) at room temperature. Then a solution of ammonium hydroxide (28.0–30.0%, 0.5 mL) in a mixture of isopropanol (20 mL) and water (5 mL) was added dropwise with stirring (~ 1 drop/s). Finally, the mixture was stirred at room temperature for 5 hours. The modified nanoparticles were centrifuged at 6,000 rpm for 30 min and then resuspended in ethanol (30 mL) for three cycles to remove excess reagents. The size of the prepared silica nanoparticles was characterized by a particle size analyzer.

To grow silica nanoparticles with larger diameters (123, 128, and 151 nm), a different method was employed to achieve silica nanoparticles with narrow size range. A colloidal suspension of silica nanoparticles (IPA-ST-ZL, 2 mL) was added to a vigorously stirred solution

of ethanol (50 mL) at room temperature. Then a solution of ammonium hydroxide (28.0–30.0%, 6 mL) in a mixture of ethanol (25 mL) and water (8 mL) was added dropwise with stirring. TEOS (1, 1.6, and 3.9 mL) was added slowly (0.0041 mL/min) into the system by a syringe pump. After all the TEOS was added, the mixture was stirred at room temperature for 1 hour. The modified nanoparticles were centrifuged at 6,000 rpm for 30 min and then resuspended in ethanol (30 mL) for three cycles to remove excess reagents. The 177 nm silica nanoparticles were prepared using 151 nm silica nanoparticles as the starting material (TEOS: 0.0030 mL/min). The prepared silica nanoparticles were characterized by TEM (Philips Mogagni 268) and the diameters of nanoparticles on the TEM images were measured using the image analysis software Simple PCI 6 (obvious overlapping particles were manually identified for exclusion from the analysis). The size distribution of nanoparticle was obtained as a histogram with number of particles in each bin corresponding to a size range.

To prepare fluorescent silica nanoparticles, 50 μmol of APTEOS was mixed with 50 μmol of a fluorescent isothiocyanate (fluorescein isothiocyanate, rhodamine B isothiocyanate, and Fmoc isothiocyanate) in ethanol, and the mixture was allowed to stir overnight. The mixture as well as 9 mg of pyridine was added to a vigorously stirred colloidal suspension of silica nanoparticles (160 mg, 30 mL) in ethanol. Finally, the mixture was refluxed overnight. The fluorescent nanoparticles were centrifuged at 6,000 rpm for 30 min and then resuspended in ethanol (30 mL) for three cycles to remove the unreacted fluorophore. The fluorescence of colloidal suspensions of the modified silica nanoparticles in ethanol was measured with a fluorescence plate reader (Molecular Devices) at excitation wavelength of 450 nm (fluorescein tagged silica nanoparticles) or 510 nm (rhodamine B tagged silica nanoparticles) using a quartz cuvette with 1 cm pathlength.

Transport of nanoparticles was conducted with a home-made transport device at 20.0 ± 1.0 °C (**Figure 4-1**). Two pieces of viton gasket were placed in between a piece of film and two cuvettes to prevent leaking. The stirring module for the multi-cell transport plate controls the stirring speed for the five cells. The suspension of fluorescent nanoparticles was placed in cell 3, and the volume of solution was 3.00 mL (2.7 mL of ethanol and 0.3 mL of 1mM $(\text{Bu})_4\text{N}^+\cdot\text{ClO}_4^-$ in water) in all cuvettes. Cuvette 1 and 5 contained a gold electrode. In a typical experiment, 3 volts were applied across cuvettes 1 (-) and 5 (+) for 96 hours. The fluorescence of the final solutions in cuvettes 1, 2, 4, and 5 was measured by the plate reader (Molecular Devices).

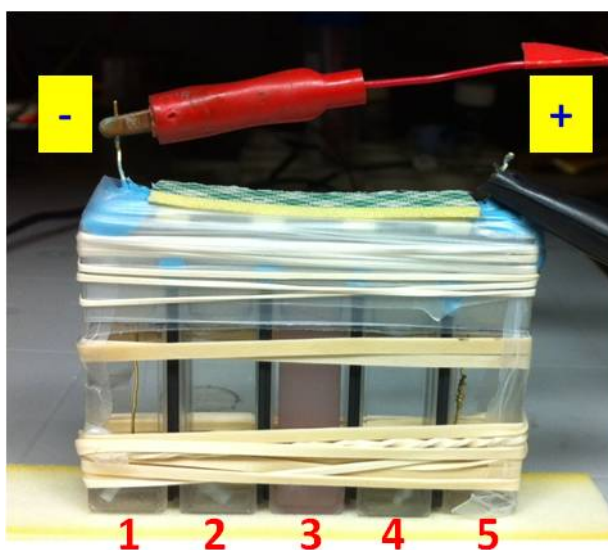


Figure 4-1. The experimental setup of nanoparticle transport across porous Teflon AF 2400 films (the porous Teflon AF films between cuvette 1 and 2 and between cuvette 4 and 5 were prepared from 70 wt% 113 nm FNP doped Teflon AF films; the porous Teflon AF films between cuvette 2 and 3 and between cuvette 3 and 4 were prepared from 70 wt% 151 nm FNP doped Teflon AF films).

4.2.5 Immobilization of Fluorous Tag on Porous Teflon AF 2400 Matrix

Porous Teflon AF 2400 films (0.5 cm×0.7 cm×40 μm, prepared from 70 wt% fluorophilic silica nanoparticle doped Teflon AF 2400 films) and solid Teflon AF 2400 films (0.5 cm×0.7 cm×40 μm) were equilibrated (1. sonicated in water/ice bath for 30 minutes; 2. shaken at 200 rpm at 20 °C for 1 hour.) in different solvents (1. ethanol with 10 v% water; 2. 1-butanol with 10 v% water; 3. dimethylformamide with 10 v% water) containing 15 μM of compound **1** (**Figure 4-13**), respectively. Films were removed from the solution and allowed to dry for 30 minutes. Both the film surface and cross section (slice width ~ 400 μm) were imaged by inverted fluorescence microscope (Olympus IX-71, EX: 350/50 nm; EM: 455/50 nm).

4.2.6 Porous Teflon AF Templated Synthesis of Porous Poly(styrene-divinylbenzene)

A porous Teflon AF 2400 film was sonicated in a mixed solution of styrene and divinylbenzene (total volume = 2 mL, volume% of divinylbenzene varies) containing 20 mg dibenzoyl peroxide (BPO) and 20 mM of compound **2** until the film sits at the bottom of solution and becomes nearly clear. The resulting Teflon AF 2400 film with reagents in the pores was then placed in a homemade leakproof container (two glass slides separated by a Teflon gasket) filled with the reagent. The polymerization temperature was controlled at 80 °C for 24 hours. The resulting Teflon AF film with poly(styrene-divinylbenzene) in the inner pores is sandwiched between two layers of pure poly(styrene-divinylbenzene) films. In order to obtain porous poly(styrene-divinylbenzene), the top and bottom layers of pure poly(styrene-divinylbenzene) films were peeled off using a blade. The middle layer was then soaked in FC-72 (a mixture of perfluorohexanes) to dissolve Teflon AF 2400 matrix. The resulting films were fractured in

liquid nitrogen and sputter-coated with palladium before subjected to SEM imaging (Philips XL-30 field emission SEM, Hillsboro, OR).

4.3 RESULTS AND DISCUSSION

4.3.1 Characterization of Porous Teflon AF 2400 Films

It is well known that silica can react effectively with hot and concentrated alkali hydroxides to form silicates. Preliminary experiments demonstrated that 50 mg of fluorophilic silica nanoparticles dispersed in 2 mL ethanol can be completely dissolved in less than half an hour in 10 mL 5 M NaOH at 60~70°C under magnetic stirring. To determine experimental conditions for the preparation of porous Teflon AF 2400 films, quantitative elemental analysis of the film cross-section against the etching time was performed by SEM/EDX for hybrid films with different filler loadings. As shown in **Figure 4-2**, 30 wt% fluorophilic silica nanoparticle doped Teflon AF 2400 films display no significant change of cross-sectional Si wt% during 6 hours. No improvement was observed by further increasing the etching time to 24 hours. For Teflon AF 2400 films containing 50 wt% and 70 wt% fluorophilic silica nanoparticles, we observed that the etching process is almost complete in 6 hours. Theoretically, in order to erode fluorophilic silica nanoparticles dispersed in Teflon AF 2400 matrix, it is required that hydroxide ion can diffuse into the polymeric matrix and then react.¹⁹⁴ We previously noted the formation of fluorophilic silica nanoparticle clusters in Teflon AF 2400 films with high filler loadings (50 wt% and 70 wt%).^{185,186} Consequently, the effective fluorophilic silica nanoparticle contacts could offer continuous hydrophilic pathways through which hydroxide ion can diffuse and react until the

etching process is complete. Therefore, compared to the 50 wt% fluorophilic silica nanoparticle doped Teflon AF 2400 films, Teflon films containing 70 wt% fillers show faster erosion kinetics because the continuous nature of fluorophilic silica nanoparticles is more significant in the latter. In contrast, data shows that fluorophilic silica nanoparticles are well dispersed (not adjacent to their neighbors) in Teflon AF 2400 films with filler loadings ≤ 30 wt%.^{185,186} Below the percolation onset, the Teflon AF 2400 matrix around the fluorophilic silica nanoparticles prevents hydroxide ion from penetrating the material and dissolving particles in the interior of the film.

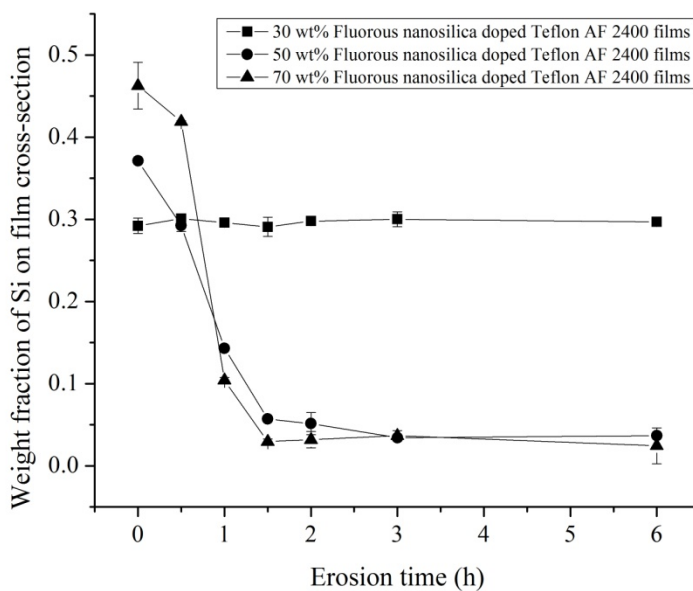


Figure 4-2. Weight percentage of Si from EDX measurements during SEM of cross-sections of fluorophilic silica nanoparticle-doped Teflon AF 2400 films plotted against the etching time: (■) 30 wt% fluorophilic silica nanoparticle doped Teflon AF 2400 films; (●) 50 wt% fluorophilic silica nanoparticle doped Teflon AF 2400 films; (▲) 70 wt% fluorophilic silica nanoparticle doped Teflon AF 2400 films.

The porous structure of Teflon AF 2400 films after the removal of template-fluorophilic silica nanoparticles, was visualized by SEM. **Figure 4-3 (A)** and **4-3 (B)** show the surface micrographs of porous Teflon AF 2400 films prepared from 50 wt% and 70 wt% fluorophilic silica nanoparticle doped Teflon AF 2400 films, respectively. Both surfaces display regular pores with the diameter about 70 nm (determined by imaging software- Simple PCI 6). **Figure 4-3 (C)** and **4-3 (D)** demonstrate the cross-sectional morphology of a 50 wt% fluorophilic silica nanoparticle doped Teflon AF 2400 film before and after etching. Initially, fluorophilic silica nanoparticles doped in Teflon matrix are well connected to each other by thin polymer threads. After erosion, the distribution of surface-connected macropores can be easily observed. Very few unreacted silica nanoparticles can still be seen remaining in the porous Teflon matrix. The N₂ adsorption and desorption isotherms for the solid Teflon AF 2400 film and porous Teflon AF 2400 films are shown in **Figure 4-4**. For all films, hysteresis is observed at low and moderate relative pressures, indicating Henry-type sorption (swelling) into condensed Teflon AF 2400 matrices.¹⁹⁵⁻¹⁹⁷ This feature is characteristic for low-temperature sorption isotherms of soft matter.^{195,196} In addition, the N₂ sorption isotherms of porous Teflon AF 2400 films exhibit mixed type I-type IV isotherms with H1 hysteresis loops, indicating porous structures with intrinsic microporosity of the polymeric skeleton.^{181,198-200} The H1 hysteresis loop is well known to be associated with regular arrays of interconnected pores having narrow size distributions.^{181,200} This is consistent with the impression given by the SEM images. Overall, the surface and cross-sectional SEM images as well as the BET data indicate the success of our approach to prepare porous Teflon AF 2400 films.

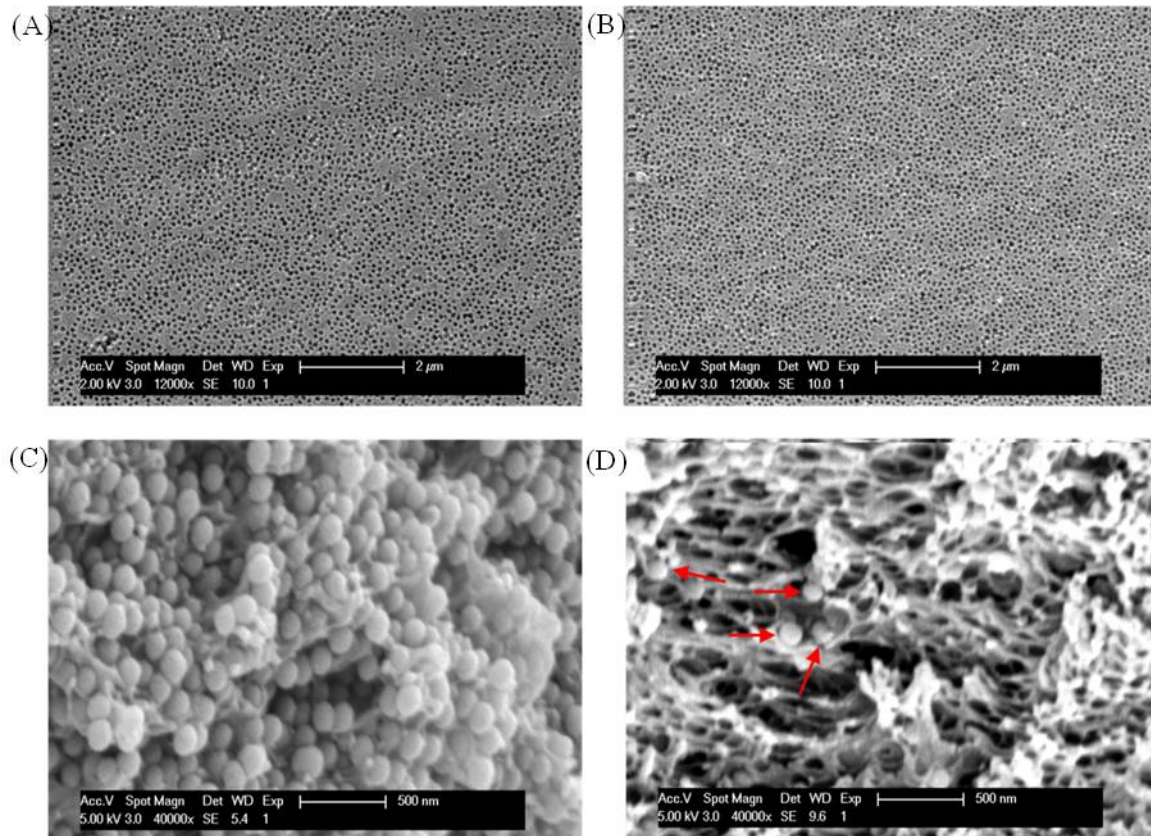


Figure 4-3. SEM micrographs: (A) and (B) are the surface view of porous Teflon AF films prepared from 50 wt% and 70 wt% fluorophilic silica nanoparticle doped Teflon AF 2400 films respectively; (C) cross-sectional view of a 50 wt% fluorophilic silica nanoparticle doped Teflon AF film (D) cross-sectional view of a porous Teflon AF film prepared from a Teflon AF 2400 film containing 50 wt% fluorophilic silica nanoparticles.

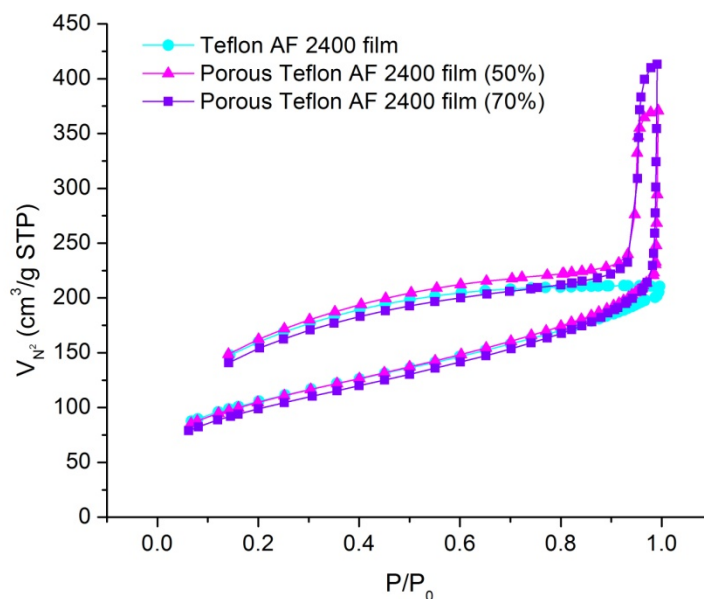


Figure 4-4. N₂ adsorption and desorption isotherms.

Water contact angle was used to demonstrate the porous surface of porous Teflon AF 2400 films. **Figure 4-5 (A), 4-5(B)** and **4-5(C)** show the representative water contact angle images on the surface of a pure Teflon AF 2400 film and porous Teflon films prepared from 50 wt% and 70 wt% fluorophilic silica nanoparticle doped Teflon AF 2400 films. The measured water contact angle of pure Teflon AF 2400 films is $(99.76 \pm 0.58)^\circ$ ($n = 12$), which is similar to the value reported by the manufacturer (105°) .²⁰¹ Porous Teflon AF 2400 films display significantly enhanced hydrophobicity due to the nano-scale surface topography. Porous films prepared from Teflon films containing 50 wt% and 70 wt% fluorophilic silica nanoparticles exhibit water contact angle of $(140.77 \pm 1.14)^\circ$ ($n = 12$) and $(141.78 \pm 0.67)^\circ$ ($n = 12$), respectively. As is well known, a smooth F-coated surface gives the contact angle between 100 and 120° .²⁰² The high hydrophobicity of porous Teflon films is attributed to the air entrapment at Teflon AF 2400/water contact interface and the roughness of the Teflon AF 2400 at surface.²⁰³

The air fraction captured by Simple PCI 6 on the surface of porous Teflon films derived from 50 wt% and 70 wt% fluorosilica doped Teflon films, are $(22.6 \pm 0.8)\%$ and $(26.9 \pm 0.5)\%$, respectively. The predicted contact angles based on Cassie's theory are between 111° and 113° , which are far below the measured values. We speculate that the surface roughness potentially induced by the rim of macropores as well as the high inner porosity of the films could be responsible for the observed high water contact angles.

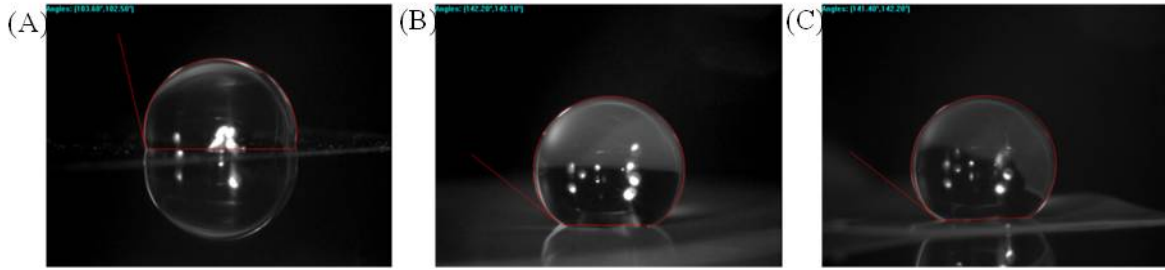


Figure 4-5. Water contact angle ($4 \mu\text{L}$) of a pure Teflon AF 2400 film (A) and porous Teflon AF 2400 films ((B) and (C)) prepared from 50 wt% and 70 wt% fluorophilic silica nanoparticle doped Teflon AF 2400 films.

We have previously reported the density of Teflon AF 2400 films containing various weight percentages of fluorophilic silica nanoparticles.^{185,186} Based on the known film composition, the measured density of hybrid films (ρ_f), and the density of pure Teflon AF 2400 films (ρ_T), the porosity of porous Teflon AF 2400 films can be calculated by assuming complete etching:

$$Porosity = 1 - \frac{\rho_f \times (1 - wt_{\text{fluorophilic silica nanoparticle}}\%) }{\rho_T} \quad (4-4)$$

Therefore, the porosity of porous Teflon AF 2400 films prepared from 50 wt% and 70 wt% fluorophilic silica nanoparticle doped Teflon films is 0.493 ± 0.07 and 0.709 ± 0.04 , respectively. Arbitrary control of porosity is feasible as long as the concentration of fluorophilic silica nanoparticle in Teflon films is above the percolation onset.

4.3.2 Transport Properties of Krytox Filled Porous Teflon AF 2400 Films

The permeabilities and selectivities of porous Teflon AF 2400 film (porosity $\approx 70\%$) based supported liquid membranes for toluene and octafluorotoluene are shown in **Figure 4-6** and **Table 4-1**, respectively. The membrane solvents tested include Krytox oils with terminal functional groups (-COOH and -OH) and non-functional perfluoropolyether. As shown in **Figure 4-6**, when functionalized Krytox oils are employed, the membrane solvent with lower molecular weight renders remarkably increased solute permeabilities due to the lower viscosity. However, the higher density of the polar functional group in Krytox oils with low molecular weight leads to decreased transport selectivity. Among all the membrane solvents tested, the non-functional perfluoropolyether shows the highest solute permeabilities as well as selectivity. For example, the permeability of octafluorotoluene through porous Teflon matrix filled with perfluoropolyether is about two times as that through a pure Teflon AF 2400 film. A 3-fold increase of transport selectivity (octafluorotoluene over toluene) was achieved by using perfluoropolyether-filled porous Teflon 2400 films.

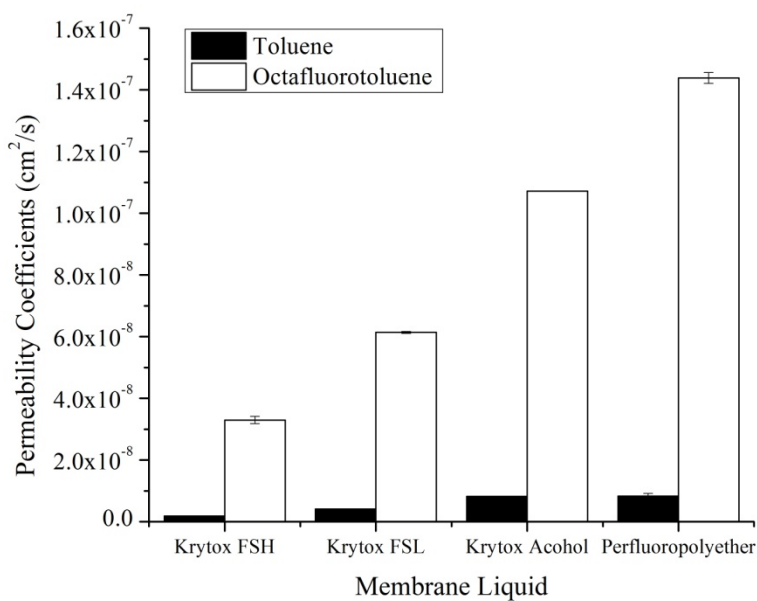


Figure 4-6. Permeability coefficients of toluene and octafluorotoluene through porous Teflon AF 2400 based supported liquid membranes at 20.0 ± 1.0 °C (solvent: CHCl_3)

Table 4-1. Selective transport of octafluorotoluene over toluene through porous Teflon AF 2400 based supported liquid membranes at 20.0 ± 1.0 °C

#	Membrane liquid	Selectivity
1	Krytox 157 FSH	17.6 ± 1.1
2	Krytox 157 FSL	15.0 ± 0.2
3	Krytox alcohol	13.1 ± 0.2
4	Perfluoropolyether	17.9 ± 1.9

4.3.3 Size-based Separation of Nanoparticles

For the preliminary feasibility study of size-based nanoparticle separation by porous Teflon AF 2400 films, silica nanoparticles of different diameters were prepared. TEM was used to characterize the silica nanoparticles prepared by the method of controlled slow TEOS addition (**Figure 4-7**). TEM images show narrow size range and good monodispersity. **Figure 4-8** further presents the size distribution of nanoparticles. The half width of size distribution increases as the nanoparticle size increases. Good monodispersity of the final silica nanoparticles is typically difficult to achieve due to the nature of two competitive steps in the formation of silica nanoparticles: nucleation ($\sim C_{\text{TEOS}}^n$) and growth ($\sim C_{\text{TEOS}} \cdot C_{\text{silanol on nanoparticles}}$). The growth of nanoparticles to a desired size can be well controlled when the nanoparticle growth is the dominant mechanism. For systems with the same starting mass concentration of silica nanoparticles (mg/L) and feed rate of TEOS (mg/min), nanoparticles with larger starting sizes lead to poorer monodispersity of the final products due to the smaller surface area of particles (m^2/g) and thus lower reaction rate of the particle growth. Further decreasing the feed rate of TEOS in the reaction may limit the competition of TEOS nucleation to the nanoparticle growth, leading to better monodispersity of the resulting nanoparticles. Overall, the preparation of silica nanoparticles with different diameters is satisfactory.

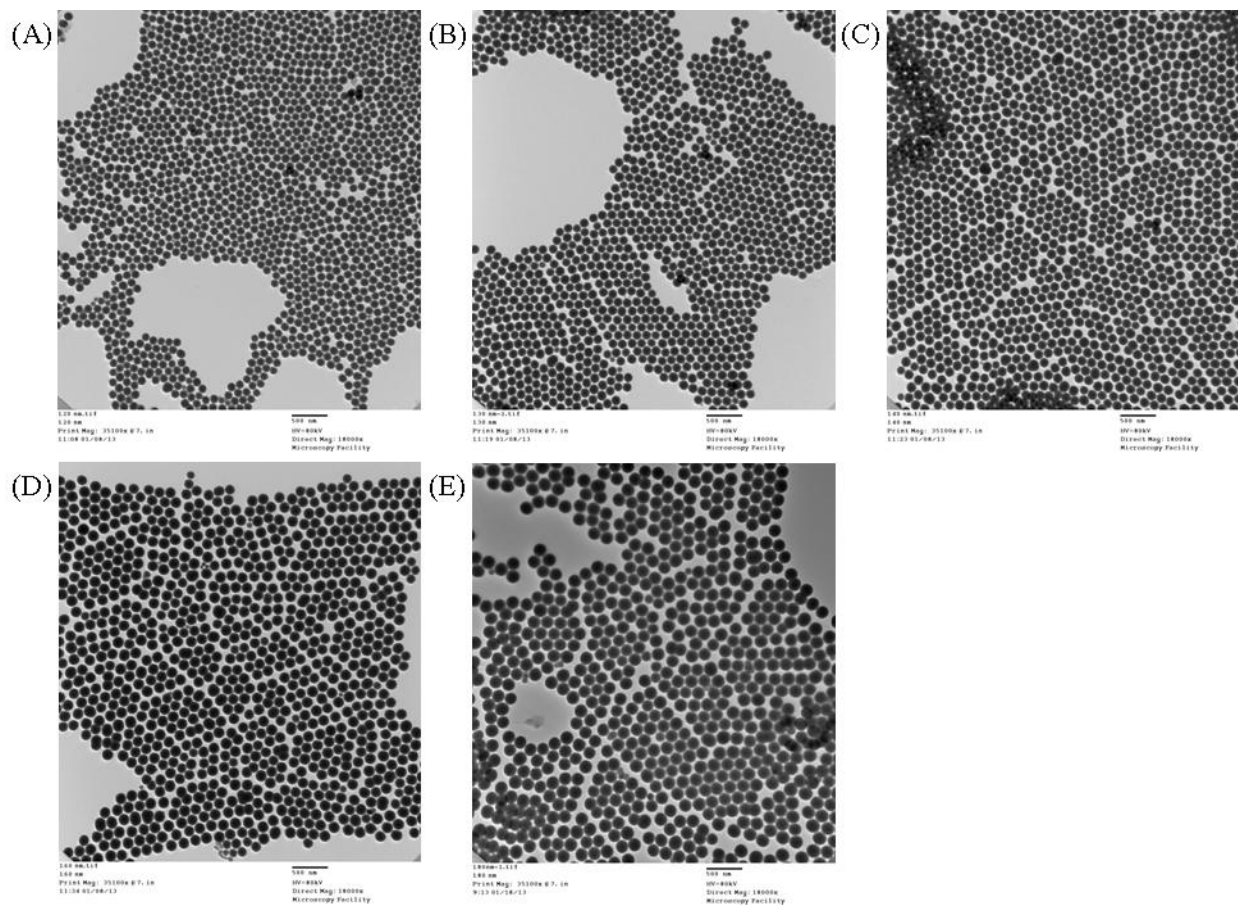


Figure 4-7. TEM micrographs of the silica nanoparticles (magnification: 18000): (A) 113 nm; (B) 123 nm; (C) 128 nm; (D) 151 nm; (E) 177 nm.

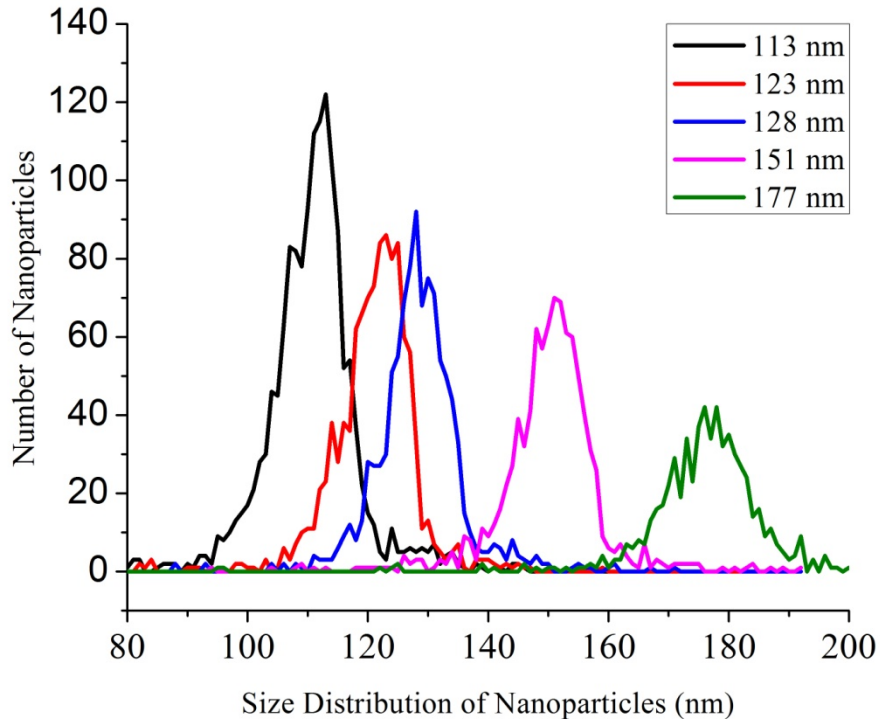


Figure 4-8. The size distribution of nanoparticles (123, 128 and 151 nm nanoparticles were prepared from the 113 nm silica nanoparticles; 177 nm nanoparticles were prepared from the 151 nm silica nanoparticles). Obvious overlapping particles in TEM images were manually identified for exclusion from the analysis by the image analysis software (Simple PCI 6).

Figure 4-9 shows the fluorescence intensity of silica nanoparticles with the modification of a fluorophore (fluorescein tagged silica nanoparticle:100nm; rhodamine B tagged silica nanoparticle:128 nm). Both fluorescent silica nanoparticles show significant fluorescence compared to the silica nanoparticles with the same size but no dye modification. The 177 nm silica nanoparticles with F-moc functionality cannot be seen by UV/fluorescence measurements due to the large nanoparticle size and thus strong light scattering in the related wavelength range. Instead, the presence of 177 nm silica nanoparticles can be identified easily from light scattering with negligible interference from nanoparticles with smaller sizes in the system as the light

scattering signal from smaller nanoparticles does not mask the presence of larger particles which exhibit the dominate light scattering signal.

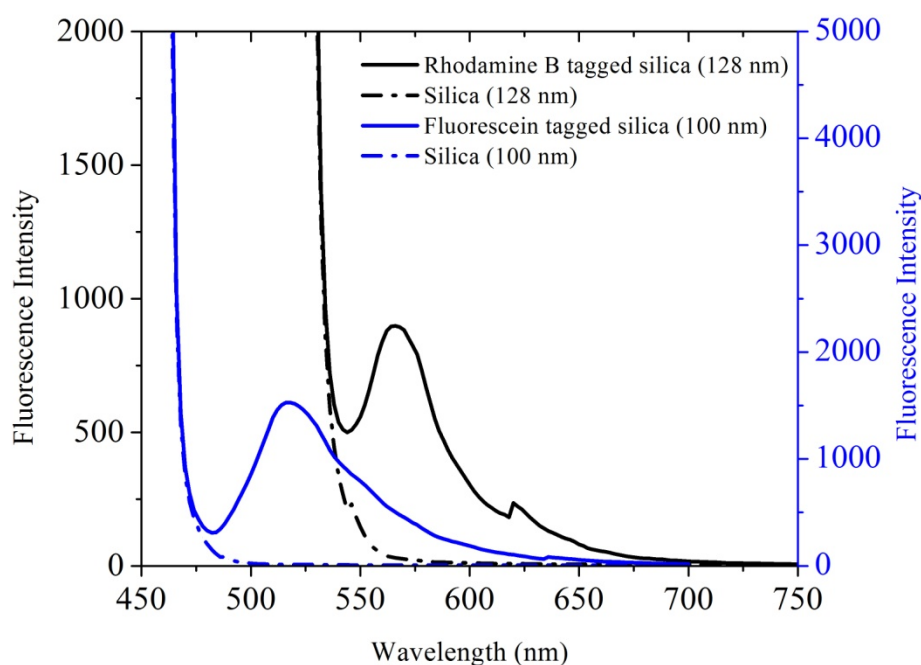


Figure 4-9. The fluorescence intensity of fluorescein tagged silica nanoparticle: 100nm (1 mg/mL; excitation: 450 nm); rhodamine B tagged silica nanoparticle: 128 nm (1 mg/mL; excitation: 510 nm).

The zeta-potential of Teflon AF 2400 films is negative.^{204,205} The negative zeta-potential of porous Teflon AF 2400 films could lead to electroosmotic flow through a porous Teflon AF 2400 film in a voltage driven transporting system. A simple and quick experiment of transporting silica nanoparticles (120 nm, no modification) through a porous Teflon AF 2400 film (prepared from 70 wt% 120 nm fluorophilic silica nanoparticle doped Teflon AF 2400 film) shows electroosmotic flow towards the “-” electrode (**Figure 4-10**). Thus, the transport of nanoparticles through porous Teflon AF 2400 films is a comprehensive effect of the electrophoresis of nanoparticles as well as the electroosmotic flow of the bulk solution.

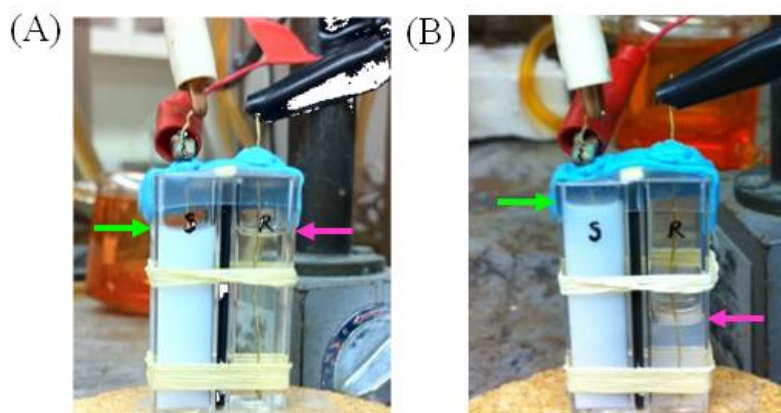


Figure 4-10. Electroosmotic flow through porous Teflon AF 2400 film: (A) 0 h; (B) 96 h. Green arrows indicate the liquid level in the source phase, and pink arrows indicate the liquid level in the receiving phase.

Teflon AF 2400 has a negative zeta potential,^{204,205} and thus the electroosmic flow is toward the negative electrode. The zeta-potentials of the fluorescent silica nanoparticles are listed in **Table 4-2**. Fluorescein tagged silica nanoparticles have negative zeta-potential while rhodamine B and F-moc tagged silica nanoparticles have positive zeta-potential. Therefore, the electrophoresis of fluorescein tagged silica nanoparticles is toward the positive electrode while those for rhodamine B and F-moc tagged silica nanoparticles are toward the negative electrode. As shown in **Figure 4-11**, the electrophoresis and electroosmotic flow of fluorescein tagged silica nanoparticles are in opposite directions: electrophoresis drives fluorescein tagged silica nanoparticles toward the positive electrode while electroosmosis drives nanoparticles toward the negative electrode. For Rhodamine B and F-moc tagged silica nanoparticles, both the electrophoresis and electroosmotic flow drive nanoparticles toward the negative electrode. **Figure 4-12** and **Figure 4-13** show the fluorescence spectra of cuvettes 1, 2, 4, and 5 after the transport experiment. The presence of Rhodamine B tagged silica nanoparticles (128 nm) in cuvette 2 indicates significant transport of the 128 nm nanoparticles through porous Teflon AF 2400 film (feature pore size: 151 nm) toward the negative electrode. The featured fluorescence

spectrum of Rhodamine B tagged silica nanoparticles (128 nm) in curvette 1 has very low intensity, indicating that very few Rhodamine B tagged silica nanoparticles (128 nm) were transported through the porous Teflon AF 2400 film (feature pore size: 113 nm). There is no Rhodamine B tagged silica nanoparticle observed in curvette 4 or 5 (toward the positive electrode). **Figure 4-13** shows that fluorescein tagged silica nanoparticles (100 nm) are present in curvette 2 only, indicating these nanoparticles were transported through porous Teflon AF 2400 films (feature pore size: 151 nm) toward the negative electrode. The measurements of curvette 4 and 5 do not show fluorescence feature of fluorescein tagged silica nanoparticles, indicating no transport of fluorescein tagged silica nanoparticles toward the positive electrode. These observations indicate that electroosmosis dominates the translocation of fluorescein tagged silica nanoparticles: the electrophoresis of fluorescein tagged-silica nanoparticles in solution [100 nm, electrophoretic velocity (electrophoretic mobility²⁰⁶ × field strength) = 3.4×10^{-7} m/s, toward “+”] has been suppressed by electroosmotic flow in the porous Teflon AF 2400 film (feature pore size: 151 nm). Interestingly, we didn’t observe any transport of fluorescein tagged silica nanoparticles (100 nm) across the porous Teflon AF 2400 with a feature pore size of 113 nm. This could be due to a pore-plugging effect: Rhodamine B tagged silica nanoparticles have an electrophoretic velocity of 2.2×10^{-6} m/s (toward “-”), can reach the porous Teflon AF film (feature pore size: 113 nm; sandwiched between curvette 1 and 2) faster than the fluorescein tagged silica nanoparticles, and will potentially block the pores. This type of pore-plugging effect was captured by computational modeling in the transport of polydisperse nanoparticles through a porous film.²⁰⁷ No transport was observed for F-moc tagged silica nanoparticles (177 nm) as the nanoparticles were not observed by dynamic light scattering in curvettes 1, 2, 4, and 5.

Table 4-2. Zeta-potential of fluorescent silica nanoparticles in ethanol.

#	Nanoparticle	Zeta-potential (mV)	Electrophoresis direction	Electroosmotic flow direction
1	Fluorescein-SiO ₂ (100 nm)	-11.40 ± 1.10	“+”	“-”
2	Rhodamine B-SiO ₂ (128 nm)	43.07 ± 2.11	“-”	“-”
3	F-moc-SiO ₂ (177 nm)	19.08 ± 0.89	“-”	“-”

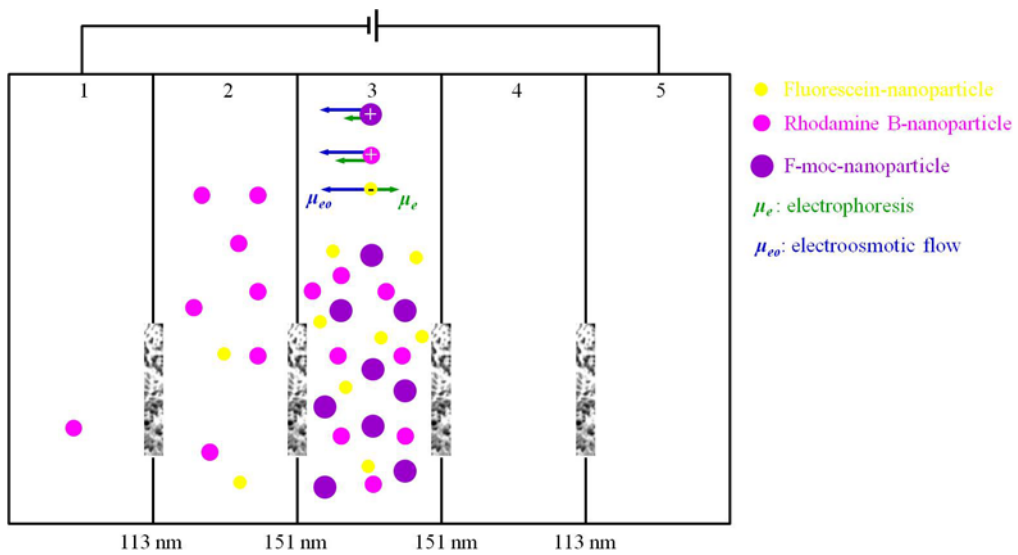


Figure 4-11. Transport of nanoparticles through porous Teflon AF films (96 hours, 3V).

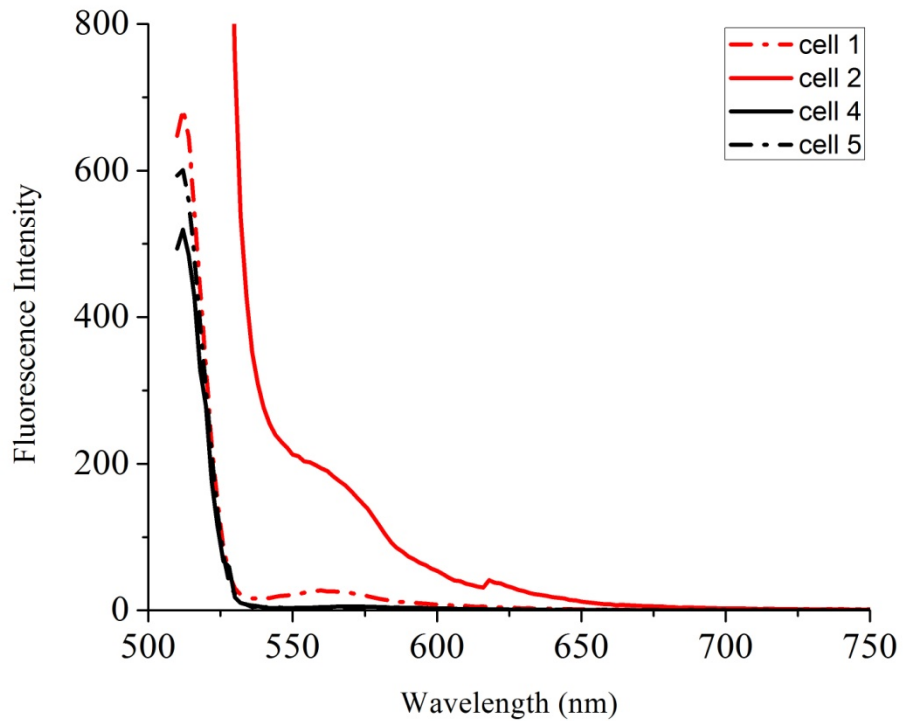


Figure 4-12. The fluorescence measure of nanoparticle transport through porous Teflon AF 2400 films (experimental setup: **Figure 4-1**; 96 hours; 3 volts). The experimental conditions for fluorescence measurements were the same as for the previous measurement on 1 mg/mL rhodamine B tagged silica nanoparticle (excitation: 510 nm).

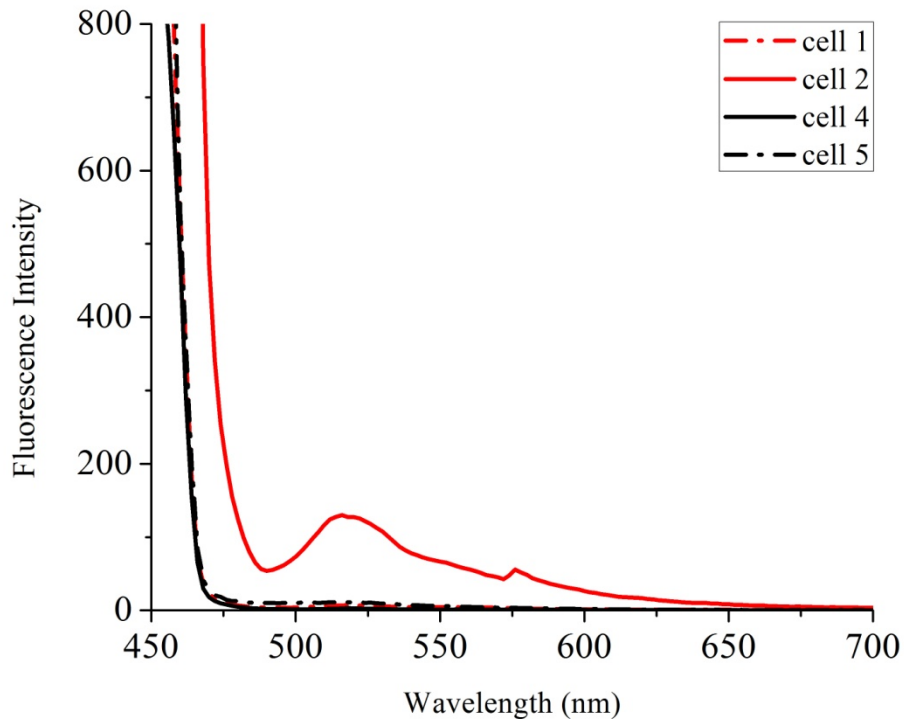


Figure 4-13. The fluorescence measure of nanoparticle transport through porous Teflon AF 2400 films (experimental setup: **Figure 4-1**; 96 hours; 3 volts). The experimental condition of fluorescence measurement is the same as previous measurement on 1 mg/mL fluorescein tagged silica nanoparticle (excitation: 450 nm).

Results in this preliminary study suggest that it is feasible to employ porous Teflon AF 2400 films for size-based separation of nanoparticles. Nanoparticles with large zeta-potential are potentially beneficial for better control/prediction of nanoparticle transport across the film. To achieve separation of polydisperse nanoparticles, the application of programmed electric field could be beneficial to prevent the plugging of pores by relatively large nanoparticles which may block the transport path of small nanoparticles.

4.3.4 Porous Teflon AF 2400 Films as Microarray Substrate

Instead of technical innovations to decrease detection limit and enlarge linear range, the improvement of surface area in arrays could achieve remarkably high detection sensitivities due to the large surface area-to-volume ratios. Inspired by this, we started to investigate the feasibility of porous Teflon AF 2400 films as microarray substrates to replace the commonly employed fluorinated glass slides for microarrays targeting protein-small molecule interactions. Our assessment used a model fluorinated compound (**1**, **Figure 4-14**) that is the basis of peptidase assays. In practical applications, a peptide would be attached at the amine group. The hydrolysis of the peptide, liberating the amine group, would lead to a fluorescence signal from **1**. Thus, the amount of fluorescence is related to the amount of hydrolysis. Here, we are testing for the *maximum* amount of fluorescence that can be obtained on two different surfaces, one porous and one not. Thus, solutions of **1** were placed in contact with nonporous and porous Teflon AF films, allowed to equilibrate, and then the fluorescence was determined. The amount of **1** adsorbed also depends on the solvent used. Thus, we tried three different solvents to make sure that our results revealed the porous/nonporous difference clearly. In the following context, we show results obtained from the ‘optimized solvent’—ethanol with 10% water.

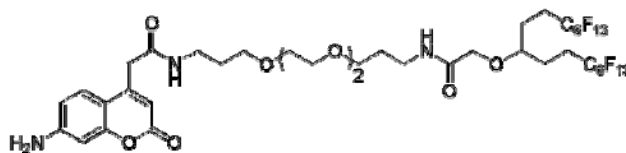


Figure 4-14. The structure of **1** ($R_f = (CF_2)_5CF_3$).

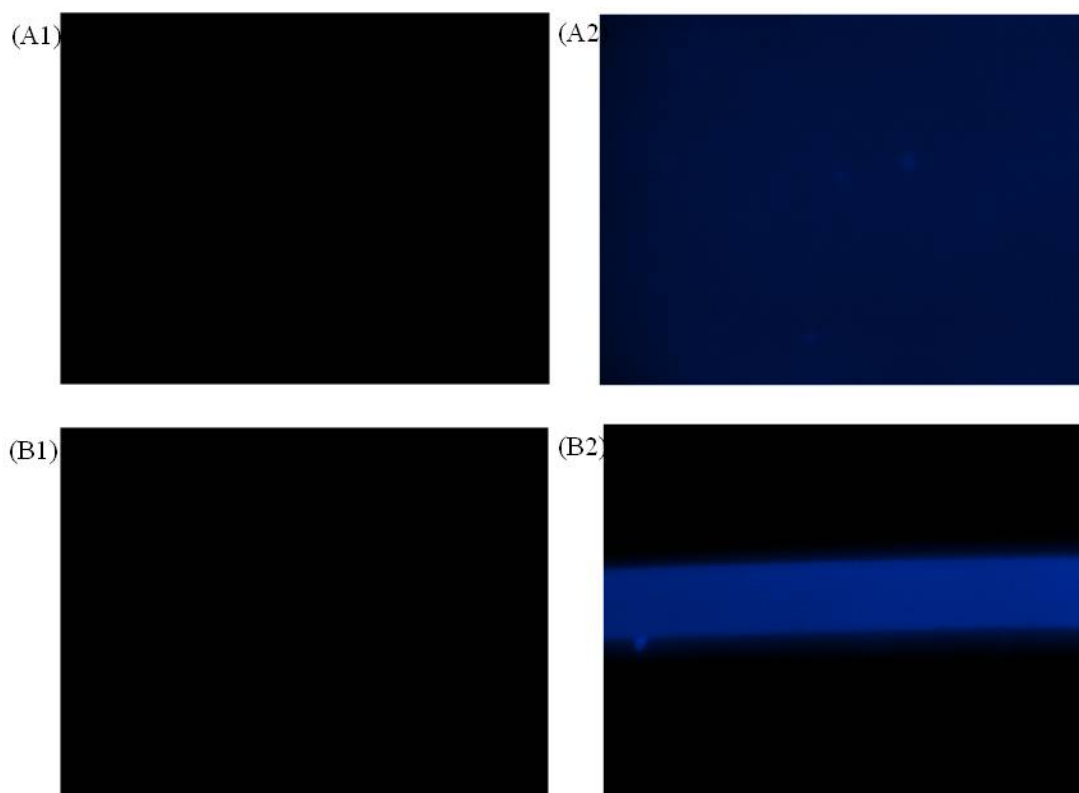


Figure 4-15. Fluorescence images (350 nm/455 nm) of Teflon AF films equilibrated with 15 μM of **1** in ethanol (10% H_2O): (A1) surface of a solid Teflon AF film (4 \times /numerical aperture: 0.16); (A2) surface of a porous Teflon AF film (4 \times /numerical aperture: 0.16); (B1) cross section of a solid Teflon AF film (40 \times /numerical aperture: 0.60); (B2) cross section of a porous Teflon AF film (40 \times /numerical aperture: 0.60). Note: the thickness of both solid and porous Teflon AFs is 40 μm . Cross section images were taken from 400 μm slices.

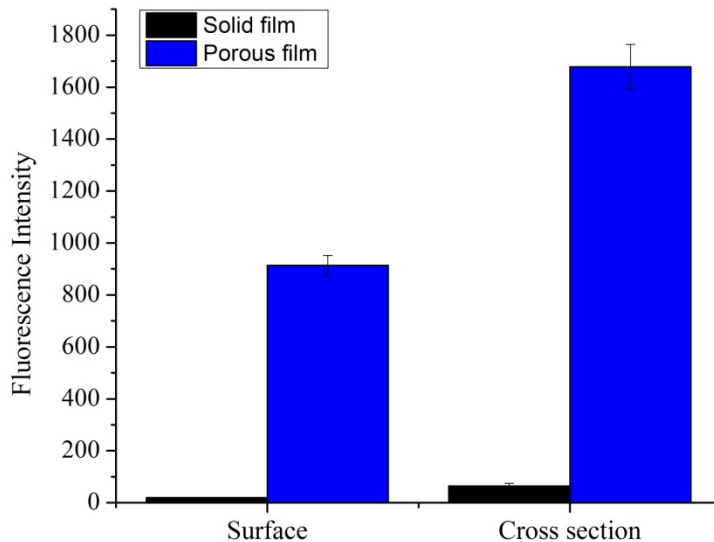


Figure 4-16. Non-covalent immobilization of **1** on porous Teflon AF 2400 films (blue) and solid Teflon AF films (black) on both film surfaces and cross sections.

Figure 4-15 shows the fluorescence images of porous Teflon AF films (**A2**, **B2**) and solid Teflon AF films (**A1**, **B1**) equilibrated with **1**. The porous films display significant fluorescence compared to solid films on both surface and cross section, indicating more immobilized fluorophore on the 3D-surface of porous films. Moreover, the homogeneity for the immobilization of **1** on the porous Teflon AF films is satisfactory.

Figure 4-16 plots the fluorescence intensity on both film surface and cross section for solid and porous Teflon AF films. Porous Teflon AF films (blue bars) display 46-fold and 26-fold fluorescence intensity enhancement on the surface and cross section, respectively. Without a doubt, the capacity for the immobilization of fluorophore increased dramatically in the 3D-Teflon AF matrix. Since many microporous and mesoporous materials display higher fluorescence background than solid materials, it is worthwhile to compare the background of the

porous Teflon AF films to that of the solid films. The background of porous films is 1.2-fold the value of the solid film when imaging the film surface ($4\times/\text{numerical aperture: } 0.16$), and 6.7-fold the value of the solid film when imaging the film cross-section ($40\times/\text{numerical aperture: } 0.60$). Therefore, even though the porous Teflon AF matrix shows higher fluorescence background than the solid Teflon film, as an array substrate, the porous matrix is significantly more sensitive than the solid matrix due to the dramatic increase of surface area and immobilization capacity.

4.3.5 Porous Teflon AF 2400 Templated Synthesis of Porous Hydrocarbon Polymer Matrix

Fluorophilic silica nanoparticles serve as endo-templates to prepare porous Teflon AF matrices. Since Teflon AF 2400 is soluble only in perfluorinated liquids and Novec engineering liquids at normal conditions (T and P), the as-prepared porous Teflon AF matrix with intrinsically high stiffness can further serve as the template for the synthesis of porous organic polymers. We started from creating porous poly(styrene-divinylbenzene), the precursor of one of the most widely used ion exchange membranes, as a proof of concept example. This strategy is straightforward. However, styrene does not wet porous Teflon AF matrix, and therefore cannot fill into the pores unless a compound (**2**, **Figure 4-17**) with both organic and fluoruous moieties is introduced. When a piece of porous Teflon AF film is placed in the solution of styrene containing 20 mM of **2**, The fluoruous moiety of **2** is preferably adsorbed on the surface of porous Teflon AF matrix, allowing the exposure of the organic moiety, which is easily wetted by styrene. Divinylbenzene was used as the cross-linking agent in order to obtain a resulting porous polymer with well defined morphology.

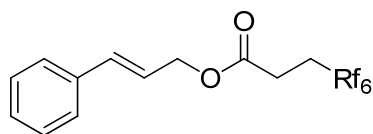


Figure 4-17. The structure of **2** ($Rf_6=(CF_2)_5CF_3$).

Bulk polymerization of styrene and divinylbenzene yields a solid film, as shown in **Figure 4-18** (A). The polymerization of styrene and divinylbenzene in the Teflon AF 2400 matrix produces connected poly(styrene-divinylbenzene) beads in the matrix. Upon the removal of the Teflon AF 2400 matrix by dissolving it in FC-72 (a mixture of perfluorohexanes), a porous poly(styrene-divinylbenzene) matrix composed of polymer beads (~ 100 nm) is clearly observed, as shown in **Figure 4-18** (C). The elemental analysis (SEM/EDX) of porous poly(styrene-divinylbenzene) from templated synthesis is consistent with the material prepared from bulk polymerization. Further increase of the volume percentage of divinylbenzene yields porous poly(styrene-divinylbenzene) materials with improved strength and morphological stability.

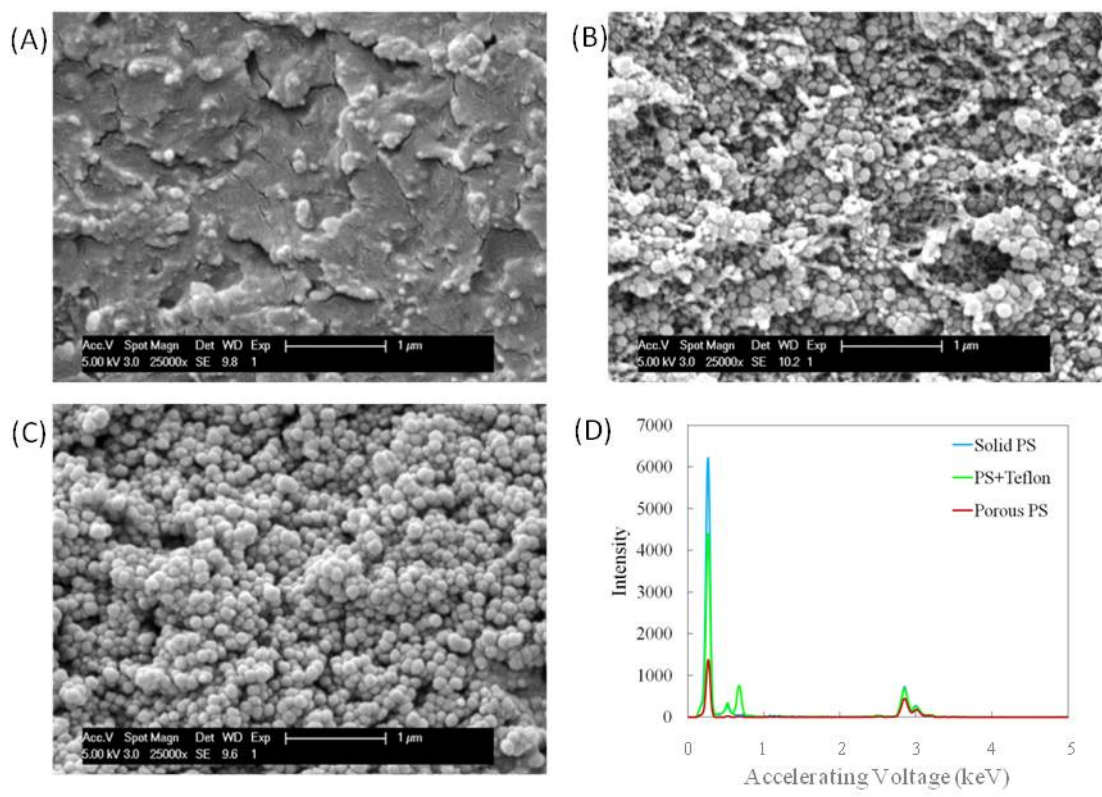


Figure 4-18. Cross-sectional SEM micrographs: (A) Poly(styrene-divinylbenzene) from bulk polymerization; (B) Poly(styrene-divinylbenzene) in porous Teflon AF 2400 matrix; (C) Poly(styrene-divinylbenzene) after the removal of Teflon AF template; (D) Elemental analysis of films in (A), (B), and (C). Note: the volume ratio of styrene to divinylbenzene in (A), (B), and (C) are 9:1.

4.4 CONCLUSION

Employing fluorophilic silica nanoparticle as the endo-template, porous Teflon AF 2400 films have been easily prepared with tunable porosity. Satisfactory homogeneity on the surface and cross-section of porous Teflon AF 2400 films was achieved. Starting from the porous Teflon AF 2400 films, we demonstrated that fluorophilic polymeric oils can be incorporated into the matrices to form fluorophilic supported liquid membranes. Such supported liquid membranes show high

solute permeability and selectivity in liquid phase transport. The regular pore size of porous Teflon AF 2400 film renders its potential application in nanoparticle fractionation. Due to the characteristic high surface area, efforts have been launched for developing porous Teflon AF 2400 matrices as fluororous microarray substrates. In addition, the unique solubility behavior of Teflon AF 2400 (soluble only in fluorocarbons and semifluorous solvents) facilitates the application of porous Teflon AF 2400 in the preparation of porous hydrocarbon polymers.

4.5 ACKNOWLEDGEMENT

We thank the National Science Foundation for support through grant CHE-0957038.

5.0 ISOTHERMAL TITRATION CALORIMETRY OF PERFLUORODECANIOIC ACID WITH PYRIDINE AND QUINAZOLINE IN AN ORGANIC, A SEMI-FLUORINATED, AND A PERFLUORINATED SOLVENT.

5.1 INTRODUCTION

Fluorous media are highly non-polar and notoriously poor solvents.^{1,208} The “fluorous nature” refers to the macroscopic phase behavior of fluorocarbons. As a third phase, fluorocarbons are widely regarded as simultaneously hydrophobic and oleophobic.^{1,55} This behavior is due to their rigid structure, large cross-sectional area, and loose molecular packing, which together lead to small van der Waals interaction per molecular contact area.^{3,209} The unique property of the fluorous media—exclusion of non-fluorinated molecules—leads to opportunities in partitioning - based chemical separations,^{58,90,185,186,210} molecular recognition-based selective extraction and sensing,^{62-64,70} as well as self assembly-based Biomaterials.^{189,211 212}

Much attention has been paid to the understanding of unique properties and applications in fluorous media. However, knowledge of the thermodynamics of molecular interactions that take place in the fluorous phase is very limited. The focus of our group has been centered on understanding the noncovalent interactions, specifically hydrogen-bonding based molecular recognition, in fluorous media.⁶²⁻⁶⁴ At room temperature, a carboxylic acid-terminated poly hexafluoropropylene oxide, Krytox 157FSH, interacts with heterocyclic bases in fluorous

solvents.²¹³ The method of continuous variation shows that Krytox 157FSH forms 1:1 complexes with relatively weak bases (pyrazine, pyrimidine, and quinazoline) in FC-72 (perfluorohexanes), whereas 3:1 complexes are formed with stronger bases (quinoline, pyridine, and isoquinoline).⁶³ Infrared and UV spectroscopic analysis indicates that 1:1 complexes are molecular (hydrogen bonded complexes without proton transfer) whereas the 3:1 complexes are ionic (hydrogen bonded complexes with proton transfer).^{62,63} It is challenging to obtain quantitative binding data from infrared and UV spectra due to the presence of more than one chemical equilibrium (complex formation between Krytox 157FSH and the base, and the self association of Krytox 157FSH). If multiple complexes are present, spectroscopic methods (e.g. UV/Vis, IR titrations) may capture only a portion of the information on complex formations because the characteristic spectroscopic signals are not typically completely orthogonal.²¹⁴ Thus, questions arise: is the formation of 3:1 complex a stepwise process, and does the proton transfer occur at a certain step? To understand better the formation of hydrogen bonded complexes, we investigate the formation of hydrogen-bonding based complexes via isothermal titration calorimetry (ITC) to gain more insight into the complex formation in fluoruous phase.

To understand better the factors influencing noncovalent interactions, the thermodynamic parameters (ΔG° , ΔH° and ΔS°) of complex formation between perfluorodecanoic acid (PFDA) and two heterocyclic bases (quinazoline and pyridine) have been obtained by ITC in three solvents with a significant range of dipolarity: FC-77 (primarily a mixture of C_8F_{18} and cyclic $C_8F_{16}O$), HFE-7500 (2-trifluoromethyl-3-ethoxydodecafluorohexane), and 1-chloropentane. Moreover, ITC experiments performed at different temperatures (25°C, 35°C, and 45°C) yield information on the change of heat capacity for the further understanding of different complexes.

A thorough understanding of noncovalent interactions will potentially benefit molecular recognition based separation and sensing in fluoruous media.

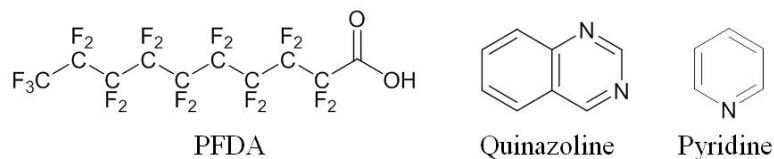


Figure 5-1. Structures of perfluorodecanoic acid and two heterocyclic bases

5.2 EXPERIMENTAL

5.2.1 Materials and methods

Pyridine was purchased from Acros Organics (NJ). Perfluorodecanoic acid (PFDA), quinazoline, 1-chloropentane, CaCl₂, and 4-nitroanisole were purchased from Sigma-Aldrich (St. Louis, MO). 1-Chloropentane was dried with CaCl₂ before use. FC-77 (primarily a mixture of C₈F₁₈ and cyclic C₈F₁₆O) and HFE-7500 (2-trifluoromethyl-3-ethoxydodecafluorohexane) were purchased from 3M (Minneapolis, MN) and used as received. The π^* values of the solvents were obtained using the measured uv/vis frequency maximum (cm⁻¹) for the electronic transition of dissolved 4-nitroanisole according to literature.²¹⁵

5.2.2 Isothermal Titration Calorimetry (ITC)

Calorimetric measurements were performed using a Nano ITC from TA Instruments (New Castle, DE). Temperature control was maintained at 25, 35, or 45 °C. In a typical ITC

experiment on dimer dissociation, the sample cell and reference cell in the calorimeter were filled with pure solvent. A solution of PFDA [$C_{\text{PFDA}}(\text{FC-77}) = 5.00 \text{ mM}$; $C_{\text{PFDA}}(\text{HFE-7500}) = 10.00 \text{ mM}$; $C_{\text{PFDA}}(\text{HFE-7500}) = 5.00 \text{ mM}$] was titrated in 40 injections of $5 \mu\text{L}$ each with a time interval of 400 s and a stirring speed of 300 rpm. The power required to maintain thermal equilibrium between the sample and the reference cell was recorded versus time. In a typical ITC experiment on PFDA and pyridine/quinazoline titration, the sample cell was filled with a solution of PFDA [for PFDA/pyridine system: $C_{\text{PFDA}}(\text{FC-77}) = 0.40 \text{ mM}$; $C_{\text{PFDA}}(\text{HFE-7500}) = 0.40 \text{ mM}$; $C_{\text{PFDA}}(\text{1-chloropentane}) = 0.25 \text{ mM}$; for PFDA/quinazoline system: $C_{\text{PFDA}}(\text{FC-77}) = 0.20 \text{ mM}$; $C_{\text{PFDA}}(\text{HFE-7500}) = 0.25 \text{ mM}$; $C_{\text{PFDA}}(\text{1-chloropentane}) = 0.40 \text{ mM}$] and the reference cell was filled with the pure solvent. A solution of pyridine/quinazoline [$C_{\text{pyridine}}(\text{FC-77}) = 3.00 \text{ mM}$; $C_{\text{pyridine}}(\text{HFE-7500}) = 3.00 \text{ mM}$; $C_{\text{pyridine}}(\text{1-chloropentane}) = 5.00 \text{ mM}$; $C_{\text{quinazoline}}(\text{FC-77}) = 4.00 \text{ mM}$; $C_{\text{quinazoline}}(\text{HFE-7500}) = 5.00 \text{ mM}$; $C_{\text{quinazoline}}(\text{1-chloropentane}) = 60.00 \text{ mM}$] was titrated in 40 injections of $4 \mu\text{L}$ each with a time interval of 400 s and a stirring speed of 300 rpm. Blank titrations (pure solvent in the syringe) were performed and subtracted from the corresponding titrations to remove the effect of dilution and perturbation of the each injection to the system in sample cell.

5.2.3 Analysis of Isothermal Titration Calorimetry Data

The analysis of the heat of dilution for monomer [HA represents the acid monomer: (PFDA)]-dimer [$(HA)_2$ represents the acid dimer: (PFDA)₂] system:



$$\beta_a = \frac{[(HA)_2]}{[HA]^2} \quad (5-2)$$

where β_a is the dimer formation constant. In ITC experiments, we measure the heat (Δq) when a small volume (v) of concentrated acid solution (the total concentration of HA : $C_0 = [HA]_0 + 2[(HA)_2]_0$) is titrated into the calorimeter cell (constant volume: V_0) containing initially pure solvent. The heat arises from the dimer present in the higher concentration solution that dissociates upon entering the lower concentration calorimeter cell.

The total concentration of HA in the calorimeter cell after the i th titration, $C_{HA}(i)$, equals:

$$C_{HA}(i) = C_0 \left[1 - \left(\frac{V-v}{V} \right)^i \right] \quad (5-3)$$

The equilibrium concentration of acid dimer equals:

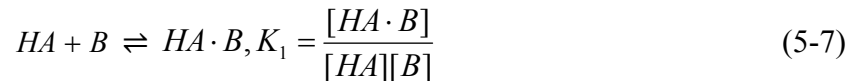
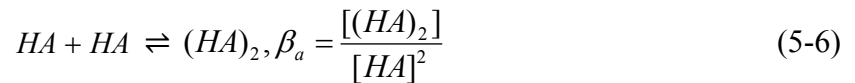
$$[(HA)_2] = \frac{4C_{HA}(i)\beta_a + 1 - \sqrt{8C_{HA}(i)\beta_a + 1}}{8\beta_a} \quad (5-4)$$

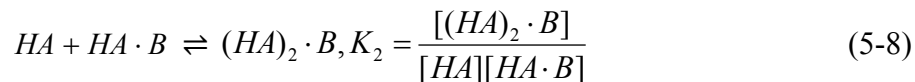
For the i th titration of a series, the observed heat is given by:

$$\Delta q(i) = \Delta H_{2HA \rightleftharpoons (HA)_2} \{ [(HA)_2]_i - [(HA)_2]_{i-1} \} (V-v) + \{ [(HA)_2]_i - [(HA)_2]_0 \} v \quad (5-5)$$

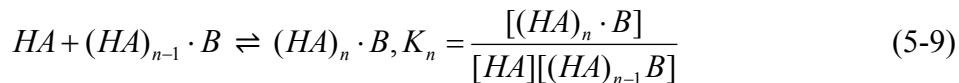
where $\Delta q(i)$ is the heat of the i th titration, $[(HA)_2]_i$ and $[(HA)_2]_{i-1}$ are the acid dimer concentrations after the i th and the $(i-1)$ th titration respectively, $[(HA)_2]_0$ is the acid dimer concentration in the concentrated solution (in the syringe), and $\Delta H_{2HA \rightleftharpoons (HA)_2}$ is the enthalpy of dimer formation. Equation (5-5) was used for the non-linear regression of experimental dilution data to obtain β_a and $\Delta H_{2HA \rightleftharpoons (HA)_2}$ values.

Analysis of heats of acid (HA represents the acid: PFDA)-base (B represents the base: pyridine/quinazoline) complex formations:





⋮



In ITC experiments, the heat (Δq) was measured when a small volume (v) of base solution (the concentration of B : C_{0B}) is titrated into the calorimeter cell (constant volume: V_0) containing acid solution (the total initial concentration of HA : $C_{0HA} = [HA]_0 + 2[(HA)_2]_0$).

The total concentration of HA in the calorimeter cell after the i th titration $C_{HA}(i)$ equals:

$$C_{HA}(i) = C_{0HA} \left(\frac{V-v}{V} \right)^i = [HA]_i + 2[(HA)_2]_i + [HA \cdot B]_i + 2[(HA)_2 \cdot B]_i + \cdots + n[(HA)_n \cdot B]_i \quad (5-10)$$

The total concentration of B in the calorimeter cell after the i th titration $C_B(i)$ equals:

$$C_B(i) = C_{0B} \left[1 - \left(\frac{V-v}{V} \right)^i \right] = [B]_i + [HA \cdot B]_i + [(HA)_2 \cdot B]_i + \cdots + [(HA)_n \cdot B]_i \quad (5-11)$$

The heat of titration arises from the shift of the coupled chemical equilibria. For the i th titration of a series, the observed heat is given by:

$$\begin{aligned} \Delta q(i) = \Delta H_{HA \rightleftharpoons 2HA \leftrightarrow (HA)_2} \{ [(HA)_2]_i V - [(HA)_2]_{i-1} (V-v) \} \\ + \sum_{j=1}^n \Delta H_{jHA+B \rightleftharpoons (HA)_j \cdot B} \{ [(HA)_j \cdot B]_i V - [(HA)_j \cdot B]_{i-1} (V-v) \} \end{aligned} \quad (5-12)$$

where $\Delta q(i)$ is the heat of the i th titration, $[(HA)_j B]_i$ and $[(HA)_j B]_{i-1}$ are the j :1 acid-base complex concentrations after the i th and the $(i-1)$ th titration respectively, and $\Delta H_{jHA+B \rightleftharpoons (HA)_j \cdot B}$ is the enthalpy of j :1 complex formation. Equation (5-12) was used to fit the experimental data to obtain complex formation constants and enthalpy values. The detailed steps in the data fitting are

as follows: (a) $[HA]_i$ is calculated from a set of chosen trial β values according to equation (5-6)–(5-11); (b) $[(HA)_2]_i$, $[(HA)\cdot B]_i$...and $[(HA)_n\cdot B]_i$ are calculated from $[HA]_i$ based on equation (5-6)–(5-11); (c) least squares fitting of ITC data to equation (5-12) based on the known species concentrations to obtain enthalpies of complex formations as well as the mean residual sum of squares from the curve fitting; (d) step (a) to (c) are repeated for each combination of K values (a stepwise change of 1% on K values) until the best fit is obtained. The whole process yields the best fit values of binding constants and enthalpies of complex formations. A typical contour plot showing the mean squared residual error in the chosen trial array is shown in **Figure B-1**. Mathcad files for the data fitting are in Appendix B.

5.3 RESULTS AND DISCUSSION

5.3.1 Effects of Solvent and Temperature on the Dimerization of PFDA

Carboxylic acids, alone or as structural fragments in molecular receptors, are able to bind tightly and selectively with specific molecules for molecular recognition applications in non-polar solvents.^{62,216-218} The capability of carboxylic acids as molecular receptors is influenced by their self-association. Experimental and theoretical studies on the association of carboxylic acids (e.g. small organic acids,²¹⁹⁻²²¹ trifluoroacetic acid,^{222,223} and perfluoropolyethers with carboxylic acid terminal groups^{224,225}) in vapor phase and non-polar solvents reveal that the cyclic dimer is the only complex of primary importance while other species (open structured dimers and oligomers) are significantly less stable. Before we examine the non-covalent interactions between PFDA and pyridine/quinazoline, the thermodynamics of hydrogen bond dimerization of PFDA as well

as the influence of solvent and temperature on the dimerization behavior were investigated via ITC.

Figure 5-2 shows the ITC profiles for the titration of PFDA solutions into the pure solvent. The corresponding thermodynamic parameters based on a single equilibrium between monomer and dimer are listed in **Table 5-1**. The dimerization energy of PFDA is close to that of trifluoroacetic acid (TFA) in CCl_4 at 25 °C (-38 kJ/mol)²²² as well as the value of TFA dimerization in CO_2 (-32 kJ/mol) from theoretical calculations.²²⁶ At each temperature, the dimerization constant of PFDA is lower in the solvent with higher dipolarity [$\beta_a(\text{FC-77}, \pi^* = -0.277) > \beta_a(\text{HFE-7500}, \pi^* = 0.222) > \beta_a(1\text{-chloropentane}, \pi^* = 0.450)$]. Dimer formation was not observed in 1-chloropentane. This trend of dimer formation constant with respect to solvent strength can be explained by the solvation behavior²²⁷ – a stronger solvent with more effective solute-solvent interactions would solvate the acid monomer better, therefore weakening the tendency to dimerize.²²⁰ In both FC-77 and HFE-7500, ΔH^0 became more negative with increased temperature, reflecting negative changes in heat capacities [$d(\Delta H)/dT$]. A negative ΔC_p accompanying the formation of the dimer reflects weakened solvation at higher temperatures.²²⁸⁻
²³¹ As the more polar PFDA requires solvation more than $(\text{PFDA})_2$, and increased temperature decreases solvation, the increase in temperature enthalpically favors complex formation. PFDA dimerization is preferable at lower temperatures as the formation of acid dimer is entropically unfavorable.

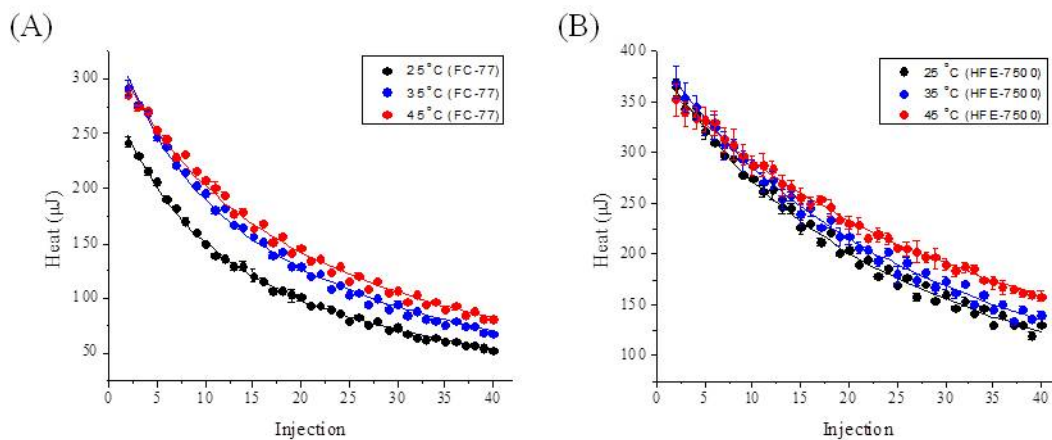


Figure 5-2. ITC profile of PFDA dimer dissociation in FC-77 and HFE-7500 at 25, 35, and 45 °C: (A) the titration of PFDA (5.00 mM in FC-77) into FC-77; (B) the titration of PFDA (10.00 mM in HFE-7500) into HFE-7500. Data points represent the averages between two duplicate experiments, and error bars represent standard error of the mean.

Table 5-1. Thermodynamic parameters of PFDA dimer formation obtained from fitting ITC titration curves. Data represents the average between two duplicate experiments, and errors are standard error of the mean.

#	T (°C)	Solvent	K_a (M^{-1})	ΔG° (kJ/mol)	ΔH° (kJ/mol)	$-T\Delta S^\circ$ (kJ/mol)
1	25	FC-77 ^a	586 ± 28	-15.79 ± 0.12	-34.19 ± 0.11	18.40 ± 0.16
2		HFE-7500 ^b	99 ± 5	-11.37 ± 0.29	-30.98 ± 0.15	19.61 ± 0.33
3	35	FC-77 ^a	484 ± 30	-15.83 ± 0.16	-42.28 ± 0.13	26.45 ± 0.21
4		HFE-7500 ^b	82 ± 3	-11.28 ± 0.35	-33.58 ± 0.49	22.30 ± 0.60
5	45	FC-77 ^a	323 ± 2	-15.28 ± 0.02	-44.48 ± 0.32	29.20 ± 0.32
6		HFE-7500 ^b	72 ± 3	-11.31 ± 0.42	-41.62 ± 0.96	30.31 ± 1.05

^a The titration of PFDA (5.00 mM in FC-77) into FC-77; ^b the titration of PFDA (10.00 mM in HFE-7500) into HFE-7500.

5.3.2 Thermodynamics of PFDA-quinazoline Complex Formations in FC-77, HFE-7500, and 1-chloropentane

The ITC titrations of PFDA with quinazoline in FC-77, HFE-7500, and 1-chloropentane at 25, 35 and 45 °C are shown in **Figure 5-3**. The ITC profiles indicate the presence of multiple equilibria in FC-77 and HFE-7500, corresponding to the formation of 1:1 and 2:1 complexes; while the experimental curves indicate the formation of 1:1 complex only in 1-chloropentane. The corresponding thermodynamic parameters and equilibrium constants are listed in **Table 5-2**.

The formation of 1:1 complex is enthalpically more favorable in FC-77, followed by HFE-7500, and 1-chloropentane. An opposite trend was observed for the entropic contribution. **Figure 5-4** plots the free energy as well as the enthalpic and entropic contributions of 1:1 complex formation in the three solvents. There is strong entropy-enthalpy compensation at three temperatures. At each temperature, the formation constant of 1:1 complex decreases as the dipolarity/polarizability of the solvent (π^*) increases. Typically, the contribution of the entropy change to the free energy parallels the enthalpy change because the stronger the hydrogen bonding between the acid and the base, the lower the complex's entropy will be when formed.²¹⁶ Our experimental observations in FC-77 and HFE-7500 agree well with this rationale: the change in entropy is more unfavorable in FC-77 as the complex formation is enthalpically more favorable. However, interestingly, the formation of the 1:1 complex in the relatively strong solvent—1-chloropentane ($\pi^* = 0.450$)—is both enthalpically and entropically favorable. The base, quinazoline, and the carboxylic acid group are better solvated in 1-chloropentane than in the other two fluorinated solvents. The exclusion of 1-chloropentane molecules upon complex formation should result in a positive entropy change because the desolvation of the carboxylic acid provides greater solvent freedom than that lost in solvating the hydrogen bonded complex.

Similar behaviors have been reported for the complex formation of picric acid and *n*-butylamine in chlorobenzene and benzene.²¹⁶ The contrasting behavior of the fluoruous systems verifies the poor solvating ability of the fluoruous solvents – fluoruous solvent molecules are not as anisotropically structured as the organic solvent molecules around the PFDA monomer and quinazoline. Therefore, the solvation contributes less to the entropy change of the complex formation in fluoruous solvents. In all three solvents, the ΔH° accompanying 1:1 complex formation becomes more negative as the temperature increases, leading to a negative change of heat capacity. This is due to different solvation strength of the 1:1 complex and its precursors (free PFDA and quinazoline). Compared to a 1:1 complex, the more polar PFDA and quinazoline have stronger interaction with solvent molecules and require solvation more than the 1:1 complex. Therefore, the weakening of solvation is more significant for PFDA and quinazoline than for the 1:1 complex as temperature increases.

Earlier spectroscopic studies only showed 1:1 complex formation between Krytox 157 FSH and quinazoline in FC-72 (perfluorohexanes).⁶³ The current work shows that PFDA and quinazoline in fact form 2:1 complexes in FC-77 and HFE-7500. The interaction between the second PFDA and the 1:1 complex is enthalpically favorable and entropically unfavorable. In FC-77, the ΔH° of 2:1 complex formation from two components (1:1 complex and an acid) becomes more negative as the temperature increases, resulting in a negative change of heat capacity (ΔC_p). This can be explained by different solvation behaviors of the 2:1 complex and the two components, which is similar to the above discussion on the 1:1 complex formation dependence on temperature. Compared to a 2:1 complex, a 1:1 complex (hydrogen bond acceptor) and a PFDA (hydrogen bond donor) cumulatively display stronger interaction with the surrounding FC-77 molecules. As temperature increases, the weakening of solvation is more

significant for the H-bond donor and acceptor than for the 2:1 complex, leading to a negative ΔC_p . It is worth mentioning that the complex formation in FC-77 is the most temperature dependent of all three systems. Complex formation becomes less favorable in FC-77 with increasing temperature while it is about constant in HFE-7500 and 1-chloropentane. As a result, 2:1 complex was observed at 45 °C in HFE-7500 but not in FC-77. In HFE-7500, the enthalpy change for 2:1 complex formation is less negative compared to that in FC-77, and the change of heat capacity ΔC_p is close to zero. This could be due to stronger solvation ability of HFE-7500 compared to FC-77. As temperature increases, the difference on weakening of solvation between the two components (1:1 complex and an acid) and the 2:1 complex is less significant in HFE-7500. In 1-chloropentane, which is a stronger solvent than HFE-7500, 2:1 complex was not observed via ITC.

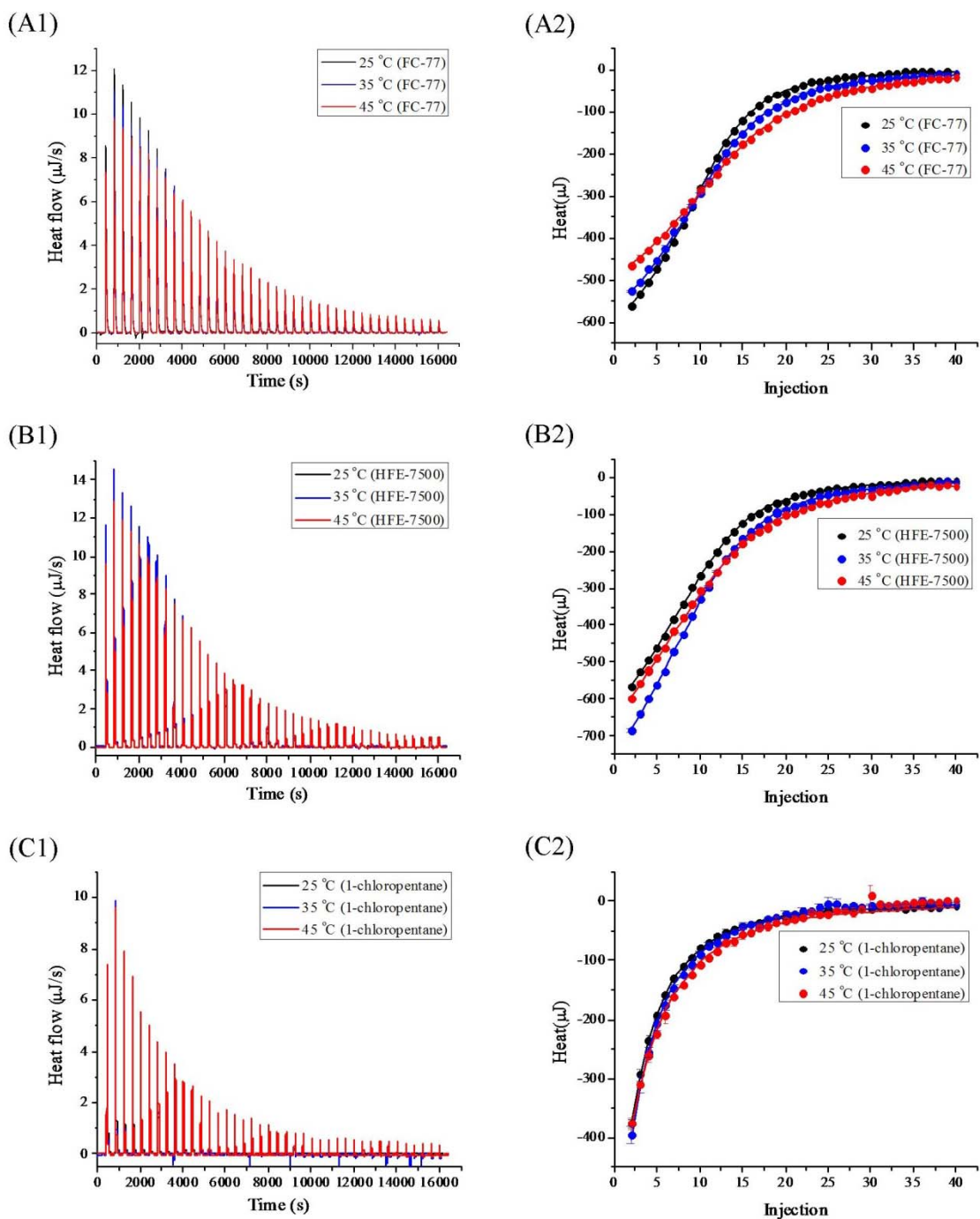


Figure 5-3. ITC profile of PFDA and quinazoline complex formations in FC-77, HFE-7500, and 1-chloropentane at 25, 35, and 45 °C: (A) the titration of quinazoline (4.00 mM in FC-77) into PFDA (0.2 mM in FC-77); (B) the titration of quinazoline (5.00 mM in HFE-7500) into PFDA (0.25 mM in HFE-7500); (C) the titration of quinazoline (60.0 mM in 1-chloropentane) into PFDA (0.40 mM in 1-chloropentane). Data points represent the averages between duplicate experiments, and error bars represent standard error of the mean.

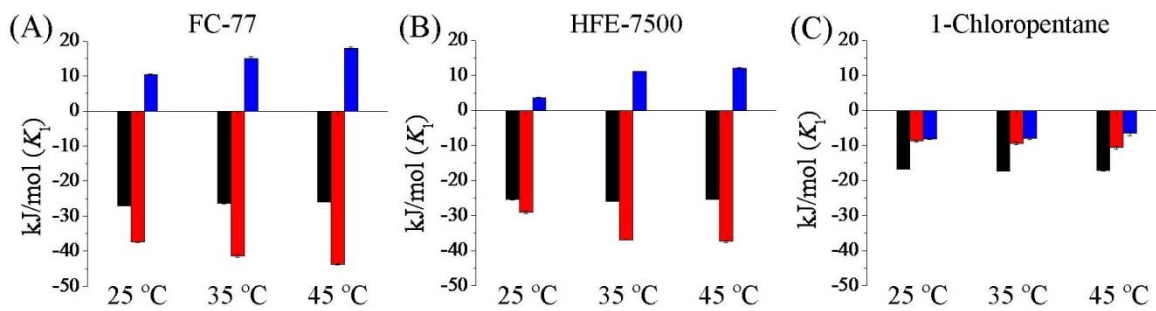


Figure 5-4. Enthalpy-entropy compensation of 1:1 complex between PFDA and quinazoline (black bars: ΔG° ; red bars: ΔH° ; blue bars: $-T\Delta S^\circ$).

Table 5-2. Thermodynamic parameters of PFDA:quinazoline complex formation obtained from fitting ITC titration curves. Data represents the average of duplicate experiments, and errors are standard error of the mean.

#	T (°C)	Solvent	K_1 (M ⁻¹)	ΔG_1° (kJ/mol)	ΔH_1° (kJ/mol)	$-T\Delta S_1^\circ$ (kJ/mol)	K_2 (M ⁻¹)	ΔG_2° (kJ/mol)	ΔH_2° (kJ/mol)	$-T\Delta S_2^\circ$ (kJ/mol)
1	25	FC-77 ^a	53400 ± 400	-29.23 ± 0.02	-37.42 ± 0.15	8.19 ± 0.15	1220 ± 20	-19.08 ± 0.04	-51.42 ± 2.11	32.34 ± 2.11
2		HFE-7500 ^b	29200 ± 400	-27.61 ± 0.04	-28.99 ± 0.33	1.38 ± 0.33	1135 ± 85	-18.89 ± 0.20	-29.95 ± 2.31	11.06 ± 2.32
3		1-chloropentane ^c	874 ± 21	-18.19 ± 0.06	-8.75 ± 0.29	-9.44 ± 0.30	N/A			
4	35	FC-77 ^a	29750 ± 850	-28.52 ± 0.08	-41.35 ± 0.47	12.83 ± 0.48	560 ± 150	-17.52 ± 0.74	-64.85 ± 13.11	47.33 ± 13.13
5		HFE-7500 ^b	24400 ± 700	-27.97 ± 0.08	-36.91 ± 0.10	8.94 ± 0.13	1140 ± 160	-19.49 ± 0.39	-28.79 ± 5.22	9.30 ± 5.23
6		1-chloropentane ^c	853 ± 9	-18.68 ± 0.03	-9.37 ± 0.37	-9.31 ± 0.37	N/A			
7	45	FC-77 ^a	17700 ± 100	-27.89 ± 0.02	-43.81 ± 0.22	15.92 ± 0.22	N/A			
8		HFE-7500 ^b	14813 ± 63	-27.39 ± 0.01	-37.35 ± 0.30	9.96 ± 0.30	672 ± 2	-18.57 ± 0.01	-26.8 ± 0.87	8.23 ± 0.87
9		1-chloropentane ^c	653 ± 28	-18.48 ± 0.12	-10.58 ± 0.47	-7.90 ± 0.49	N/A			

^a the titration of quinazoline (4.00 mM) into PFDA (0.20 mM); ^b the titration of quinazoline (5.00 mM) into PFDA (0.25 mM); ^c the titration of quinazoline (60.00 mM) into PFDA (0.40 mM).

5.3.3 Thermodynamics of PFDA-pyridine Complex Formation in FC-77, HFE-7500, and 1-Chloropentane

The ITC titrations of PFDA with pyridine in FC-77, HFE-7500, and 1-chloropentane at 25, 35 and 45 °C are shown in **Figure 5-5**. In FC-77, PFDA interacts with pyridine and forms 1:1, 2:1, and 3:1 complexes. In HFE-7500 and 1-chloropentane, the experimental curves indicate the formation of 1:1 and 2:1 complexes. The thermodynamic parameters and equilibrium constants are listed in **Table 5-3**.

Similar to the PFDA/quinazoline system, the formation of a 1:1 complex between PFDA and pyridine is enthalpically more favorable in FC-77, followed by HFE-7500, and 1-chloropentane at all temperatures. The calorimetric data show a strong enthalpy-entropy compensation (**Figure 5-6**) that leads to almost constant free energy in HFE-7500 and 1-chloropentane at different temperatures (**Table 5-3**). In contrast, the binding affinity of the 1:1 complex in FC-77 shows a significant temperature dependence—the binding constant decreases along with the increase of the temperature (**Table 5-3**). In FC-77 and HFE-7500, the entropy change for 1:1 complex formation is unfavorable. The entropy change is more negative in FC-77 as the 1:1 complex is enthalpically more favorable. In 1-chloropentane, 1:1 complex formation between PFDA and pyridine demonstrates a positive entropic change, which is similar to our previous observation in the PFDA/quinazoline system and can be attributed to the relatively stronger solvation of 1-chloropentane to individual species than the complex thus the exclusion of solvent molecules upon the complex formation. In all three solvents we investigated, a second molecule of PFDA can form a hydrogen bond with the 1:1 complex to yield a 2:1 complex. The 2:1 complex formation is enthalpically favorable. However, the favorable enthalpy is opposed by

a strong unfavorable entropy change of binding due to the structural rigidity in the presence of multiple hydrogen bonds. Overall, the formation constant of the 2:1 complex in each solvent is one to two orders of magnitude smaller than that of 1:1 complex. Interestingly, the free energy for the formation of 2:1 complex (from 1:1 complex and PFDA) is more negative than that of the PFDA dimerization. This could be attributed to weaker solvation of the 1:1 complex compared to a PFDA, leading to a more favorable free energy when forming the 2:1 complex.

In addition to 1:1 and 2:1 complexes, PFDA interacts with pyridine to form a 3:1 complex in the perfluorinated solvent, FC-77. The thermodynamic data shows that the formation of the 3:1 complex [PFDA+2:1] is enthalpically *unfavorable* with a large *favorable* entropy that is strong enough to overcome the unfavorable enthalpy. This observation cannot be explained by solely forming more hydrogen bonds, which would yield a favorable enthalpy change and an unfavorable entropy change as observed for the formation of 1:1 and 2:1 complexes. To further understand the nature of complex formations in FC-77, the enthalpy changes for the association of PFDA with pyridine and quinazoline versus temperature are plotted in **Figure 5-7**. The slopes of these lines correspond to the change in heat capacity at constant pressure, ΔC_p . Interestingly, the sign of ΔC_p for 3:1 complex is opposite to that of the 1:1 complexes. As ΔC_p reflects the temperature dependence in enthalpy between the state of solvated components and the state of the solvated complex,²²⁸⁻²³¹ the opposite sign of ΔC_p indicates different solvation behaviors of 1:1 and 3:1 complexes. Compared to the 1:1 complex, pyridine and PFDA have exposed polar groups and stronger interaction with the FC-77 molecules. As temperature increases, the weakening of solvation is more significant for pyridine and PFDA than the 1:1 complex, leading to a negative ΔC_p . For the 3:1 complex formation, a positive ΔC_p indicates that the weakening of solvation as temperature increases is more significant for the 3:1 complex than the precursors

(1:1 complex and two PFDA molecules). This is consistent with the ionic feature of the 3:1 complex observed via spectroscopic methods.⁶³

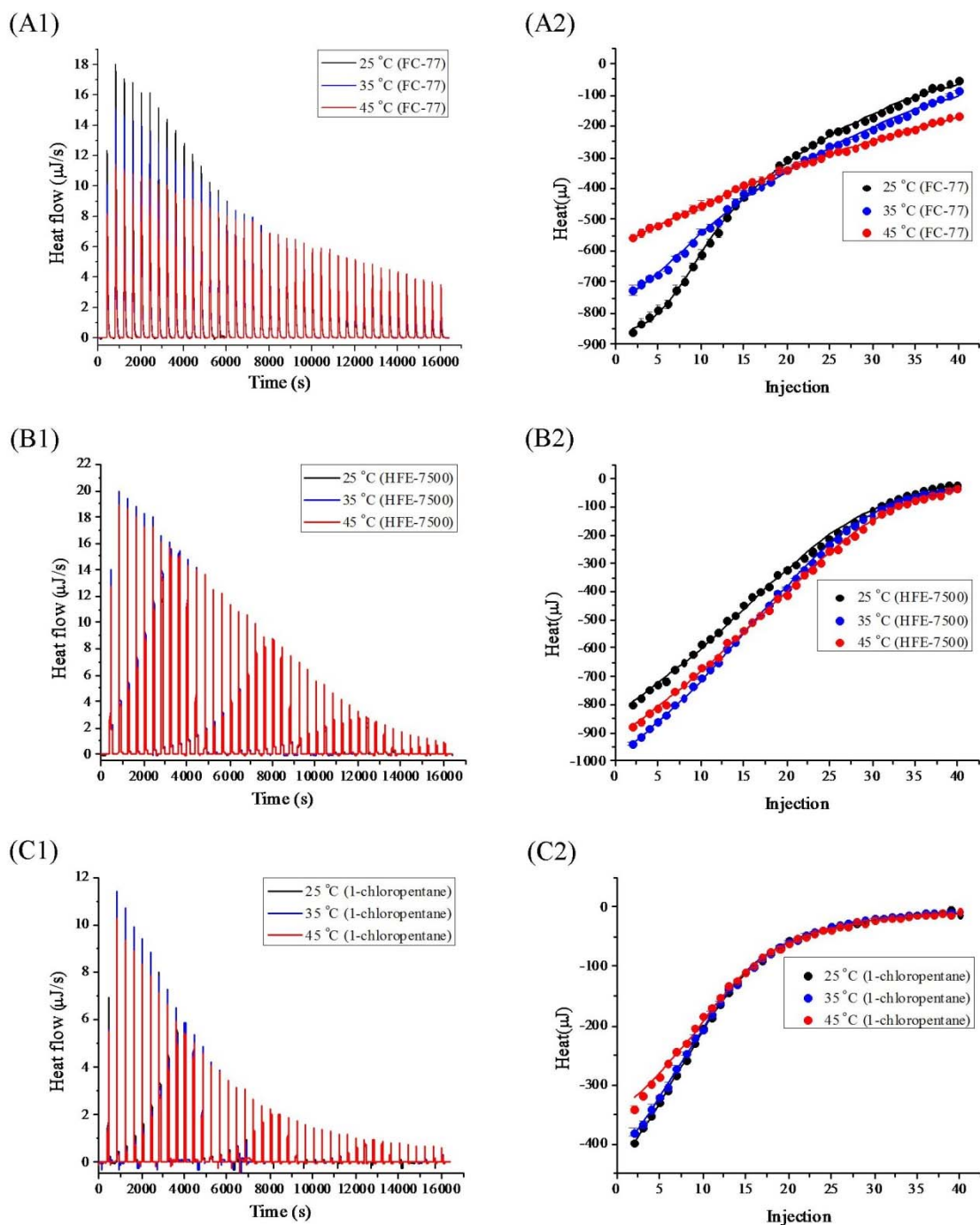


Figure 5-5. ITC profile of PFDA and pyridine complex formations in FC-77, HFE-7500, and 1-chloropentane at 25, 35, and 45 °C: (A) the titration of pyridine (3.00 mM in FC-77) into PFDA (0.4 mM in FC-77); (B) the titration of

pyridine (3.00 mM in HFE-7500) into PFDA (0.4 mM in HFE-7500); (C) the titration of pyridine (5.00 mM in 1-chloropentane) into PFDA (0.25 mM in 1-chloropentane). Data points represent the averages between duplicate experiments, and error bars represent standard error of the mean.

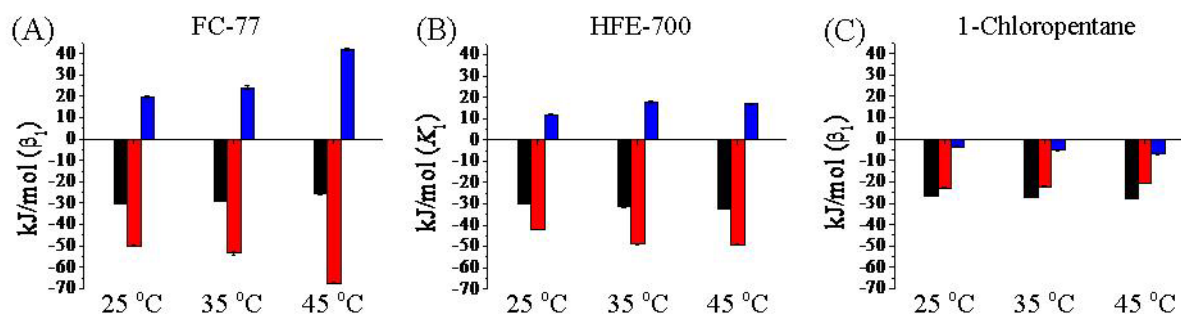


Figure 5-6. Enthalpy-entropy compensation of 1:1 complex between PFDA and pyridine (black bars: ΔG° ; red bars: ΔH° ; blue bars: $-T\Delta S^\circ$).

Table 5-3. Thermodynamic parameters of PFDA and pyridine complex formations obtained from fitting ITC titration curves. Data represents the average between duplicate experiments, and errors are standard error of the mean.

#	T (°C)	Solvent	K_1 (M ⁻¹)	ΔG_1° (kJ/mol)	ΔH_1° (kJ/mol)	$-\Delta S_1^\circ$ (kJ/mol)	K_2 (M ⁻¹)	ΔG_2° (kJ/mol)	ΔH_2° (kJ/mol)	$-\Delta S_2^\circ$ (kJ/mol)	K_3 (M ⁻¹)	ΔG_3° (kJ/mol)	ΔH_3° (kJ/mol)	$-\Delta S_3^\circ$ (kJ/mol)
1	25	FC-77 ^a	86 000±500	-30.51±0.02	-49.96±0.52	19.45±0.52	1 795±5	-20.12±0.01	-70.7±6.84	50.58±6.84	35 500±3500	-28.14±0.26	25.63±6.52	-53.77±6.53
2		HFE-7500 ^a	74 250±250	-30.12±0.01	-41.94±0.15	11.82±0.15	2 013±13	-20.43±0.02	-71.69 ±1.08	51.26±1.08	N/A			
3		1-chloropentane ^b	19 395±665	-26.51±0.09	-22.82±0.29	-3.69±0.30	483±68	-16.60±0.38	-22.11±4.42	5.51±4.44	N/A			
4	35	FC-77 ^a	40 000±0	-29.34±0.00	-53.40±0.84	24.06±0.84	600±40	-17.71±0.18	-68.95±8.02	51.24±8.02	30 050±50	-28.55±0.00	26.41±7.31	-54.96±7.31
5		HFE-7500 ^a	86 750±3750	-31.48±0.12	-48.91±0.46	17.43±0.48	2 313±388	-21.45±0.46	-78.15±8.96	56.70±8.97	N/A			
6		1-chloropentane ^b	19 740±0	-27.38±0.00	-22.17±0.29	-5.21±0.29	470±40	-17.03±0.24	-18.93±4.21	1.90±4.22	N/A			
7	45	FC-77 ^a	8000±700	-25.63±0.25	-67.36±0.34	41.73±0.42	N/A				4050000 ±650000 ^c	-43.39±0.46 ^c	-14.16±1.02 ^c	-28.23±1.12 ^c
8		HFE-7500 ^a	84 750±250	-32.36±0.01	-49.16±0.32	16.80±0.32	1 413±63	-20.68±0.13	-88.72±3.43	68.04±3.43	N/A			
9		1-chloropentane ^b	17 140±230	-27.80±0.04	-20.78±0.08	7.02±0.09	N/A				N/A			

^a the titration of pyridine (3.00 mM) into PFDA (0.40 mM); ^b the titration of pyridine (5.00 mM) into PFDA (0.25 mM); ^c the binding constant and

thermodynamic parameters correspond to $2\text{PFDA} + [\text{PFDA} \cdot \text{Pyridine}] \rightarrow [\text{PFDA}_3 \cdot \text{Pyridine}]$.

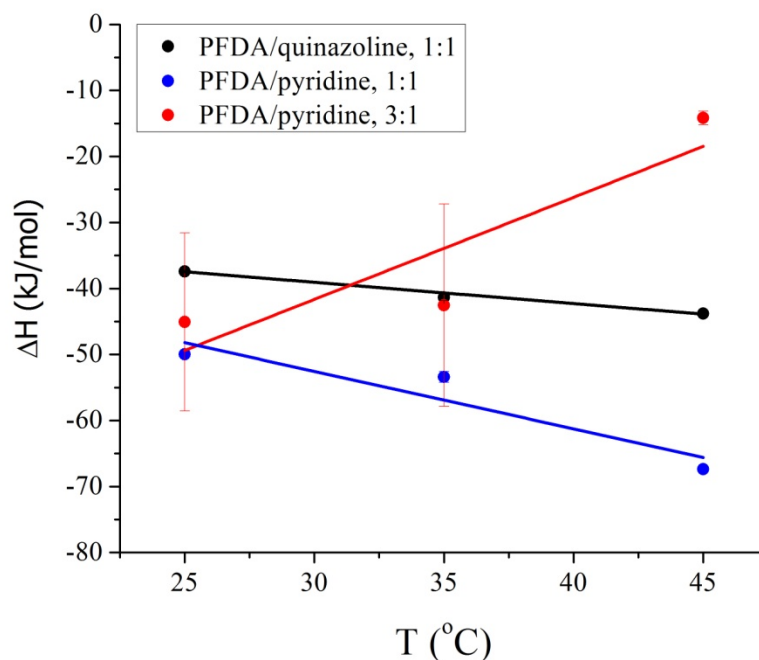


Figure 5-7. Heat capacity changes for association of PFDA with quinazoline/pyridine in FC-77:

- (●) PFDA+quinazoline \rightarrow [PFDA \cdot quinazoline]; (●) PFDA+Pyridine \rightarrow [PFDA \cdot Pyridine];
- (●) 2PFDA+[PFDA \cdot Pyridine] \rightarrow [PFDA₃ \cdot Pyridine].

5.3.4 Discussion

The association of PFDA with both quinazoline and pyridine reveals that the stoichiometry of complex formation strongly depends on the solvent. As shown in **Table 5-4**, the trend of stoichiometry of complex formation goes to high acid:base stoichiometry from 1-chloropentane to HFE-7500 to FC-77. Poor solvent favors the formation of acid-base complexes with multiple acid molecules. This observation is analogous to the complex formation between perfluorinated carboxylic acid and isoquinoline:⁶³ The 1:1 complex forms in more dipolar organic solvents acetonitrile ($\pi^* = 0.75$), chlorobenzene ($\pi^* = 0.71$) and benzene ($\pi^* = 0.59$]. The 1:1 and 2:1

complexes are present in solvents with relatively lower dipolarity [chloroform ($\pi^* = 0.58$), toluene ($\pi^* = 0.54$), butyl chloride ($\pi^* = 0.39$), and carbon tetrachloride ($\pi^* = 0.28$)]. A 3:1 complex forms in perfluorohexanes [FC-72 ($\pi^* = -0.41$)].⁶³ An enthalpy-entropy compensation plot (ΔH versus ΔS) for the binding of PFDA with quinazoline/pyridine (1:1, 2:1, and 3:1 complexes) in three solvents at different temperatures is shown in **Figure 5-8**. The linearity of the data ($R^2 = 0.93$) presented in this figure displays a close compensation of enthalpy and entropy.

Table 5-4. Stoichiometry of complex formation between PFDA and quinazoline/pyridine.

#	Base	Solvent	π^*	Complex Stoichiometry PFDA:Quinazoline/Pyridine
1	Quinazoline ($pK_a = 3.4$)	FC-77	-0.277	1:1/2:1
2		HFE-7500	0.222	1:1/2:1
3		1-chloropentane	0.450	1:1
4	Pyridine ($pK_a = 5.2$)	FC-77	-0.277	1:1/2:1/3:1 (ionic)
5		HFE-7500	0.222	1:1/2:1
6		1-chloropentane	0.450	1:1/2:1

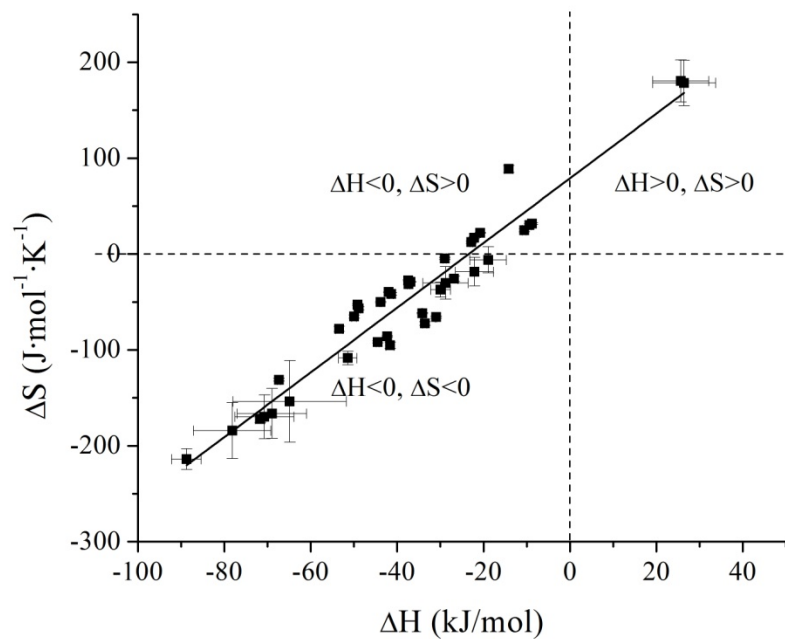


Figure 5-8. Enthalpy-entropy compensation of complex formation between PFDA and quinazoline/pyridine.

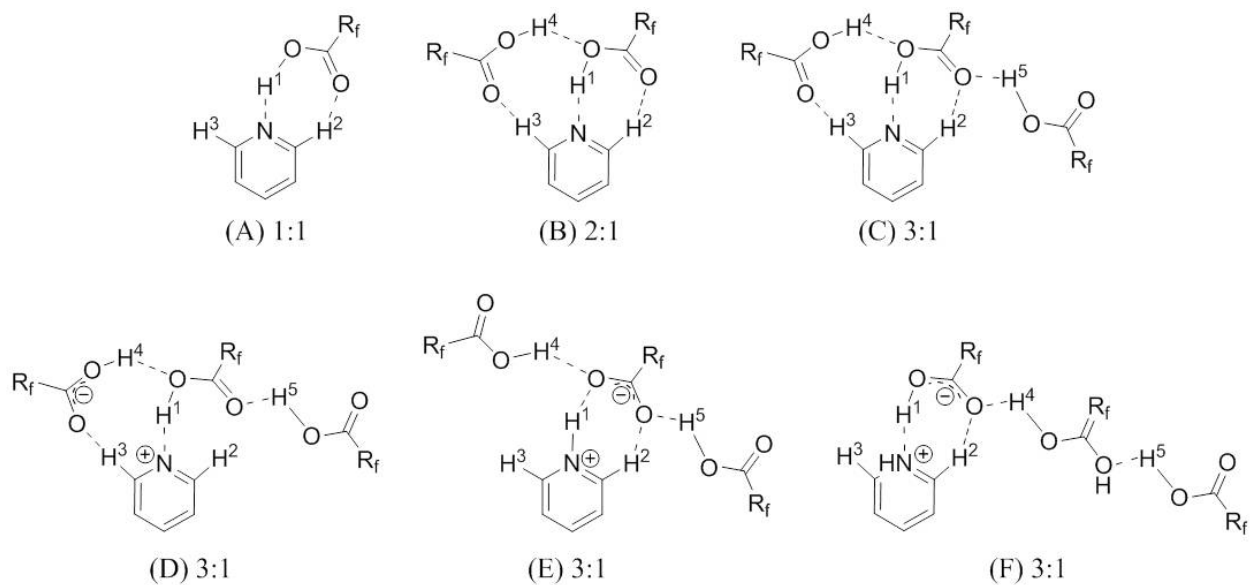


Figure 5-9. Schematic structure of PFDA/pyridine complexes: (A) 1:1; (B) 2:1; (C) 3:1; (D) 3:1; (E) 3:1; (F) 3:1.

The interaction of PFDA with pyridine is a system of most interesting and complex phenomena. **Figure 5-9** shows the structure of PFDA/pyridine 1:1 complex (A, crystal structure as reported by O'Neal and coworkers)⁶², a proposed structure of PFDA/pyridine 2:1 complex (B) according to the crystal structure of carboxylic acid-pyridine complex from organic solvents reported by Balevicius and coworkers,²³² and a proposed structure of PFDA/pyridine 3:1 complex (C) according to the structure of PFDA/pyridine 2:1 complex as well as the structure of Krytox 157FSH/pyridine 3:1 complex as suggested by O'Neal and coworkers.⁶² The formation of two hydrogen bonds (relatively strong $N\cdots H^1-O$, and weak $C-H^2\cdots O$)²³³ and the cyclic structure in the 1:1 complex leads to a favorable enthalpy change and unfavorable entropy change to the free energy. The joining of the second PFDA yields two more hydrogen bonds ($O-H^4\cdots O$, and $C-H^3\cdots O$) and a fused cyclic structure, leading to enthalpy gain but significant loss in entropy. The electron density on the oxygens of the first PFDA decreases when an oxygen forms hydrogen bond with H^4 in the second PFDA, which can lead to a shift of H^1 towards pyridine. The third PFDA, upon joining the 2:1 complex, serves as a hydrogen bonding donor and leads to a further decrease of electron density at oxygens in the hydrogen-bonded relay "chain".²³⁴ Further decrease of the electron density at the oxygen in the $O-H\cdots N$ bond can cause more shift of H^1 towards pyridine and lead to proton transfer.

ITC data suggested that PFDA/pyridine 3:1 complex formation from the 2:1 complex is enthalpically unfavorable and entropically favorable; which is not consistent with the proposed structure (C). This structure would be consistent with a moderate negative enthalpy change due to the hydrogen bond formation ($O-H^5\cdots O$) and a negative entropy change due to the decrease of freedom upon the joining of the third acid. It is worth pointing out that as the electron density at oxygens in the hydrogen-bonded relay "chain" decreases, the oxygens on the carbonyl groups

become weaker hydrogen bond acceptors.²³⁵ Therefore, the weak C–H^{2/3}···O bonds will be weakened and thus broken upon the joining of the third PFDA. **Figure 5-9 (D–F)** show the potential configurations of PFDA/pyridine 3:1 complex (with one C–H···O bond broken), which are consistent with Bene’s theoretical study on the structures of HF/trimethylpyridine 3:1 complexes – the site of interaction between trimethylpyridine and acid occurs at the terminal and the middle of the relay “chain”.²³⁶ An increase in the number of structural configurations as well as the disruption of a hydrogen-bonded ring structure existing in the 2:1 complex together lead to an increase in the configurational entropy and thus a favorable contribution for the free energy. Further break down of the second C–H···O is also possible. Breaking of C–H···O hydrogen bond(s) as well as the increased exposure of carboxylic acid functional groups to solvent (in comparison to the conversion of acid + 1:1 to 2:1 complex) explains our observation of slightly positive enthalpy change from 2:1 complex to 3:1 complex even though a new O–H···O is created upon the joining of the third PFDA. From the acidity perspective, an acid trimer, in the relay “chain” structure, has a free carboxylic acid group which is not stabilized by hydrogen bonding. This makes the acid trimer a stronger acid than the acid dimer in which both carboxylic acid groups are stabilized in the cyclic hydrogen bonded structure.

Previous spectroscopic studies demonstrated proton transfer from acid to pyridine when acid was in excess. Golubev and coworkers investigated the complex formation between acetic acid and pyridine (solvent: a mixture of CDClF₂ and CDF₃¹³) at 109K via NMR. They found out that the hydrogen on carboxylic acid group is gradually shifted from acetic acid to pyridine upon the formation of complexes with more acid molecules.²³⁴ In a pioneer work focusing on hydrogen bonding based noncovalent interaction in fluorine media, O’Neal and coworkers discovered the formation of 3:1 complex between Krytox 157FSH and pyridine in

perfluorohexanes at room temperature.⁶² UV/Vis and IR studies showed proton transfer in Krytox 157FSH/pyridine 3:1 complex.^{62,63} There are still many questions left unanswered: Is the complex formation a stepwise process? Does the proton transfer occur at certain step? With this view, we have now revealed the stepwise complex formation between PFDA and pyridine, rationalized a gradual shift of the hydrogen from PFDA to pyridine,²³⁴ and identified that the structure rearrangement accompanying proton transfer occurs not until the joining of the third PFDA. Among the three solvents we investigated, PFDA/pyridine 3:1 complex has been observed only in FC-77 which has the lowest dipolarity. One driving force to the formation of the 3:1 complex from the 2:1 complex is the poor solvation of the PFDA by FC-77. Interestingly, the joining of the third PFDA leads to stabilized 3:1 complex with ionic property in the highly nonpolar solvent.

5.4 CONCLUSION

Noncovalent associations behave markedly different in solvents with different dipolarity/polarizability (π^*). For hydrogen bond based complexes, both the strength of the hydrogen bonding interactions and the solvation property contribute to the overall free energy of complex formations. With the calorimetric method, our study on the dimerization of PFDA indicates that the dimer formation constant increases in poorer solvent. The formation of complexes between PFDA and quinazoline/pyridine is generally preferred in a poor solvent. Solvents with lower π^* promotes the formation of complexes containing more than one PFDA. The thermodynamic data (ΔH° , ΔS° , and ΔC_p) reveals a stepwise complex formation process, supports our previous report on proton transfer in 3:1 complex (Krytox 157FSH/pyridine) by

spectroscopic methods, and identified that proton transfer occurs only upon the joining of the third PFDA.

Results from this work reveal the first example of quantitative thermodynamic study of hydrogen-bond based sequential complex formations in fluororous media. The free energy of complex formation between an organic base and a perfluorinated acid can serve as the driving force to transfer the polar organic base from organic/aqueous phase into the notoriously poor fluororous media. Based on the experimentally determined binding affinities, 10 mM of PFDA in FC-77 can enhance the extraction of pyridine at low concentrations by more than 10^5 times compared to partitioning into FC-77 alone. The ability of forming complexes containing different number of acid molecules provides binding selectivity to certain targets. For example, 10 mM of PFDA in FC-77 is more than 200 times selective for pyridine than quinazoline due to their different binding affinities with PFDA. Our work suggests the possibility of rationally creating/optimizing fluororous media embedded with fluororous molecular receptors for extraction and sensing applications.

5.5 ACKNOWLEDGEMENT

We thank the National Science Foundation for support through grant CHE-0957038.

6.0 SUMMARY AND FUTURE DIRECTIONS

Fluoropolymers represent prospective fluoruous media for partitioning and molecular recognition based separations and sensing. We developed three types of Teflon AF 2400 composite films: Teflon AF 2400/FC-70, Teflon AF 2400/fluorophilic silica nanoparticles, and Teflon AF 2400/FNP/FC-70. Teflon AF 2400 composite films show different transport behaviors for the selective transport of fluorinated molecules against their hydrocarbon counterparts. Doping FC-70 in Teflon AF 2400 decreases the sorption of organic solvent (CHCl_3) in Teflon AF 2400, restores the fluorophilicity of the film, and leads to an increase of transport selectivity (octafluorotoluene over toluene). Teflon AF 2400/FNP composites containing ≥ 50 wt% FNP show significant increase of free volume and sorption of CHCl_3 , increased solute permeability, and decreased transport selectivity (octafluorotoluene over toluene). Teflon AF 2400/FNP/FC-70 composites represent a novel type of composite film: the soft Teflon AF 2400/FC-70 phase which is not dimensionally stable by itself is well supported by the FNPs. The Teflon AF 2400/FC-70 phase in the three-component films shows low CHCl_3 sorption, and high solute permeability as well as transport selectivity (octafluorotoluene over toluene). Porous Teflon AF 2400 films made from Teflon AF 2400/FNP films show potential applications in separations, template assisted synthesis, and microarrays.

Molecular recognition based extractions are highly selective in fluoruous media because molecular interactions can be strengthened in fluorocarbons while the partitioning of

interferences is minimized. We investigated the association of perfluorodecanoic acid (PFDA) with pyridine and quinazoline (separately via isothermal titration calorimetry (ITC) to gain quantitative understanding of noncovalent interactions in fluorous media. Thermodynamic data suggests stronger noncovalent interaction in perfluorinated solvent than that in semi-fluorinated and organic solvents. A poor solvent prefers the formation of complexes with acid:base stoichiometry greater than 1:1. PFDA and pyridine form 3:1 complex in FC-77, and proton transfer in [PFDA₃·pyridine] occurs upon the joining of the third acid. The free energy of complex formation between organic compounds and perfluorinated molecular receptors can serve as the driving force to improve molecular receptor-based extraction and sensing in fluorous media.

The physical properties as well as transport behavior of Teflon AF 2400 films suggest that fluorophilic silica nanoparticles (120 nm) effectively disrupt the packing of Teflon AF 2400 polymeric chains. As the radius of gyration of Teflon AF 2400 in FC-77 is 23 nm, a worthwhile goal now within reach is to study composite materials containing fluorophilic silica nanoparticles with different sizes (smaller than and comparable to the radius of gyration of Teflon AF 2400) to reveal the size effect to the morphology and transport properties. In a view of the future, the application of molecular receptor doped Teflon AF 2400/FNP/FC-70 films and Teflon AF 2400 films containing nanoparticles with dual functional modifications (fluorocarbon and molecular receptor modifications) would certainly benefit selective transport and sensing.

APPENDIX A

3.0 PROPERTIES AND TRANSPORT BEHAVIOR OF TEFLON AF 2400 NANOCOMPOSITE FILMS

This Appendix contains supporting information for section 3.0 Properties and transport behavior of Teflon AF 2400 nanocomposite films. It contains density analysis of Teflon AF/FNP/FC-70 films (**Table A-1**) as well as Figures showing: (**Figure A-1 to A-5**)

Table A-1. Density analysis of Teflon AF/FNP/FC-70 films (70 wt% FNP)

Teflon AF (wt%)	FC-70 (wt%)	Film density (g/cm ³)	Shell density ¹ (g/cm ³)	Shell thickness (nm)
0	0	1.761±0.007	-	-
25	5	1.875±0.009	2.023	8.3
20	10	1.863±0.010	1.992	8.4
15	15	1.818±0.010	1.981	8.4
10	20	1.878±0.014	1.970	8.5

¹Density of Teflon/FC-70 materials are estimated from Chapter 2 (**Figure 2-4**).

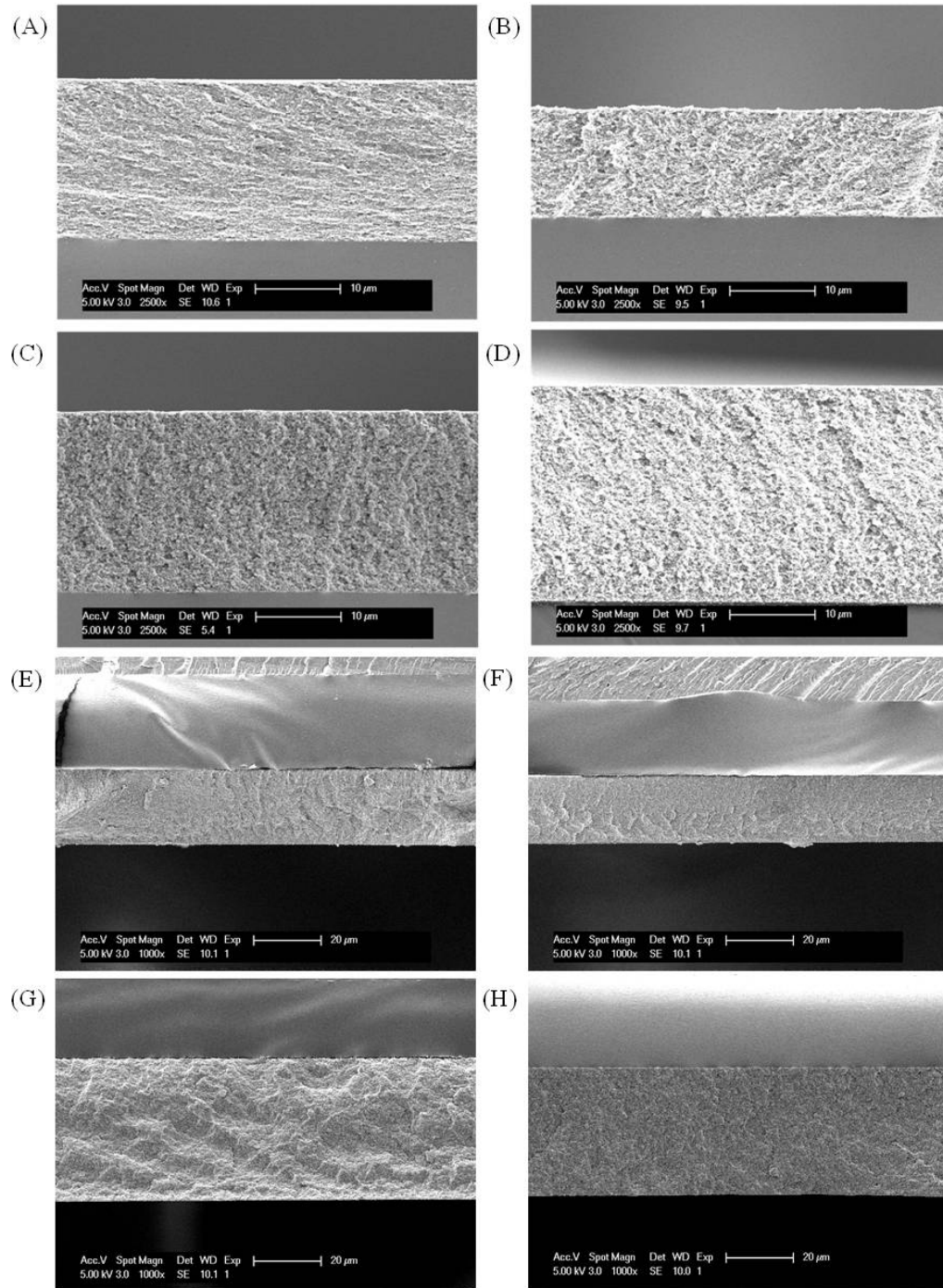


Figure A-1. Low magnification cross-sectional SEM images of Teflon AF 2400 films containing various weight percentages of FNP and FC-70: (A) 15 wt% (12 v%) FNPs; (B) 30 wt% (25 v%) FNPs; (C) 50 wt% (40 v%) FNPs; (D) 70 wt% (53 v%) FNPs; (E) 70 wt% FNPs and 5 wt% FC-70; (F) 70 wt% FNPs and 10 wt% FC-70; (G) 70 wt% FNPs and 15 wt% FC-70; (H) 70 wt% FNPs and 20 wt% FC-70.

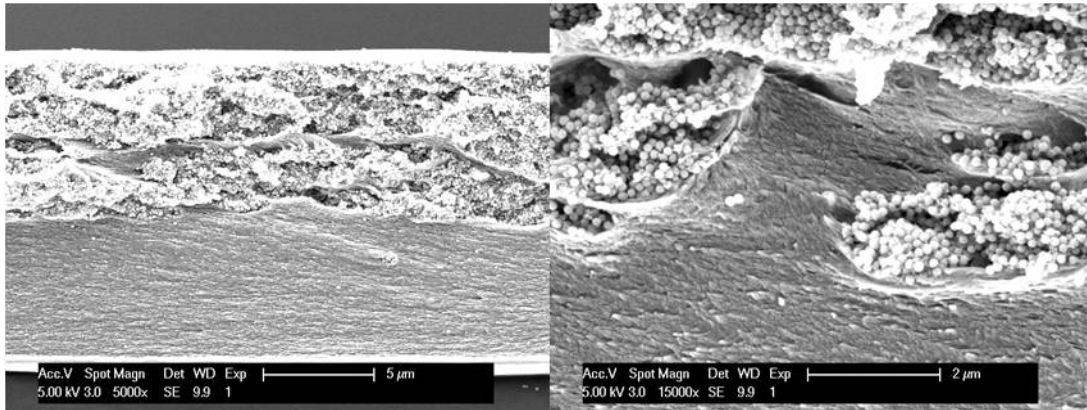


Figure A-2. Cross-sectional SEM images of a Teflon AF 2400 film containing 15 wt% (12 v%) octylsilane modified silica nanoparticles. The top side shown in the images corresponds to the bottom surface that contacts the glass Petri dish during film preparation while the bottom in the image is the surface contacting air in the thin film casting process.

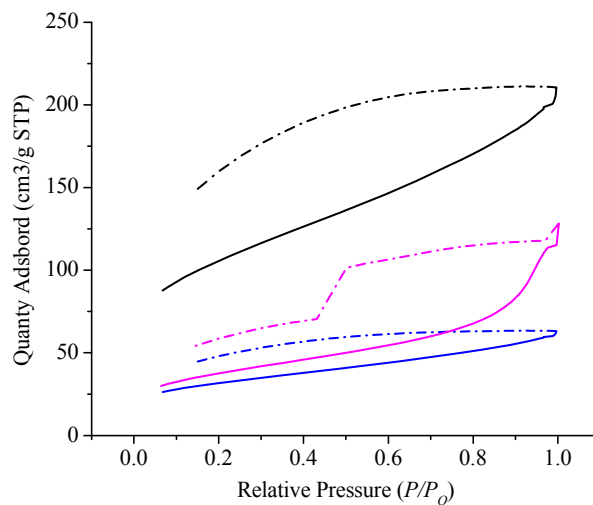


Figure A-3. Isotherm plot of pure Teflon AF 2400 (black lines), and 70 wt% FNP doped Teflon AF 2400 (magenta lines). For better comparison, the blue lines represent the 30% of the adsorbed quantity in pure Teflon AF 2400. Solid lines represent adsorption process and dashed lines represent the desorption process.

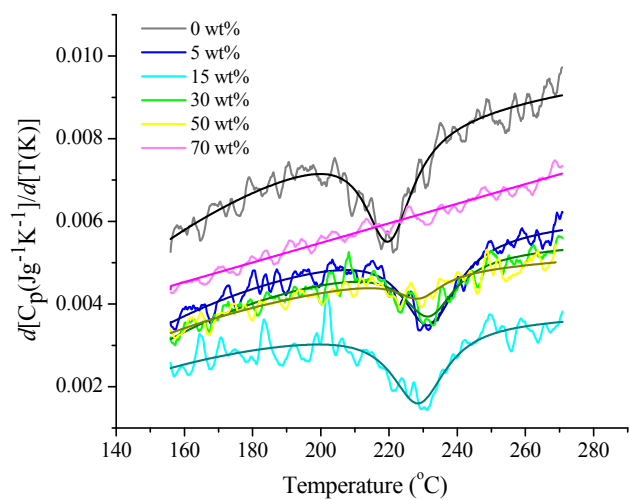


Figure A-4. Temperature derivative of heat capacity of FNP doped Teflon AF films. The noisy lines represent the experimental data and smooth lines are the best fit by PeakFit.

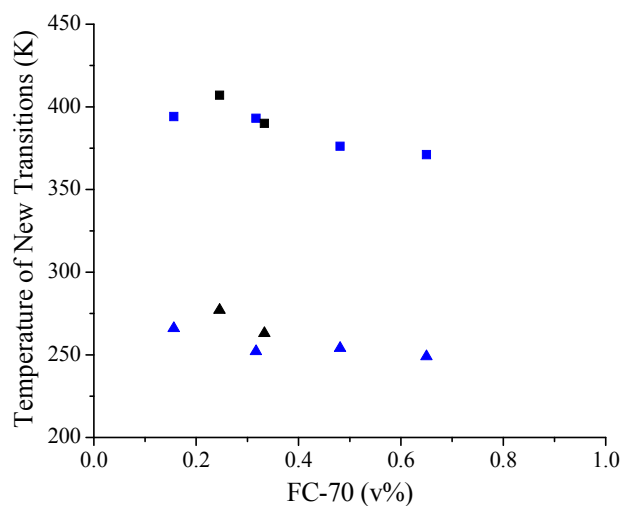


Figure A-5. New transition temperatures of Teflon AF/FC-70 system. Blue data points are from three-component films (the volume percent axis excludes the volume of FNPs). Black data points are from Chapter 2 (page 42, line 8).¹³⁷

APPENDIX B

5.0 ISOTHERMAL TITRATION CALORIMETRY OF PERFLUORODECANOIC ACID WITH PYRIDINE AND QUINAZOLINE IN AN ORGANIC, A SEMI-FLUORINATED, AND A PERFLUORINATED SOLVENT

This Appendix contains supporting information for section 5.0 Isothermal Titration Calorimetry to Determine Thermodynamics of Non-covalent Interaction in Fluorous Media.

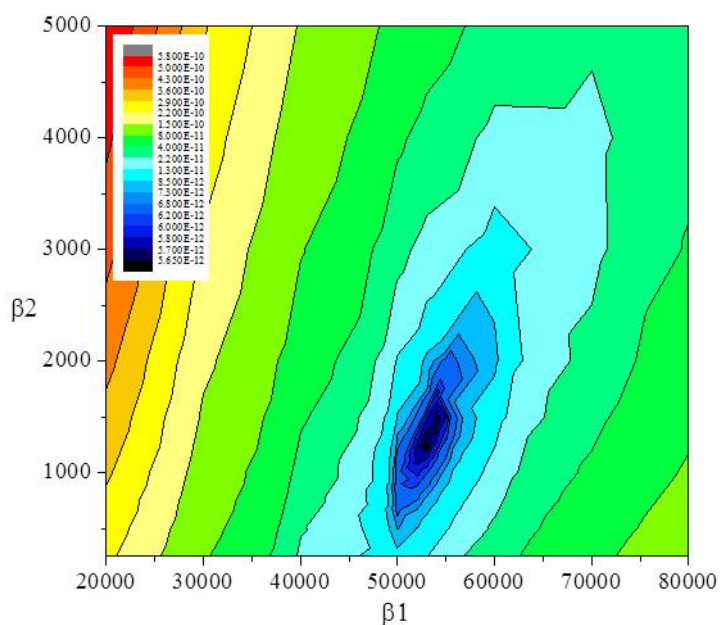


Figure B-1. Contour map for the titration of PFDA with quinazoline in FC-77 at 25 °C. The best fit corresponds to $\beta_1=53000$; $\beta_2=1240$.

Appendix B-2. Data fitting of dimer dissociation by Mathcad

PFDA Dimer Dissociation (FC-77, 25 °C)

data :=

	0	1
0	2	$2.375 \cdot 10^{-4}$
1	3	$2.299 \cdot 10^{-4}$
2	4	$2.196 \cdot 10^{-4}$
3	5	$2.069 \cdot 10^{-4}$
4	6	$1.931 \cdot 10^{-4}$
5	7	$1.83 \cdot 10^{-4}$
6	8	$1.74 \cdot 10^{-4}$
7	9	...

$X := \text{data}^{(0)}$ $Y := \text{data}^{(1)}$

$v1 := 5 \cdot 10^{-6}$ $v := 5 \cdot 10^{-6}$ $V := 950 \cdot 10^{-6}$ $C0 := 5 \cdot 10^{-3}$

$$C(i) := \frac{C0 \cdot v1}{V} \cdot \left(\frac{V-v}{V}\right)^{i-1} - C0 \cdot \left(\frac{V-v}{V}\right)^{i-1} + C0$$

$$q(i, H, k) := \left[\begin{array}{l} H \cdot \left(v \cdot \frac{4C(i) - 4C(i-1) - \sqrt{k^2 + 8C(i) \cdot k} + \sqrt{k^2 + 8C(i-1) \cdot k}}{8} - v \cdot \frac{4C0 - 4C(i-1) - \sqrt{k^2 + 8C0 \cdot k} + \sqrt{k^2 + 8C(i-1) \cdot k}}{8} \right) \\ v \cdot \frac{4C(i) - 4C(i-1) - \sqrt{k^2 + 8C(i) \cdot k} + \sqrt{k^2 + 8C(i-1) \cdot k}}{8} - v \cdot \frac{4C0 - 4C(i-1) - \sqrt{k^2 + 8C0 \cdot k} + \sqrt{k^2 + 8C(i-1) \cdot k}}{8} \\ \frac{H}{8} \cdot \left[v \cdot \left[\left(\frac{-1}{(k^2 + 8C(i-1) \cdot k)^2} \cdot (k + 4C(i-1)) - \frac{-1}{(k^2 + 8C(i) \cdot k)^2} \cdot (k + 4C(i)) \right) \right] - v \cdot \left[\left(\frac{-1}{(k^2 + 8C(i-1) \cdot k)^2} \cdot (k + 4C(i-1)) - \frac{-1}{(k^2 + 8C0 \cdot k)^2} \cdot (k + 4C0) \right) \right] \right] \end{array} \right]$$

$$\text{guess} := \begin{pmatrix} 30000 \\ 0.001 \end{pmatrix}$$

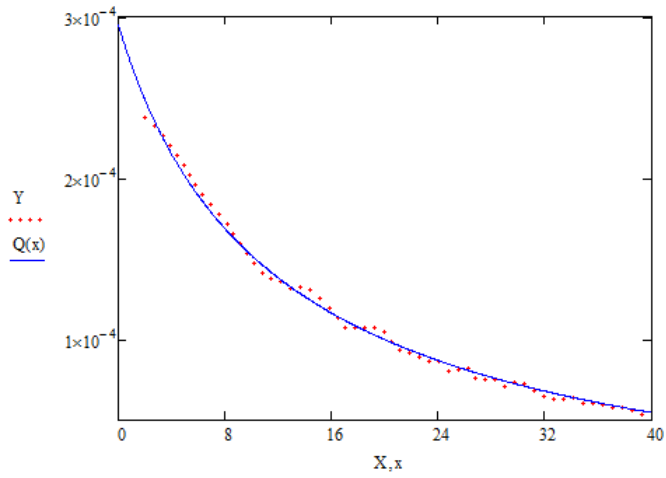
$\text{cg} := \text{genfit}(X, Y, \text{guess}, q)$

$$\text{cg} = \begin{pmatrix} -3.429 \times 10^4 \\ 1.792 \times 10^{-3} \end{pmatrix}$$

$$\text{cg}_0 = -3.429 \times 10^4$$

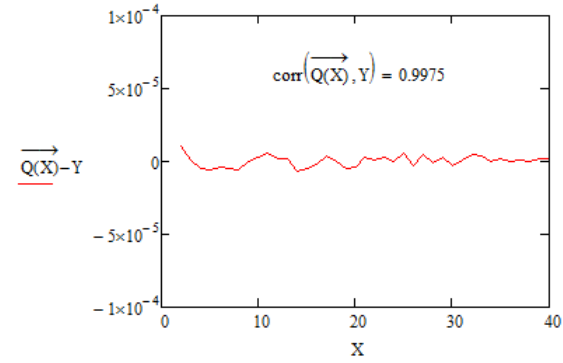
$$\frac{1}{cg_1} = 558.044$$

$$Q(n) := cg_0 \cdot V \cdot \left[\frac{4C(n) - 4C(n-1) - \sqrt{(cg_1)^2 + 8C(n) \cdot cg_1} + \sqrt{(cg_1)^2 + 8C(n-1) \cdot cg_1}}{8} - \frac{4C0 - 4C(n-1) - \sqrt{(cg_1)^2 + 8C0 \cdot cg_1} + \sqrt{(cg_1)^2 + 8C(n-1) \cdot cg_1}}{8} \right]$$



$$\max(\overrightarrow{Q(X)} - Y) = 1.097 \times 10^{-5}$$

$$\min(\overrightarrow{Q(X)} - Y) = \bullet$$



+

Appendix B-3. Data fitting of the system containing 2:1 complex, 1:1 complex, and acid dimer by Mathcad

1 to 1, 2 to 1, and acid dimer system data fitting (FC-77, PFDA/Quinazoline, 25 °C)

```

a(c,K) :=
  c_A ← c<0>
  c_B ← c<1>
  nrow ← rows(c)
  i ← 0
  β11 ← K0
  β12 ← K1
  K2 ← β11·β12
  Ka ← 586.173
  denom ← 2·Ka·K2
  d4 ← 1
  for i ∈ 0..nrow - 1
    ca ← cAi
    cb ← cBi
    d2 ←  $\frac{\beta_{11} + 2K_a - K_2 \cdot c_a + 2K_2 \cdot c_b}{denom}$ 
    d0 ←  $\frac{c_a}{denom}$ 
    d1 ←  $\frac{1 - \beta_{11} \cdot c_a + \beta_{11} \cdot c_b}{denom}$ 
    d3 ←  $\frac{(\beta_{11} \cdot \beta_{12} + 2 \cdot K_a \cdot \beta_{11})}{denom}$ 
  f(x) ← d4·x4 + d3·x3 + d2·x2 + d1·x + d0
  
```

0.000199158	1.68421E-05
0.000198319	3.36133E-05
0.000197484	5.03139E-05
0.000196653	6.69441E-05
0.000195825	8.35044E-05
0.000195	9.99949E-05
0.000194179	0.000116416
0.000193362	0.000132768
0.000192547	0.000149051
0.000191737	0.000165265
0.000190929	0.000181412
0.000190125	0.00019749
0.000189325	0.000213501
0.000188528	0.000229444
0.000187734	0.00024532
0.000186944	0.000261129
0.000186156	0.000276872
0.000185373	0.000292548
0.000184592	0.000308158
0.000183815	0.000323703
0.000183041	0.000339182
0.00018227	0.000354596
0.000181503	0.000369945
0.000180739	0.000385229
0.000179978	0.00040045
0.00017922	0.000415606

C_{tot} :=

+

```

    outi ← root(f(x), x, 0, ca)
    i ← 1 + i
  out

```

$K := \begin{pmatrix} 5.3 \cdot 10^4 \\ 1240 \end{pmatrix}$

a(C,K) =

	0
0	1.53737·10 ⁻⁴
1	1.40527·10 ⁻⁴
2	1.2766·10 ⁻⁴
3	1.15217·10 ⁻⁴
4	1.03291·10 ⁻⁴
5	9.19863·10 ⁻⁵
6	8.14167·10 ⁻⁵
7	7.16859·10 ⁻⁵
8	6.28811·10 ⁻⁵
9	5.50586·10 ⁻⁵
10	4.82268·10 ⁻⁵
11	4.23473·10 ⁻⁵
12	3.7343·10 ⁻⁵
13	3.31121·10 ⁻⁵
14	2.95445·10 ⁻⁵
15	...

```

0.00018405 0.000450698
0.000177714 0.000445726
0.000176965 0.000460692
0.00017622 0.000475594
0.000175478 0.000490434
0.000174739 0.000505211
0.000174004 0.000519926
0.000173271 0.000534579
0.000172542 0.00054917
0.000171815 0.0005637
0.000171092 0.000578168
0.000170371 0.000592576
0.000169654 0.000606923
0.00016894 0.00062121

```

```

A2(c,K) :=
  cB ← c<1>
  nrow ← rows(c)
  i ← 0
  β11 ← K0
  β12 ← K1
  K2 ← β11·β12
  Ka ← 586.173
  for i ∈ 0..nrow - 1
    outi ← Ka·a(c,K)i·a(c,K)i
    i ← 1 + i
  out

```

	0
0	1.38542·10 ⁻⁵
1	1.15757·10 ⁻⁵
2	9.55289·10 ⁻⁶
3	7.78136·10 ⁻⁶
4	6.25391·10 ⁻⁶
5	4.95989·10 ⁻⁶
6	3.88555·10 ⁻⁶
7	3.01226·10 ⁻⁶
8	2.31775·10 ⁻⁶
9	1.77695·10 ⁻⁶
10	1.36333·10 ⁻⁶
11	1.05118·10 ⁻⁶
12	8.17418·10 ⁻⁷
13	...

A2(C,K)

```

AB(c,K) :=
  cB ← c<1>
  nrow ← rows(c)
  i ← 0
  β11 ← K0
  β12 ← K1
  K2 ← β11·β12
  Ka ← 586.173
  for i ∈ 0..nrow - 1
    outi ←  $\frac{\beta_{11} \cdot a(c,K)_i \cdot c_{B_i}}{1 + \beta_{11} \cdot a(c,K)_i + K_2 \cdot a(c,K)_i \cdot a(c,K)_i}$ 
    i ← 1 + i
  out

```

	0
0	1.28237·10 ⁻⁵
1	2.5688·10 ⁻⁵
2	3.85223·10 ⁻⁵
3	5.12342·10 ⁻⁵
4	6.37074·10 ⁻⁵
5	7.58008·10 ⁻⁵
6	8.73534·10 ⁻⁵
7	9.81944·10 ⁻⁵
8	1.08162·10 ⁻⁴
9	1.17129·10 ⁻⁴
10	1.25023·10 ⁻⁴
11	1.3183·10 ⁻⁴
12	1.37604·10 ⁻⁴
13	...

AB(C,K)

```

A2B(c,K) :=
  cB ← c<1>
  nrow ← rows(c)
  i ← 0
  β11 ← K0
  β12 ← K1
  K2 ← β11·β12
  Ka ← 586.173
  for i ∈ 0..nrow - 1
    outi ←  $\frac{K_2 \cdot a(c,K)_i \cdot a(c,K)_i \cdot c_{B_i}}{1 + \beta_{11} \cdot a(c,K)_i + K_2 \cdot a(c,K)_i \cdot a(c,K)_i}$ 
    i ← 1 + i
  out

```

	0
0	2.44462·10 ⁻⁶
1	4.47624·10 ⁻⁶
2	6.09802·10 ⁻⁶
3	7.31976·10 ⁻⁶
4	8.15971·10 ⁻⁶
5	8.64607·10 ⁻⁶
6	8.81891·10 ⁻⁶
7	8.72855·10 ⁻⁶
8	8.4337·10 ⁻⁶
9	7.99673·10 ⁻⁶
10	7.4765·10 ⁻⁶
11	6.9225·10 ⁻⁶
12	6.37178·10 ⁻⁶
13	...

A2B(C,K)

```

deltaA2(c,K) :=
nrow ← rows(c) - 1
i ← 0
for i ∈ 0..nrow - 1
  outi ← A2(c,K)i+1·0.00095 - A2(c,K)i·0.000946
  i ← 1 + i
out

```

	0
0	-2.10914·10 ⁻⁹
1	-1.87538·10 ⁻⁹
2	-1.64474·10 ⁻⁹
3	-1.41995·10 ⁻⁹
4	-1.20431·10 ⁻⁹
5	-1.00078·10 ⁻⁹
6	-8.14083·10 ⁻¹⁰
7	-6.4774·10 ⁻¹⁰
8	-5.04486·10 ⁻¹⁰
9	-3.85827·10 ⁻¹⁰
10	-2.91092·10 ⁻¹⁰
11	-2.17871·10 ⁻¹⁰
12	-1.62724·10 ⁻¹⁰
13	-1.21908·10 ⁻¹⁰
14	-9.19604·10 ⁻¹¹
15	...

deltaA2(C,K) =

```

deltaAB(c,K) :=
nrow ← rows(c) - 1
i ← 0
for i ∈ 0..nrow - 1
  outi ← AB(c,K)i+1·0.00095 - AB(c,K)i·0.000946
  i ← 1 + i
out

```

	0
0	1.22725·10 ⁻⁸
1	1.22953·10 ⁻⁸
2	1.22304·10 ⁻⁸
3	1.20545·10 ⁻⁸
4	1.17436·10 ⁻⁸
5	1.12781·10 ⁻⁸
6	1.06484·10 ⁻⁸
7	9.86237·10 ⁻⁹
8	8.95129·10 ⁻⁹
9	7.967·10 ⁻⁹
10	6.96746·10 ⁻⁹
11	6.01197·10 ⁻⁹
12	5.13937·10 ⁻⁹
13	4.37224·10 ⁻⁹
14	3.71568·10 ⁻⁹
15	...

deltaAB(C,K) =

```

deltaA2B(c,K) :=
nrow ← rows(c) - 1
i ← 0
for i ∈ 0..nrow - 1
  outi ← A2B(c,K)i+1·0.00095 - A2B(c,K)i·0.000946
  i ← 1 + i
out

```

	0
0	1.93982·10 ⁻⁹
1	1.55859·10 ⁻⁹
2	1.18504·10 ⁻⁹
3	8.27236·10 ⁻¹⁰
4	4.94679·10 ⁻¹⁰
5	1.98782·10 ⁻¹⁰
6	-5.05684·10 ⁻¹¹
7	-2.45189·10 ⁻¹⁰
8	-3.81388·10 ⁻¹⁰
9	-4.62231·10 ⁻¹⁰
10	-4.96394·10 ⁻¹⁰
11	-4.95497·10 ⁻¹⁰
12	-4.71908·10 ⁻¹⁰
13	-4.35905·10 ⁻¹⁰
14	-3.94847·10 ⁻¹⁰
15	...

deltaA2B(C,K) =

deltaC := augment(deltaA2(C,K), deltaAB(C,K), deltaA2B(C,K))

	0	1	2
0	-2.10914·10 ⁻⁹	1.22725·10 ⁻⁸	1.93982·10 ⁻⁹
1	-1.87538·10 ⁻⁹	1.22953·10 ⁻⁸	1.55859·10 ⁻⁹
2	-1.64474·10 ⁻⁹	1.22304·10 ⁻⁸	1.18504·10 ⁻⁹
3	-1.41995·10 ⁻⁹	1.20545·10 ⁻⁸	8.27236·10 ⁻¹⁰
4	-1.20431·10 ⁻⁹	1.17436·10 ⁻⁸	4.94679·10 ⁻¹⁰
5	-1.00078·10 ⁻⁹	1.12781·10 ⁻⁸	1.98782·10 ⁻¹⁰
6	-8.14083·10 ⁻¹⁰	1.06484·10 ⁻⁸	-5.05684·10 ⁻¹¹
7	-6.4774·10 ⁻¹⁰	9.86237·10 ⁻⁹	-2.45189·10 ⁻¹⁰
8	-5.04486·10 ⁻¹⁰	8.95129·10 ⁻⁹	-3.81388·10 ⁻¹⁰
9	-3.85827·10 ⁻¹⁰	7.967·10 ⁻⁹	-4.62231·10 ⁻¹⁰
10	-2.91092·10 ⁻¹⁰	6.96746·10 ⁻⁹	-4.96394·10 ⁻¹⁰
11	-2.17871·10 ⁻¹⁰	6.01197·10 ⁻⁹	-4.95497·10 ⁻¹⁰
12	-1.62724·10 ⁻¹⁰	5.13937·10 ⁻⁹	-4.71908·10 ⁻¹⁰
13	-1.21908·10 ⁻¹⁰	4.37224·10 ⁻⁹	-4.35905·10 ⁻¹⁰
14	-9.19604·10 ⁻¹¹	3.71568·10 ⁻⁹	-3.94847·10 ⁻¹⁰
15	-7.00605·10 ⁻¹¹	3.16213·10 ⁻⁹	...

H_{A2} := -34185

data :=

	0	1
0	2	-5.59·10 ⁻⁴
1	3	-5.32·10 ⁻⁴
2	4	-5.04·10 ⁻⁴
3	5	-4.74·10 ⁻⁴
4	6	-4.45·10 ⁻⁴
5	7	-4.12·10 ⁻⁴
6	8	-3.7·10 ⁻⁴
7	9	...

+

$$X := \text{data}^{(0)} \quad Y := \text{data}^{(1)}$$

$$q(X, H_{AB}, H_{A2B}) := H_{AB} \cdot (\text{deltaC}^{(1)})_{X-2} + H_{A2B} \cdot (\text{deltaC}^{(2)})_{X-2} + H_{A2} \cdot (\text{deltaC}^{(0)})_{X-2}$$

Initial guess for H_{AB} and H_{A2B} are -30000 and -80000 respectively $\alpha := -30000$ $\beta := -80000$

$$\text{resid}(\alpha, \beta) := Y - \overrightarrow{q(X, \alpha, \beta)}$$

Given

$$0 = \text{resid}(\alpha, \beta)$$

Parameters for best fit:

$$\begin{pmatrix} \alpha 1 \\ \beta 1 \end{pmatrix} := \text{Minerr}(\alpha, \beta) \quad \begin{pmatrix} \alpha 1 \\ \beta 1 \end{pmatrix} = \begin{pmatrix} -3.75687 \times 10^4 \\ -8.68793 \times 10^4 \end{pmatrix}$$

Sum of squares implicitly minimized by this method:

$$\text{SSE}(\alpha, \beta) := \sum \text{resid}(\alpha, \beta)^2$$

$$\Delta H_{AB} := \frac{\alpha 1}{1000}$$

$$\Delta H_{A2B} := \frac{\beta 1}{1000}$$

Mean squared error (zero if a true solution existed):

$$\frac{\text{SSE}(\alpha 1, \beta 1)}{39 - 2} = 5.62475 \times 10^{-12}$$

$$\Delta H_{AB} = -37.56872$$

$$\Delta H_{A2B} = -86.87931$$

+

Appendix B-4. Data fitting of the system containing 3:1 complex, 2:1 complex, 1:1 complex, and acid dimer by Mathcad

1 to 1, 2 to 1, 3 to 1, and acid dimer system data fitting (FC-77, PFDA/pyridine, 25 °C)

```

a(c,K) :=
  c_A ← c(0)
  c_B ← c(1)
  nrow ← rows(c)
  i ← 0
  β11 ← K0
  β12 ← K1
  β13 ← K2
  K2 ← β11·β12
  K3 ← β11·β12·β13
  Ka ← 586.173
  denom ← 2·Ka·K3
  d5 ← 1
  for i ∈ 0..nrow - 1
    ca ← cAi
    cb ← cBi
    d2 ←  $\frac{\beta_{11} + 2K_a - K_2 \cdot c_a + 2K_2 \cdot c_b}{denom}$ 
    d0 ←  $\frac{c_a}{denom}$ 
    d4 ←  $\frac{K_3 + 2 \cdot K_a \cdot K_2}{denom}$ 

```

```

C :=
  (0.000398316 1.26316E-05)
  (0.000396639 2.521E-05)
  (0.000394969 3.77354E-05)
  (0.000393306 5.02081E-05)
  (0.00039165 6.26283E-05)
  (0.000390001 7.49962E-05)
  (0.000388358 8.7312E-05)
  (0.000386723 9.95759E-05)
  (0.000385095 0.000111788)
  (0.000383473 0.000123949)
  (0.000381859 0.000136059)
  (0.000380251 0.000148118)
  (0.00037865 0.000160125)
  (0.000377056 0.000172083)
  (0.000375468 0.00018399)
  (0.000373887 0.000195847)
  (0.000372313 0.000207654)
  (0.000370745 0.000219411)
  (0.000369184 0.000231119)
  (0.00036763 0.000242777)
  (0.000366082 0.000254386)
  (0.00036454 0.000265947)
  (0.000363006 0.000277459)
  (0.000361477 0.000288922)
  (0.000359955 0.000300337)

```

+

C :=

```

d1 ← (1 - β11·ca + β11·cb) / denom
d3 ← ((β11·β12 + 2·Ka·β11 + 3·K3·cb - K3·ca) / denom)
f(x) ← d5·x^5 + d4·x^4 + d3·x^3 + d2·x^2 + d1·x + d0
out1 ← root(f(x), x, 0, ca)
i ← 1 + i
out

```

```

0.000358439 0.000311704
0.00035693 0.000323023
0.000355427 0.000334295
0.000353931 0.000345519
0.000352441 0.000356696
0.000350957 0.000367825
0.000349479 0.000378908
0.000348007 0.000389944
0.000346542 0.000400934
0.000345083 0.000411877
0.00034363 0.000422775
0.000342183 0.000433626
0.000340742 0.000444432
0.000339308 0.000455192
(0.000337879 0.000465907)

```

a(C,K) =

	0
0	2.75956·10 ⁻⁴
1	2.55334·10 ⁻⁴
2	2.35092·10 ⁻⁴
3	2.15474·10 ⁻⁴
4	1.96751·10 ⁻⁴
5	1.79192·10 ⁻⁴
6	1.63017·10 ⁻⁴
7	1.48358·10 ⁻⁴
8	1.35242·10 ⁻⁴
9	1.23606·10 ⁻⁴
10	1.13326·10 ⁻⁴
11	1.04247·10 ⁻⁴
12	9.62103·10 ⁻⁵
13	8.90646·10 ⁻⁵
14	8.26791·10 ⁻⁵
15	...

$$\underline{\underline{K}} := \begin{pmatrix} 86500 \\ 1800 \\ 39000 \end{pmatrix}$$

```

A2(c,K) :=
  cB ← c<1>
  nrow ← rows(c)
  i ← 0
  β11 ← K0
  β12 ← K1
  K2 ← β11·β12
  Ka ← 586.173
  for i ∈ 0..nrow - 1
    outi ← Ka·a(c,K)i·a(c,K)i
    i ← 1 + i
  out

```

A2(C,K) =

	0
0	4.46382·10 ⁻⁵
1	3.82159·10 ⁻⁵
2	3.23968·10 ⁻⁵
3	2.72154·10 ⁻⁵
4	2.26913·10 ⁻⁵
5	1.88219·10 ⁻⁵
6	1.55773·10 ⁻⁵
7	1.29017·10 ⁻⁵
8	...

```

AB(c,K) :=
  cB ← c<1>
  nrow ← rows(c)
  i ← 0
  β11 ← K0
  β12 ← K1
  β13 ← K2
  K2 ← β11·β12
  K3 ← β11·β12·β13
  Ka ← 586.173
  for i ∈ 0..nrow - 1
    outi ←  $\frac{\beta_{11} \cdot a(c,K)_i \cdot c_{B_i}}{1 + \beta_{11} \cdot a(c,K)_i + K_2 \cdot a(c,K)_i \cdot a(c,K)_i + K_3 \cdot a(c,K)_i \cdot a(c,K)_i \cdot a(c,K)_i}$ 
    i ← 1 + i
  out

```

AB(C,K) =

	0
0	1.83479·10 ⁻⁶
1	1.14528·10 ⁻⁶
2	7.05047·10 ⁻⁶
3	1.06807·10 ⁻⁵
4	1.51627·10 ⁻⁵
5	2.05967·10 ⁻⁵
6	2.70326·10 ⁻⁵
7	3.44544·10 ⁻⁵
8	...

```

A2B(c,K) :=
  c_B ← c<1>
  nrow ← rows(c)
  i ← 0
  β11 ← K0
  β12 ← K1
  β13 ← K2
  K2 ← β11·β12
  K3 ← β11·β12·β13
  Ka ← 586.173
  for i ∈ 0..nrow - 1
    outi ←  $\frac{K_2 \cdot a(c,K)_i \cdot a(c,K)_i \cdot c_{B_i}}{1 + \beta_{11} \cdot a(c,K)_i + K_2 \cdot a(c,K)_i \cdot a(c,K)_i + K_3 \cdot a(c,K)_i \cdot a(c,K)_i \cdot a(c,K)_i}$ 
    i ← 1 + i
  out

```

A2B(C,K) =

	0
0	9.11382·10 ⁻⁷
1	1.90518·10 ⁻⁶
2	2.98352·10 ⁻⁶
3	4.14255·10 ⁻⁶
4	5.3699·10 ⁻⁶
5	6.64339·10 ⁻⁶
6	7.93219·10 ⁻⁶
7	9.20086·10 ⁻⁶
8	...

```

A3B(c,K) :=
  c_B ← c<1>
  nrow ← rows(c)
  i ← 0
  β11 ← K0
  β12 ← K1
  β13 ← K2
  K2 ← β11·β12
  K3 ← β11·β12·β13
  Ka ← 586.173
  for i ∈ 0..nrow - 1
    outi ←  $\frac{K_3 \cdot a(c,K)_i \cdot a(c,K)_i \cdot a(c,K)_i \cdot c_{B_i}}{1 + \beta_{11} \cdot a(c,K)_i + K_2 \cdot a(c,K)_i \cdot a(c,K)_i + K_3 \cdot a(c,K)_i \cdot a(c,K)_i \cdot a(c,K)_i}$ 
    i ← 1 + i
  out

```

A3B(C,K) =

	0
0	9.80856·10 ⁻⁶
1	1.89719·10 ⁻⁵
2	2.73547·10 ⁻⁵
3	3.48118·10 ⁻⁵
4	4.12047·10 ⁻⁵
5	4.64273·10 ⁻⁵
6	5.04301·10 ⁻⁵
7	5.32358·10 ⁻⁵
8	...

+

```

deltaA2(c,K) :=
nrow ← rows(c) - 1
i ← 0
for i ∈ 0..nrow - 1
  outi ← A2(c,K)i+1 · 0.00095 - A2(c,K)i · 0.000946
  i ← 1 + i
out

```

deltaA2(C,K) =

	0
0	-5.92258 · 10 ⁻⁹
1	-5.37528 · 10 ⁻⁹
2	-4.79277 · 10 ⁻⁹
3	-4.18909 · 10 ⁻⁹
4	-3.58514 · 10 ⁻⁹
5	-3.0071 · 10 ⁻⁹
6	-2.47948 · 10 ⁻⁹
7	-2.01975 · 10 ⁻⁹
8	-1.63437 · 10 ⁻⁹
9	-1.32047 · 10 ⁻⁹
10	-1.06988 · 10 ⁻⁹
11	-8.71656 · 10 ⁻¹⁰
12	-7.15538 · 10 ⁻¹⁰
13	-5.92093 · 10 ⁻¹⁰
14	-4.94022 · 10 ⁻¹⁰
15	...

```

deltaAB(c,K) :=
nrow ← rows(c) - 1
i ← 0
for i ∈ 0..nrow - 1
  outi ← AB(c,K)i+1 · 0.00095 - AB(c,K)i · 0.000946
  i ← 1 + i
out

```

deltaAB(C,K) =

	0
0	2.2023 · 10 ⁻⁹
1	2.77651 · 10 ⁻⁹
2	3.47693 · 10 ⁻⁹
3	4.30064 · 10 ⁻⁹
4	5.22297 · 10 ⁻⁹
5	6.19644 · 10 ⁻⁹
6	7.15889 · 10 ⁻⁹
7	8.05004 · 10 ⁻⁹
8	8.82525 · 10 ⁻⁹
9	9.46092 · 10 ⁻⁹
10	9.9543 · 10 ⁻⁹
11	1.03132 · 10 ⁻⁸
12	1.05561 · 10 ⁻⁸
13	1.06953 · 10 ⁻⁸
14	1.07482 · 10 ⁻⁸
15	...

```

deltaA2B(c,K) := | nrow ← rows(c) - 1
                  | i ← 0
                  | for i ∈ 0..nrow - 1
                  |   outi ← A2B(c,K)i+1 · 0.00095 - A2B(c,K)i · 0.000946
                  |   i ← 1 + i
                  | out

```

deltaA2B(C,K) =

	0
0	9.47753 · 10 ⁻¹⁰
1	1.03204 · 10 ⁻⁹
2	1.11301 · 10 ⁻⁹
3	1.18256 · 10 ⁻⁹
4	1.23129 · 10 ⁻⁹
5	1.25093 · 10 ⁻⁹
6	1.23697 · 10 ⁻⁹
7	1.19016 · 10 ⁻⁹
8	1.11584 · 10 ⁻⁹
9	1.02156 · 10 ⁻⁹
10	9.15048 · 10 ⁻¹⁰
11	8.02728 · 10 ⁻¹⁰
12	6.89629 · 10 ⁻¹⁰
13	5.78648 · 10 ⁻¹⁰
14	4.72024 · 10 ⁻¹⁰
15	...

```

deltaA3B(c,K) := | nrow ← rows(c) - 1
                  | i ← 0
                  | for i ∈ 0..nrow - 1
                  |   outi ← A3B(c,K)i+1 · 0.00095 - A3B(c,K)i · 0.000946
                  |   i ← 1 + i
                  | out

```

deltaA3B(C,K) =

	0
0	8.74437 · 10 ⁻⁹
1	8.03959 · 10 ⁻⁹
2	7.19366 · 10 ⁻⁹
3	6.21254 · 10 ⁻⁹
4	5.12621 · 10 ⁻⁹
5	3.98846 · 10 ⁻⁹
6	2.86705 · 10 ⁻⁹
7	1.82515 · 10 ⁻⁹
8	9.07914 · 10 ⁻¹⁰
9	1.36199 · 10 ⁻¹⁰
10	-4.90967 · 10 ⁻¹⁰
11	-9.85768 · 10 ⁻¹⁰
12	-1.36682 · 10 ⁻⁹
13	-1.65301 · 10 ⁻⁹
14	-1.8614 · 10 ⁻⁹
15	...

deltaC := augment(deltaA2(C,K), deltaAB(C,K), deltaA2B(C,K), deltaA3B(C,K))

	0	1	2	3
0	$-5.92258 \cdot 10^{-9}$	$2.2023 \cdot 10^{-9}$	$9.47753 \cdot 10^{-10}$	$8.74437 \cdot 10^{-9}$
1	$-5.37528 \cdot 10^{-9}$	$2.77651 \cdot 10^{-9}$	$1.03204 \cdot 10^{-9}$	$8.03959 \cdot 10^{-9}$
2	$-4.79277 \cdot 10^{-9}$	$3.47693 \cdot 10^{-9}$	$1.11301 \cdot 10^{-9}$	$7.19366 \cdot 10^{-9}$
3	$-4.18909 \cdot 10^{-9}$	$4.30064 \cdot 10^{-9}$	$1.18256 \cdot 10^{-9}$	$6.21254 \cdot 10^{-9}$
4	$-3.58514 \cdot 10^{-9}$	$5.22297 \cdot 10^{-9}$	$1.23129 \cdot 10^{-9}$	$5.12621 \cdot 10^{-9}$
5	$-3.0071 \cdot 10^{-9}$	$6.19644 \cdot 10^{-9}$	$1.25093 \cdot 10^{-9}$	$3.98846 \cdot 10^{-9}$
6	$-2.47948 \cdot 10^{-9}$	$7.15889 \cdot 10^{-9}$	$1.23697 \cdot 10^{-9}$	$2.86705 \cdot 10^{-9}$
7	$-2.01975 \cdot 10^{-9}$	$8.05004 \cdot 10^{-9}$	$1.19016 \cdot 10^{-9}$	$1.82515 \cdot 10^{-9}$
8	$-1.63437 \cdot 10^{-9}$	$8.82525 \cdot 10^{-9}$	$1.11584 \cdot 10^{-9}$	$9.07914 \cdot 10^{-10}$
9	$-1.32047 \cdot 10^{-9}$	$9.46092 \cdot 10^{-9}$	$1.02156 \cdot 10^{-9}$	$1.36199 \cdot 10^{-10}$
10	$-1.06988 \cdot 10^{-9}$	$9.9543 \cdot 10^{-9}$	$9.15048 \cdot 10^{-10}$...

H_{A2} := -34185

data :=

	0	1
0	2	$-8.71 \cdot 10^{-4}$
1	3	$-8.45 \cdot 10^{-4}$
2	4	$-8.31 \cdot 10^{-4}$
3	5	$-8.01 \cdot 10^{-4}$
4	6	$-7.84 \cdot 10^{-4}$
5	7	$-7.42 \cdot 10^{-4}$
6	8	$-7.08 \cdot 10^{-4}$
7	9	...

X := data^{<0>} Y := data^{<1>}

$$q(X, H_{AB}, H_{A2B}, H_{A3B}) := \begin{bmatrix} H_{AB} \cdot (\text{deltaC}^{(1)})_{X-2} + H_{A2B} \cdot (\text{deltaC}^{(2)})_{X-2} + H_{A2} \cdot (\text{deltaC}^{(0)})_{X-2} - H_{A3B} \cdot (\text{deltaC}^{(3)})_{X-2} \\ (\text{deltaC}^{(1)})_{X-2} \\ (\text{deltaC}^{(2)})_{X-2} \\ (\text{deltaC}^{(3)})_{X-2} \end{bmatrix} \quad \text{guess} := \begin{pmatrix} -40000 \\ -80000 \\ -120000 \end{pmatrix}$$

$$cg := \text{genfit}(X, Y, \text{guess}, q)$$

$$cg = \begin{pmatrix} -5.047 \times 10^4 \\ -1.27 \times 10^5 \\ -9.183 \times 10^4 \end{pmatrix}$$

$$\text{resid}(\alpha, \beta, \gamma) := Y - q(X, \alpha, \beta, \gamma)$$

Sum of squares implicitly minimized by this method:

$$\text{SSE}(\alpha, \beta, \gamma) := \sum \text{resid}(\alpha, \beta, \gamma)^2$$

Mean squared error (zero if a true solution existed):

$$\frac{\sum \left[Y - \text{deltaC} \begin{pmatrix} H_{A2} \\ c\beta_0 \\ c\beta_1 \\ c\beta_2 \end{pmatrix} \right]^2}{36} = 8.15665 \times 10^{-11}$$

$$\Delta H_{AB} := \frac{c\beta_0}{1000}$$

$$\Delta H_{A2B} := \frac{c\beta_1}{1000}$$

$$\Delta H_{A3B} := \frac{c\beta_2}{1000}$$

$$\Delta H_{AB} = -50.47354$$

$$\Delta H_{A2B} = -126.97991$$

$$\Delta H_{A3B} = -94.82908$$

+

BIBLIOGRAPHY

- (1) O'Neal, K. L.; Zhang, H.; Yang, Y.; Hong, L.; Lu, D.; Weber, S. G. *J. Chromatogr. A* **2010**, *1217*, 2287.
- (2) Dalvi, V. H.; Rosicky, P. J. *Proc. Natl. Acad. Sci. U.S.A.*, *107*, 13603.
- (3) Goss, K. U.; Bronner, G. *J. Phys. Chem. A* **2006**, *110*, 9518.
- (4) Gladysz, J. A.; Curran, D. P.; Horvath, I. T. *Handbook of Fluorous Chemistry*, 2004.
- (5) Genzer, J.; Efimenko, K. *Biofouling* **2006**, *22*, 339.
- (6) Curran, D. P. *Angew. Chem., Int. Ed.* **1998**, *37*, 1174.
- (7) Zhang, W. *Curr. Opin. Drug Discovery Dev.* **2004**, *7*, 784.
- (8) Dandapani, S. *QSAR Comb. Sci.* **2006**, *25*, 681.
- (9) Studer, A.; Hadida, S.; Ferritto, R.; Kim, S.; Jeger, P.; Wipf, P.; Curran, D. P. *Science* **1997**, *275*, 823.
- (10) Luo, Z.; Zhang, Q.; Oderaotoshi, Y.; Curran, D. P. *Science* **2001**, *291*, 1766.
- (11) Horvath, I. T.; Rabai, J. *Science* **1994**, *266*, 72.
- (12) de Wolf, E.; van Koten, G.; Deelman, B. J. *Chem. Soc. Rev.* **1999**, *28*, 37.
- (13) Horvath, I. T. *Acc. Chem. Res.* **1998**, *31*, 641.
- (14) Nakamura, H.; Linclau, B.; Curran, D. P. *J. Am. Chem. Soc.* **2001**, *123*, 10119.
- (15) Yampolskii, Y.; Pinnau, I.; Freeman, B. D. *Material Science of Membranes for Gas and Vapor Separation*, 2006.
- (16) Arcella, V.; Ghielmi, A.; Tommasi, G. *Ann. N.Y. Acad. Sci.* **2003**, *984*, 226.
- (17) Rindfleisch, F.; DiNoia, T. P.; McHugh, M. A. *J. Phys. Chem.* **1996**, *100*, 15581.
- (18) Tuminello, W. H.; Dee, G. T.; McHugh, M. A. *Macromolecules* **1995**, *28*, 1506.
- (19) Yampolskii, Y. P.; Belov, N.; Tokarev, A.; Bondarenko, G. *Desalination* **2006**, *199*, 469.
- (20) Boswell, P. G.; Buhlmann, P. *J. Am. Chem. Soc.* **2005**, *127*, 8958.
- (21) Ballermann, B. J. *News Physiol. Sci.* **1998**, *13*, 154.
- (22) Shiu, J.; Kuo, C. W.; Whang, W.; Chen, P. *J. Adhes. Sci. Technol.* **2010**, *24*, 1023.
- (23) Song, E. H.; Pohl, N. L. B. *Future Med. Chem.* **2009**, *1*, 889.
- (24) Golemme, G.; Nagy, J. B.; Fonseca, A.; Algieri, C.; Yampolskii, Y. *Polymer* **2003**, *44*, 5039.
- (25) Shantarovich, V. P.; Kevdina, I. B.; Yampolskii, Y. P.; Alentiev, A. Y. *Macromolecules* **2000**, *33*, 7453.
- (26) Yampolskii, Y. *Russ. J. Gen. Chem.* **2009**, *79*, 657.
- (27) Scheirs, J. *Modern Fluoropolymers: High Performance Polymers for Diverse Applications*, 1997.

- (28) Zhang, H.; Weber, S. In *Fluorous Chemistry*; Horvath, I. T., Ed.; Springer: 2012; Vol. 308, p 307.
- (29) Polyakov, A. M.; Starannikova, L. E.; Yampolskii, Y. P. *J. Membr. Sci.* **2004**, 238, 21.
- (30) Dasgupta, P. K.; Zhang, G.; Poruthoor, S. K.; Caldwell, S.; Dong, S.; Liu, S. Y. *Anal. Chem.* **1998**, 70, 4661.
- (31) Gangal, S. V. *Perfluorinated Polymers, Tetrafluoroethylene-Perfluorodioxole Copolymers.*; John Wiley & Sons, Inc., 2002.
- (32) Yang, M. K.; French, R. H.; Tokarsky, E. W. *J. Micro/Nanolithogr. MEMS MOEMS* **2008**, 7, 033010/1.
- (33) Pollack, M. G.; Fair, R. B.; Shenderov, A. D. *Appl. Phys. Lett.* **2000**, 77, 1725.
- (34) Dubois, P.; Marchand, G.; Fouillet, Y.; Berthier, J.; Douki, T.; Hassine, F.; Gmouh, S.; Vaultier, M. *Anal. Chem.* **2006**, 78, 4909.
- (35) Song, H.; Li, H.; Munson, M. S.; Ha, T.; Ismagilov, R. F. *Anal. Chem.* **2006**, 78, 4839.
- (36) Finkelshtein, E. S.; Makovetskii, K. L.; Gringolts, M. L.; Rogan, Y. V.; Golenko, T. G.; Starannikova, L. E.; Yampolskii, Y. P.; Shantarovich, V. P.; Suzuki, T. *Macromolecules* **2006**, 39, 7022.
- (37) Yampolskii, Y. P.; Finkelshtein, E. S.; Makovetskii, K. L.; Bondar, V. I.; Shantarovich, V. P. *J. Appl. Polym. Sci.* **1996**, 62, 349.
- (38) Yampolskii, Y. P.; Soloviev, S. A.; Gringolts, M. L. *Polymer* **2004**, 45, 6945.
- (39) Hofmann, D.; Entrialgo-Castano, M.; Lerbret, A.; Heuchel, M.; Yampolskii, Y. *Macromolecules* **2003**, 36, 8528.
- (40) Alexander, S. *J. Membr. Sci.* **1994**, 94, 1.
- (41) Pinnau, I.; Toy, L. G. *J. Membr. Sci.* **1996**, 109, 125.
- (42) Freeman, B. D.; Pinnau, I. *Polymer Membranes for Gas and Vapor Separation*; American Chemical Society, 1999.
- (43) Merkel, T. C.; Bondar, V.; Nagai, K.; Freeman, B. D.; Yampolskii, Y. P. *Macromolecules* **1999**, 32, 8427.
- (44) Alentiev, A. Y.; Shantarovich, V. P.; Merkel, T. C.; Bondar, V. I.; Freeman, B. D.; Yampolskii, Y. P. *Macromolecules* **2002**, 35, 9513.
- (45) Bondar, V. I.; Freeman, B. D.; Yampolskii, Y. P. *Macromolecules* **1999**, 32, 6163.
- (46) Hildebrand, J. H.; Prausnitz, J. M.; Scott, R. L. In *The Solubility of Gases, Liquids, and Solids* 1970.
- (47) Fleming, G. K.; Koros, W. J. *Macromolecules* **1986**, 19, 2285.
- (48) Ferrari, M. C.; Galizia, M.; De Angelis, M. G.; Sarti, G. C. *Ind. Eng. Chem. Res.* **2010**, 49, 11920.
- (49) Merkel, T. C.; He, Z.; Pinnau, I.; Freeman, B. D.; Meakin, P.; Hill, A. J. *Macromolecules* **2003**, 36, 8406.
- (50) Merkel, T. C.; Freeman, B. D.; Spontak, R. J.; He, Z.; Pinnau, I.; Meakin, P.; Hill, A. J. *Science* **2002**, 296, 519.
- (51) De Sitter, K.; Andersson, A.; D'Haen, J.; Leysen, R.; Mullens, S.; Maurer, F. H. J.; Vankelecom, I. F. J. *J. Membr. Sci.* **2008**, 321, 284.
- (52) Polyakov, A. M.; Starannikova, L. E.; Yampolskii, Y. P. *J. Membr. Sci.* **2003**, 216, 241.

- (53) Polyakov, A.; Bondarenko, G.; Tokarev, A.; Yampolskii, Y. *J. Membr. Sci.* **2006**, *277*, 108.
- (54) Jansen, J. C.; Friess, K.; Drioli, E. *J. Membr. Sci.* **2010**, *367*, 141.
- (55) Vincent, J. M. *J. Fluorine Chem.* **2008**, *129*, 903.
- (56) Zhao, H.; Ismail, K.; Weber, S. G. *J. Am. Chem. Soc.* **2004**, *126*, 13184.
- (57) Zhao, H.; Zhang, J.; Wu, N.; Zhang, X.; Crowley, K.; Weber, S. G. *J. Am. Chem. Soc.* **2005**, *127*, 15112.
- (58) Zhang, H.; Hussam, A.; Weber, S. G. *J. Am. Chem. Soc.* **2010**, *132*, 17867.
- (59) Zhang, H.; Hong, L.; Weber, S. G. *PMSE Prepr.* **2009**, *100*, 358.
- (60) Lehn, J. M. *Chem. Soc. Rev.* **2007**, *36*, 151.
- (61) Valenta, J. N.; Dixon, R. P.; Hamilton, A. D.; Weber, S. G. *Anal. Chem.* **1994**, *66*, 2397.
- (62) O'Neal, K. L.; Geib, S.; Weber, S. G. *Anal. Chem.* **2007**, *79*, 3117.
- (63) O'Neal, K. L.; Weber, S. G. *J. Phys. Chem. B* **2008**, *113*, 149.
- (64) O'Neal, K. L.; Weber, S. G. *J. Phys. Chem. B* **2009**, *113*, 7449.
- (65) Shimizu, S.; Kiuchi, T.; Pan, N. *Angew. Chem., Int. Ed.* **2007**, *46*, 6442.
- (66) Gattuso, G.; Pappalardo, A.; Parisi, M. F.; Pisagatti, I.; Crea, F.; Liantonio, R.; Metrangolo, P.; Navarrini, W.; Resnati, G.; Pilati, T.; Pappalardo, S. *Tetrahedron* **2007**, *63*, 4951.
- (67) El Bakkari, M.; Fronton, B.; Luguya, R.; Vincent, J. M. *J. Fluorine Chem.* **2006**, *127*, 558.
- (68) Boswell, P. G.; Lugert, E. C.; Rabai, J.; Amin, E. A.; Buhlmann, P. *J. Am. Chem. Soc.* **2005**, *127*, 16976.
- (69) Boswell, P. G.; Szijjarto, C.; Jurisch, M.; Gladysz, J. A.; Rabai, J.; Buhlmann, P. *Anal. Chem.* **2008**, *80*, 2084.
- (70) Lai, C. Z.; Koseoglu, S. S.; Lugert, E. C.; Boswell, P. G.; Rabai, J.; Lodge, T. P.; Buhlmann, P. *J. Am. Chem. Soc.* **2009**, *131*, 1598.
- (71) Lugert, E. C.; Lodge, T. P.; Buhlmann, P. *J. Polym. Sci., Part B: Polym. Phys.* **2008**, *46*, 516.
- (72) Bernardo, P.; Drioli, E.; Golemme, G. *Ind. Eng. Chem. Res.* **2009**, *48*, 4638.
- (73) Chung, T. S.; Jiang, L. Y.; Li, Y.; Kulprathipanja, S. *Prog. Polym. Sci.* **2007**, *32*, 483.
- (74) Pandey, P.; Chauhan, R. S. *Prog. Polym. Sci.* **2001**, *26*, 853.
- (75) Stern, S. A. *J. Membr. Sci.* **1994**, *94*, 1.
- (76) Park, H. B.; Jung, C. H.; Lee, Y. M.; Hill, A. J.; Pas, S. J.; Mudie, S. T.; Van Wagner, E.; Freeman, B. D.; Cookson, D. J. *Science* **2007**, *318*, 254.
- (77) Xu, T. *J. Membr. Sci.* **2005**, *263*, 1.
- (78) Nghiem, L. D.; Mornane, P.; Potter, I. D.; Perera, J. M.; Cattrall, R. W.; Kolev, S. *D. J. Membr. Sci.* **2006**, *281*, 7.
- (79) O'Rourke, M.; Cattrall, R. W.; Kolev, S. D.; Potter, I. D. *Solvent Extr. Res. Dev.* **2009**, *16*, 1.
- (80) Walt, D. R. *Chem. Soc. Rev.* **2010**, *39*, 38.
- (81) Dane, E. L.; King, S. B.; Swager, T. M. *J. Am. Chem. Soc.* **2010**, *132*, 7758.
- (82) Millefiorini, S.; Tkaczyk, A. H.; Sedev, R.; Efthimiadis, J.; Ralston, J. *J. Am. Chem. Soc.* **2006**, *128*, 3098.
- (83) Aldred, N.; Li, G.; Gao, Y.; Clare, A. S.; Jiang, S. *Biofouling* **2010**, *26*, 673.

- (84) Nickson, C. M.; Doherty, P. J.; Williams, R. L. *J. Biomater. Appl.* **2010**, *24*, 437.
- (85) Villa-Diaz, L. G.; Nandivada, H.; Ding, J.; Nogueira-de-Souza, N. C.; Krebsbach, P. H.; O'Shea, K. S.; Lahann, J.; Smith, G. D. *Nat. Biotechnol.* **2010**, *28*, 581.
- (86) Duan, H.; Kuang, M.; Wang, Y. A. *Chem. Mater.* **2010**, *22*, 4372.
- (87) Laforgue, A.; Robitaille, L. *Chem. Mater.* **2010**, *22*, 2474.
- (88) Brady, J. E.; Carr, P. W. *Anal. Chem.* **2002**, *54*, 1751.
- (89) Palomo, C.; Aizpurua, J. M.; Loinaz, I.; Fernandez-Berridi, M. J.; Irusta, L. *Org. Lett.* **2001**, *3*, 2361.
- (90) Yang, Y.; Hong, L.; Vaidyanathan, N.; Weber, S. G. *J. Membr. Sci.* **2009**, *345*, 170.
- (91) Yang, Y.; Vaidyanathan, N.; Weber, S. G. *J. Fluorine Chem.* **2009**, *130*, 1022.
- (92) Consolati, G.; Genco, I.; Pegoraro, M.; Zanderighi, L. *J. Polym. Sci., Part B: Polym. Phys.* **1996**, *34*, 357.
- (93) Pinnau, I.; He, Z.; Merkel, T. *PMSE Prepr.* **2003**, *89*, 16.
- (94) Hayes, H. J.; McCarthy, T. J. *Polym. Mater. Sci. Eng.* **1999**, *81*, 537.
- (95) Yampolskii, Y. P.; Alentiev, A. Y.; Shishatskii, S. M.; Shantarovich, V. P.; Freeman, B. D.; Bondar, V. I. *Polym. Prepr.* **1998**, *39*, 884.
- (96) Polyakov, A. M.; Starannikova, L. E.; Yampolskii, Y. P. *Polym. Mater. Sci. Eng.* **2001**, *85*, 321.
- (97) Wang, W.; Lee, K.; Kim, T.; Park, I.; Yang, S. *Smart Mater. Struct.* **2007**, *16*, 1382.
- (98) Kebabian, P. L.; Freedman, A. *Meas. Sci. Technol.* **2006**, *17*, 703.
- (99) Zook, L. A.; Leddy, J. *Anal. Chem.* **1996**, *68*, 3793.
- (100) Oberbroeckling, K. J.; Dunwoody, D. C.; Minter, S. D.; Leddy, J. *Anal. Chem.* **2002**, *74*, 4794.
- (101) Ueberreiter, K.; Kanig, G. *J. Colloid Sci.* **1952**, *7*, 569.
- (102) Lee, W. M. *Polym. Eng. Sci.* **1980**, *20*, 65.
- (103) Bondi, A. *Physical Properties of Molecular Crystals, Liquids, and Glasses*, 1968.
- (104) Maeda, Y.; Paul, D. R. *J. Polym. Sci., Part B: Polym. Phys.* **1987**, *25*, 1005.
- (105) Crank, J. *The Mathematics of Diffusion*, 1975.
- (106) Jost, W. *Diffusion in Solids, Liquids, Gases*, 1951.
- (107) Zhang, X.; Zhao, H.; Chen, Z.; Nims, R.; Weber, S. G. *Anal. Chem.* **2003**, *75*, 4257.
- (108) Hussam, A.; Basu, S. C.; Hixon, M.; Olumee, Z. *Anal. Chem.* **1995**, *67*, 1459.
- (109) Galdamez, J. R.; Serna, L. V.; Duda, J. L.; Danner, R. P. *J. Polym. Sci., Part B: Polym. Phys.* **2007**, *45*, 2071.
- (110) Ruiz-Trevino, F. A.; Paul, D. R. *J. Polym. Sci., Part B: Polym. Phys.* **1998**, *36*, 1037.
- (111) Vrentas, J. S.; Duda, J. L.; Ling, H. C. *Macromolecules* **1988**, *21*, 1470.
- (112) Maeda, Y.; Paul, D. R. *J. Polym. Sci., Part B: Polym. Phys.* **1987**, *25*, 981.
- (113) Maeda, Y.; Paul, D. R. *J. Polym. Sci., Part B: Polym. Phys.* **1987**, *25*, 957.
- (114) Anderson, S. L.; Grulke, E. A.; DeLassus, P. T.; Smith, P. B.; Kocher, C. W.; Landes, B. G. *Macromolecules* **2002**, *28*, 2944.
- (115) Wu, S. *J. Polym. Sci., Part B: Polym. Phys.* **1989**, *27*, 723.
- (116) Clara, R. A.; Gomez Marigliano, A. C.; Solimo, H. N. *J. Chem. Eng. Data* **2006**, *51*, 1473.

- (117) Vlasov, V. M.; Khalifina, I. A. *J. Phys. Org. Chem.* **2000**, *13*, 630.
- (118) Jing, P.; Rodgers, P. J.; Amemiya, S. *J. Am. Chem. Soc.* **2009**, *131*, 2290.
- (119) Nyquist, R. A.; Settineri, S. E. *Appl. Spectrosc.* **1990**, *44*, 1552.
- (120) Darder, M.; López-Blanco, M.; Aranda, P.; Leroux, F.; Ruiz-Hitzky *Chem. Mater.* **2005**, *17*, 1969.
- (121) Saxena, A.; Tripathi, B. P.; Shahi, V. K. *J. Phys. Chem. B* **2007**, *111*, 12454.
- (122) Shen, S.; Dong, Y. C.; Ng, W. K.; Chia, L.; Tan, R. B. H. In *Nanotechnologies for the Life Sciences*; Wiley-VCH GmbH & Co.: 2012.
- (123) Hoshi, R.; Webb, A. R.; Qiu, H.; Ameer, G. A. In *Advances in Regenerative Medicine: Role of Nanotechnology, and Engineering Principles*; Shastri, V. P., Altankov, G., Lendlein, A., Eds.; Springer: 2010, p 175.
- (124) Csetneki, I.; Filipcsei, G.; Zrinyi, M. *Macromolecules* **2006**, *39*, 1939.
- (125) Vaia, R. A.; Maguire, J. F. *Chem. Mater.* **2007**, *19*, 2736.
- (126) Hooper, J. B.; Schweizer, K. S. *Macromolecules* **2006**, *39*, 5133.
- (127) Pomposo, J. A.; Ruiz de Luzuriaga, A.; Etxeberria, A.; Rodriguez, J. *Phys. Chem. Chem. Phys.* **2008**, *10*.
- (128) Tuteja, A.; Duxbury, P. M.; Mackay, M. E. *Macromolecules* **2007**, *40*, 9427.
- (129) Balazs, A. C.; Emrick, T.; Russell, T. P. *Science* **2006**, *314*, 1107.
- (130) Davies, M. L.; Hamilton, C. J.; Murphy, S. M.; Tighe, B. J. *Biomaterials* **1992**, *13*, 971.
- (131) Koda, Y.; Terashima, T.; Nomura, A.; Ouchi, M.; Sawamoto, M. *Macromolecules* **2011**, *44*, 4574.
- (132) Piletsky, S. A.; Panasyuk, T. L.; Piletskaya, E. V.; Nicholls, I. A.; Ulbricht, M. *J. Membr. Sci.* **1999**, *157*, 263.
- (133) Takeuchi, T.; Haginaka, J. *J. Chromatogr., B: Anal. Technol. Biomed. Life Sci.* **1999**, *728*, 1.
- (134) Johan, M. R.; Ting, L. M. *Int. J. Electrochem. Sci.* **2011**, *6*, 4737.
- (135) Lee, K. Y.; Kim, D. W.; Heo, J.; Kim, J. S.; Yang, J. K.; Cheong, G. W.; Han, S. *W. Bull. Korean Chem. Soc.* **2006**, *27*, 2081.
- (136) Zhang, S. Q.; Xie, S.; Chen, C. H. *Mater. Sci. Eng., B* **2005**, *B121*, 160.
- (137) Zhang, H.; Hussam, A.; Weber, S. G. *J. Am. Chem. Soc.* **2010**, *132*, 17867-17879.
- (138) Lee, J.; Tripathi, A. *Anal. Chem.* **2005**, *77*, 7137.
- (139) Sunseri, J. D.; Gedris, T. E.; Stiegman, A. E.; Dorsey, J. G. *Langmuir* **2003**, *19*, 8608.
- (140) Berendsen, G. E.; Pikaart, K. A.; De Galan, L.; Olieman, C. *Anal. Chem.* **1980**, *52*, 1990.
- (141) Hozumi, A.; Ushiyama, K.; Sugimura, H.; Takai, O. *Langmuir* **1999**, *15*, 7600.
- (142) Odlyha, M.; Akapo, S. O.; Simpson, C. F. *Thermochim. Acta* **1988**, *134*, 457.
- (143) Lee, S. J.; Han, S. W.; Kim, K. *Chem. Commun.* **2002**, 442.
- (144) Grosse, A. V.; Cady, G. H. *J. Ind. Eng. Chem.* **1947**, *39*, 367.
- (145) Hao, T.; Riman, R. E. *J. Colloid Interface Sci.* **2006**, *297*, 374.
- (146) Joshi, R.; Provder, T.; Ziemer, P.; Mao, W.; Shen, W.; Jones, F. J. *Coat. Technol. Res.* **2009**, *6*, 47.
- (147) Chu, B.; Wu, C.; Buck, W. *Macromolecules* **1989**, *22*.
- (148) He, S.; Lin, J. *Appl. Mech. Mater.* **2012**, *108*, 91.
- (149) Trachenko, K.; Brazhkin, V. V. *Phys. Rev. B* **2011**, *83*.

- (150) Merkel, T. C.; He, Z.; Pinnau, I.; Freeman, B. D.; Meakin, P.; Hill, A. J. *Macromolecules* **2003**, *36*, 6844.
- (151) Barrer, R. M.; Barrie, J. A.; Raman, N. K. *Polymer* **1962**, *3*, 605.
- (152) Grazia De Angelis, M.; Sarti, G. C. *Ind. Eng. Chem. Res.* **2008**, *47*.
- (153) Fleischer, G. *Colloid Polym. Sci.* **1984**, *261*, 919.
- (154) Cong, H.; Hu, X.; Radosz, M.; Shen, Y. *Ind. Eng. Chem. Res.* **2007**, *46*, 2567.
- (155) Van Hecke, M. J. *Phys.: Condens. Matter* **2010**, *22*, 033101.
- (156) Mohan, L.; Bonnecaze, T. R. *Soft Matter* **2012**, *8*, 4216.
- (157) Hoa, M. L. K.; Lu, M.; Zhang, Y. *Adv. Colloid Interface Sci.* **2006**, *121*, 9.
- (158) Thomas, A.; Goettmann, F.; Antonietti, M. *Chem. Mater.* **2008**, *20*, 738.
- (159) Potter, O. G.; Hilder, E. F. *J. Sep. Sci.* **2008**, *31*, 1881.
- (160) Ferey, G. *Chem. Soc. Rev.* **2008**, *37*, 191-214.
- (161) Thomas, A.; Kuhn, P.; Weber, J.; Titirici, M.-M.; Antonietti, M. *Macromol. Rapid Commun.* **2009**, *30*, 221.
- (162) Burton, A. *Nat. Mater.* **2003**, *2*, 438.
- (163) Sakintuna, B.; Yurum, Y. *Ind. Eng. Chem. Res.* **2005**, *44*, 2893.
- (164) Lee, J.; Kim, J.; Hyeon, T. *Adv. Mater.* **2006**, *18*, 2073.
- (165) Granitzer, P.; Rumpf, K. *Materials* **2010**, *3*, 943.
- (166) Czaja, A. U.; Trukhan, N.; Muller, U. *Chem. Soc. Rev.* **2009**, *38*, 1284.
- (167) Silva, C. G.; Corma, A.; Garcia, H. J. *Mater. Chem.* **2010**, *20*, 3141.
- (168) Xue, M. J.; Xiao, W. T.; Zhang, Z. J. *Adv. Mater.* **2008**, *20*, 439.
- (169) Antonietti, M.; Göltner, C.; Hentze, H.-P. *Langmuir* **1998**, *14*, 2670.
- (170) Arcella, V.; Ghielmi, A.; Tommasi, G. *Ann. N. Y. Acad. Sci.* **2003**, *984*, 226.
- (171) Thomas, R. R. *Material properties of fluoropolymers and perfluoroalkyl-based polymers*; Kluwer Academic/Plenum Publishers: New York, 1999; Vol. 2.
- (172) Banerjee, S.; Curtin, D. E. In *Fluorine in Alternative Energy Sources* 2004; Vol. 125, p 1211-1216.
- (173) Schmidt-Rohr, K.; Chen, Q. *Nat. Mater.* **2008**, *7*, 75.
- (174) Hestekin, J. A.; Gilbert, E. P.; Henry, M. P.; Datta, R.; St. Martin, E. J.; Snyder, S. W. *J. Membr. Sci.* **2006**, *281*, 268.
- (175) Chaouk, H.; Wilkie, J. S.; Meijs, G. F.; Cheng, H. Y. *J. Appl. Polym. Sci.* **2001**, *80*, 1756-1763.
- (176) Johnson, G.; Meijs, G. F.; Laycock, B. G.; Griffith, M. G.; Chaouk, H.; Steele, J. G. *J. Biomater. Sci., Polym Ed.* **1999**, *10*, 217.
- (177) Xie, R. Z.; Evans, M. D. M.; Bojarski, B.; Hughes, T. C.; Chan, G. Y.; Nguyen, X.; Wilkie, J. S.; McLean, K. M.; Vannas, A.; Sweeney, D. F. *Invest. Ophthalmol. Vis. Sci.* **2006**, *47*, 574.
- (178) Wegener, M.; Wirges, W.; Tiersch, B. *J. Porous Mater.* **2007**, *14*, 111.
- (179) Nam, Y. S.; Yoon, J. J.; Park, T. G. *J. Biomed. Mater. Res.* **2000**, *53*, 1.
- (180) Cooper, A. I. *J. Mater. Chem.* **2000**, *10*, 207.
- (181) Weber, J.; Antonietti, M.; Thomas, A. *Macromolecules* **2007**, *40*, 1299-1304.
- (182) Johnson, S. A.; Ollivier, P. J.; Mallouk, T. E. *Science* **1999**, *283*, 963-965.
- (183) Choi, D.-H.; Ryoo, R. *J. Mater. Chem.*, *20*, 5544-5550.
- (184) Krishnamoorti, R. *MRS Bulletin* **2007**, *32*, 341.
- (185) Zhang, H.; Wang, S.; Weber, S. G. *Anal. Chem.* **2012**, *84*, 9920.
- (186) Zhang, H.; Wang, S.; Weber, S. G. *J. Membr. Sci.* **2013**, *443*, 115.

- (187) Long, Z.; Hill, K.; Sepaniak, M. J. *Anal. Chem.* **2010**, *82*, 4114.
- (188) Levit, N.; Pestov, D.; Tepper, G. *Sens. Actuators B*, **2002**, *82*, 241.
- (189) Ko, K.-S.; Jaipuri, F. A.; Pohl, N. L. *J. Am. Chem. Soc.* **2005**, *127*, 13162.
- (190) Mamidyala, S. K.; Ko, K.-S.; Jaipuri, F. A.; Park, G.; Pohl, N. L. *J. Fluorine Chem.* **2006**, *127*, 571.
- (191) Jaipuri, F. A.; Collet, B. Y. M.; Pohl, N. L. *Angew. Chem. Inter. Ed.* **2008**, *47*, 1707.
- (192) Vegas, A. J.; Bradner, J. E.; Tang, W.; McPherson, O. M.; Greenberg, E. F.; Koehler, A. N.; Schreiber, S. L. *Angew. Chem. Inter. Ed.* **2007**, *46*, 7960.
- (193) Nicholson, R. L.; Ladlow, M. L.; Spring, D. R. *Chem. Commun.* **2007**, 3906.
- (194) Zhang, Q.; Zhang, T.; Ge, J.; Yin, Y. *Nano Lett.* **2008**, *8*, 2867.
- (195) Weber, J.; Antonietti, M.; Thomas, A. *Macromolecules* **2008**, *41*, 2880.
- (196) Weber, J.; Thomas, A. *J. Am. Chem. Soc.* **2008**, *130*, 6334.
- (197) Tsujita, Y. *Prog. Polym. Sci.* **2003**, *28*, 1377.
- (198) Miguel, G. S.; Fowler, G. D.; Sollars, C. J. *Ind. Eng. Chem. Res.* **1998**, *37*, 2430.
- (199) Jiao, F.; Bruce, P. G. *Angew. Chem. Int. Ed.* **2004**, *43*, 5958.
- (200) Sing, K. S. W.; Everett, D. H.; Haul, R. A. W.; Moscou, L.; Pierotti, R. A.; Rouquerol, J.; Siemieniewska, T. *Pure Appl. Chem.* **1985**, *57*, 603.
- (201) DuPontTM Teflon[®] AF Product Information, http://www2.dupont.com/Teflon_Industrial/en_US/assets/downloads/h44587.pdf.
- (202) Hsieh, C.-T.; Chen, W.-Y.; Wu, F.-L.; Shen, Y.-S. *J. Adhes Sci Technol* **2008**, *22*, 265.
- (203) Yabu, H.; Shimomura, M. *Chem. Mater.* **2005**, *17*, 5231.
- (204) Quinn, A.; Sedev, R.; Ralston, J. *J. Phys. Chem. B* **2003**, *107*, 1163.
- (205) Drechsler, A.; Petong, N.; Zhang, J.; Kwok, D. Y.; Grundke, K. *Colloids Surf., A* **2004**, *250*, 357-366.
- (206) Lyklema, J. *Fundamentals of Interface and Colloid Science*; Academic Press: London, 2001; Vol. Volume II: Solid-Liquid Interfaces
- (207) Jubery, T. Z.; Prabhu, A. S.; Kim, M. J.; Dutta, P. *Electrophoresis* **2012**, *33*, 325-333.
- (208) Gladysz, J. A.; Emnet, C. In *Handbook of Fluorous Chemistry*; Wiley-VCH Verlag GmbH & Co. KGaA: 2005, p 11-23.
- (209) Dalvi, V. H.; Rossky, P. J. *Proc. Nat. Acad. Sci.* **2010**, *107*, 13603.
- (210) Gladysz, J. A.; Corrêa da Costa, R. In *Handbook of Fluorous Chemistry*; Wiley-VCH Verlag GmbH & Co. KGaA: 2005, p 24-40.
- (211) Vegas, A. J.; Bradner, J. E.; Tang, W.; McPherson, O. M.; Greenberg, E. F.; Koehler, A. N.; Schreiber, S. L. *Angew. Chem. Inter. Ed.* **2007**, *46*, 7960.
- (212) Orner, B. P.; Derda, R.; Lewis, R. L.; Thomson, J. A.; Kiessling, L. L. *J. Am. Chem. Soc.* **2004**, *126*, 10808.
- (213) O'Neal, K. L.; Weber, S. G. *J. Phys. Chem. B* **2008**, *113*, 149.
- (214) Amendola, V.; Fabbriizzi, L.; Mosca, L.; Schmidtchen, F.-P. *Chem. Eur. J.* **2011**, *17*, 5972.
- (215) Lagalante, A. F.; Hall, R. L.; Bruno, T. J. *J. Phys. Chem. B* **1998**, *102*, 6601.
- (216) Parbhoo, D. M.; Chetty, D. K.; Bayles, J. W. *J. Chem. Soc., Perkin Trans.* **1975**, 1057.
- (217) Tamada, J. A.; King, C. J. *Ind. Eng. Chem. Res.* **1990**, *29*, 1327.

- (218) Abraham, M. H.; Duce, P. P.; Schulz, R. A.; Morris, J. J.; Taylor, P. J.; Barratt, D. *G. J. Chem. Soc., Faraday Trans. 1* **1986**, *82*, 3501.
- (219) Chocholousova, J.; Vacek, J.; Hobza, P. *J. Phys. Chem. A* **2003**, *107*, 3086.
- (220) Pham, H. H.; Taylor, C. D.; Henson, N. J. *J. Chem. Phys. B* **2012**, *117*, 868.
- (221) Bezrodna, T. *J. of Mol. Struct.* **2013**, *1040*, 112.
- (222) Christian, S. D.; Stevens, T. L. *J. Phys. Chem.* **1972**, *76*, 2039.
- (223) Higazy, W. S.; Taha, A. A. *J. Phys. Chem.* **1970**, *74*, 1982.
- (224) O'Neal, K. L.; Geib, S.; Weber, S. G. *Anal. Chem.* **2007**, *79*, 3117.
- (225) Doan, V.; Koppe, R.; Kasai, P. H. *J. Am. Chem. Soc.* **1997**, *119*, 9810.
- (226) Bell, P. W.; Thote, A. J.; Park, Y.; Gupta, R. B.; Roberts, C. B. *Ind. Eng. Chem. Res.* **2003**, *42*, 6280.
- (227) Arnett, E. M.; Chawla, B. *J. Am. Chem. Soc.* **1979**, *101*, 7141.
- (228) Trzaska, S. M.; Toone, E. J.; Crumbliss, A. L. *Inorg. Chem.* **2000**, *39*, 1071.
- (229) Jelesarov, I.; Bosshard, H. R. *J. Mol. Recognit.* **1999**, *12*, 3-18.
- (230) Norris, A. L.; Serpersu, E. H. *Biochemistry* **2011**, *50*, 9309-9317.
- (231) Smithrud, D. B.; Wyman, T. B.; Diederich, F. *J. Am. Chem. Soc.* **1991**, *113*, 5420.
- (232) Balevicius, V.; Bariseviciute, R.; Aidas, K.; Svoboda, I.; Ehrenberg, H.; Fuess, H. *Phys. Chem. Chem. Phys.* **2007**, *9*, 3181.
- (233) Jeffrey, G. A. *An Introduction to Hydrogen Bonding*; Oxford University Press, 1997.
- (234) Golubev, N. S.; Smirnov, S. N.; Gindin, V. A.; Denisov, G. S.; Benedict, H.; Limbach, H.-H. *J. Am. Chem. Soc.* **1994**, *116*, 12055.
- (235) Koch, U.; Popelier, P. L. A. *J. Phys. Chem.* **1995**, *99*, 9747.
- (236) Del Bene, J. E.; Elguero, J. *J. Phys. Chem. A* **2005**, *110*, 1128.